

Modeling of Spatial and Morphological Changes in Bhairab-Atai-Rupsha River Confluence

By

Chandan Mondal

A thesis submitted in partial fulfillment of the requirements for the degree of
Master of Science in Civil Engineering in the Department of Civil Engineering




Khulna University of Engineering & Technology

Khulna 9203, Bangladesh

March 2018

Declaration

This is to certify that the thesis work entitled "*Modeling of Spatial and Morphological Changes in Bhairab-Atai-Rupsha River Confluence*" has been carried out by *Chandan Mondal* in the *Department of Civil Engineering*, Khulna University of Engineering & Technology, Khulna, Bangladesh. The above thesis work or any part of this work has not been submitted anywhere for the award of any degree or diploma.



Signature of Supervisor




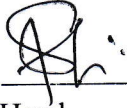
Signature of Candidate


Approval


This is to certify that the thesis work submitted by Chandan Mondal entitled "Modeling of Spatial and Morphological Changes in Bhairab-Atai-Rupsha River Confluence" has been approved by the board of examiners for the partial fulfillment of the requirements for the degree of Master of Science in Civil Engineering in the Department of Civil Engineering, Khulna University of Engineering & Technology, Khulna, Bangladesh in March 2018.


BOARD OF EXAMINERS

1. 

Dr. Md. Jahir Uddin
Associate Professor
Khulna University of Engineering & Technology
Chairman
(Supervisor)
2. 

Head
Department of Civil Engineering
Khulna University of Engineering & Technology
Member
3. 

Dr. Md. Shahjahan Ali
Professor
Khulna University of Engineering & Technology
Member
4. 

Dr. S. M. Moniruzzaman
Professor
Khulna University of Engineering & Technology
Member
5. 

Prof. Dr. M. Monowar Hossain
Executive Director
Institute of Water Modelling (IWM), Dhaka
Member
(External)

Acknowledgement

In prolog, all thanks to the Almighty for granting me blessings all along the way that I have completed this thesis within fixed schedule. I wish to thank all those people who have reinforced me throughout this study directly or indirectly.

Especially, I am appreciative to the both sponsors of University Grants Commission (UGC) and the higher administration of Khulna University of Engineering & Technology (KUET), Khulna, Bangladesh for sufficient funding for the completion of my research work.

I would express my gratitude to my supervisor, Dr. Md. Jahir Uddin, Associate Professor, Department of Civil Engineering, KUET, who has led me and presented me with a challenging new research theme. It was a great privilege and honor to work and study under his guidance. His cooperation throughout the thesis periods have brought me to the point of successfully completing this thesis work. It would have been impossible for me to complete this thesis without his continuous support. It was a valuable experience to work under the guidance of Dr. Md. Jahir Uddin, a person having highly disciplined life style, well behaved even in adverse situations and capable of giving right and prompt decision with philosophical opinion.

I would also like to acknowledge Prof. Dr. M. Monowar Hossain, Executive Director, Institute of Water Modeling (IWM), Bangladesh, whose valuable comments and corrections concerning my first draft directed me correctly to rearrange the whole report precisely.

I am also grateful to Dr. Md. Shahjahan Ali, Professor, Department of Civil Engineering, KUET for his generous help as always, not only the useful comments on my study, but meticulous checking on my research procedure.

The invaluable insights, advice and support of Dr. S. M. Moniruzzaman, Professor, Department of Civil Engineering, KUET are always thoughtful and highly appreciated.

Also I am grateful to Md. Esraz-UI-Zannat, Assistant Professor, Department of Urban and Regional Planning, KUET for unveiling a new horizon of obscure knowledge, really necessary for my research.

Lastly, wish to give the especial gratitude to my parents for their selfless dedication, great efforts without any complaints, never-endless care and encouragement during my long time study.

To

Mythical bird Phoenix, who always inspires me to rise from zero

Abstract

The Rupsha River, also known as Pasur, which is formed of the union of the Bhairab and Atai rivers. At present, much of its water is from the Gorai diverted through the Nabaganga. From near Batiaghata upazila the Rupsa changes its name to Kazibacha, which is given up near Chalna in favour of Pasur. Near the Mongla port, the Pasur receives Mongla river, and near the forest outpost at Chandpai it receives the Mirgamari cross-channel from the Bhola, both on the left-bank. On the right bank the Manki, Dhaki and Bhadra are linked to the Shibsra system. In the lower delta, the Rupsa-Pasur is second only to the Meghna in size. Formerly it was third, after the Gorai-Madhupati, but with the considerable diversion of the Ganges water at upstream and due to less flow in the Gorai, the Gorai-Modhumati flow dwindled and as a result the Pasur gradually become bigger. Notable Nabaganga also receives flow from Modhumati. The Bhairab-Atai-Rupsha confluence system is the life line at upstream, situated at the center of Khulna city. Bhairab and Atai are the only gateways to reach to the upstream through Rupsha and Pasur. Therefore, morphological and environmental pattern study, of this three rivers system and their catchment area is very important. In this study, morphological behavior of total length of Atai and Rupsa River and two of the confluences in between their accumulated length is accomplished. Moreover, environmental and land surface pattern of the catchment area are studied in different point of view, such as Land Surface Temperature (LST), vegetation cover, amount of water body, barren and urban area etc.

Two types of solver, named Nays2DH and River2D of iRIC 2.3 version software package, are used for modeling flow pattern in channel meander and confluence respectively. ArcGIS 10.4.1 version software package is used to study the environmental and land surface pattern of the catchment area. All the morphological data are collected from Bangladesh Water development Board (BWDB). Necessary satellite data, for selecting catchment area and environmental study, are collected from different website of the National Aeronautics and Space Administration (NASA), as <https://glovis.usgs.gov/>, <https://earthexplorer.usgs.gov/> etc. The catchment area is selected from SRTM 1 Arc-Second Global digital elevation model (DEM) data. Before morphological modeling, a previous experimental work and related numerical models are compared with present numerical model, to observe applicability of the present study. During morphological modeling of meander and confluence, both high and ebb-tide condition is considered, as this river system is under tidal influence. For the simulation of high and ebb-tide condition, fixed discharge is considered and discharge data are collected from the Mongla Port Authority (MPA). Satellite image processing technique is used, during modeling of environmental and land surface pattern of the catchment area.

From modeling of river meander, positions are recognized along the length of Atai and Rupsha River, where flow velocity is decreased. From flow velocity and elevation relationship of the model, it is observed that velocity is decreased significantly, where flow depth is lower. It happens mainly because of channel bed friction, which significantly affects the channel flow. Also, it is found that secondary current is strong

at both banks of the river, which creates a three dimensional effect and reduce the primary flow velocity magnitude near the banks. This flow velocity reduction causes siltation to a particular position of the channel, which brings inefficient navigability. So from this model, position of necessary future dredging work can be determined.

Determination of separation zone is an important task to understand the complex flow pattern near the estuary of the confluence. During modeling of the confluence, these separation zones are detected both for high- tide and ebb-tide condition. So, from the separation zones, place of siltation near the estuary also be detected. Formation of separation zone is largely dependent on the channel geometry near the estuary. A hypothesis is proposed to reduce the intensity of the separation zone, by changing the geometry near the estuary. After changing geometry, the confluences are remodeled and a partial success is observed as separation zone is reduced in size and in some case eliminated.

Lastly the modeling of environmental and land surface pattern of the catchment area shows that, at present large vegetation areas like Sundarban is under drought condition, while at past it was totally different. The reason may be increase of salinity in the western part of Bangladesh. Also, it is observed that barren area is mostly replaced by small vegetation like crop field. Lastly Land Surface Temperature (LST) decreases recently rather than the past because of replacement of barren area by small vegetation.

A morphological model developed in this study largely reflects the flow pattern in Bhairab, Atai and Rupsha river geometries. Also the environmental and land surface pattern model of the catchment area reflects the present land surface pattern as compared with past years. From these models, several decisions can be made to keep the channel and estuaries functional as well as the catchment area habitable. This type of model based study addressed in this research, really convenient, helpful, cheap and less time consuming for predicting and making an engineering decision for different morphological and environmental condition.

Content

Title	Page No.
Declaration	i
Approval	ii
Board of Examiners	iii
Acknowledgement	iv
Abstract	vi-vii
Content	viii-xviii

Chapter 1	Introduction	
	1.1	General 1
	1.2	Importance of Morphological and Environmental Study 5
	1.3	Objective and Scope of the Study 6
	1.3.1	Objective 6
	1.3.2	Scope of the Study 6
Chapter 2	Literature Review	
	2.1	Background of the Study 8
	2.2	Software and Tools 11
	2.2.1	iRIC 11
	2.2.2	Nays2DH 12
	2.2.3	River2D 13
	2.2.4	ArcGIS 14
	2.2.5	Erdas Imagine 14
	2.2.6	Microsoft Excel 15
	2.2.7	Microsoft Word 15
Chapter 3	Modeling of Channel Meander	
	3.1	Introduction 16
	3.2	Governing Equation 16
	3.2.1	Basic flow equations in orthogonal coordinates 16
	3.2.2	Transformation into General Curvilinear Coordinates 17
	3.2.3	Basic equations in a general curvilinear coordinate system 19
	3.2.4	Turbulence model by depth-averaged $k-\varepsilon$ model 21

3.2.5	Model of River Bed Friction	22
3.2.6	Method for Calculating Resistance by Vegetation	23
3.2.7	Dimensionless River Bed Shearing Force	23
3.2.8	Bed Load Transport	23
3.2.9	Calculation of Bedload Transport Vector	24
3.2.10	Streamline Curvature	25
3.2.11	Upward Flux of Suspended Load From River Bed	26
3.2.12	Continuity equation of suspended load concentration	27
3.2.13	Continuity Equation of Sediment Transport	27
3.3	Numerical Method	28
3.3.1	Finite Difference Method	28
3.3.2	Accuracy and Order	29
3.3.3	Upwind Difference Method	30
3.3.4	First-Order Upwind Scheme	30
3.3.5	Compact Form	31
3.3.6	Stability	31
3.4	Applicability of Present Study for Modeling Flow in Meander	32
3.4.1	Numerical Method Followed by Seo and Park (2010)	32
3.4.2	Laboratory Setup for Experiment by Seo and Park (2010)	33
3.4.3	Numerical Solution by iRIC Nays2DH (Present study)	33
3.4.4	Comparison of Simulation Result from Present Study with Seo and Park (2010)	34
3.5	Modeling of River Meander	37
3.6	Input of Cross-section Geometry in Nays2DH	40
3.7	Result	41
3.7.1	High-tide	42
3.7.2	Ebb-tide	48
3.7.3	Particle Movement and Velocity Distribution	53
3.7.4	Simulation of Combined Length of the Rivers	56

	3.8	Conclusion	61
Chapter 4		Modeling of Channel Confluence	
	4.1	Introduction	62
	4.2	Governing Equation	62
	4.2.1	Basic Flow Equation	62
	4.2.2	Bed Resistance Model	63
	4.2.3	Transverse Shear Model	64
	4.2.4	Wet/Dry Area Treatment	65
	4.2.5	Boundary Extraction Module	65
	4.3	Numerical Method	68
	4.3.1	The Finite Element Method	68
	4.3.2	Weighted Residual Methods	71
	4.3.3	General Formulation of WRM	71
	4.3.4	Upwind Type Finite Elements – A Petrov Galerkin Formulation	72
	4.3.5	Discretization Error	76
	4.3.6	Solution Methods	77
	4.4	Applicability of Present Study for Modeling Flow in Confluence	78
	4.4.1	Laboratory Setup by Weber et al. (2001)	78
	4.4.2	Model Developed by Thanh et al. (2010)	81
	4.4.3	Numerical Modeling of Weber et al. (2001) (Present Study)	82
	4.4.4	Comparison of Present Study with Weber et al. (2001) and Thanh et al. (2010)	83
	4.5	Applicability of Present Study for Modeling Flow in Diversion	88
	4.5.1	Laboratory Setup by Barkdoll et al. (1998)	88
	4.5.2	Model Developed by Ashari et al. (2015)	90
	4.5.3	Numerical Modeling of Barkdoll et al. (1998) (Present study)	90
	4.5.4	Comparison of Present Study with Barkdoll et al. (1998) and Ashari et al. (2015)	92
	4.6	Modeling of River Confluence	96
	4.6.1	Source of Data	97
	4.6.2	Input of Elevation Data in River2D	97
	4.7	Result	99
	4.8	Hypothesis of Changing Confluence Geometry	102

	4.9	Remodeled result	104
	4.10	Conclusion	112
Chapter 5		Modeling of Bank and Confluence Shifting	
	5.1	Introduction	113
	5.2	Methodology	113
	5.3	Governing equation	114
	5.3.1	Linear regression	114
	5.3.2	Percent error	116
	5.4	Result	116
	5.5	Conclusion	125
Chapter 6		Modeling of Land Surface Temperature (LST)	
	6.1	Introduction	127
	6.2	Study Area	127
	6.3	Resources and Techniques	127
	6.4	Governing Equation for LST and Other Indices	128
	6.4.1	Normalized Difference Water Index	128
	6.4.2	Normalized Difference Vegetation Index	128
	6.4.3	Normalized Difference Built-up Index	129
	6.4.4	Land Surface Temperature calculation	130
	6.5	Result and Discussion	131
	6.6	Conclusion	141
Chapter 7		Summary and Discussion	
	7.1	Introduction	142
	7.2	Summary of the study	142
	7.2.1	Morphological Model	142
	7.2.2	Spatial & Environmental Model	144
	7.3	Conclusion	144
	7.4	Recommendation for Future Study	145
References			146

List of Figures

		Page No.
Figure 1.1	River network map of Bangladesh shows the position of Rupsha river in Khulna	2
Figure 1.2	Location of the study area in Bangladesh and coverage on Dhaka and Khulna division, Bangladesh	3
Figure 1.3	Position of Bhairab, Atai and Rupsha river and other river and channel in study area	4
Figure 1. 4	Magnified view of Bhairab, Atai and Rupsha River in the study area	5
Figure 2.1	Flow diagram of iRIC Operations	12
Figure 3. 1	Calculation steps in upwind scheme	31
Figure 3. 1	Sketches of S-curved laboratory channel (top: plan view, bottom: side view; unit: cm) (Seo and Park, 2010)	33
Figure 3.2	Grid shape and position for numerical solution	34
Figure 3.3	Vector maps of velocity profiles (Seo and Park, 2010)	35
Figure 3.5	Vector maps of velocity profiles (present study)	35
Figure 3.4	Velocity contour map (present study)	36
Figure 3.7	Comparison of primary flow at the first bend (Section 4)	36
Figure 3. 8	Comparison of primary flow at the second bends (Section 9)	37
Figure 3. 5	Part A, Part B and Part C along the length of river	38
Figure 3.6	Cross-section position and number arrangement during high-tide	39
Figure 3.11	Cross-section position and number arrangement during ebb-tide	39
Figure 3.12	Concept of River Survey File data	40
Figure 3.13	Elevation, Water Surface Elevation, Velocity, Froude Number contour of Section A during high-tide (Flow from South to North)	42
Figure 3.14	Elevation, Water Surface Elevation, Velocity, Froude Number along the length of Section A from left bank to right bank during high-tide.	43
Figure 3. 15	Elevation, Water Surface Elevation, Velocity, Froude Number contour of Part B during high-tide (Flow from South to North)	44

Figure 3.16	Elevation, Water Surface Elevation, Velocity, Froude Number along the length of Part B from left bank to right bank during high-tide.	45
Figure 3.17	Elevation, Water Surface Elevation, Velocity, Froude Number contour of Part C during high-tide (Flow from South to North)	46
Figure 3.18	Elevation, Water Surface Elevation, Velocity, Froude Number along the length of Part C from left bank to right bank during high-tide.	47
Figure 3.19	Elevation, Water Surface Elevation, Velocity, Froude Number contour of Part A during ebb-tide (Flow from North to South)	48
Figure 3.20	Elevation, Water Surface Elevation, Velocity and Froude Number along the length of Part A from left bank to right bank during ebb-tide.	49
Figure 3.21	Elevation, Water Surface Elevation, Velocity, Froude Number contour of Part B during ebb-tide (Flow from North to South)	50
Figure 3.22	Elevation, Water Surface Elevation, Velocity, Froude Number along the length of Part B from left bank to right bank during ebb-tide	51
Figure 3.23	Elevation, Water Surface Elevation, Velocity, Froude Number contour of Part C during ebb-tide (Flow from North to South)	52
Figure 3.24	Elevation, Water Surface Elevation, Velocity, Froude Number along the length of Part C from left bank to right bank during ebb-tide.	53
Figure 3.25	Particle movement and velocity distribution along the length of Part A the cross-section during high-tide (left) and ebb-tide (right)	54
Figure 3.26	Particle movement and velocity distribution along the length of Part B across the cross-section during high-tide (left) and ebb-tide (right)	55
Figure 3.27	Particle movement and velocity distribution along the length of Part C across the cross-section during high-tide (left) and ebb-tide (right)	55
Figure 3.28	Simulation of high-tide condition of the combined length of two rivers	56
Figure 3.29	Elevation, Water Surface Elevation, Velocity, Froude Number along the combined length from left bank to right bank during high-tide	57-58
Figure 3.30	Simulation of ebb-tide condition of the combined length of two rivers	59

Figure 3. 31	Elevation, Water Surface Elevation, Velocity, Froude Number along the combined length from left bank to right bank during ebb-tide	60
Figure 4. 1	The relationship between stream function and discharge: (a) a schematic of a stream tube and (b) the calculation of discharge across an elemental stream tube.	67
Figure 4. 2	A sample triangulation.	70
Figure 4.3	Mesh of 5 equi-length linear elements	73
Figure 4.4	One dimensional mesh of equi-length linear elements	73
Figure 4. 5	Distortion of the upwind side	74
Figure 4.6	Performance of Petrov GFEM with bubble functions with four different upwinding parameters. All results are for $Pe = 5$	75
Figure 4.7	Error related to piecewise interpolation.	76
Figure 4. 8	Experimental Flume Layout by Weber et al. (2001)	78
Figure 4. 9	(a) Location of: Cross Sections (b) Location of Flow Velocity Measurements (Weber et al., 2001)	80
Figure 4.10	Grid shape for numerical simulation in present study	82
Figure 4.11	Color contour of velocity distribution for condition $q^* = 0.25$ (Present study)	84
Figure 4. 12	Comparison of longitudinal velocity component at some locations for $q^* = 0.25$	85-86
Figure 4.13	Color contour of velocity distribution for condition $q^* = 0.75$ (Present study)	87
Figure 4.14	Comparison of longitudinal velocity component at some locations for $q^* = 0.75$	87-88
Figure 4.15	Test Section of Experimental Setup by Barkdoll et al (1998)	89
Figure 4. 16	Grid shape for numerical simulation in present study	91
Figure 4.17	Color contour of velocity distribution	92
Figure 4. 18	Evaluation of computational velocity profiles at different sections of the main channel	93-94
Figure 4.19	Evaluation of computational velocity profiles at different sections of the branch channel	95-96
Figure 4. 20	Position of the two confluences in study area	96
Figure 4. 21	Extracted elevation data of Confluence 1 from DEM after importing in River2D as *.tpo file.	98
Figure 4. 22	Extracted elevation data of Confluence 2 from DEM after importing in River2D as *.tpo file.	98

Figure 4.23	Velocity magnitude contour due to channel flow during high-tide at Confluence 1	99
Figure 4.24	Velocity magnitude contour due to channel flow during ebb-tide at Confluence 1	100
Figure 4.25	Velocity magnitude contour due to channel flow during high-tide at Confluence 2	101
Figure 4.26	Velocity magnitude contour due to channel flow during ebb-tide at Confluence 2	101
Figure 4.27	Concept of changing of branch estuary geometry	102
Figure 4.28	Formation of flow separation and stagnation zone based on flow direction	103
Figure 4.29	Estuary geometry changing operation	103
Figure 4.30	Expected flow scenario in converted estuary	104
Figure 4.31	Velocity magnitude contour due to channel flow during high-tide at Confluence 1 after changing geometry	104
Figure 4.32	Velocity magnitude contour due to channel flow during ebb-tide at Confluence 1 after changing geometry	105
Figure 4.33	Comparison of Confluence 1 before (a) and after (b) changing geometry of branch estuary, during high-tide	105
Figure 4.34	Comparison of Confluence 1 before (a) and after (b) changing geometry of branch estuary, during ebb-tide	106
Figure 4.35	Velocity magnitude contour due to channel flow during high-tide at Confluence 2 after changing geometry	106
Figure 4.36	Velocity magnitude contour due to channel flow during ebb-tide at Confluence 2 after changing geometry	107
Figure 4.37	Comparison of Confluence 2 before (a) and after (b) changing geometry of branch estuary, during high-tide	107
Figure 4.38	Comparison of Confluence 2 before and after changing geometry of branch estuary, during ebb-tide	108
Figure 4.39	Velocity magnitude contour due to channel flow during high-tide at Confluence 2 after changing geometry (second time)	108
Figure 4.40	Velocity magnitude contour due to channel flow during ebb-tide at Confluence 2 after changing geometry (second time)	109
Figure 4.41	Comparison of Confluence 2 before and after changing geometry of branch estuary, during high-tide (second time)	109
Figure 4.42	Comparison of Confluence 2 before and after changing geometry of branch estuary, during ebb-tide (second time)	110
Figure 4.43	Velocity magnitude contour due to channel flow during high-tide at Confluence 2 after changing geometry (third time)	110

Figure 4.44	Velocity magnitude contour due to channel flow during ebb-tide at Confluence 2 after changing geometry (third time)	111
Figure 4.45	Comparison of Confluence 2 before and after changing geometry of branch estuary, during high-tide (third time)	111
Figure 4.46	Comparison of Confluence 2 before and after changing geometry of branch estuary, during ebb-tide (second time)	112
Figure 5. 1	Position of the cross-sections in Confluence 1 and Confluence 2 (RGB image 2018)	114
Figure 5. 2	Relative comparison of Confluence 1 in between 1988 and 2018	117
Figure 5. 3	Relative comparison of Confluence 2 in between 1988 and 2018	118
Figure 5. 4	Calculated coordinates of the left and right bank of each section on actual pattern of Confluence 1 during 2018	119
Figure 5. 5	Calculated coordinates of the left and right bank of each section on actual pattern of Confluence 2 during 2018	120
Figure 5. 6	Human activities around Confluence 2	121
Figure 5. 7	Predicted coordinates during 2030 on actual pattern of Confluence 1 in 2018	124
Figure 5. 8	Predicted coordinates during 2030 on actual pattern of Confluence 2 in 2018	125
Figure 6. 1	Logic of variation of NDVI value due to vegetation heath (courtesy NASA)	129
Figure 6. 2	Highest and lowest temperature of the study area in year 1991, 1996, 2002, 2006, 2011 and 2017	131
Figure 6. 3	Spatial distribution of temperature variation at study area in year 1991, 1996, 2002, 2006, 2011 and 2017	132
Figure 6. 4	Surface covered by vegetation and other type of features according to NDVI	133
Figure 6. 5	Surface covered by water-body and other type of features according to NDWI	134
Figure 6. 6:	Surface covered by build-up and barren area and other type of features according to NDBI	134
Figure 6. 7	Chronological conversion of barren area to vegetation covered area	136
Figure 6. 8	Highest, lowest value of NDVI and spatial coverage of vegetation during 1991, 1996, 2002, 2006, 2011 and 2017	137
Figure 6. 9	Highest, lowest value of NDWI and spatial coverage of water body during 1991, 1996, 2002, 2006, 2011 and 2017	138

Figure 6. 10 Spatial distribution of build-up and barren areas and other 139
type (vegetation, water) of coverage during year 1991,
1996, 2002, 2006, 2011 and 2017

List of Tables

	Page No.
Table 3.1 Model constants	22
Table 3.2 Calculation condition for numerical simulation	34
Table 3.3 Length and Position of Part A, Part B, Part C	37
Table 3.4 Structure of River Survey File (*.riv)	40
Table 4. 1 Experimental Flow Conditions	79
Table 4. 2 Repeatability of Measurements from Single Test Session	81
Table 4. 3 Repeatability of Measurements from Multiple Test Sessions	81
Table 4. 4 Calculation condition for modeling Weber et al (2001)	82
Table 4. 5 Conditions of geometric similarity of present model with prototype by Weber et al (2001)	83
Table 4.6 Calculation condition for numerical simulation	91
Table 4.7 Conditions of geometric similarity of present model with prototype by Barkdoll et al (1998)	91
Table 4.8 Position and accumulated rivers at the confluences	97
Table 4.9 Example of an elevation data file	97
Table 5.1 Actual, measured vales and percent errors of coordinates of the sections	121-123

CHAPTER 1

Introduction

1.1 General

The Rupsha River flows through southwestern part of Bangladesh and a distributary of the Ganges in the Ganges-Brahmaputra Delta. Rupsha is one of the major river of south-west of Bangladesh. It forms from the confluence of the Bhairab and Atai rivers, and flows into the Pasur River. Its entire length is affected by tides. It flows by the side of Khulna, and connects to the Bay of Bengal through Poshur River at Mongla channel. From Chalna, it is known as Pasur River and flows into the Bay of Bengal (Figure 1.1).

Generally, tidal rivers like Rupsha, are short rivers with relatively low discharge rates but high overall discharge; generally this implies a shallow river with a large coastal mouth. In some cases, high tides impound downstream flowing freshwater, reversing the flow and increasing the water level of the lower section of river, forming large estuaries. Rupsha is a meandering river but its meandering process is quite slow and geometry is very stable so that bank erosion is not severe like Dhorila river at Kurigram. A meander is one of a series of regular sinuous curves, bends, loops, turns, or windings in the channel of a river, stream, or other watercourse. It is produced by a stream or river swinging from side to side as it flows across its floodplain or shifts its channel within a valley. A meander is produced by a stream or river as it erodes the sediments comprising an outer, concave bank (cut bank) and deposits this and other sediment downstream on an inner, convex bank which is typically a point bar. The result of sediments being eroded from the outside concave bank and their deposition on an inside convex bank is the formation of a sinuous course as a channel migrates back and forth across the down-valley axis of a floodplain.

Rupsha meets with several rivers and channels and forms several numbers of confluences. In geography, a confluence occurs where two or more flowing bodies of water join together to form a single channel. A confluence can occur in several configurations: at the point where a tributary joins a larger river (main stem); or where two streams meet to become the source of a river of a new name (such as the confluence of the Bhairab and Atai rivers forming the Rupsha); or where two separated channels of a river (forming a river island) rejoin at the downstream end.

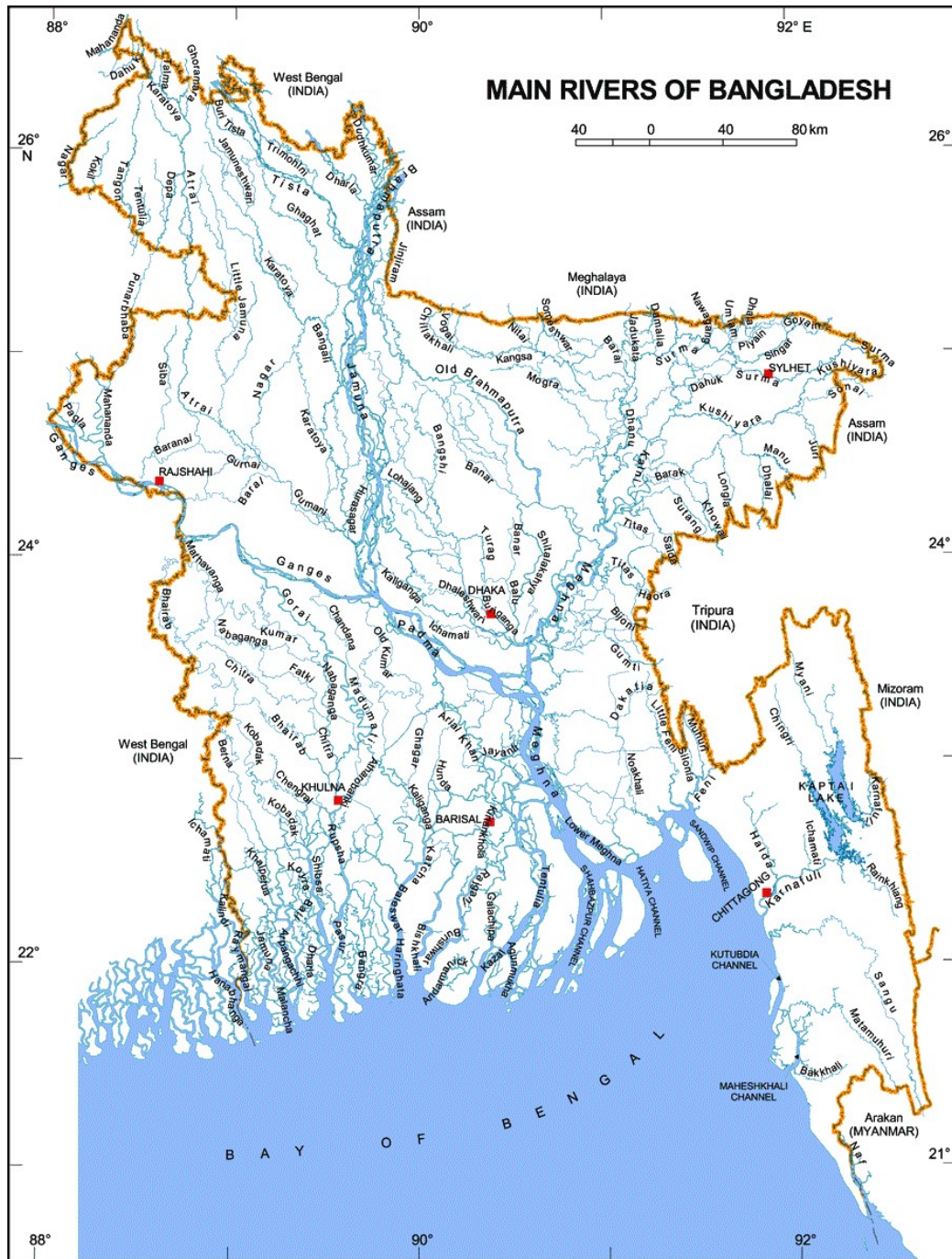


Figure 1. 1: River network map of Bangladesh shows the position of Rupsha river in Khulna (Source: <https://www.thebangladesh.net/rivers-of-bangladesh>)

Confluences are studied in a variety of sciences. Hydrology studies the characteristic flow patterns of confluences and how they give rise to patterns of erosion, bars, and scour pools. The water flows and their consequences are often studied with mathematical models. Confluences are relevant to the distribution of living organisms as well; the general pattern (downstream of confluences) of increasing stream flow and

decreasing slopes drives a corresponding shift in habitat characteristics (Collins et al., 2002).

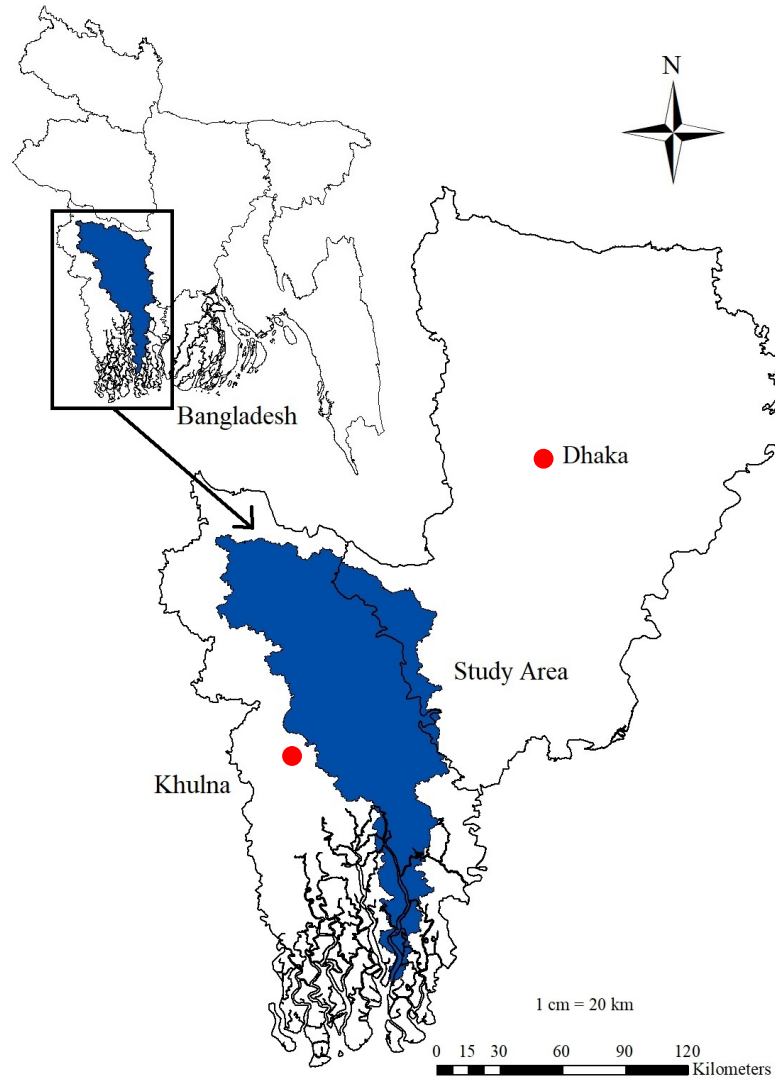


Figure 1.2: Location of the study area in Bangladesh and coverage on Dhaka and Khulna division, Bangladesh

Figure 1.2 shows the location of the study area in Bangladesh. Bhairab, Atai and Rupsha confluence zone is situated in heart of Khulna city, which is shown in Figure 1.3 and the magnified view is shown in Figure 1.4. Khulna is the third-largest city of Bangladesh. It is the administrative seat of Khulna District and Khulna Division. Khulna has an old river port located on the Rupsha River. It is an important hub of Bangladeshi industry and hosts many national companies. It is served by Port of Mongla, the second largest seaport in the country. It has also one of the two principal naval command centres of the Bangladesh Navy. Navy base BNS Titumir is located at the Bhairab, Atai and Rupsha confluence zone in the city.

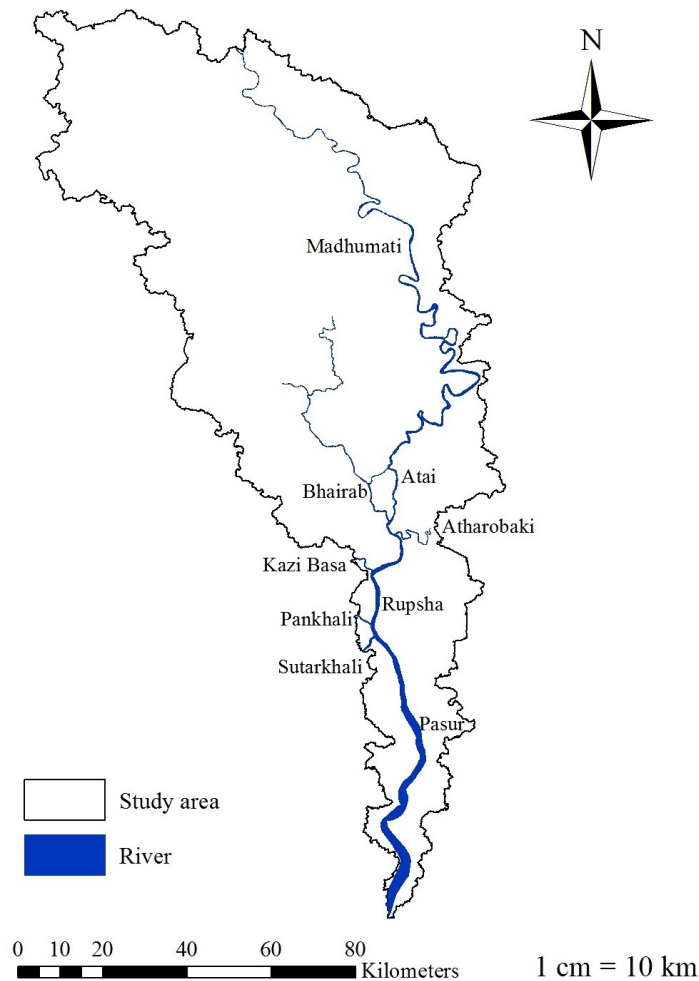


Figure 1. 3: Position of Bhairab, Atai and Rupsha river and other river and channel in study area

Figure 1.3 shows that the catchment area which covers 9072.94 square kilometer and the confluence comprised of several channels and rivers beside these three rivers. Upper part of the catchment area covers some part of the south-western corner of Dhaka division and the lower part ends at the center of Sundarban and before reaching Sundarban, Rupsha changes to Pasur. This catchment area covers both the urban, rural and cultivable areas of Khulna. These natural water bodies play an important role to keep the eco-system in a stable condition.

Now a day's weather pattern is changing and has become a global concern, especially country like ours which is not much above the sea level. If the sea level will rise abnormally, southern part of Bangladesh like Khulna, Barishal will be affected first. For this reason everyone should be concerned, about not only the morphological natures of the water bodies but the environmental condition of the catchment area as well. Because if it is possible, to keep an eye on analyzing morphological and environmental natures of the water bodies and their catchment area then their reservoir capacity is improved and thus these water bodies will play an important role by

reducing the intensity of natural disaster like flash flood or storm by storing excess flow of water. Besides this role, local water body can keep ambient environment favorable for living.



Figure 1. 4: Magnified view of Bhairab, Atai and Rupsha River in the study area

1.2 Importance of Morphological and Environmental Study

If morphological behavior of river network and environmental nature of its catchment area can be studied parallel, then it is possible to observe the local environmental change along with the river network. Because local eco-system as well as the local economy largely depends on the soil condition, vegetation, temperature and these types of variables profoundly relates with water body. Water body plays an important role in transportation, saves local community from disaster like flood by acting like a reservoir and passes the surplus water to the sea or lake at downstream, provide necessary water supply for irrigation. Well water reserve capacity of water body can keep ground water away from salinity by recharging ground water reserve and reducing the backward flow of saline water from downstream to upstream.

Study of flow pattern in a meandering river and confluence is very important to keep the river effective for both transportation and as a reservoir. Bar formation and siltation is great problem that reduce the capacity and capability of a river network. Studying morphology on a particular river network help to understand the particular nature of the network and the catchment area. Thus this study can be helpful during river bank management for erosion control, necessary dredging for navigability and construction of hydraulic structure that can reduce both scouring and siltation.

1.3 Objective and Scope of the Study

The objective of the study reflects the way of research to be directed and scope shows the type of study to do.

1.3.1 Objective

- To study the spatial and temporal change of Bhairab, Atai and Rupsha River catchment area.
- To develop a numerical model of Bhairab, Atai and Rupsha river confluence.
- To study the habitat changes of Bhairab, Atai and Rupsha River catchment area.

1.3.2 Scope of the Study

Channel meandering

- To perform validity analysis study to determine the level of accuracy during modeling of the meandering channel.
- To set up relations among velocity profile, depth of channel, water surface elevation and Froude number in case of real river.
- To study the flow pattern and all the above mentioned parameter in a real river channel during high-tide and ebb-tide.

Open channel confluence

- To perform validity analysis study to predict the level of accuracy during modeling both channel confluence and channel diversion.
- To study the separation zone and mixing length created, in both channel confluence and channel diversion during high-tide and ebb-tide.
- To analyze the reasons of velocity drop near the branch estuary.
- To introduce new concept to reduce the problem created due to separation zone.

Bank and confluence pattern migration

- To compare the past and future pattern of the confluences.

- To determine the accuracy of the prediction method by comparing the calculated data with real one.
- To determine the level of accuracy by calculating percent errors of the calculated data.
- To apply the prediction method for the determination of the confluence pattern at future.

Environmental study

- To develop a model of changing land surface pattern and vegetation.
- To study relation of land surface temperature variation with vegetation, water body, urban area and barren land area cover.
- To study the future condition that may hamper the catchment area both environmentally and economically.

CHAPTER 2

Literature Review

2.1 Background of the Study

Open-channel confluences are common in nature as well as in hydraulic structures and play an important role in fluvial channel processes (Thanh et al., 2010). Water has been diverted from its original pathway since a long time ago for a variety of applications, including agriculture, urban water supply, etc. Rivers are one of the cheapest and most available water resources for irrigation of green areas and agriculture, including fish farming which impoundment for different applications is important (Ashari et al., 2015). In this area of flow, fluid particles in the vicinity of the left wall of intake channel (toward the entry of the main channel) are rotational and actually this area of the lateral channel will have no effect on flow discharge rate. Due to the changes in velocity distribution in the intake area, sedimentation usually occurs at the intake entrance, which leads to the reduction in intake efficiency, entry of coarse sediments into the network and the increase in administrative costs for sediment removal operations. Every step which leads to the reduction in the secondary and vortex flows at intake entrance, will lead to the reduction in sediment accumulation at intake entrance as well as reduction in the sediment entering in to the intake. Law & Reynolds (1966) performed an analytical and experimental study on the main channel and deviation with equal width and succeeded to present a relation for the ratio of discharges, Froude number before and after the junction, and the ratio of widths of the two channels. Chen & Lian (1992), two-dimensionally simulated the geometry of T-junction, which was studied experimentally by Popp & Sallet in 1983, using standard K- ϵ model with above Reynolds numbers. The results obtained for the ratio of small discharges had proper agreement with the previous experimental measurements, but in the bigger discharges ratio, their predictions were significantly different with the measurements. Neary & Odgaard (1993) performed experimental studies on the flow hydraulics at 90 degree intakes. In this study, flow pattern, flow separation line, rest area, and the vortex formation area were investigated and the power of rotational flow in the vortex formation area increased with increasing the ratio of velocity in the intake channel to the main channel. Hager (1987), performed experimental studies on the measurement of length and width of the flow rotation area at 90 degree intake of a rectangular channel, and concluded that the dimensions of the flow separation zone depend on the ratio of diverted discharge and length and width of the rotation area at intake channel entrance decrease with increasing the intake ratio. Ramamurthy et al (2007) performed experimental studies at 90 degree intake for an open channel of rectangular section and

used three-dimensional precise instrumentations to measure velocity at different sections. Issa & Oliveira (1994) performed three-dimensional simulation of turbulent flow for T-shaped geometries. They solved Reynolds time-averaged Navier–Stokes equations (RANS) through K- ϵ -Standard model with wall functions. In their research, the equations were solved using Finite- Volume Method (FVM) with accuracy of one-order. Neary et al (1996) surveyed the layer flow pattern at 90 degree intake by providing a three-dimensional numerical model. These researchers used Finite-Volume method for solving the equations and managed to examine flow pattern in this field and qualitatively simulate the movement of bed load sediment particles. Neary et al (1999) performed a parametric study on the flow pattern in the lateral intake three-dimensionally using K- ω turbulence model. Shamloo & Pirzadeh (2008), numerically simulated flow hydraulics in the river lateral intakes using the Fluent Software. In this research, by choosing K- ϵ -Standard turbulence model, flow velocity profiles were evaluated three-dimensionally and a good agreement has been found between the obtained values and the experimental results. Goudarzizadeh et al (2010) numerically investigated a three-dimensional examination of the flow pattern in the intake in the direct path using the Finite Volume method.

The morphology of natural river channels is determined by the interaction of fluid flow, sediment transport, bank erosion, and bed morphology (Knighton 1984). Investigating the complex mechanism of patterning processes with various control factors has intrigued geomorphologists and river engineers for several decades, and with rapid development of numerical methods in fluid mechanics, computational model has become an important tool for studying the evolution of channel patterns. A common class of high-resolution models of river morphology is two-dimensional (2D) in the horizontal plane (Mosselman 1998). To simulate the bend development and lateral migration of alluvial channels, a 2D numerical model must account for bend flow effects and river bank erosion processes. Subsequent works on helical flow and forces on sediment grains on a transversely sloping bed (e.g., Einstein and Shen 1964; Engelund 1974; Bathurst et al . 1979; De Vriend 1977; Odgaard 1981; Kalkwijk and de Vriend 1980) resulted in 2D numerical models. River bank failures are modes of morphological evolution in addition to bed level and bed sediment composition changes. Physical principles have become a major concern over the past years. Meander models based on linearized physics-based equations (Ikeda et al. 1981; Johannesson and Parker 1989; Zolezzi and Seminara 2001; Crosato 2008) and 2D non-linear physics-based morphological models with erodible banks (Osman and Thorne 1988; Mosselman 1998; Darby et al. 2002; Duan 2005) have been established to simulate the channel planform evolution. Based on advances in numerical modeling and fundamental study on the physical mechanisms of channel evolution, some researchers have suggested using 2D numerical models to study the cause-and-effect relationship between river patterns and various control variables. Meandering rivers (Duan 2005; Duan and Julien 2010; Hyungsuk et al. 2011) and braided channels (Nicholas and Smith 1999; Xia et al. 2003; Schuurman et al. 2013) have been replicated in idealized experiment conditions with detailed data of river characteristics.

To understand not only the total morphological behavior but the environmental scenario of whole catchment area remote sensing study may be convenient. Global

warming is a global concern now. So studying vegetation, water content of soil and water body, expansion of urban area and land surface temperature may be indicators that express the condition of the catchment area.

Urbanization and transformation of the earth surface to urban application illustrate huge changes in global usage of the land and provide considerable influence on the environment (Weng & Yang, 2004). The population in global urban areas has risen quickly from 13% in 1900 up to 46% in 2000, and it is believed that it can go up to 69% by 2050. The influence of climate change is foreseeable in the shape of altering weather patterns and extreme weather events, like heavy rainfall, flood, windstorm, heat waves and windstorms (IPCC 2007). One of the main reasons for this type extreme weather condition occurring so frequently is global warming. Rapid urbanization, deforestation, filling up water body is some of the causes of global warming. Land Surface Temperature (LST) is a popular indicator of global warming, which is largely depends on vegetation, amount of water body and mostly urbanization. The Land Surface Temperature (LST) is the radiative skin temperature of the land surface, as measured in the direction of the remote sensor. It is estimated from Top-of-Atmosphere (TOA) brightness temperatures from the infrared spectral channels of a constellation of geostationary satellites. Its estimation further depends on the albedo, the vegetation cover and the soil moisture. LST is a mixture of vegetation and bare soil temperatures. The multi spectral remote sensing images are very efficient for obtaining a better understanding of the earth environment (Ahmadi & Nusrath, 2010). It is the science and art of acquiring information and extracting the features in form of spectral, spatial and temporal about some objects, area or phenomenon, such as vegetation, land cover classification, urban area, agriculture land and water resources without coming into physical contact of these objects (Karaburun, 2010). Certain pigments in plant leave strongly absorb wavelengths of visible (red) light. The leaves themselves strongly reflect wavelengths of near-infrared light, which is invisible to human eyes. As a plant canopy changes from early spring growth to late-season maturity and senescence, these reflectance properties also change. Many sensors carried aboard satellites measure red and near-infrared light waves reflected by land surfaces. Using mathematical formulas (algorithms), scientists transform raw satellite data about these light waves into vegetation indices. A vegetation index is an indicator that describes the greenness, the relative density and health of vegetation, for each picture element, or pixel, in a satellite image. Although there are several vegetation indices, one of the most widely used is the Normalized Difference Vegetation Index (NDVI) ranges from +1.0 to -1.0 (Remote Sensing Phenology 2015).

Drought is caused by long-term lack of soil water content which would affect agriculture, ecology and socio-economy; it is particularly harmful to food production (Zhang & Huai-Liang 2016). Plants experience water stress either when the water supply to their roots becomes limiting or when the transpiration rate becomes intense. Water stress is primarily caused by the water deficit, i.e. drought or high soil salinity (Lisar et al., 2012). The Normalized Difference Water Index (NDWI) is known to be strongly related to the plant water content. It is therefore a very good proxy for plant water stress. It is real-time retrieval of soil moisture, which has high retrieval accuracy (Gao, 1995).

Urban land accounts for a small fraction of the Earth's surface area but has a disproportionate influence on its surroundings in terms of mass, energy and resource fluxes (Lambin and Geist 2001). Mapping urban land in a timely and accurate manner is indispensable for watershed run-off prediction and other planning applications (Small 2003). Remote sensing images are useful for monitoring the spatial distribution and growth of urban built-up areas because of their ability to provide timely and synoptic views of land cover (Guindon et al. 2004, Xu 2008, Bhatta 2009, Griffiths et al. 2010). Zha et al. (2003) proposed the normalized difference built-up index (NDBI) to automatically map urban built-up areas. The method takes advantage of the unique spectral responses of built-up areas and other land covers. Built-up areas are effectively mapped through the arithmetic manipulation of recoded NDVI and NDBI images derived from Landsat Thematic Mapper (TM) imagery.

In this study, an attempt is taken to develop 2D models that express the flow characteristics in the meandering River and its confluences. Before modeling, the applicability of the models is studied. Also an attempt is taken to figure out some relation among LST, NDVI, NDWI and NDBI, where NDVI is an indicator of vegetation presence; NDWI mainly stands for a very good proxy for plant water stress which mainly denotes availability of water sources, for instance water body and soil moisture and NDBI is an indicator of urbanization. All the parameters mainly indicates the environmental change of the catchment area.

2.2 Software and Tools

2.2.1 iRIC

For river meandering and confluence modeling iRIC 2.3 version software is adopted. iRIC (International River Interface Cooperative) is a river flow and riverbed variation analysis software package which combines the functionality of MD_SWMS, developed by the USGS (U.S. Geological Survey) and RIC-Nays, developed by the Foundation of Hokkaido River Disaster Prevention Research Center. The amalgamation of these pieces of software was proposed by Professor Yasuyuki Shimizu (Hokkaido University) and Dr. Jon Nelson (USGS), bringing together the accumulated analysis technology and software developments of MD_SWMS and RIC-Nays. Our vision is to continue to work on cutting-edge technology, incorporating the requests and opinions of our users to develop and provide even more useful software. iRIC provides a comprehensive, unified environment in which data that are necessary for river analysis solvers (hereafter: solvers) can be compiled, rivers can be simulated and analytical results can be visualized. The highly flexible iRIC interface allows various solvers to be imported, or user can use one of the iRIC solvers. Upon selecting the solver, iRIC selects functions suitable for the solver and prepares the optimal simulation environment. Because the iRIC functions vary depending on the solver, the method of using the iRIC application depends on the solver.

Figure 2.1 shows the general operations for iRIC simulations, and the window for each process. During pre-processing, calculation lattices and setting calculation conditions (e.g. hydrologic conditions, calculation methods) are created. Calculation lattices can be created from survey data such as river survey data and DEM data. Furthermore, for experimental and test calculation purposes, calculation lattices can be created based on geometric configuration settings. . During pre-processing calculation are analyzed and results are visualized. Visualization of calculation results can be used for purposes such as creation of vector, contour, and other diagrams, as well as creation of graphs. Furthermore, visualization results can be output to file in graphic formats such as JPG, or output to Google Earth.

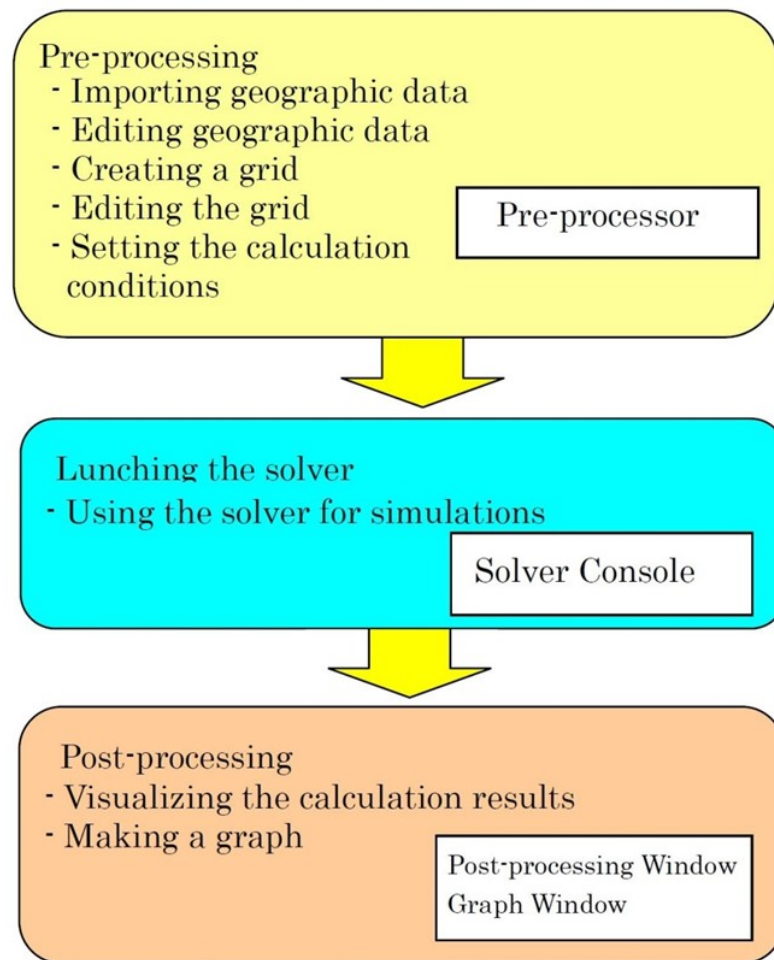


Figure 2.1: Flow diagram of iRIC Operations

2.2.2 Nays2DH

Nays2DH solver is used for river meandering modeling in iRIC software. Nays2DH is a computational model for simulating horizontal two-dimensional (2D) flow, sediment transport, morphological changes of bed and banks in rivers. Although iRIC has provided several 2D solvers, such as Nays2D, Morpho2D, FaSTMECH, etc., we believe that the users sometimes may confuse which solver is preferable for their own

case. Therefore, we decided to combine Nays2D and Morpho2D to provide a more powerful and user friendly tool for iRIC users, we called it Nays2DH.

Nays2D, developed by Dr. Yasuyuki Shimizu in Hokkaido University in Japan, is a plane 2D solver for calculating flow, sediment transport, bed evolution and bank erosion in rivers. By joining many developers to Nays2D project, several functions, for instance, river confluence model, mixture grain size model and Hot start function, have been added. Nays2D is attached to iRIC and RIC-Nays which is a predecessor project of iRIC. Nays2D includes several options for simulating river flows such as an unsteady vortex generation in open channel flows and river morphodynamics. River morphodynamics includes the initiation and development of free bars in rivers and the interaction between free bars and forced bars in meandering channels. In addition, Nays2D has been applied to several practical applications: bed evolution process in rivers affected by trees and vegetation, calculation and prediction of inundation on floodplains, sedimentation in river confluences, analysis of bank erosion and flood disasters.

Morpho2D developed by Dr. Hiroshi Takebayashi is a solver to simulate the two-dimensional morphodynamical changes in rivers. Initially, it was attached in the RIC-Nays as 'Mixture grain size model'. Since iRIC released version 1, this solver has been reformed as Morpho2D. Morpho2D includes several possibilities for simulating the morphological changes of river bed with uniform and mixture sediment, and simulating the development of free bars with sorting of sediment particles on the river bed. Morpho2D has also been applied to several real world applications in river engineering, such as analysis the bed evolution under vegetation effects, sediment transport and bed evolution with the non-erosional bed (e.g. bedrocks and fixed beds).

Both solvers have their own advantages, but they include a common part as they are both 2D models. We developed a new and more powerful solver by combining the functions of these models. In this version, the user can choose a sediment transport model based on the functions which were implemented in the both solvers. The user also can combine a river confluence model, bank erosion model, bedload-suspended load simulation in mixture sediment, bedload layer model and fixed bed model, and also able to change the sediment supply rate from the upstream end. However, there are some uncoupled parts in the current version. The combination of the functions explained above may not work in some points, and the seepage flow model used in Morpho2D is not implemented. These points will be improved in the near future.

2.2.3 River2D

River2D solver is used for river confluence modeling in iRIC software. River2D is a two dimensional depth averaged finite element hydrodynamic model that has been customized for fish habitat evaluation studies. The River2D model suite actually consists of four programs: R2D_Bed , R2D_Ice, R2D_Mesh and River2D. All three programs have graphical user interfaces that are supported by any 32 bit version of

Windows. R2D_Bed, R2D_Ice, and R2D_Mesh are graphical file editors. R2D_Bed was designed for editing bed topography data while R2D_Ice is intended for developing ice topographies to be used in the modelling of ice-covered domains. The R2D_Mesh program is used for the development of computational meshes that will ultimately be input for River2D.

These programs are typically used in succession. The normal modelling process would involve creating a preliminary bed topography file (text) from the raw field data, then editing and refining it using R2D_Bed. If an ice-covered domain were being modelled, R2D_Ice would be used to develop ice topography. The resulting bed topography file is used (inconjunction with an ice topography file where relevant) in R2D_Mesh to develop a computational discretization as input to River2D. River2D is then used to solve for the water depths and velocities throughout the discretization. Finally, River2D is used to visualize and interpret the results and perform PHABSIM type fish habitat analyses. An iterative approach at various stages, including modification of the bed topography (and ice topography), is usual.

2.2.4 ArcGIS

For remote sensing study ArcMap which is the main component of ArcGIS software is adopted. ArcGIS is a geographic information system (GIS) for working with maps and geographic information. It is used for creating and using maps, compiling geographic data, analyzing mapped information, sharing and discovering geographic information, using maps and geographic information in a range of applications, and managing geographic information in a database.

The system provides an infrastructure for making maps and geographic information available throughout an organization, across a community, and openly on the Web.

ArcMap is the main component of ArcGIS suite of geospatial processing programs, and is used primarily to view, edit, create, and analyze geospatial data. ArcMap allows the user to explore data within a data set, symbolize features accordingly, and create maps. This is done through two distinct sections of the program, the table of contents and the data frame.

2.2.5 Erdas Imagine

For removal of scan line fault of Landsat 7 satellite images Erdas Imagine software is used. ERDAS Imagine is a remote sensing application with raster graphics editor abilities designed by ERDAS for geospatial applications. The latest version is 2015. Imagine is aimed mainly at geospatial raster data processing and allows users to prepare, display and enhance digital images for mapping use in geographic information system (GIS) and computer-aided design (CAD) software. It is a toolbox allowing the user to perform numerous operations on an image and generate an answer to specific geographical questions.

By manipulating imagery data values and positions, it is possible to see features that would not normally be visible and to locate geo-positions of features that would otherwise be graphical. The level of brightness, or reflectance of light from the surfaces in the image can be helpful with vegetation analysis, prospecting for minerals etc. Other usage examples include linear feature extraction, generation of processing work flows (spatial models in Imagine), import/export of data for a wide variety of formats, ortho-rectification, mosaicking of imagery, stereo and automatic feature extraction of map data from imagery.

2.2.6 Microsoft Excel

Microsoft Excel has the basic features of all spreadsheets, using a grid of cells arranged in numbered rows and letter-named columns to organize data manipulations like arithmetic operations. It has a battery of supplied functions to answer statistical, engineering and financial needs. In addition, it can display data as line graphs, histograms and charts, and with a very limited three-dimensional graphical display. It allows sectioning of data to view its dependencies on various factors for different perspectives (using pivot tables and the scenario manager). It has a programming aspect, Visual Basic for Applications, allowing the user to employ a wide variety of numerical methods, for example, for solving differential equations of mathematical physics, and then reporting the results back to the spreadsheet. It also has a variety of interactive features allowing user interfaces that can completely hide the spreadsheet from the user, so the spreadsheet presents itself as a so-called application, or decision support system (DSS), via a custom-designed user interface, for example, a stock analyzer, or in general, as a design tool that asks the user questions and provides answers and reports. In a more elaborate realization, an Excel application can automatically poll external databases and measuring instruments using an update schedule, analyze the results, make a Word report or PowerPoint slide show, and e-mail these presentations on a regular basis to a list of participants. Excel was not designed to be used as a database.

2.2.7 Microsoft Word

Microsoft Word is a widely used commercial word processor designed by Microsoft. Microsoft Word is a component of the Microsoft Office suite of productivity software, but can also be purchased as a stand-alone product. It was initially launched in 1983 and has since been revised numerous times. Microsoft Word is available for both Windows and Macintosh operating systems. Microsoft Word is often called simply Word or MS Word.

CHAPTER 3

Modeling of Channel Meander

3.1 Introduction

This chapter describes the modeling of channel meander by the solver Nays2DH of iRIC software package. Two types of analysis have been, done such as validity analysis of the method by the software package and applying the method on natural river channel meander modeling. Meandering of a channel is a natural process that changes the channel straight pattern to a sinuous shape. This natural process gradually turns river to an acute meandering condition, so that a cut off is made to reduce the navigation length, thus a oxbow lake is created. An oxbow lake is a U-shaped lake that forms when a wide meander from the main stem of a river is cut off, creating a free-standing body of water. Meandering occurs due to the erosion and deposition at the river bank. Both laboratory and natural channel flow pattern study can help to predict the nature of the prototype, thus preventive step can minimize acuteness of the meandering.

3.2 Governing Equation

3.2.1 Basic Flow Equations in Orthogonal Coordinates

The basic equations in an orthogonal coordinate system (x, y) are as follows:

Continuity equation

$$\frac{\partial h}{\partial t} + \frac{\partial(hu)}{\partial x} + \frac{\partial(hv)}{\partial y} = 0 \quad (3.1)$$

Momentum equations in x and y-directions

$$\frac{\partial(uh)}{\partial t} + \frac{\partial(hu^2)}{\partial x} + \frac{\partial(huv)}{\partial y} = -gh \frac{\partial H}{\partial x} - \frac{\tau_x}{\rho} + D^x + \frac{F_x}{\rho} \quad (3.2)$$

$$\frac{\partial(vh)}{\partial t} + \frac{\partial(huv)}{\partial x} + \frac{\partial(hv^2)}{\partial y} = -gh \frac{\partial H}{\partial y} - \frac{\tau_y}{\rho} + D^y + \frac{F_y}{\rho} \quad (3.3)$$

in which

$$\frac{\tau_x}{\rho} = C_f u \sqrt{u^2 + v^2} \quad (3.4)$$

$$\frac{\tau_y}{\rho} = C_f v \sqrt{u^2 + v^2} \quad (3.5)$$

$$D^x = \frac{\partial}{\partial x} \left[v_t h \frac{\partial u}{\partial x} \right] + \frac{\partial}{\partial y} \left[v_t h \frac{\partial u}{\partial y} \right] \quad (3.6)$$

$$D^y = \frac{\partial}{\partial x} \left[v_t h \frac{\partial v}{\partial x} \right] + \frac{\partial}{\partial y} \left[v_t h \frac{\partial v}{\partial y} \right] \quad (3.7)$$

$$\frac{F_x}{\rho} = \frac{1}{2} C_D a_s h_v u \sqrt{u^2 + v^2} \quad (3.8)$$

$$\frac{F_y}{\rho} = \frac{1}{2} C_D a_s h_v v \sqrt{u^2 + v^2} \quad (3.9)$$

where h is water depth, t is time, u and v are depth-averaged velocities in x- and y-directions, g is gravitational acceleration, H is total water depth, τ_x and τ_y are the components of the shear stress of river bed in x and y-directions, F_x and F_y are components of drag force by vegetation in the x and y-direction, C_f is the drag coefficient of the bed shear stress, v_t is eddy viscosity coefficient, C_D is drag coefficient of vegetation, a_s is the area of interception by vegetation per unit volume, and h_v is minimum value of water depth and height of vegetation.

3.2.2 Transformation into General Curvilinear Coordinates

Next, basic equations of two-dimensional plane flow at orthogonal coordinates are transformed into general coordinates (ξ, η) . By transforming the equations into general coordinates, it becomes possible to set a calculation mesh of any shape (fitted with the boundary conditions). The following describes how the equations can be transformed from orthogonal coordinates into general curvilinear coordinates:

$$\frac{\partial}{\partial x} = \frac{\partial \xi}{\partial x} \frac{\partial}{\partial \xi} + \frac{\partial \eta}{\partial x} \frac{\partial}{\partial \eta} \quad (3.10)$$

$$\frac{\partial}{\partial y} = \frac{\partial \xi}{\partial y} \frac{\partial}{\partial \xi} + \frac{\partial \eta}{\partial y} \frac{\partial}{\partial \eta} \quad (3.11)$$

or,

$$\begin{bmatrix} \frac{\partial}{\partial x} \\ \frac{\partial}{\partial y} \end{bmatrix} = \begin{bmatrix} \xi_x & \eta_x \\ \xi_y & \eta_y \end{bmatrix} \begin{bmatrix} \frac{\partial}{\partial \xi} \\ \frac{\partial}{\partial \eta} \end{bmatrix} \quad (3.12)$$

where,

$$\xi_x = \frac{\partial \xi}{\partial x}, \quad \xi_y = \frac{\partial \xi}{\partial y}, \quad \eta_x = \frac{\partial \eta}{\partial x}, \quad \eta_y = \frac{\partial \eta}{\partial y} \quad (3.13)$$

likewise,

$$\frac{\partial}{\partial \xi} = \frac{\partial x}{\partial \xi} \frac{\partial}{\partial x} + \frac{\partial y}{\partial \xi} \frac{\partial}{\partial y} \quad (3.14)$$

$$\frac{\partial}{\partial \eta} = \frac{\partial x}{\partial \eta} \frac{\partial}{\partial x} + \frac{\partial y}{\partial \eta} \frac{\partial}{\partial y} \quad (3.15)$$

or,

$$\begin{bmatrix} \frac{\partial}{\partial \xi} \\ \frac{\partial}{\partial \eta} \end{bmatrix} = \begin{bmatrix} x_\xi & y_\xi \\ x_\eta & y_\eta \end{bmatrix} \begin{bmatrix} \frac{\partial}{\partial x} \\ \frac{\partial}{\partial y} \end{bmatrix} \quad (3.16)$$

where,

$$x_\xi = \frac{\partial x}{\partial \xi}, \quad x_\eta = \frac{\partial x}{\partial \eta}, \quad y_\xi = \frac{\partial y}{\partial \xi}, \quad y_\eta = \frac{\partial y}{\partial \eta} \quad (3.17)$$

Hence

$$\begin{bmatrix} \frac{\partial}{\partial \xi} \\ \frac{\partial}{\partial \eta} \end{bmatrix} = \frac{1}{\xi_x \eta_y - \xi_y \eta_x} \begin{bmatrix} \eta_y & -\eta_x \\ -\xi_y & \xi_x \end{bmatrix} \begin{bmatrix} \frac{\partial}{\partial x} \\ \frac{\partial}{\partial y} \end{bmatrix} = \begin{bmatrix} x_\xi & y_\xi \\ x_\eta & y_\eta \end{bmatrix} \begin{bmatrix} \frac{\partial}{\partial x} \\ \frac{\partial}{\partial y} \end{bmatrix} \quad (3.18)$$

Here, assuming $J = \xi_x \eta_y - \xi_y \eta_x$ we obtain

$$\frac{1}{J} \begin{bmatrix} \eta_y & -\eta_x \\ -\xi_y & \xi_x \end{bmatrix} = \begin{bmatrix} x_\xi & y_\xi \\ x_\eta & y_\eta \end{bmatrix} \quad (3.19)$$

Therefore

$$x_\xi = \frac{1}{J}\eta_y, \quad y_\xi = \frac{1}{J}\eta_x, \quad x_\eta = -\frac{1}{J}\xi_y, \quad y_\eta = -\frac{1}{J}\xi_x \quad (3.20)$$

or,

$$\eta_y = Jx_\xi, \quad \eta_x = -Jy_\xi, \quad \xi_y = -Jx_\eta, \quad \xi_x = Jy_\eta \quad (3.21)$$

$$J = \xi_x \eta_y - \xi_y \eta_x = J^2(x_\xi y_\eta - x_\eta y_\xi) \quad (3.22)$$

Thus we obtain

$$J = \frac{1}{x_\xi y_\eta - x_\eta y_\xi} \quad (3.23)$$

Letting the (ξ, η) components of velocity be (u^ξ, u^η) , then

$$u^\xi = \xi_x u + \xi_y v \quad (3.24)$$

$$u^\eta = \eta_x u + \eta_y v \quad (3.25)$$

or,

$$\begin{bmatrix} u^\xi \\ u^\eta \end{bmatrix} = \begin{bmatrix} \xi_x & \xi_y \\ \eta_x & \eta_y \end{bmatrix} \begin{bmatrix} u \\ v \end{bmatrix} \quad (3.26)$$

$$\begin{bmatrix} u \\ v \end{bmatrix} = \frac{1}{J} \begin{bmatrix} \eta_y & -\xi_y \\ -\eta_x & \xi_x \end{bmatrix} \begin{bmatrix} u^\xi \\ u^\eta \end{bmatrix} \quad (3.27)$$

3.2.3 Basic Equations in a General Curvilinear Coordinate System

Basic equations as obtained by transforming basic equations in an orthogonal coordinates system (x, y) into a general curvilinear coordinate system are shown below:

Continuity equation

$$\frac{\partial}{\partial t} \left(\frac{h}{J} \right) + \frac{\partial}{\partial \xi} \left(\frac{hu^\xi}{J} \right) + \frac{\partial}{\partial \eta} \left(\frac{hu^\eta}{J} \right) = 0 \quad (3.28)$$

Momentum equations

$$\begin{aligned}
& \frac{\partial u^\xi}{\partial t} + u^\xi \frac{\partial u^\xi}{\partial \xi} + u^\eta \frac{\partial u^\xi}{\partial \eta} + \alpha_1 u^\xi u^\xi + \alpha_2 u^\xi u^\eta + \alpha_3 u^\eta u^\eta = \\
& -g \left[(\xi_x^2 + \xi_y^2) \frac{\partial H}{\partial \xi} + (\xi_x \eta_x + \xi_y \eta_y) \frac{\partial H}{\partial \eta} \right] \\
& - \left(C_f + \frac{1}{2} C_D a_s h_v \right) \frac{u^\xi}{hJ} \sqrt{(\eta_y u^\xi - \xi_y u^\eta)^2 + (-\eta_x u^\xi + \xi_x u^\eta)^2} + D^\xi
\end{aligned} \tag{3.29}$$

$$\begin{aligned}
& \frac{\partial u^\eta}{\partial t} + u^\xi \frac{\partial u^\eta}{\partial \xi} + u^\eta \frac{\partial u^\eta}{\partial \eta} + \alpha_4 u^\xi u^\xi + \alpha_5 u^\xi u^\eta + \alpha_6 u^\eta u^\eta = \\
& -g \left[(\eta_x^2 + \eta_y^2) \frac{\partial H}{\partial \eta} + (\eta_x \xi_x + \eta_y \xi_y) \frac{\partial H}{\partial \xi} \right] \\
& - \left(C_f + \frac{1}{2} C_D a_s h_v \right) \frac{u^\eta}{hJ} \sqrt{(\eta_y u^\xi - \xi_y u^\eta)^2 + (-\eta_x u^\xi + \xi_x u^\eta)^2} + D^\eta
\end{aligned} \tag{3.30}$$

where,

$$\alpha_1 = \xi_x \frac{\partial^2 x}{\partial \xi^2} + \xi_y \frac{\partial^2 y}{\partial \xi^2}, \alpha_2 = 2 \left(\xi_x \frac{\partial^2 x}{\partial \xi \partial \eta} + \xi_y \frac{\partial^2 y}{\partial \xi \partial \eta} \right), \alpha_3 = \xi_x \frac{\partial^2 x}{\partial \eta^2} + \xi_y \frac{\partial^2 y}{\partial \eta^2} \tag{3.31}$$

$$\alpha_4 = \eta_x \frac{\partial^2 x}{\partial \xi^2} + \eta_y \frac{\partial^2 y}{\partial \xi^2}, \alpha_5 = 2 \left(\eta_x \frac{\partial^2 x}{\partial \xi \partial \eta} + \eta_y \frac{\partial^2 y}{\partial \xi \partial \eta} \right), \alpha_6 = \eta_x \frac{\partial^2 x}{\partial \eta^2} + \eta_y \frac{\partial^2 y}{\partial \eta^2} \tag{3.32}$$

$$D^\xi = \left(\xi_x \frac{\partial}{\partial \xi} + \eta_x \frac{\partial}{\partial \eta} \right) \left[v_i \left(\xi_x \frac{\partial u^\xi}{\partial \xi} + \eta_x \frac{\partial u^\xi}{\partial \eta} \right) \right] + \left(\xi_y \frac{\partial}{\partial \xi} + \eta_y \frac{\partial}{\partial \eta} \right) \left[v_i \left(\xi_y \frac{\partial u^\xi}{\partial \xi} + \eta_y \frac{\partial u^\xi}{\partial \eta} \right) \right] \tag{3.33}$$

$$D^\eta = \left(\xi_x \frac{\partial}{\partial \xi} + \eta_x \frac{\partial}{\partial \eta} \right) \left[v_i \left(\xi_x \frac{\partial u^\eta}{\partial \xi} + \eta_x \frac{\partial u^\eta}{\partial \eta} \right) \right] + \left(\xi_y \frac{\partial}{\partial \xi} + \eta_y \frac{\partial}{\partial \eta} \right) \left[v_i \left(\xi_y \frac{\partial u^\eta}{\partial \xi} + \eta_y \frac{\partial u^\eta}{\partial \eta} \right) \right] \tag{3.34}$$

$$\xi_x = \frac{\partial \xi}{\partial x}, \xi_y = \frac{\partial \xi}{\partial y}, \eta_x = \frac{\partial \eta}{\partial x}, \eta_y = \frac{\partial \eta}{\partial y} \tag{3.35}$$

$$u^\xi = \xi_x u + \xi_y v, u^\eta = \eta_x u + \eta_y v \tag{3.36}$$

$$J = \frac{1}{x_\xi y_\eta - x_\eta y_\xi} \tag{3.37}$$

As for diffusion terms D^ξ and D^η in the momentum equations in general coordinates, since developing those terms will make the number of terms huge, they are simplified by assuming the following conditions:

The second-order derivative for the metric coefficient is assumed to be locally zero. Those terms are locally treated as pseudo-orthogonal coordinates. As a result, the diffusion terms can be approximated as follows:

$$D^\xi \cong \frac{\partial}{\partial \xi} \left(v_i \xi_r^2 \frac{\partial u^\xi}{\partial \xi} \right) + \frac{\partial}{\partial \eta} \left(v_i \eta_r^2 \frac{\partial u^\xi}{\partial \eta} \right) \quad (3.38)$$

$$D^\eta \cong \frac{\partial}{\partial \xi} \left(v_i \xi_r^2 \frac{\partial u^\eta}{\partial \xi} \right) + \frac{\partial}{\partial \eta} \left(v_i \eta_r^2 \frac{\partial u^\eta}{\partial \eta} \right) \quad (3.39)$$

where ξ_r and η_r are parameters each representing the ratio of the local grid size in general coordinates to the full-scale length of the grid. They are defined as follows:

$$\frac{\Delta \xi}{\Delta \tilde{\xi}} = \xi_r, \quad \frac{\Delta \eta}{\Delta \tilde{\eta}} = \eta_r \quad (3.40)$$

Note that to derive the approximate equations of D^ξ and D^η above, the following relations are used, based on the assumption of a relationship of local orthogonality.

$$\xi_x^2 + \xi_y^2 = \xi_r^2 (\tilde{\xi}_x^2 + \tilde{\xi}_y^2) = \xi_r^2 (\sin^2 \theta + \cos^2 \theta) = \xi_r^2 \quad (3.41)$$

$$\xi_x \eta_x + \xi_y \eta_y = \xi_r \eta_r (\tilde{\xi}_x \tilde{\eta}_x + \tilde{\xi}_y \tilde{\eta}_y) = \xi_r \eta_r (-\cos \theta \sin \theta + \cos \theta \sin \theta) = 0 \quad (3.42)$$

$$\eta_x^2 + \eta_y^2 = \eta_r^2 (\tilde{\eta}_x^2 + \tilde{\eta}_y^2) = \eta_r^2 (\sin^2 \theta + \cos^2 \theta) = \eta_r^2 \quad (3.43)$$

$$J = \xi_x \eta_y - \xi_y \eta_x = \xi_r \eta_r (\tilde{\xi}_x \tilde{\eta}_y - \tilde{\xi}_y \tilde{\eta}_x) = \xi_r \eta_r (\sin^2 \theta + \cos^2 \theta \sin \theta) = \xi_r \eta_r \quad (3.44)$$

where θ represents the angle formed by x -axis and ξ -axis (or y -axis and η -axis).

3.2.4 Turbulence Model by Depth-Averaged k - ε Model

Turbulence means disordered flow that contains eddies of various sizes and structures.

$$v_t = C_\mu \frac{k^2}{\varepsilon} \quad (3.45)$$

where C_μ is a model constant. k and ε are obtained by the following equations:

$$\frac{\partial k}{\partial t} + u \frac{\partial k}{\partial x} + v \frac{\partial k}{\partial y} = \frac{\partial}{\partial x} \left(\frac{v_t}{\sigma_k} \frac{\partial k}{\partial x} \right) + \frac{\partial}{\partial y} \left(\frac{v_t}{\sigma_k} \frac{\partial k}{\partial y} \right) + P_h + P_{kv} - \varepsilon \quad (3.46)$$

$$\frac{\partial \varepsilon}{\partial t} + u \frac{\partial \varepsilon}{\partial x} + v \frac{\partial \varepsilon}{\partial y} = \frac{\partial}{\partial x} \left(\frac{v_t}{\sigma_\varepsilon} \frac{\partial \varepsilon}{\partial x} \right) + \frac{\partial}{\partial y} \left(\frac{v_t}{\sigma_\varepsilon} \frac{\partial \varepsilon}{\partial y} \right) + C_{1\varepsilon} \frac{\varepsilon}{k} P_h + P_{\varepsilon v} - C_{2\varepsilon} \frac{\varepsilon^2}{k} \quad (3.47)$$

Table 3.1: Model constants

C_μ	$C_{1\varepsilon}$	$C_{2\varepsilon}$	σ_k	σ_ε
0.09	1.44	1.92	1.0	1.3

where $C_{1\varepsilon}$, $C_{2\varepsilon}$, σ_k and σ_ε are model constants. Their respective values are shown in Table 3.2.

P_h , P_{kv} and $P_{\varepsilon v}$ are calculated by the following equations:

$$P_h = \nu_t \left[2 \left(\frac{\partial u}{\partial x} \right)^2 + 2 \left(\frac{\partial v}{\partial y} \right)^2 + \left(\frac{\partial u}{\partial y} \right)^2 + \left(\frac{\partial v}{\partial x} \right)^2 + 2 \frac{\partial u}{\partial y} \frac{\partial v}{\partial x} \right] \quad (3.48)$$

$$P_{kv} = C_k \frac{u_*^3}{h} \quad (3.49)$$

$$P_{\varepsilon v} = C_\varepsilon \frac{u_*^4}{h^2} \quad (3.50)$$

3.2.5 Model of River Bed Friction

In Nays2DH, the friction of river bed is set using Manning's roughness parameter. For Manning's roughness parameter, the user can define this parameter locally in each computational cell.

In Equation 3.4 and 3.5, bed shear forces τ_x and τ_y are expressed by using coefficient of bed shear force C_f . The coefficient of bed shear force C_f is estimated by Manning's roughness parameter n_m as follows:

$$C_f = \frac{gn_m^2}{h^{1/3}} \quad (3.51)$$

This Manning's roughness parameter can be estimated from the relative roughness height, k_s , by using the Manning-Strickler equation as follows:

$$n_m = \frac{k_s^{1/6}}{7.66\sqrt{g}} \quad (3.52)$$

where k_s is the relative roughness height which is defines as αd , d is sediment diameter, α is an empirical constant in the range of 1 to 3, and g is the gravitational acceleration.

3.2.6 Method for Calculating Resistance by Vegetation

Resistance exerted by vegetation is set with the drag coefficient of vegetation C_D , the area of interception by vegetation per unit volume a_s and the height of vegetation. The area of interception by vegetation per unit volume a_s can be set at each computational cell.

The area of interception by vegetation per unit volume a_s is calculated by the following equation:

$$a_s = \frac{n_s D_s}{S_s^2} \quad (3.53)$$

where n_s is the number of vegetation, D_s is the average diameter of trunks and S_s is the sampling grid width.

3.2.7 Dimensionless River Bed Shearing Force

Composite velocity V is defined by the following equation:

$$V = \sqrt{u^2 + v^2} \quad (3.54)$$

The Shields number τ_* exerted on the riverbed is as follows:

$$\tau_* = \frac{h I_e}{s_g d} \quad (3.55)$$

where h is depth, I_e is energy slope, s_g is specific weight of bed material in fluid and d is grain size of bed material. By applying Manning's formula to I_e , τ_* is expressed as follows:

$$\tau_* = \frac{C_f V^2}{s_g g d} = \frac{n_m^2 V^2}{s_g g h^{1/3}} \quad (3.56)$$

3.2.8 Bed Load Transport

Total bedload transport q_b can be estimated in the depth-averaged velocity direction (in the direction of V) by using Ashida and Michiue formula as follows:

$$q_b = 17 \tau_{*e}^{1.5} \left(1 - K_c \frac{\tau_{*c}}{\tau_*} \right) \left(1 - \sqrt{K_c \frac{\tau_{*c}}{\tau_*}} \right) \sqrt{s_g g d^3 r_b} \quad (3.57)$$

where, effective Shields number is calculated as follows:

$$u_{*e}^2 = \frac{V^2}{\left[6 + 2.5 \ln \frac{h}{d(1+2\tau_*)}\right]^2}, \quad \tau_{*e} = \frac{u_{*e}^2}{sgd} \quad (3.58)$$

where τ_{*c} is critical Shields number which is calculated by Iwagaki formula. K_c is the modification function of the effect of the local bed slope on the sediment transport as follows:

$$K_c = 1 + \frac{1}{\mu_s} \left[\left(\frac{\rho}{\rho_s - \rho} \right) \cos \alpha \tan \theta_x + \sin \alpha \tan \theta_y \right] \quad (3.59)$$

where α is the angle of deviation of near-bed flow from x -direction and defined as follows:

$$\alpha = \arctan \left(\frac{v_b}{u_b} \right) \quad (3.60)$$

μ_s is the static friction coefficient of bed material. θ_x and θ_y are bed inclinations in the x and y -directions, respectively. These inclinations are evaluated as follows,

$$\theta_x = \arctan \left(\frac{\partial \xi}{\partial x} \frac{\partial z_b}{\partial \xi} + \frac{\partial \eta}{\partial x} \frac{\partial z_b}{\partial \mu} \right), \quad \theta_y = \arctan \left(\frac{\partial \xi}{\partial y} \frac{\partial z_b}{\partial \xi} + \frac{\partial \eta}{\partial y} \frac{\partial z_b}{\partial \mu} \right) \quad (3.61)$$

r_b is the function of the exchange layer thickness as follows:

$$r_b = 1 \quad E_{sd} \geq E_{be} \quad (3.62)$$

$$r_b = \frac{E_b}{E_{be}} \quad E_{sd} \leq E_{be} \quad (3.63)$$

3.2.9 Calculation of Bedload Transport Vector

The total bedload transport is divided to the contravariant form of bedload fluxes in ξ and η directions by considering the effect of secondary flows to the velocity field near river bed and the local bed slope effect to the sediment transport direction. Bedload flux in ξ and η directions can be calculated by Watanabe formula. Bed load transport in ξ and η -directions is given by the following equations:

$$\tilde{q}_b^\xi = q_b \left[\frac{\tilde{u}_b^\xi}{V_b} - \gamma \left(\frac{\partial z_b}{\partial \tilde{\xi}} + \cos \theta \frac{\partial z_b}{\partial \tilde{\eta}} \right) \right] \quad (3.64)$$

$$\tilde{q}_b^\eta = q_b \left[\frac{\tilde{u}_b^\eta}{V_b} - \gamma \left(\frac{\partial z_b}{\partial \tilde{\eta}} + \cos \theta \frac{\partial z_b}{\partial \tilde{\xi}} \right) \right] \quad (3.65)$$

where \tilde{u}_b^ξ and \tilde{u}_b^η are flow velocities near river bed in ξ and η -directions, respectively, V_b is composite velocity near the riverbed, and θ is the angle formed the ξ and η axes. γ is a correction coefficient for local bed slope effect, which is given by the following equation according to Hasegawa:

$$\gamma = \sqrt{\frac{\tau_{*c}}{\mu_s \mu_k \tau_*}} \quad (3.66)$$

where μ_s and μ_k are static friction coefficient and dynamic friction coefficient of bed material, respectively.

The following simple relational equation is given for the relationship between depth-averaged velocity and near-bed velocity along the depth-averaged flow:

$$\tilde{u}_b^s = \beta V \quad (3.67)$$

where \tilde{u}_b^s is near-bed velocity along the streamline of the depth-averaged flow (hereafter simply called streamline). According to Engelund, if we apply a parabolic distribution to the velocity distribution in the depth direction, then β is given by the following equation:

$$\beta = 3 \frac{1-\sigma}{3-\sigma}, \quad \sigma = \frac{3}{\phi_0 \kappa + 1} \quad (3.68)$$

where ϕ_0 is velocity coefficient ($= V / u_*$)

Evaluation of secondary flows can be determined by setting the strength of it. The following equation is used for calculating the near-bed velocity under the effect of such secondary flow:

$$\tilde{u}_b^n = \tilde{u}_b^s N_* \frac{h}{r_s} \quad (3.69)$$

Where \tilde{u}_b^n is near-bed velocity in transverse direction, r_s is curvature radius of the streamline and N_* is a constant whose value is considered 7 by Engelund (1974).

3.2.10 Streamline Curvature

The streamline curvature applied in equation is obtained by the following equation:

$$\frac{1}{r_s} = \frac{\partial \theta_s}{\partial s} \quad (3.70)$$

where, θ_s is the angle between the x-axis and the s-direction defined as follows;

$$\theta_s = \tan^{-1}\left(\frac{v}{u}\right) \quad (3.71)$$

hence

$$\frac{1}{r_s} = \frac{\partial}{\partial s} [\tan^{-1}(T)] = \frac{\partial}{\partial T} [\tan^{-1}(T)] \frac{\partial T}{\partial s} = \frac{1}{1+T^2} \frac{\partial T}{\partial s} \quad (3.72)$$

where $T = v/u$. Here,

$$\frac{1}{1+T^2} = \frac{1}{1+\left(\frac{v}{u}\right)^2} = \frac{u^2}{u^2+v^2} = \frac{u^2}{V^2} \quad (3.73)$$

$$\frac{\partial T}{\partial s} = \frac{\partial}{\partial s} \left(\frac{v}{u}\right) = \frac{u \frac{\partial v}{\partial s} - v \frac{\partial u}{\partial s}}{u^2} \quad (3.74)$$

$$\frac{\partial}{\partial s} = \frac{\partial x}{\partial s} \frac{\partial}{\partial x} + \frac{\partial y}{\partial s} \frac{\partial}{\partial y} = \frac{u}{V} \frac{\partial}{\partial x} + \frac{v}{V} \frac{\partial}{\partial y} = \frac{u}{V} \left(\xi_x \frac{\partial}{\partial \xi} + \eta_x \frac{\partial}{\partial \eta} \right) + \frac{v}{V} \left(\xi_y \frac{\partial}{\partial \xi} + \eta_y \frac{\partial}{\partial \eta} \right) \quad (3.75)$$

Therefore, curvature $\frac{1}{r_s}$ is expressed by the following equation:

$$\frac{1}{r_s} = \frac{1}{V^3} \left[\begin{array}{l} u^2 \left(\xi_x \frac{\partial v}{\partial \xi} + \eta_x \frac{\partial v}{\partial \eta} \right) + uv \left(\xi_y \frac{\partial v}{\partial \xi} + \eta_y \frac{\partial v}{\partial \eta} \right) \\ - uv \left(\xi_x \frac{\partial u}{\partial \xi} + \eta_x \frac{\partial u}{\partial \eta} \right) - v^2 \left(\xi_y \frac{\partial u}{\partial \xi} + \eta_y \frac{\partial u}{\partial \eta} \right) \end{array} \right] \quad (3.76)$$

3.2.11 Upward Flux of Suspended Load From River Bed

For upward flux of suspended load from river bed can be determined from Itakura and Kishi formula as follows:

$$q_{su} = K \left[a_* \frac{\rho_s - \rho}{\rho_s} \cdot \frac{gd}{u_*} \Omega - w_f \right] r_b \quad (3.77)$$

$$\Omega_k = \frac{\tau_*}{B_*} \cdot \frac{\int_{a'}^{\infty} \xi \frac{1}{\sqrt{\pi}} \exp[-\xi^2] d\xi}{\int_{a'}^{\infty} \frac{1}{\sqrt{\pi}} \exp[-\xi^2] d\xi} + \frac{\tau_*}{B_* \eta_0} - 1 \quad (3.78)$$

$$a' = \frac{B_*}{\tau_*} - \frac{1}{\eta_0}, \quad \eta_0 = 0.5, \quad a_* = 0.14, \quad K = 0.008 \quad (3.79)$$

where q_{su} is the upward flux of suspended load from river bed and w_f is the settling velocity of suspended sediment, which is obtained with Rubey's equation. B_* is a conversion factor for applying friction velocity to the velocity in lift force calculation. The constant value of $B_* = 0.143$ is used in the case of uniform grain size.

3.2.12 Continuity Equation of Suspended Load Concentration

The continuity equation of suspended load concentration in the general curvilinear coordinate system is represented as follows:

$$\frac{\partial}{\partial t} \left(\frac{ch}{J} \right) + \frac{\partial}{\partial \xi} \left(\frac{u^\xi ch}{J} \right) + \frac{\partial}{\partial \eta} \left(\frac{u^\eta ch}{J} \right) = \frac{q_{su} - w_f c_b}{J} \quad (3.80)$$

where c is depth-averaged suspended load concentration and c_b is reference concentration of suspended load. Diffusion terms have been omitted from the equation, for simplicity. The reference concentration of suspended load is calculated by assuming an exponential distribution of suspended sediment in vertical direction as follows:

$$c_b = \frac{\beta_c c}{1 - \exp(-\beta_c)} \quad (3.81)$$

with,

$$\beta_c = \frac{6w_f}{\kappa u_*} \quad (3.82)$$

3.2.13 Continuity Equation of Sediment Transport

First, a continuity equation of sediment transport in two-dimensional orthogonal coordinates is given by:

$$\frac{\partial}{\partial t} (c_b E_b) + (1 - \lambda) \frac{\partial z}{\partial t} + \left[\frac{\partial q_{bx}}{\partial x} + \frac{\partial q_{by}}{\partial y} + q_{su} - w_f c_b \right] = 0 \quad (3.83)$$

where t is time, z is riverbed elevation, and λ is a void ratio of bed material.

When bed load only is selected, suspended load supplied per unit area, settling velocity of suspended sediment and concentration at the control point area assumed to be zero. Next, just as for the continuity equation of flow, we transform the above equation into general coordinates.

$$\frac{\partial}{\partial t} \left(\frac{c_b E_b}{J} \right) + (1-\lambda) \frac{\partial}{\partial t} \left(\frac{z}{J} \right) + \left[\frac{\partial}{\partial \xi} \left(\frac{q_b^\xi}{J} \right) + \frac{\partial}{\partial \eta} \left(\frac{q_b^\eta}{J} \right) + \frac{q_{su} - w_f c_b}{J} \right] = 0 \dots E_{sd} \geq E_{be} \frac{c_b}{1-\lambda} \quad (3.84)$$

$$\frac{\partial}{\partial t} \left(\frac{z}{J} \right) = 0 \dots E_{sd} \leq E_{be} \frac{c_b}{1-\lambda} \quad (3.85)$$

3.3 Numerical method

For the finite differentiation, applied to the advection terms in the momentum equations, Upwind difference method (first order) is applied.

3.3.1 Finite Difference Method

In mathematics, finite-difference methods (FDM) are numerical methods for solving differential equations by approximating them with difference equations, in which finite differences approximate the derivatives. Derivation of FDM from Taylor's polynomial is given below. Taylor Series expansion is expressed as follows:

$$f(x_0 + h) = f(x_0) + \frac{f'(x_0)}{1!} h + \frac{f^{(2)}(x_0)}{2!} h^2 + \dots + \frac{f^{(n)}(x_0)}{n!} h^n + R_n(x) \quad (3.86)$$

where $n!$ denotes the factorial of n , and $R_n(x)$ is a remainder term, denoting the difference between the Taylor polynomial of degree n and the original function. We will derive an approximation for the first derivative of the function " f " by first truncating the Taylor polynomial:

$$f(x_0 + h) = f(x_0) + f'(x_0)h + R_1(x) \quad (3.87)$$

Setting, $x_0 = a$

$$f(a + h) = f(a) + f'(a)h + R_1(x) \quad (3.88)$$

Dividing across by h gives:

$$\frac{f(a + h)}{h} = \frac{f(a)}{h} + f'(a) + \frac{R_1(x)}{h} \quad (3.89)$$

Solving for $f'(a)$

$$f'(a) = \frac{f(a + h) - f(a)}{h} - \frac{R_1(x)}{h} \quad (3.90)$$

Assuming that $R_1(x)$ is sufficiently small, the approximation of the first derivative of "f" is:

$$f'(a) \approx \frac{f(a+h) - f(a)}{h} \quad (3.91)$$

3.3.2 Accuracy and Order

The error in a method's solution is defined as the difference between the approximation and the exact analytical solution. The two sources of error in finite difference methods are round-off error, the loss of precision due to computer rounding of decimal quantities, and truncation error or discretization error, the difference between the exact solution of the original differential equation and the exact quantity assuming perfect arithmetic (that is, assuming no round-off).

To use a finite difference method to approximate the solution to a problem, one must first discretize the problem's domain. This is usually done by dividing the domain into a uniform grid (see image to the right). Note that this means that finite-difference methods produce sets of discrete numerical approximations to the derivative, often in a "time-stepping" manner.

An expression of general interest is the local truncation error of a method. Typically expressed using Big-O notation, local truncation error refers to the error from a single application of a method. That is, it is the quantity $f'(x_i) - f'_i$ if $f'(x_i)$ refers to the exact value and f'_i to the numerical approximation. The remainder term of a Taylor polynomial is convenient for analyzing the local truncation error. Using the Lagrange form of the remainder from the Taylor polynomial for $f(x_0 + h)$, which is

$$R_n(x_0 + h) = \frac{f^{(n+1)}(\zeta)}{(n+1)!} (h)^{n+1}, \text{ where } x_0 < \zeta < x_0 + h \quad (3.92)$$

the dominant term of the local truncation error can be discovered. For example, again using the forward-difference formula for the first derivative, knowing that

$$f(x_i) = f(x_0 + ih) \quad (3.93)$$

$$f(x_0 + ih) = f(x_0) + f'(x_0)ih + \frac{f''(\zeta)}{2!}(ih)^2 \quad (3.94)$$

and with some algebraic manipulation, this leads to

$$\frac{f(x_0 + ih) - f(x_0)}{ih} = f'(x_0) + \frac{f''(\zeta)}{2!}ih \quad (3.95)$$

and further noting that the quantity on the left is the approximation from the finite difference method and that the quantity on the right is the exact quantity of interest plus

a remainder, clearly that remainder is the local truncation error. A final expression of this example and its order is:

$$\frac{f(x_0 + ih) - f(x_0)}{ih} = f'(x_0) + O(h) \quad (3.96)$$

This means that, in this case, the local truncation error is proportional to the step sizes. The quality and duration of simulated FDM solution depends on the discretization equation selection and the step sizes (time and space steps). The data quality and simulation duration increase significantly with smaller step size. Therefore, a reasonable balance between data quality and simulation duration is necessary for practical usage. Large time steps are useful for increasing simulation speed in practice. However, time steps which are too large may create instabilities and affect the data quality.

3.3.3 Upwind Difference Method

In computational physics, upwind schemes denote a class of numerical discretization methods for solving hyperbolic partial differential equations. Upwind schemes use an adaptive or solution-sensitive finite difference stencil to numerically simulate the direction of propagation of information in a flow field. The upwind schemes attempt to discretize hyperbolic partial differential equations by using differencing biased in the direction determined by the sign of the characteristic speeds.

To illustrate the method, consider the following one-dimensional linear advection equation

$$\frac{\partial f}{\partial t} + C \frac{\partial f}{\partial x} = 0 \quad (3.97)$$

which describes a wave propagating along the x -axis with a velocity C . This equation is also a mathematical model for one-dimensional linear advection. Consider a typical grid point i in the domain. In a one-dimensional domain, there are only two directions associated with point i -left (towards negative infinity) and right (towards positive infinity). If C is positive, the travelling wave solution of the equation above propagates towards the right, the left side of i is called upwind side and the right side is the downwind side. Similarly, if C is negative the travelling wave solution propagates towards the left, the left side is called downwind side and right side is the upwind side. If the finite difference scheme for the spatial derivative, $\partial u / \partial x$ contains more points in the upwind side, the scheme is called an upwind-biased or simply an upwind scheme.

3.3.4 First-Order Upwind Scheme

The simplest upwind scheme possible is the first-order upwind scheme (Figure 3.1). It is given by

$$\frac{f_i^{n+1} - f_i^n}{\Delta t} + C \frac{f_i^n - f_{i-1}^n}{\Delta x} = 0 \quad \text{for } C > 0 \quad (3.98)$$

$$\frac{f_i^{n+1} - f_i^n}{\Delta t} + C \frac{f_{i+1}^n - f_i^n}{\Delta x} = 0 \quad \text{for } C < 0 \quad (3.99)$$

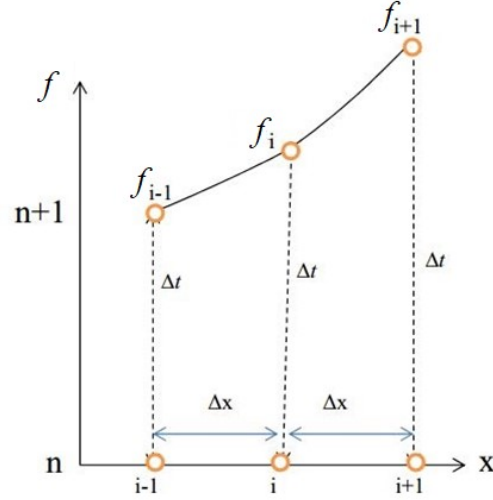


Figure 3. 1: Calculation steps in upwind scheme

3.3.5 Compact Form

$$C^+ = \max(C, 0), C^- = \min(C, 0) \quad (3.100)$$

and

$$u_x^- = \frac{f_i^n - f_{i-1}^n}{\Delta x}, u_x^+ = \frac{f_{i+1}^n - f_i^n}{\Delta x} \quad (3.101)$$

the two conditional equations (3.98) and (3.99) can be combined and written in a compact form as

$$u_i^{n+1} = u_i^n - \Delta t [a^+ u_x^- + a^- u_x^+] \quad (3.102)$$

Equation (3.102) is a general way of writing any upwind-type schemes.

3.3.6 Stability

The upwind scheme is stable if the following Courant–Friedrichs–Lewy condition (CFL) is satisfied.

$$c = \left| \frac{C \Delta t}{\Delta x} \right| \leq 1 \quad (3.103)$$

A Taylor series analysis of the upwind scheme discussed above will show that it is first-order accurate in space and time. Modified wavenumber analysis shows that the first-order upwind scheme introduces severe numerical diffusion/dissipation in the solution where large gradients exist due to necessity of high wavenumbers to represent sharp gradients.

3.4 Applicability of Present Study for Modeling Flow in Meander

For validity analysis of the model, developed for river channel meander study, result of experimental and numerical study performed by Seo and Park (2010) is adopted and compared with the simulated result by iRIC Nays2DH, of present study. This study shows the difference between numerically simulated result of present study with experimental result and other numerically simulated result. Thus the accuracy level of presently developed model can be determined. Then the model is used for further modeling of natural river meander.

3.4.1 Numerical Method Followed by Seo and Park (2010)

RAMS (River Analysis and Modeling System) is 2D river flow analysis software package which consists of river flow analysis model (RAM2), pollutant transport model (RAM4), bed elevation change model (RAM6), and graphic user interface (RAMS-GUI). This software can simulate the movements of water, pollutant, and sediment in natural rivers with complex topography by 2D finite element numerical calculations with underlying consistency and generality. This software would provide accurate and stable solutions to open channel flow equation, and mass transport equation for various types of problems. Flow model, RAM2, is a finite element model based on Streamline Upwind / Petrov-Galerkin (SU/PG) scheme for analyzing and simulating two-dimensional flow characteristics of irregular natural rivers with complex geometries. The type of elements in a mesh can be a triangular, quadrilateral or mixed one. A triangular element could have either 3-nodes or 6-nodes and a quadrilateral element either 4-nodes or 8-nodes. This mesh can be constructed from DEM and TIN format in the tools of GIS. RAM4 is a FEM model for pollutant transport analysis in two-dimensional flow fields and it is developed based on the depth-averaged mass transport equation. It can calculate the advection and dispersion of injected substances in a two-dimensional flow field. This engine can treat the conservative or non-conservative substances as pollutant tracers.

RMA2 and is the 2D depth-averaged finite element hydrodynamic model of commercial software SMS (Surface-water modeling system). It computes a finite element solution of the Reynolds form of the Navier-Stokes equations for turbulent flow. Friction is calculated with the Manning's or Chezy equation, and eddy viscosity coefficients are used to define turbulent characteristics. In this model, both steady and unsteady state problems can be simulated. The generalized computer program RMA2

solves the depth-integrated equations of fluid mass and momentum conservation in two horizontal directions.

3.4.2 Laboratory Setup for Experiment by Seo and Park (2010)

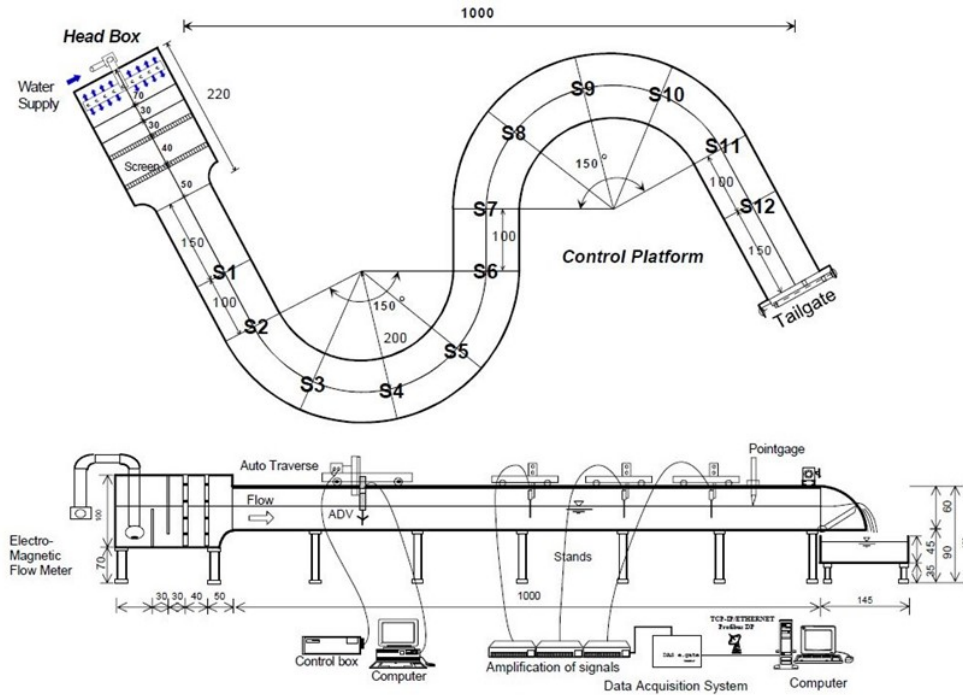


Figure 3. 2: Sketches of S-curved laboratory channel (top: plan view, bottom: side view; unit: cm) (Seo and Park, 2010)

In this study, flow and tracer experiments were conducted in the S-curved meandering laboratory channel with a rectangular cross-section which is 16.5 m long, 1 m wide, and 0.6 m high. It consists of two circular bends connected by straight sections as shown in Figure 3.2. The radius of curvature of the bend region is 2.0 m, the wavelength is 7.5 m, and the arc angle is 150°. Velocity was measured by micro-ADV (Acoustic Doppler Velocimetry). Different type of hydraulic condition is created during experiment. Where one condition is represented comparing with numerically solved result. In this hydraulic condition flow depth, average velocity, discharge and Froude number considered as 20 cm, 15 cm/s, 30 l/s and 0.11 respectively.

3.4.3 Numerical Solution by iRIC Nays2DH (Present study)

The above mentioned experimental condition is simulated by solver Nays2DH of iRIC. In this numerical solution depth-averaged $k-\epsilon$ model is used for turbulence modeling. Secondary flows are also considered during calculation, which is the main reason for losing energy of flow near the channel boundary. Total numbers of grids are $i \times j = 80 \times 11=880$ (Figure 3.3). The calculation condition is represented in Table 3.2.

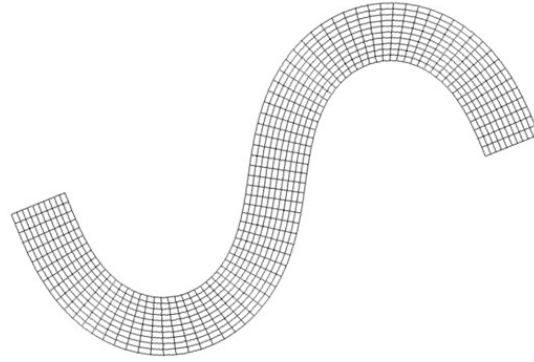


Figure 3. 3: Grid shape and position for numerical solution

Table 3. 2: Calculation condition for numerical simulation

Solver type	Advanced
Bed deformation	Disable
Finite difference method of advection terms	Upwind scheme
Confluence	Disable
Bed material type	Uniform
Sediment transport type	Bed load
Bed load transport formula for uniform sediment	Ashida and Michiue formula
Vector of bed load transport	Watanabe formula
Formula of upward flux of suspended load from river bed	Itakura and Kishi formula
Bank erosion	Disabled
Slope collapse model	No
Turbulent model	K-epsilon model
Periodic boundary condition	Disable
Water surface at downstream	Uniform flow
Velocity at upstream	Uniform flow
Discharge	30 l/s
Water level	20 cm
Calculation time step (Δt)	0.01
Maximum number of iteration of water surface calculation	10
Initial water surface	Uniform flow
Secondary flow model	Equilibrium model
Intensity of Secondary flows for sediment transport	7
Simulation time	4 hours

3.4.4 Comparison of Simulation Result from Present Study with Seo and Park (2010)

Velocity is measured in twelve cross sections during experiment by Seo and Park (2010). In Figure 3.4 it is noteworthy that transverse distribution of the primary velocity skews toward the inner bank at the bends and at the crossovers, al-most symmetric. The maximum velocities in each transverse section were detected along the shortest course of the channel. This flow pattern is opposite to the flow characteristics found in the natural meandering channels. The reason of this discrepancy in the flow

pattern is that experiments were conducted on the rectangular cross-section channel, whereas the cross-sectional shape of the natural stream is usually triangular or trapezoidal and skewed to the outer bank. Figure 3.5 shows similar result like Seo and Park (2010), observed in the numerical solution performed by Nays2DH solver. Velocity profiles along the cross-sections of present study shows the same pattern of velocity distribution as compared with experimental result. In Figure 3.6 it is also observed that intensity of flow velocity is always higher in inner bank, which is similar to experimental result performed by and Park (2010).

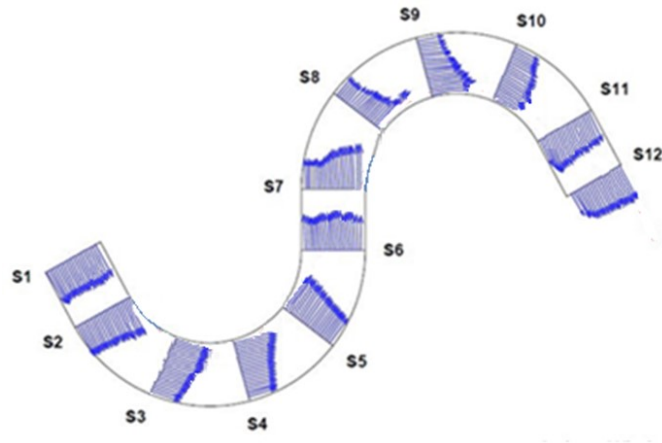


Figure 3.4: Vector maps of velocity profiles (Seo and Park, 2010)

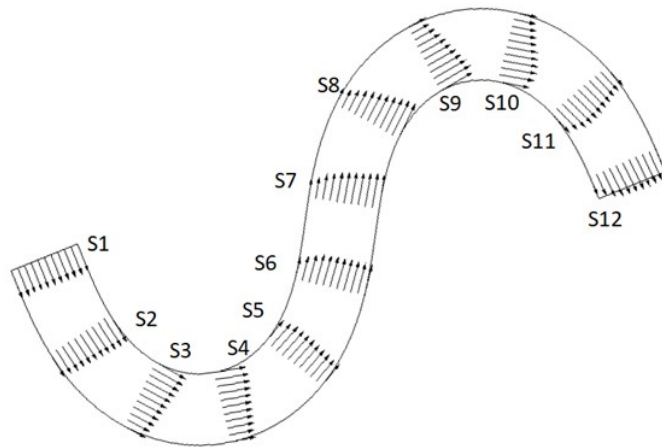


Figure 3.5: Vector maps of velocity profiles (present study)

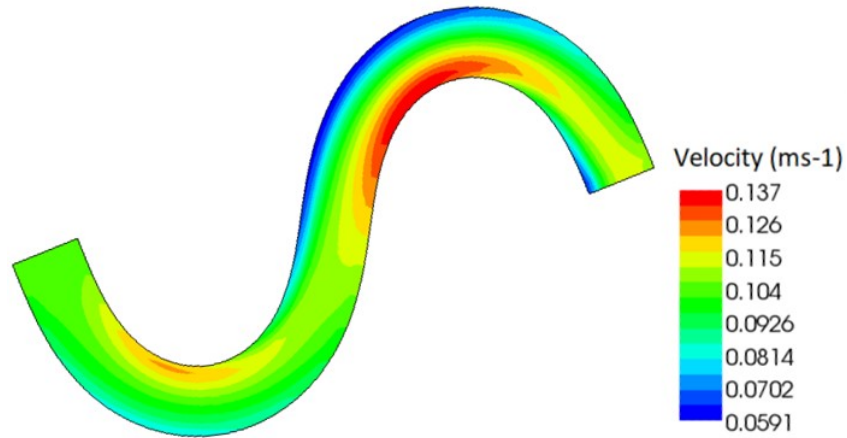


Figure 3.6: Velocity contour map (present study)

Magnitudes of primary flow of the simulated and observed results at the first bend (S4) and second bend (S9) are represented in Figure 3.7 and 3.8 respectively. Figure 3.7 and Figure 3.8 show that predicted values by both models used by Seo and Park (2010) are in good agreements with the experimental data in the outer bank of the bends. But RMA-2 model overestimates the experimental result while RAM2 model underestimates it. Similar to RMA-2 and RAM2 models, Nays2DH developed model is also in good agreements with the experimental data. While Nays2DH model overestimates the experimental result and shows similarity to RMA-2 model. Result of S4 from present, is almost similar to RMA-2 model. But result of S9 of present study is most likely to experimental result at the outer bank and from middle of channel section result is nearly exact to the RMA-2 model towards inner bank.

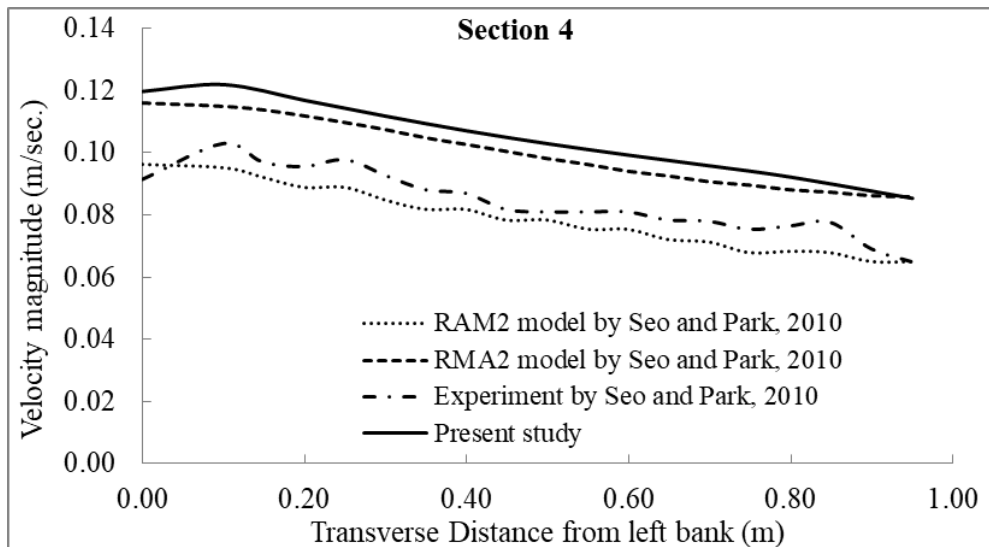


Figure 3.7: Comparison of primary flow at the first bend (Section 4)

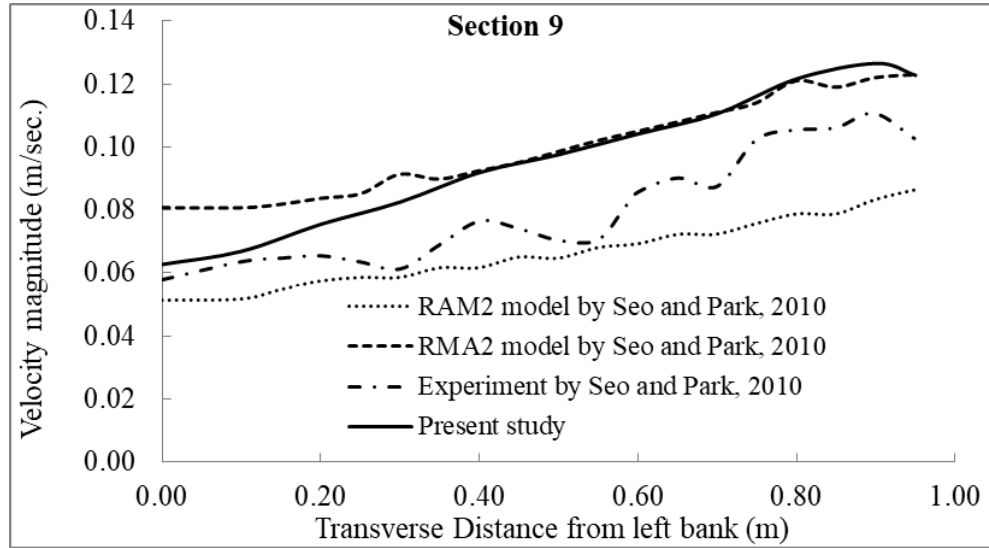


Figure 3. 8: Comparison of primary flow at the second bends (Section 9)

3.5 Modeling of River Meander

In this study, Nays2DH solver is used for modeling Natural River meander. Here combined flow of Atai and Rupsha River is adopted for numerical modeling. Total 58.2 kilometer length of the two rivers are considered for simulation. Total river length is divided into three parts such as Part A, Part B and Part C. Length and position of the three parts are summarized in Table 3.3 and shown in Figure 3.9. Part A consists upstream of Atai. Part B consists downstream of Atai at the junction of Bhairab and upstream of Rupsha from that junction. Part C consists only the downstream of Rupsha till Pasur.

Table 3.3: Length and Position of Part A, Part B, Part C

Part	River name	Length (Km)	Position	
			From	To
Part A (upper reach)	Atai	13.2	22°58'59.75"N, 89°33'34.81"E	22°52'41.13"N, 89°34'3.03"E
Part B (middle reach)	Atai, Rupsha	17.8	22°52'41.13"N, 89°34'3.03"E	22°45'8.24"N, 89°32'58.23"E
Part C (lower reach)	Rupsha	27.2	22°45'8.24"N, 89°32'58.23"E	22°32'12.14"N, 89°34'28.64"E

Each Part is divided into several cross-sections. The cross-section data is collected from Bangladesh Water Development Board (BWDB). Historical cross-section data set is being found from BWDB but data collected at the year 2015 is used for this study. BWDB collects data at an interval of 3 years for Atai and Rupsha River. The cross-section data used for study was the latest update when this study started. Echo sounding system is used by BWDB to measure the river depth. Discharge data is collected from Mongla port authority.

Total length is divided into 54 cross-section, whereas in Part A, cross-section 1 to 18 are situated, in Part B cross-section 18 to 36 are situated, in Part C cross-section 36 to 54 are situated. During simulation direction of flow is considered from both end of each section. This operation procedure is used to create both high-tide and ebb-tide condition. During high-tide, water flows from south to north and its north to south during ebb-tide. In Nays2DH solver, cross-section name is expressed as a number. And according to the position of cross-section this numbers (names) are arranged either ascending or descending order. Here direction of flow is always from highest numbered cross-section to lowest numbered cross-section. Position of cross-section is shown in Figure: 3.10 and Figure: 3.11.

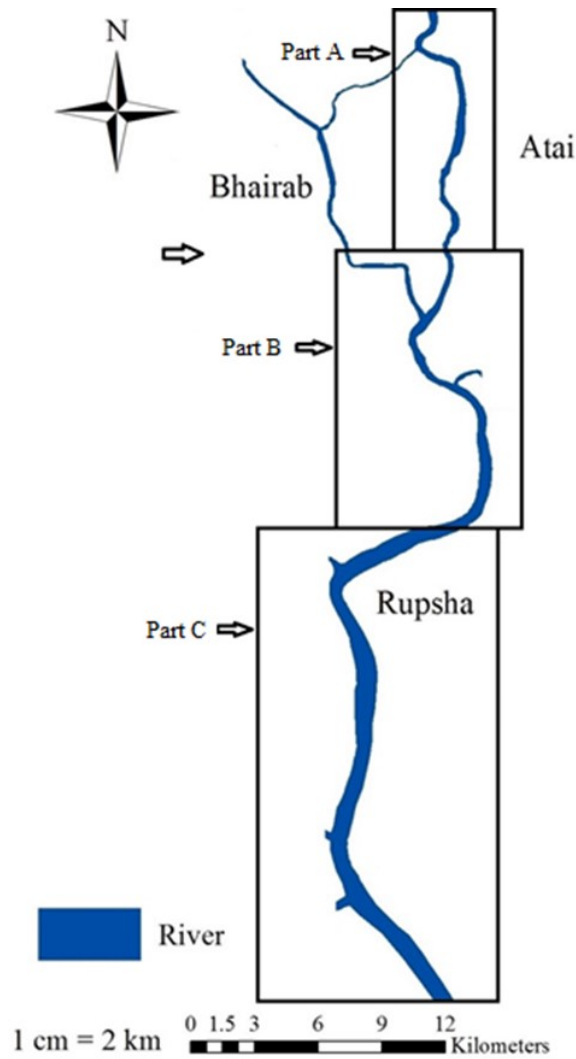


Figure 3. 9: Part A, Part B and Part C along the length of river

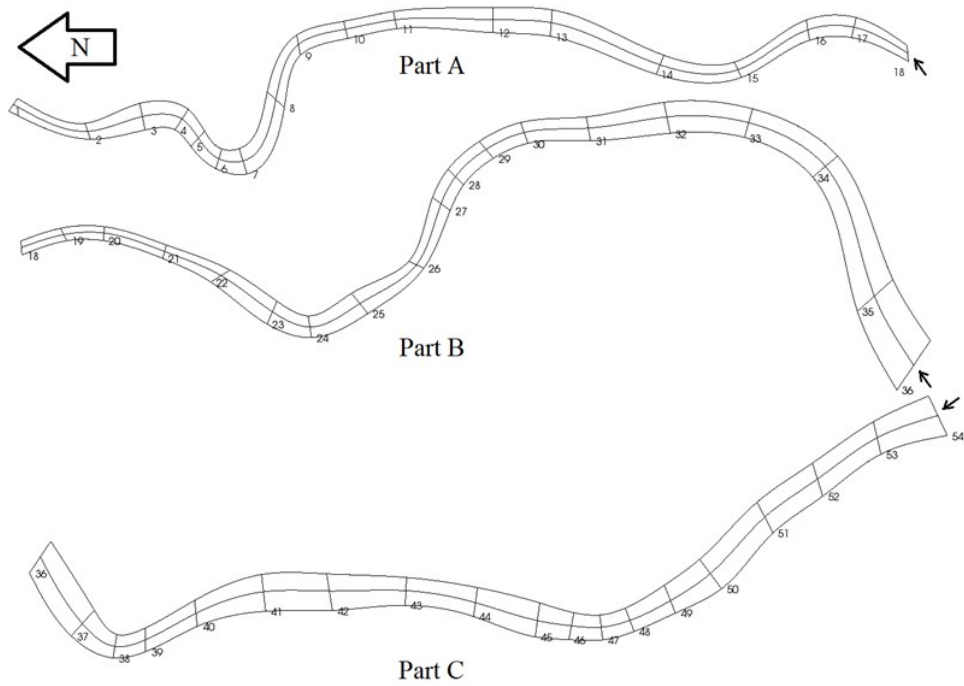


Figure 3.10: Cross-section position and number arrangement during high-tide

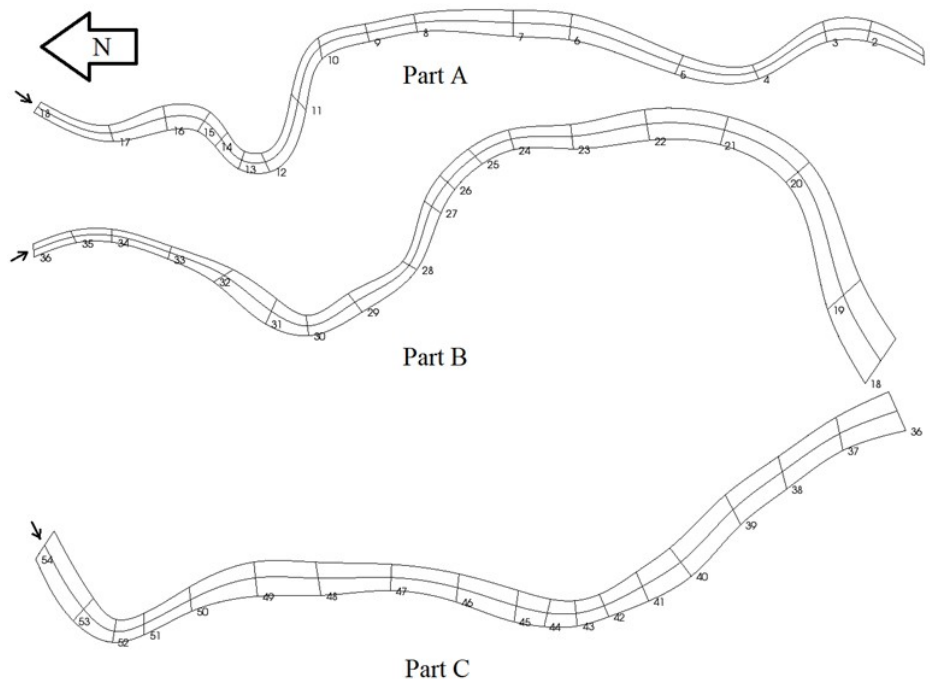


Figure 3.11: Cross-section position and number arrangement during ebb-tide

3.6 Input of Cross-section Geometry in Nays2DH

The River Survey File (*.riv) contains transverse data (x and y coordinates of left/right banks) and cross-section data (distance from left bank and riverbed elevation). *.riv should be ASCII files. Table: 3.4 and Figure: 3.12 show the structure and concept, respectively.

- Break points of input data (for example, cross-section identification number and x-coordinate value) are identified by "space", "tab" or "rerun" characters. When break points are properly identified, iRIC automatically recognizes the data. Please note that cross-section identification number must be a real number.
 - Rows after the "#survey" row are recognized as cross-section data.
- Each row contains data for one cross-section.
- Data row: (Cross-section identification number) (x-coordinate value of the left bank) (y-coordinate value of the left bank) (x-coordinate value of the right bank) (y-coordinate value of the right bank)

Table 3.4: Structure of River Survey File (*.riv)

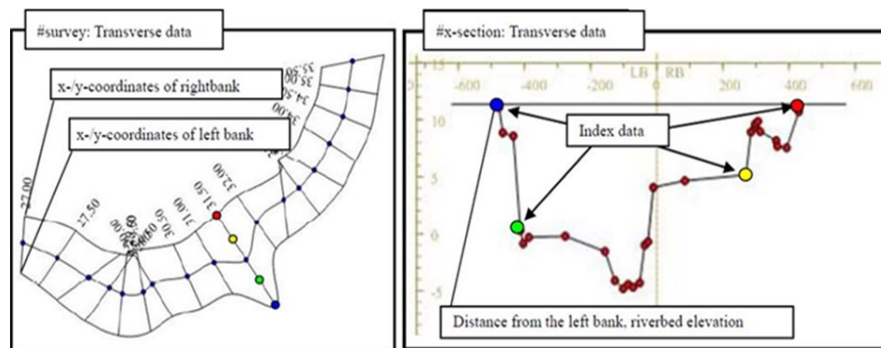
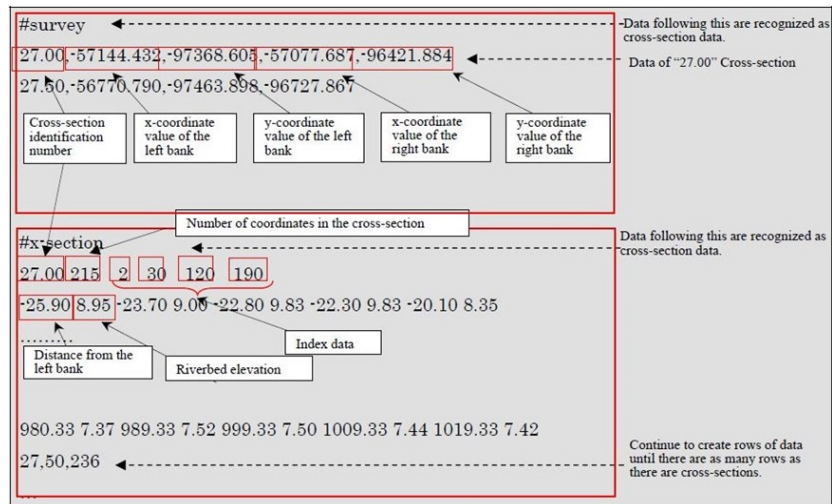


Figure 3.12: Concept of River Survey File data

- Rows after the "#x-section" row are recognized as cross-section data (consisting of the "header line" and "data lines").

→ Header line: (Cross-section identification number) (No. of coordinates) (Index 1) (Index 2) (Index 3) (Index 4).

Indexes 1 to 4 specify points on a cross-sectional coordinate system by sequential integer numbers. (The top is 1.) Data prior to Index 1 and after Index 4 are discarded. The point specified by Index 1 is set as the left bank and the point specified by Index 4 is set as the right bank. The points specified by Indexes 2 and 3 are to be the division points (or nodes) of the automatically created grid. The Center Point of the river is set at the point midway between Indexes 2 and 3.

Index data can be omitted. In such case, all the coordinate cross-section data are read and the first point of the coordinate cross-section data is set as the left bank and the last point is set as the right bank. The Center Point of the river is set at the mid-point between the left and right banks.

When Index data are not set for every cross-section data, the index data of all cross-sections are ignored.

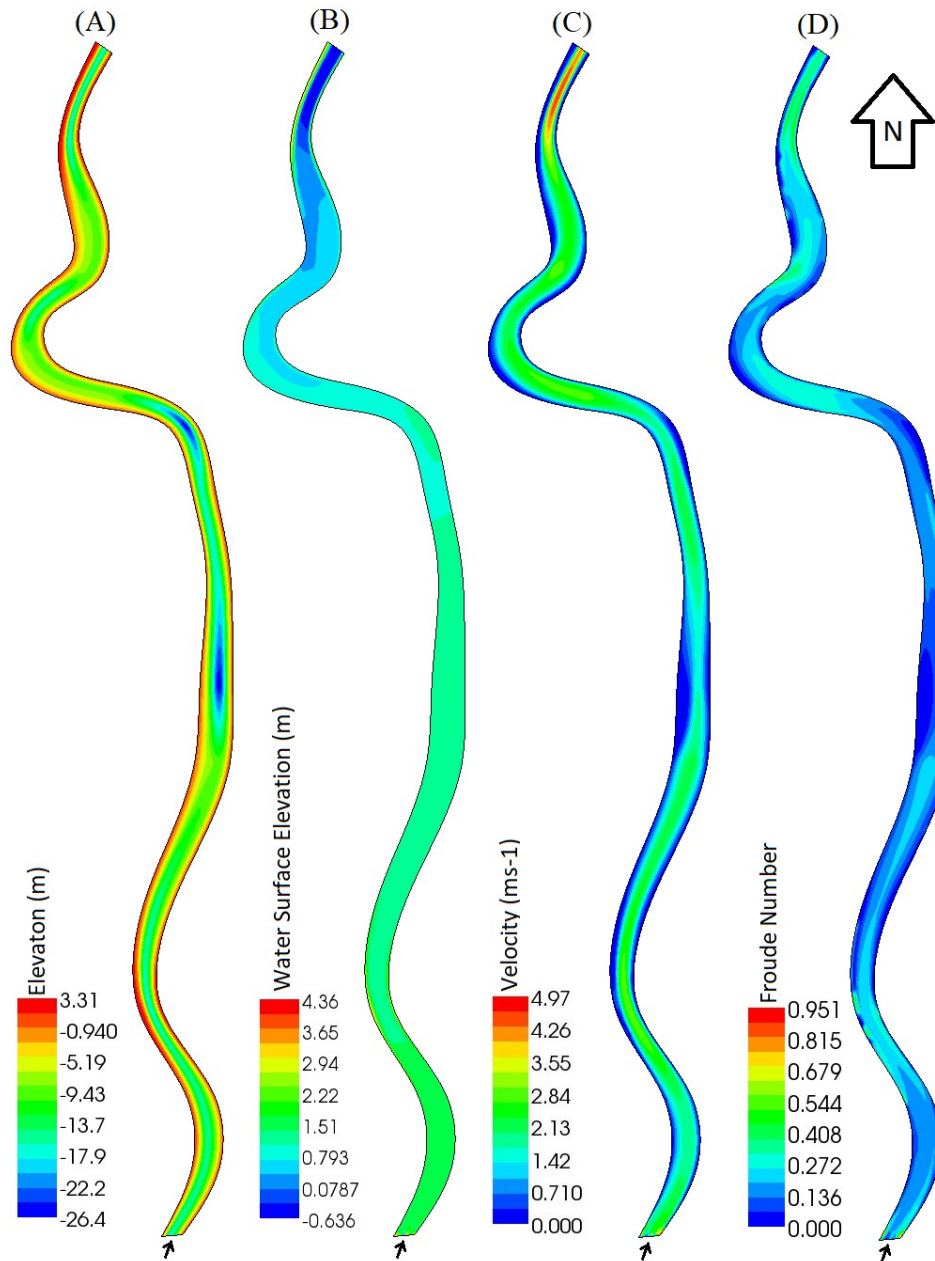
- Data line: (Distance from left bank) (Riverbed elevation) ----Continue to create rows of data until there are as many rows as there are cross-sections. Each row describes up to five sets of combinations of (Distance from left bank) and (Riverbed elevation) data.
- Figure: 3.12 shows the concept of the River Survey File data. iRIC does not display the four dots (data of Indexes 1 to 4).

The coordinates in the cross-sectional direction displayed in the [Cross-section] window have been converted as follows; note that they are different from [Distance from left bank] in the cross-section data of the River Survey File.

3.7 Result

Numerical simulation is done to create an artificial high-tide and ebb-tide environment in all the three Part A, B and C. During high-tide, water flows from south to north and during ebb-tide water flows from north to south. Each time 6000 m³/s constant discharge (data collected from MPA) is considered to flow through the three parts during both high and ebb-tide and total simulation is continued for six hours.

3.7.1 High-tide



Legend

(A) Elevation (m), (B) Water Surface Elevation (m), (C) Velocity (m/s),
(D) Froude Number

Input Data

Discharge $6000 \text{ m}^3/\text{s}$, Water Level 3.04 m, Manning's Roughness Coefficient 0.025

Simulation End Time 21600 s, Result 21600 s

Figure 3.13: Elevation, Water Surface Elevation, Velocity, Froude Number contour of Section A during high-tide (Flow from South to North)

From Figure: 3.13, it is observed that flow velocity is higher at the position where elevation is lower or water depth is higher. So it is clear that velocity is higher at the middle of the cross-section. It is also seen that during high-tide flow is sub-critical, because Froude number is less than 1.

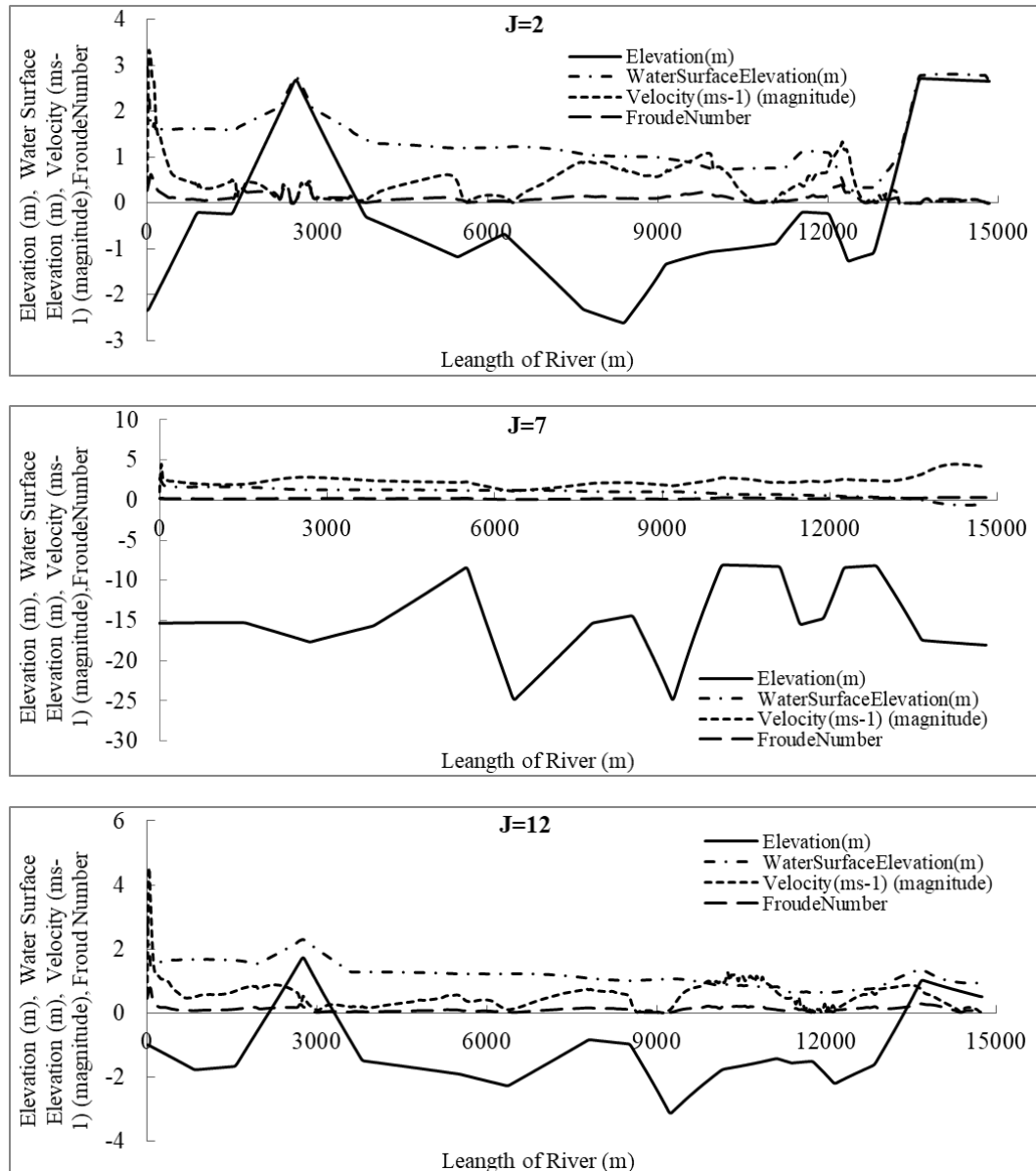


Figure 3.14: Elevation, Water Surface Elevation, Velocity, Froude Number along the length of Section A from left bank to right bank during high-tide.

Figure 3.14 shows the graphical representation of four variables (Elevation, Water Surface Elevation, Velocity, Froude Number) along the Part A. Numbers of grids is created for the simulation are, $i \times j = 497 \times 13 = 6461$. Where along river cross-section $j = 13$ numbers of grids is taken. Change of the variables along the length of the section is represented graphically in each grid across the river cross-section. From all the 13 numbers of transverse grid $j = 2, 7$ and 12 numbered grids are considered for left bank

middle of the section and right bank study respectively. Figure 3.14 represents graphical representation of all those four variables at the 2, 7 and 12 numbered grids. From the figure, it is clear that velocity is higher in the middle of the section, where channel depth is also higher. It is also seen that through the channel, velocity is higher where depth is higher and drops where depth decreases. It is also observed that velocity magnitude is low but fluctuates frequently at both left and right bank where depth is lowest along the river length. In case of Froude Number, it is also fluctuates frequently at the two banks but almost remains same at the middle of the channel. In every 3 number of graphs, flow is sub-critical. One of the key reasons is climbing of water from downstream to upstream against gravitational force during high-tide.



Legend

(A) Elevation (m), (B) Water Surface Elevation (m), (C) Velocity (m/s), (D) Froude Number

Input Data

Discharge $6000 \text{ m}^3/\text{s}$, Water Level 3.04 m, Manning's Roughness Coefficient 0.025
Simulation End Time 21600 s, Result 21600 s

Figure 3. 15: Elevation, Water Surface Elevation, Velocity, Froude Number contour of Part B during high-tide (Flow from South to North)

From Figure 3.15, a preliminary detail of the high-tide condition of Part B can be realized. Similar like Part A, it observed that flow velocity is higher, where flow depth is higher, especially at the middle of the section. Total $i \times j = 641 \times 13 = 8333$ number of grids are considered for the simulation of Part B. Similar like Part A, $j = 2, 7$ and 12 numbered grid are considered for both banks and middle of the channel study.

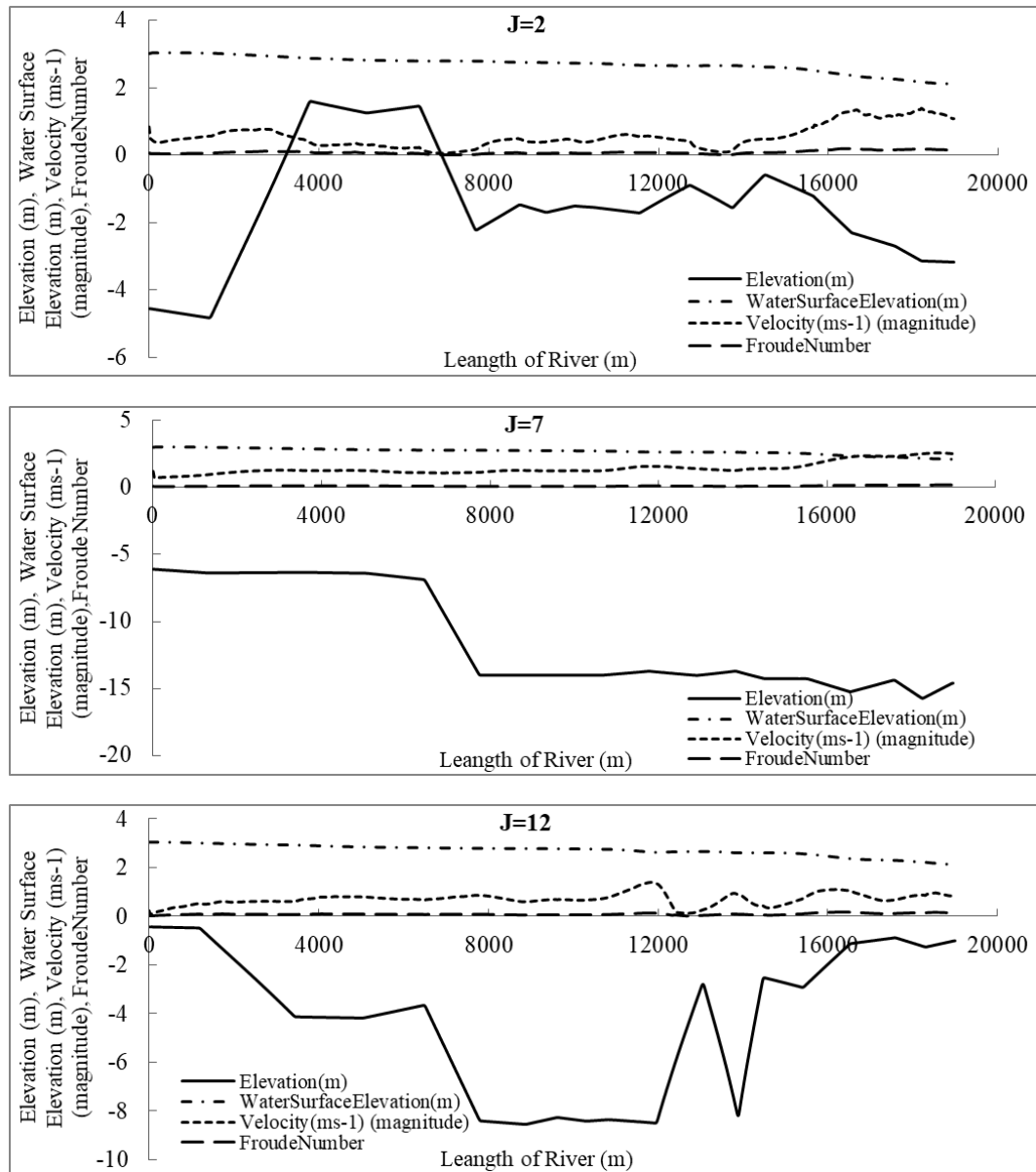
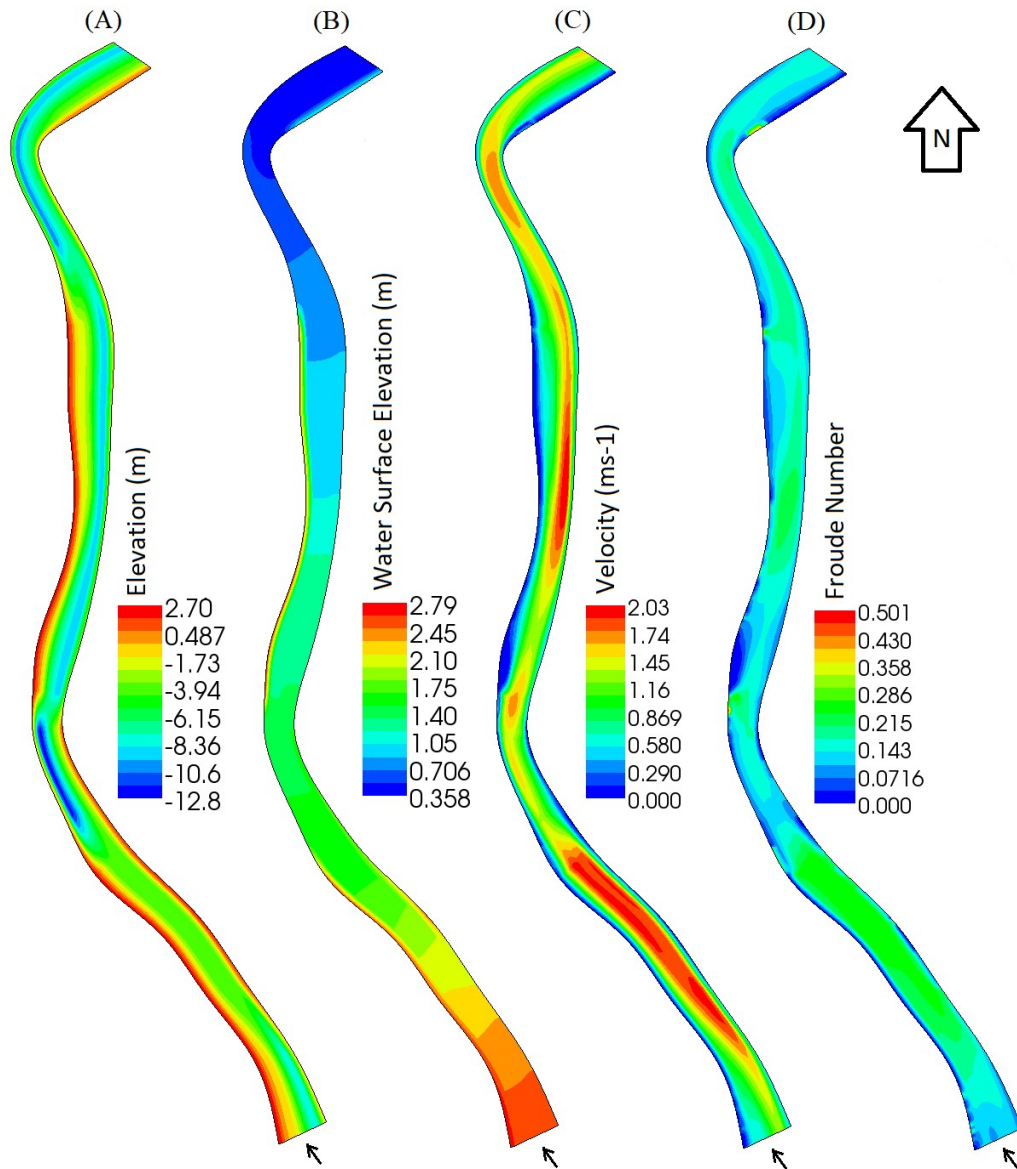


Figure 3.16: Elevation, Water Surface Elevation, Velocity, Froude Number along the length of Part B from left bank to right bank during high-tide.

Figure 3.16 shows that at middle of the section ($j = 7$), after about 5000 meter away from upstream channel depth increases suddenly. At the same time velocity is also increased from the same position of increased depth. Water surface and Froude number

show that at middle of the river flow is laminar. Whereas left and right bank shows same nature as Part A.

Again Figure 3.17 shows same nature of Part C, like Part A and B as mentioned above discussion. Also in this case velocity is higher where flow depth is higher. Value of Froude number shows the laminar nature of the flow through the channel.



Legend

(A) Elevation (m), (B) Water Surface Elevation (m), (C) Velocity (m/s), (D) Froude Number

Input Data

Discharge 6000 m³/s, Water Level 3.04 m, Manning's Roughness Coefficient 0.025

Simulation End Time 21600 s, Result 21600 s

Figure 3. 17: Elevation, Water Surface Elevation, Velocity, Froude Number contour of Part C during high-tide (Flow from South to North)

Part C is discretized into 11297 numbers of grids, that is $i \times j = 869 \times 13 = 11297$. Like Part A and B, at both left and right bank water surface and velocity fluctuate abruptly as shown in Figure 3.18. But at the middle of the channel velocity does not change abruptly. Also in this case velocity is higher, where depth is higher and laminar in nature through the entire length. From the above mentioned high-tide condition at Part A, Part B and Part C, it is clearly observed that velocity fluctuate near the banks as well as the water surface, whatever Froude number indicates that in this reasons flow is subcritical. The reason of the fluctuation of these parameters, is secondary current which is strong near channel boundary. And also transverse shear stress, channel bed friction are responsible for this abnormality.

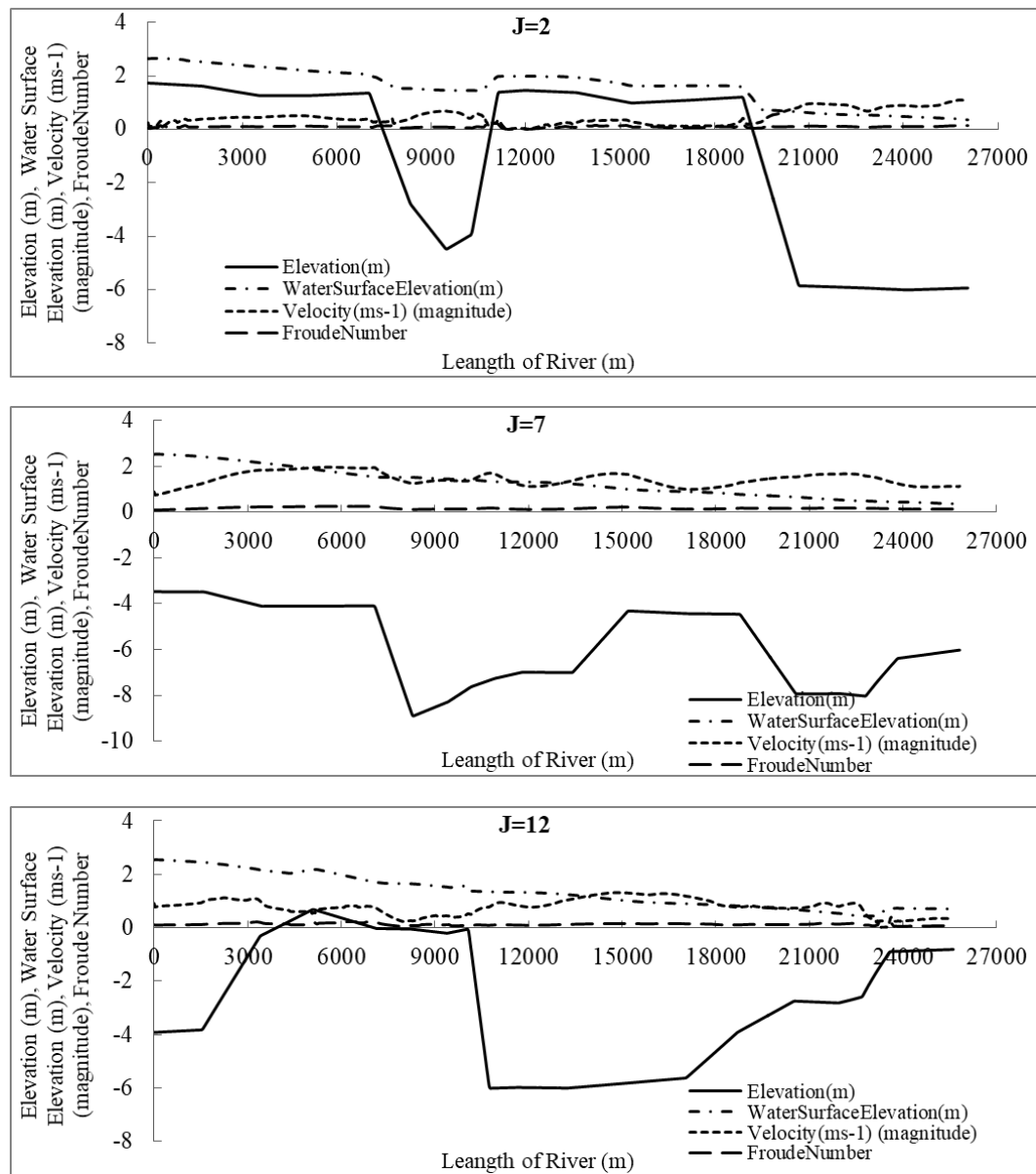
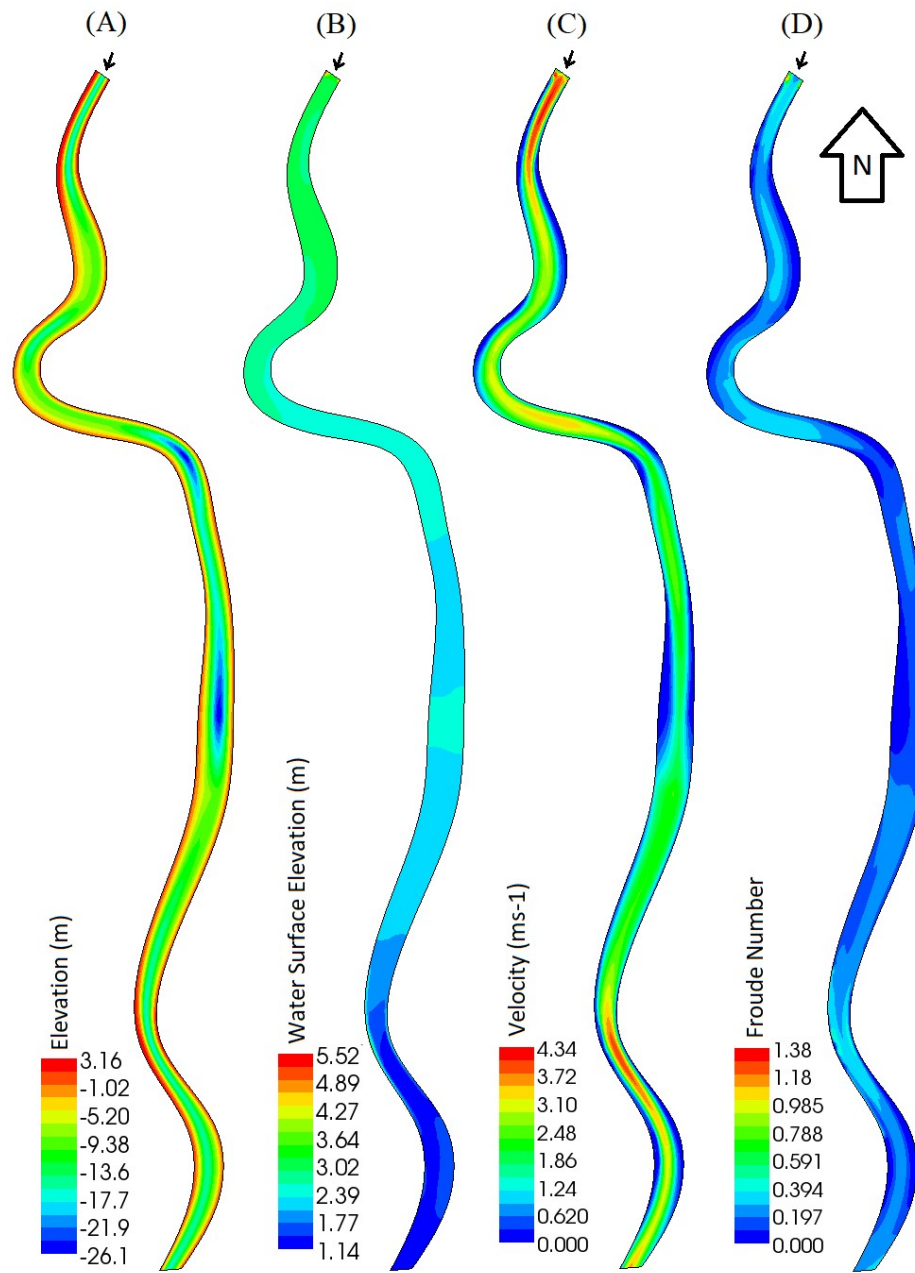


Figure 3. 18: Elevation, Water Surface Elevation, Velocity, Froude Number along the length of Part C from left bank to right bank during high-tide.

3.7.2 Ebb-tide



Legend

(A) Elevation (m), (B) Water Surface Elevation (m), (C) Velocity (m/s),
(D) Froude Number

Input Data

Discharge 6000 m³/s, Water Level -0.3 m, Manning's Roughness Coefficient
0.025

Simulation End Time 21600 s, Result 21600 s

Figure 3.19: Elevation, Water Surface Elevation, Velocity, Froude Number contour of Part A during ebb-tide (Flow from North to South)

Figure: 3.19 shows that flow velocity is higher at the position where elevation is lower or water depth is higher during ebb-tide like high-tide at Part A. So it is clear that velocity is higher at the middle of the cross-section. It is also seen that during high-tide flow is sub-critical, because Froude number is less than 1 all through the channel. The key reason may be the almost flat slop at southern part of Bangladesh near the Bay of Bangle.

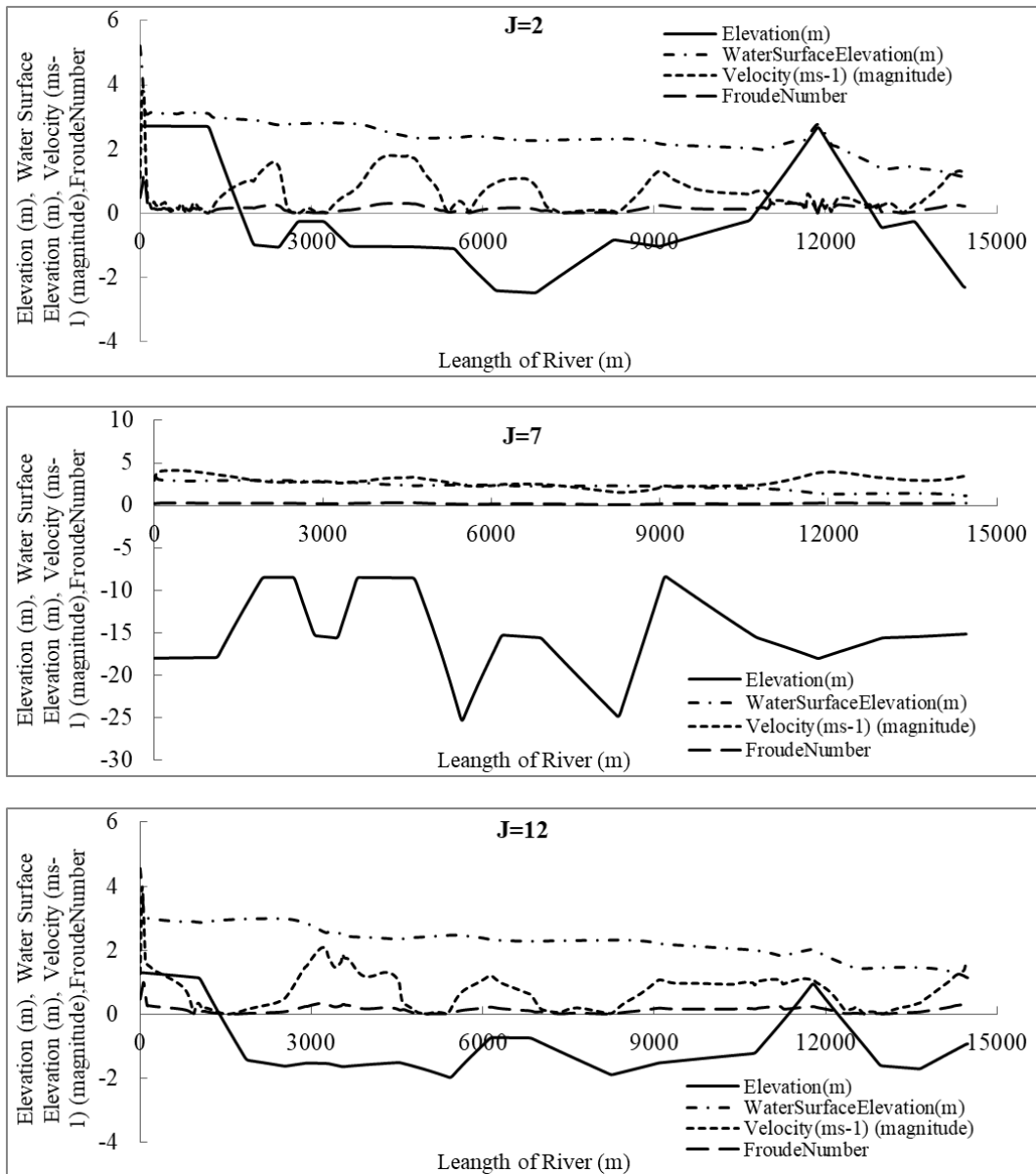
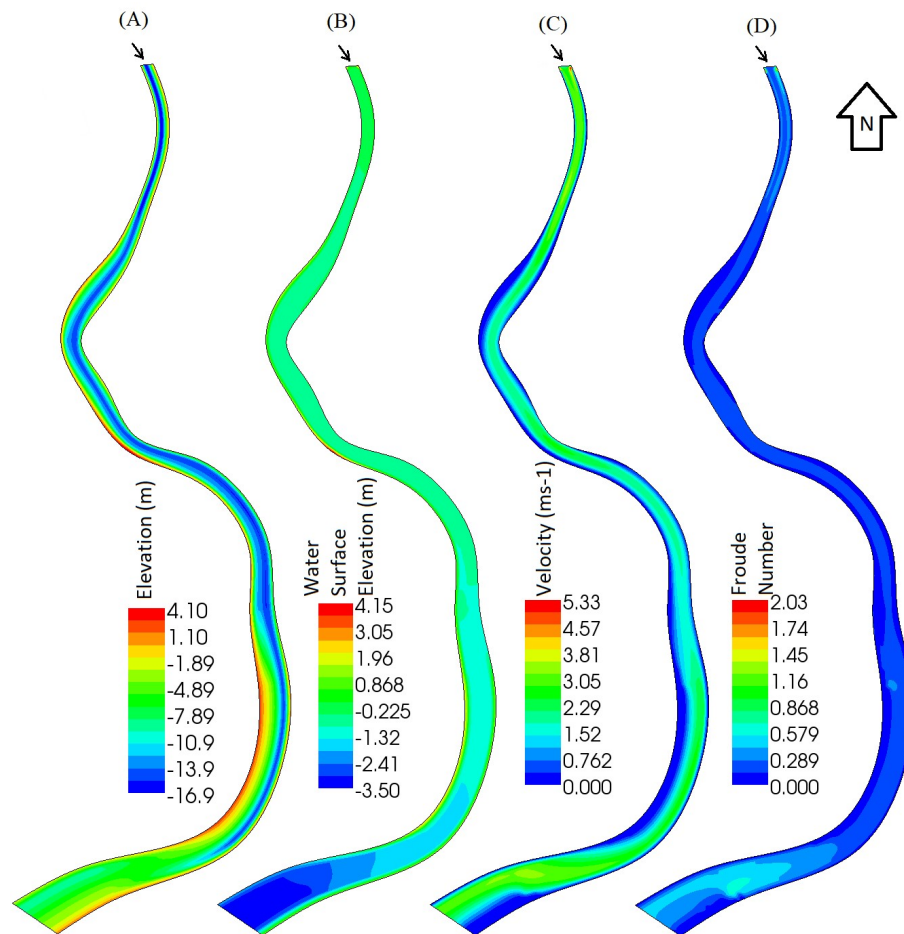


Figure 3.20: Elevation, Water Surface Elevation, Velocity and Froude Number along the length of Part A from left bank to right bank during ebb-tide.

Figure 3.20 shows the graphical representation of four variables (Elevation, Water Surface Elevation, Velocity, Froude Number) along the Part A, during ebb-tide. Numbers of grids are created for the simulation, same as high-tide condition of Part A.

Figure 3.20 represents graphical representation of all those four variables at the 2, 7 and 12 numbered grids during ebb-tide. From the figure, it is clear that velocity is higher in the middle of the section, where channel depth is also higher as mentioned at high-tide condition. It is also observed that velocity magnitude is low but fluctuates frequently at both left and right bank where depth is lowest along the river length. This happens mainly due to secondary current. Froude Number, is also fluctuate frequently at the two banks but almost remains same at the middle of the channel like high-tide. In every 3 number of graphs, flow is sub-critical during ebb-tide. One of the key reasons is almost flat channel slope. Whatever flow near the banks is subcritical during ebb-tide but have a high value of Froude number near 1, which is almost critical in nature. This is due to secondary flow and influence of gravitational force during ebb-tide.



Legend
 (A) Elevation (m), (B) Water Surface Elevation (m), (C) Velocity (m/s), (D) Froude Number
Input Data
 Discharge $6000 \text{ m}^3/\text{s}$, Water Level -0.3 m , Manning's Roughness Coefficient 0.025
 Simulation End Time 21600 s , Result 21600 s

Figure 3. 21 Elevation, Water Surface Elevation, Velocity, Froude Number contour of Part B during ebb-tide (Flow from North to South)

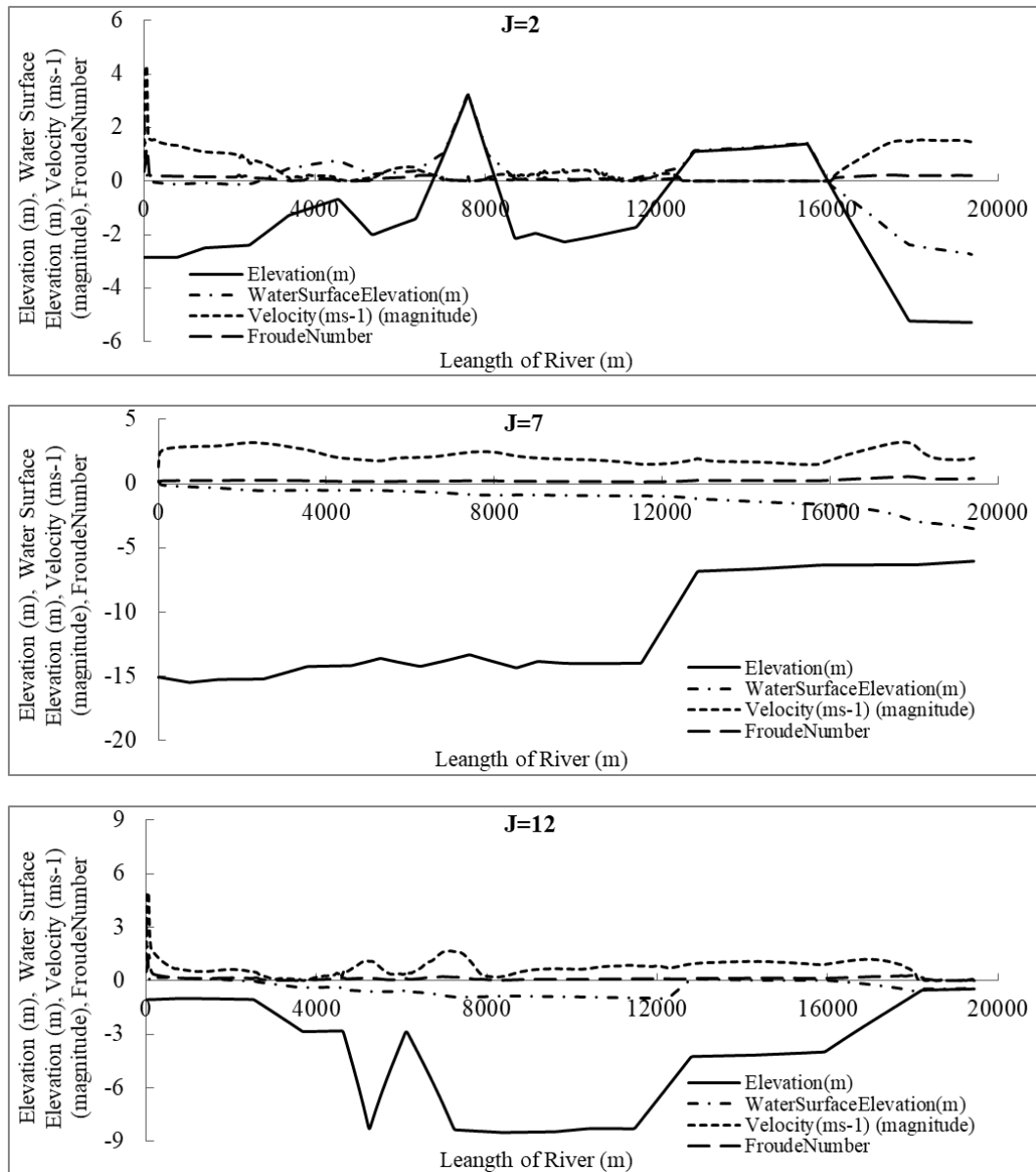
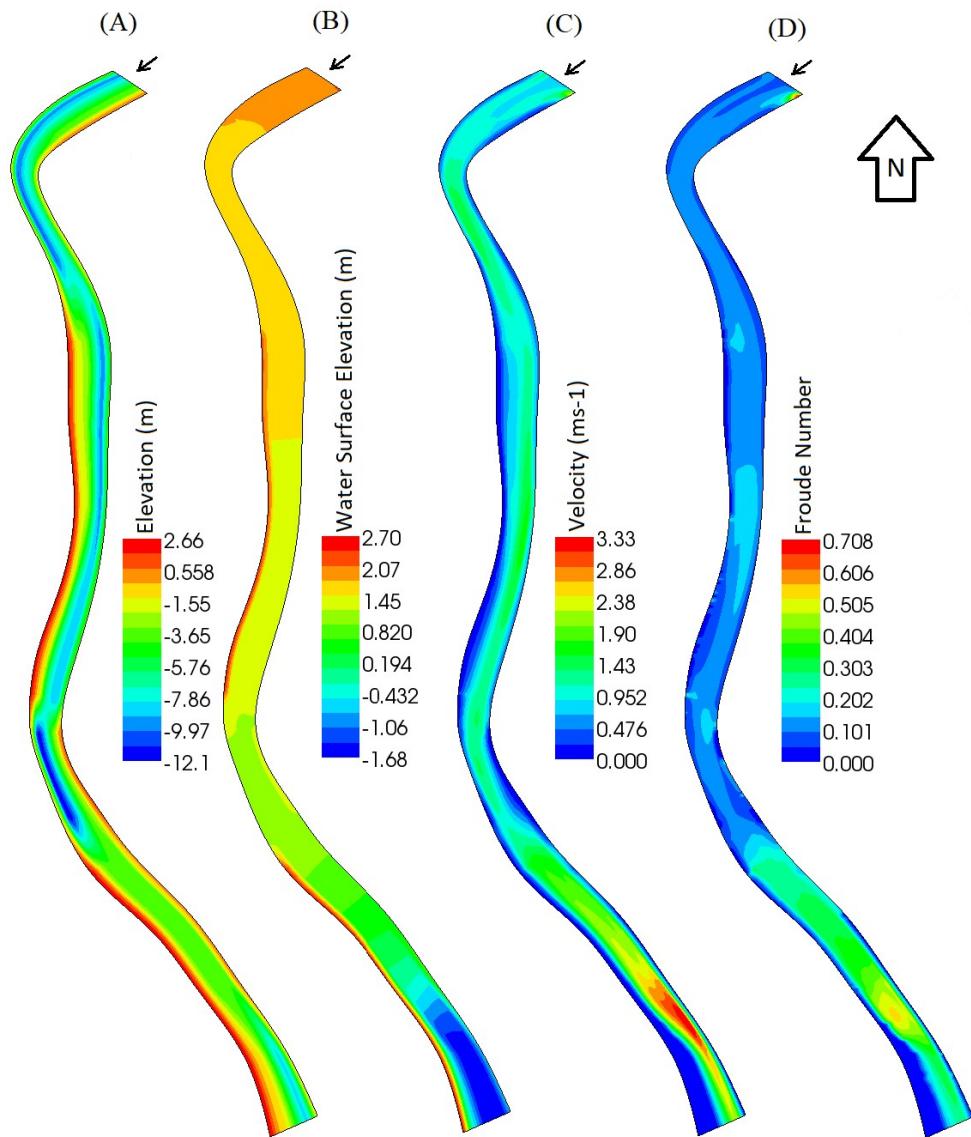


Figure 3. 22: Elevation, Water Surface Elevation, Velocity, Froude Number along the length of Part B from left bank to right bank during ebb-tide

Figure 3.21 and 3.22 show the ebb-tide condition of Part B which is pretty much similar to Part A during ebb-tide condition. Also the velocity is higher at the deepest part of the channel and flow is subcritical all through the length of the river. Again Froude number is near to 1 at some position close to both banks and turns flow to a critical nature. This happens due to action of gravitational force on an almost flat slope.

Figure 3.23 and 3.24 shows the ebb-tide condition of Part C, which represents the same result as mentioned during Part A and B. The difference in case of Part C is a hydraulic drop observed at the middle of the channel near the downstream. A hydraulic drop is a type of local phenomena found in open channel flow. It is a rapid change in the depth

of flow from a high stage to a low stage that results in a steep depression in the water surface. It is often caused by an abrupt change in the channel slope. Also sudden bottom elevation change, forms a weir like formation, on which flow depth decreases but velocity increases. This phenomenon also observed in middle of the section of Part B at Figure 3.22. sudden undulation at the river bed creates weir type formation, which is responsible for this type of flow anomaly. It is also a critical place to navigation as this place is most susceptible for eddy formation.



Legend

(A) Elevation (m), (B) Water Surface Elevation (m), (C) Velocity (m/s), (D) Froude Number

Input Data

Discharge $6000 \text{ m}^3/\text{s}$, Water Level -0.3 m , Manning's Roughness Coefficient 0.025

Simulation End Time 21600 s , Result 21600 s

Figure 3. 23: Elevation, Water Surface Elevation, Velocity, Froude Number contour of Part C during ebb-tide (Flow from North to South)

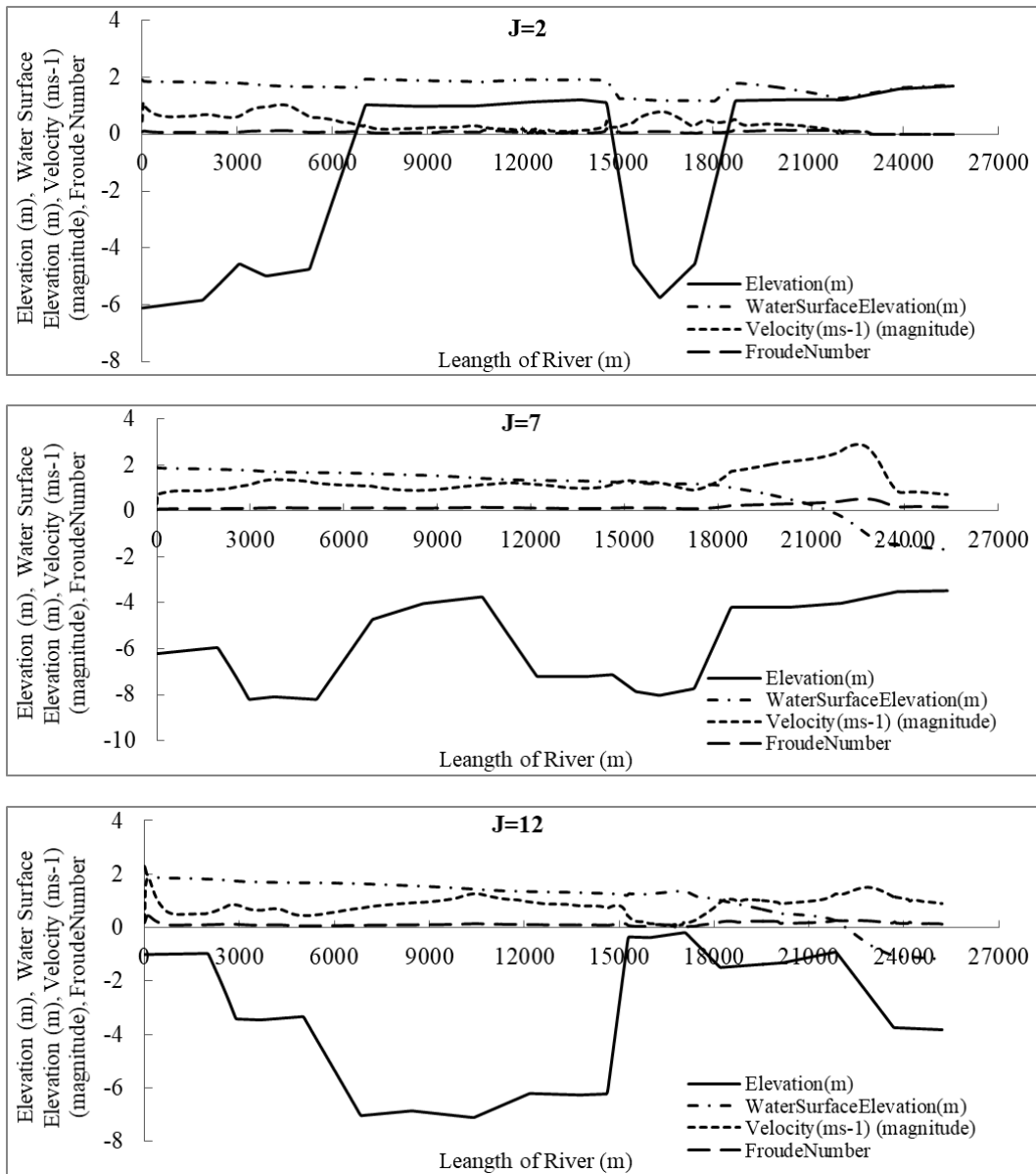


Figure 3. 24: Elevation, Water Surface Elevation, Velocity, Froude Number along the length of Part C from left bank to right bank during ebb-tide.

3.7.3 Particle Movement and Velocity Distribution

Figure 3.25, 3.26 and 3.27 show the correlation between transverse velocity distribution and particle movement during high-tide and ebb-tide. From the following figures it is observed that particle moves higher in quantity in the deepest part of the river, especially where velocity is higher in magnitude.

For settling particles that are considered individually, there are two main forces enacting upon any particle. The primary force is an applied force, such as gravity, and a drag force that is due to the motion of the particle through the fluid. The applied force

is usually not affected by the particle's velocity, whereas the drag force is a function of the particle velocity.

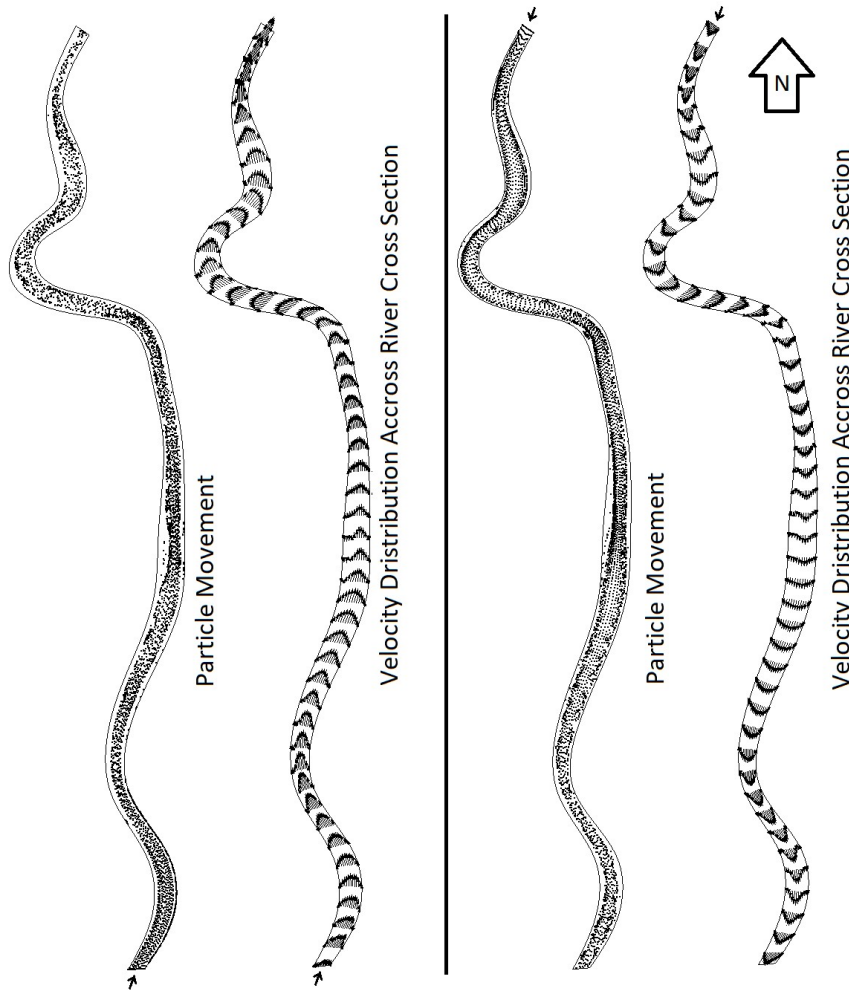


Figure 3.25: Particle movement and velocity distribution along the length of Part A the cross-section during high-tide (left) and ebb-tide (right)

A particle at rest no drag force will be exhibited, which causes the particle to accelerate due to the applied force. When the particle accelerates, the drag force acts in the direction opposite to the particle's motion, retarding further acceleration, in the absence of other forces drag directly opposes the applied force. As the particle increases in velocity eventually the drag force and the applied force will approximately equate, causing no further change in the particle's velocity. This velocity is known as the fall velocity of the particle. This is readily measurable by examining the rate of fall of individual particles. From the following figure it is clearly observed that higher velocity provides more drag force to overcome applied force on particle, hence in this region particles are always in a dynamic state.

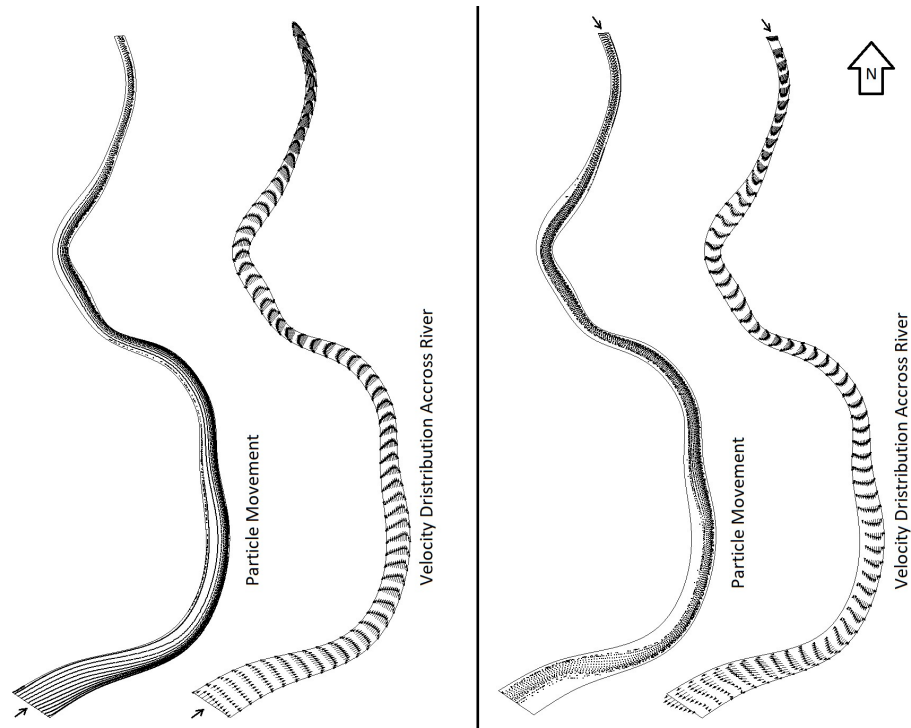


Figure 3. 26: Particle movement and velocity distribution along the length of Part B across the cross-section during high-tide (left) and ebb-tide (right)

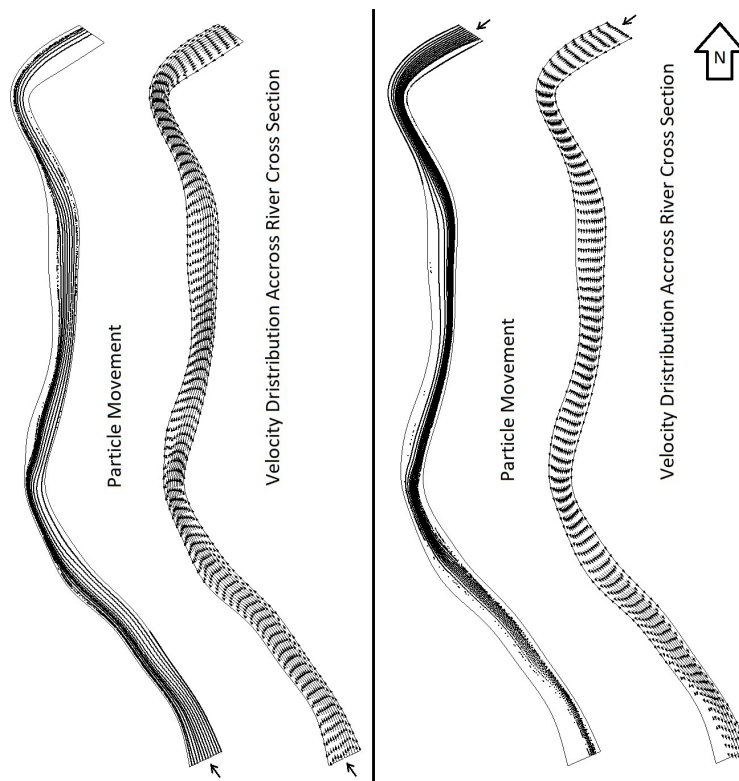
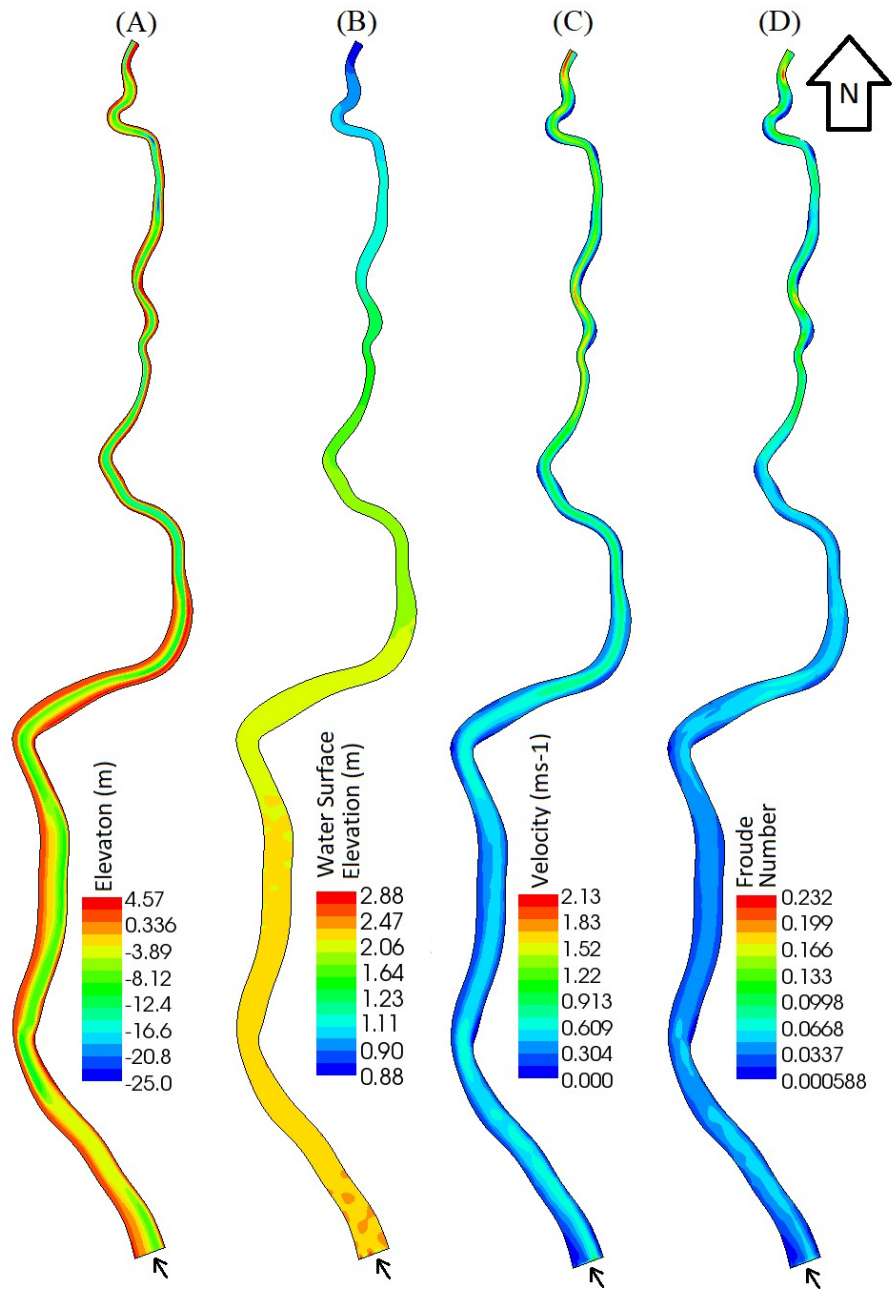


Figure 3. 27: Particle movement and velocity distribution along the length of Part C across the cross-section during high-tide (left) and ebb-tide (right)

3.7.4 Simulation of Combined Length of the Rivers



Legend

(A) Elevation (m), (B) Water Surface Elevation (m), (C) Velocity (m/s),
(D) Froude Number

Input Data

Discharge $6000 \text{ m}^3/\text{s}$, Water Level 3.04 m, Manning's Roughness Coefficient 0.025

Simulation End Time 43000 s, Result 43000 s

Figure 3. 28: Simulation of high-tide condition of the combined length of two rivers

In this section combined length of the two rivers is considered for simulation of high-tide and ebb-tide condition, where total number of grids are $i \times j = 611 \times 17 = 10387$. Result of 2, 9 and 16 number of grids along transverse direction are represented graphically, considered as left bank, middle of the channel and right bank respectively. The purpose of the study of this section is to observe the variation of result, while whole length of the two rivers is considered for simulation, at a same time. In Figure 3.28 and 3.29, channel bottom elevation is constant and water level shows no significant variation among simulated previous simulated high-tide condition in part and presents high-tide condition in combined length. The main perceptible variation is observed in the of velocity magnitude, as well as in Froude number. In previous high-tide condition flow velocity is so high, that is impractical. Whatever Froude number shows the flow is sub-critical in previous case but the value of the number is almost 1 in many cases, which makes the flow impractically near to critical.

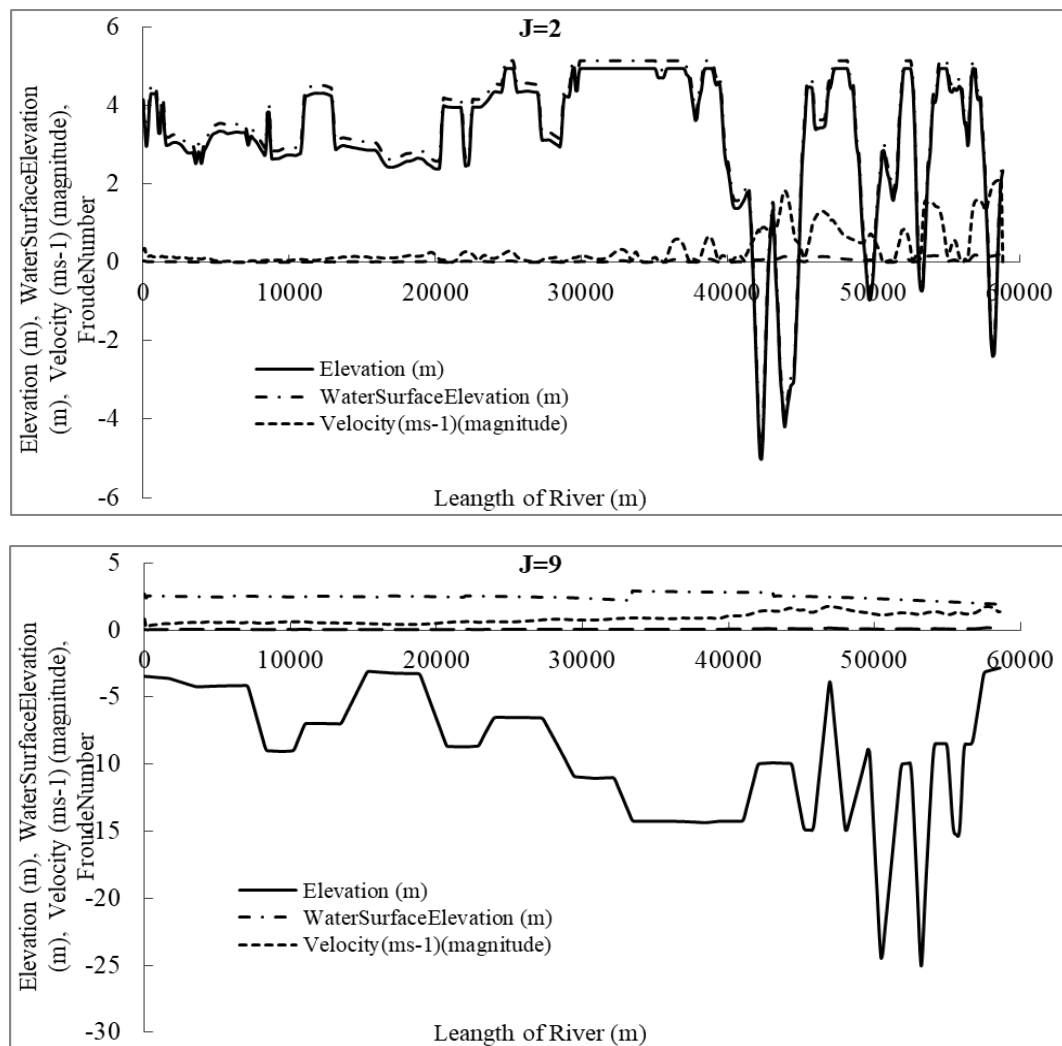


Figure 3.29: Elevation, Water Surface Elevation, Velocity, Froude Number along the combined length from left bank to right bank during high-tide (continued).

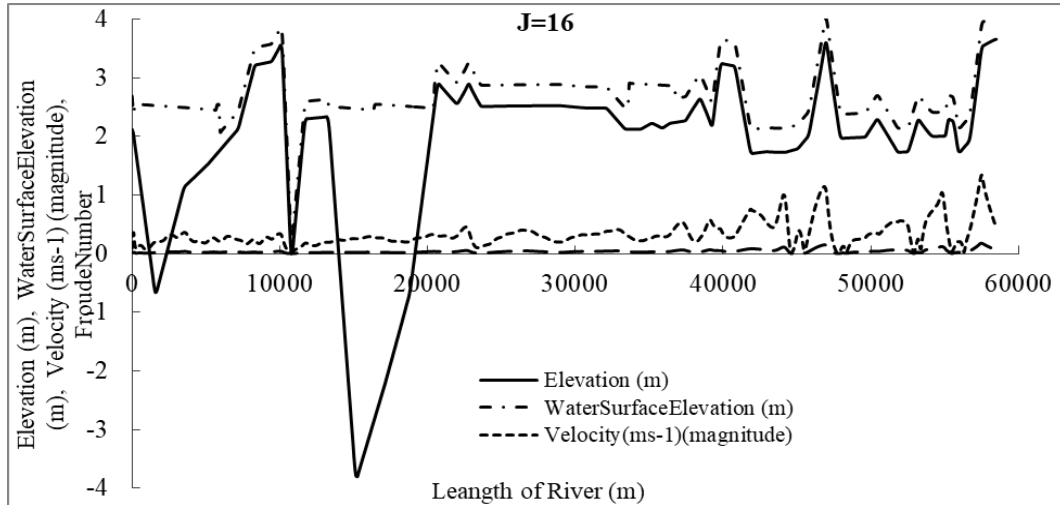
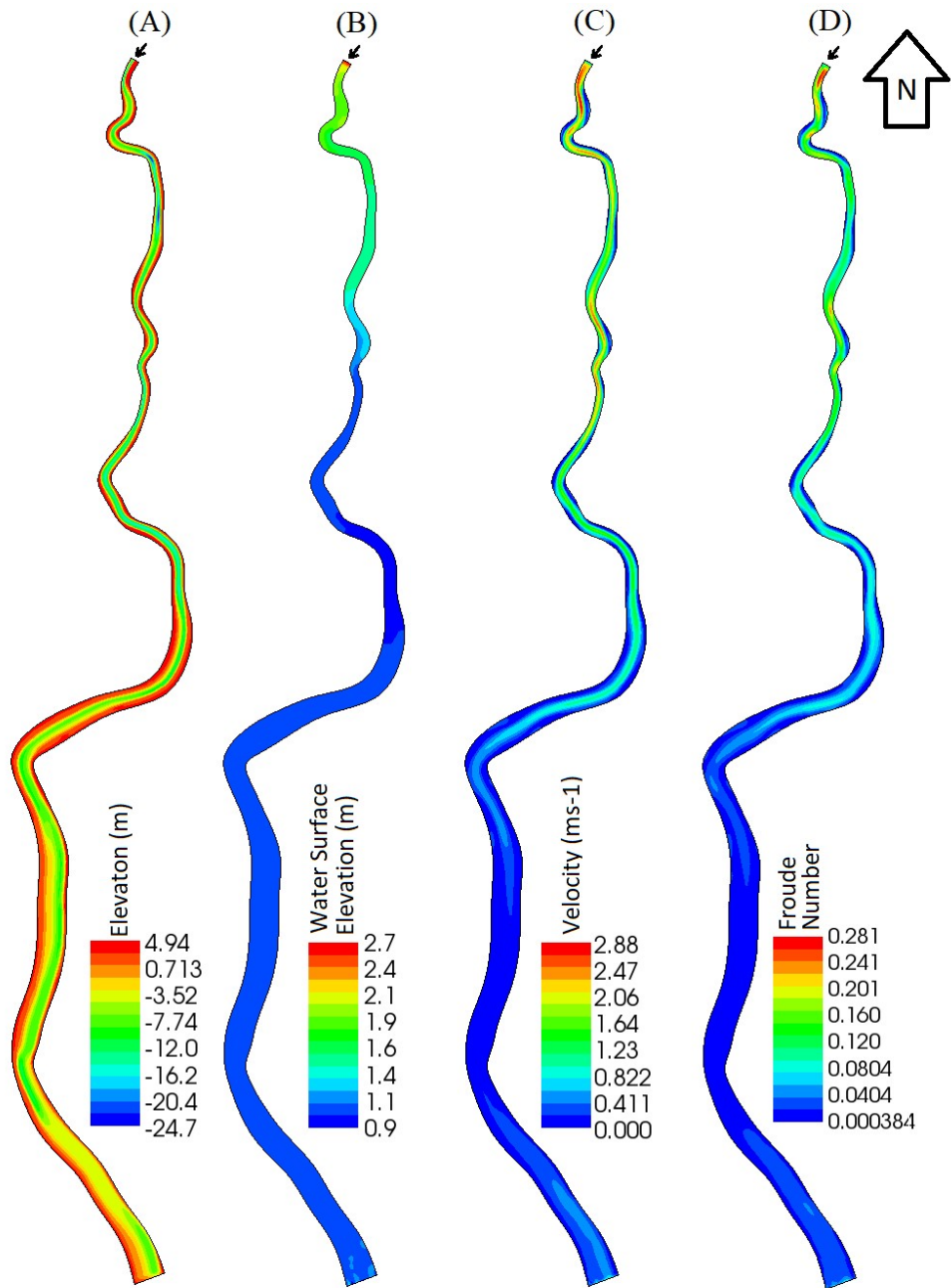


Figure 3. 29: Elevation, Water Surface Elevation, Velocity, Froude Number along the combined length from left bank to right bank during high-tide.

Considering combined length of the two rivers shows practical result, where flow velocity more or less 0.6 m/s at middle of the channel (Figure 3.28 and 3.29) and Froude number represents the flow as subcritical perfectly. The key reason of this variation in present high-tide condition with the previous conditions may be channel bed friction and transverse bed shear stress. Considering large scale length of channel makes it more practical, while the discharge is fixed along with time. Huge length provides more bed resistance with other parameter, which make the flow energy weak. Whatever considering shortest distance shows more detail result and easy to simulate the flow condition. But it is necessary to be more careful, while considering different values of different parameters, which affects the flow. Also in this simulation secondary current is taken as a parameter and during considering combined length, it shows more effect on channel flow.

Figure 3.30 and 3.31 show the ebb-tide condition in the combined total length of the channel, which represents similarity with the high-tide condition. Also present ebb-tide condition shows less value of velocity magnitude and Froude number than previous simulated ebb-tide condition in part. Figure 3.30 shows that velocity magnitude ranges from 0.411 to 2.88 m/s, which is lower than previous ebb-tide condition. Also Froude number shows flow is far from critical state.

From the present study of this section, some points can be noted that during simulation, considering large scale length is more practical than perform it partly. Also simulating such a huge length, care should be taken during discretize the channel geometry. But simulating in small part shows more detail result. In this case input of detail upstream data can provide more reliable result.



Legend

(A) Elevation (m), (B) Water Surface Elevation (m), (C) Velocity (m/s), (D) Froude Number

Input Data

Discharge $6000 \text{ m}^3/\text{s}$, Water Level 3.04 m, Manning's Roughness Coefficient 0.025

Simulation End Time 43000 s, Result 13600 s

Figure 3. 30: Simulation of ebb-tide condition of the combined length of two rivers

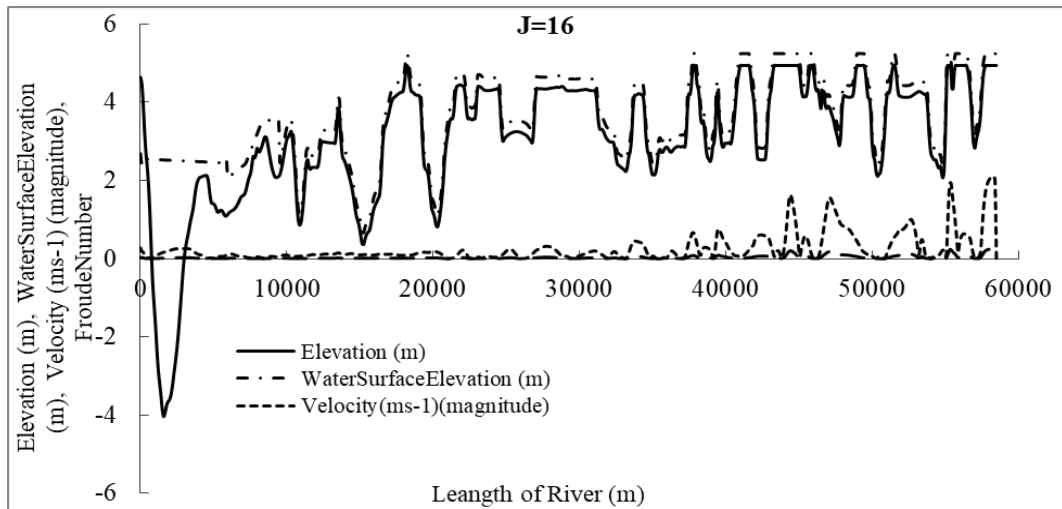
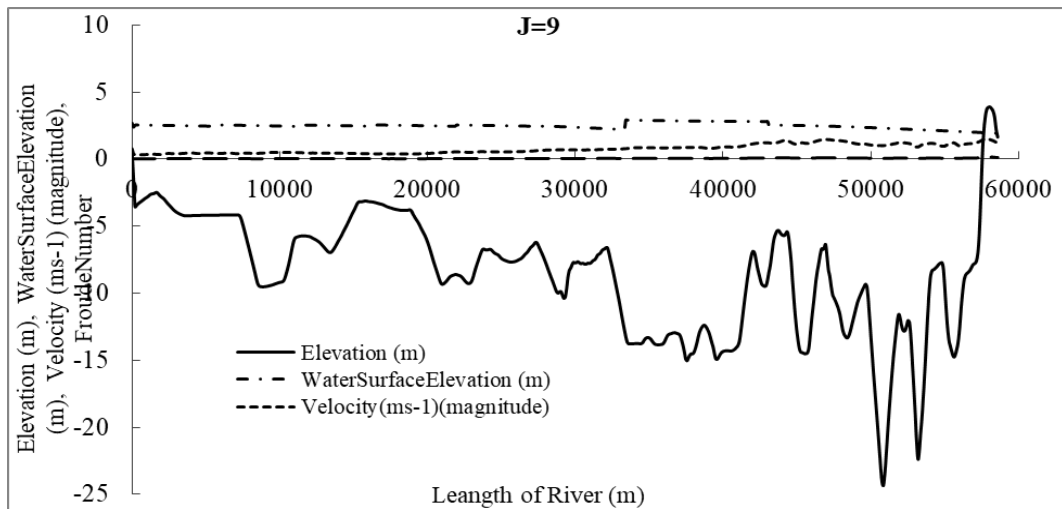
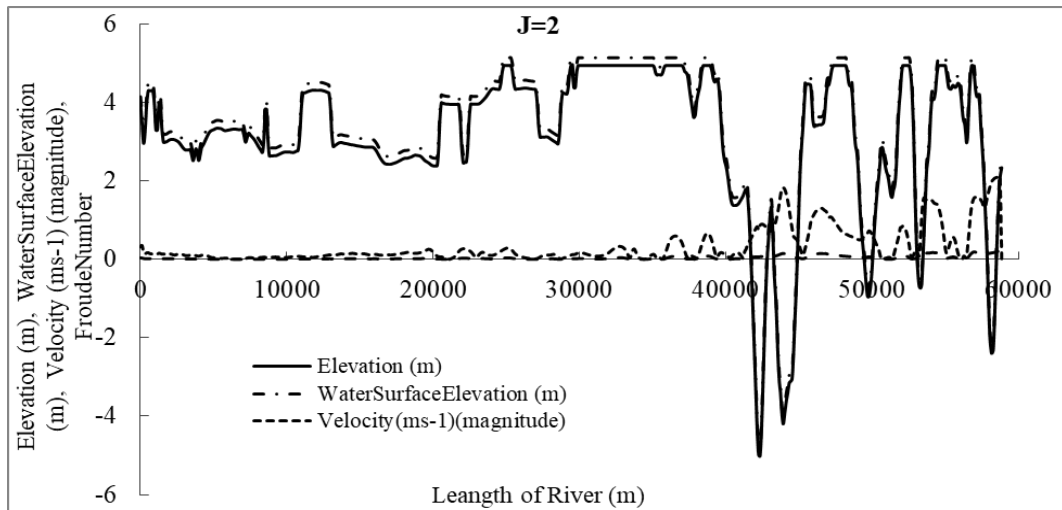


Figure 3. 31: Elevation, Water Surface Elevation, Velocity, Froude Number along the combined length from left bank to right bank during ebb-tide.

3.8 Conclusion

From above analysis, following decision can be made precisely:

- The velocity magnitude is fluctuated frequently near the bank of the river.
- Velocity magnitude is higher at the outer curve of the river bend, which is very common in trapezoidal shape cross section.
- At the middle of the channel section and position where channel depth is higher, velocity magnitude is also higher. It happens because, at the middle of the channel, factors which affect the primary flow are less effective. These factors may be secondary flow, bed resistance or transverse shear stress etc.
- In all the cases flow is subcritical because always Froude number is less than one.
- Near the bank of the river, value of Froude number is so high that the flow tends to be critical.
- Particle movement is found higher at the position, where channel depth is higher. This means position of higher of depth, is less likely to be silted.
- The simulation of high-tide and ebb-tide conditions is performed in three part geometry of the total length.
- In this type of small part of geometry, velocity magnitude shows exceptional higher value along the length of the channel and value of Froude number represents the flow tends to critical. This type of result is not practical for the real river.
- These three part geometry is simulated again in a combined form of total length.
- Simulation of high-tide and ebb-tide condition in the combined geometry of the total length shows reasonable value of velocity magnitude and Froude number.
- Simulation of combined length shows low velocity magnitude which is more practical in real river.
- Froude number shows reasonable low value less than 1, in case of simulation of the combined geometry, which represents the channel flow more likely to subcritical. This result is more reliable for natural river in a flat slope like Rupsha.
- Simulation in a combined geometry of the river length shows more reliable result than the part. It happens because, factors such as secondary flow, bed resistance etc. which is mainly responsible to reduce the velocity magnitude of primary flow, show combined effect along the total length of river. But simulation of such a huge length of river is time consuming and needs more powerful computer to do it.

CHAPTER 4

Modeling of Channel Confluence

4.1 Introduction

In this study, both convergent and divergent type flow is simulated in the natural river junction. Because water flows in a tidal force influenced river confluence from both upstream and downstream, during high-tide and ebb-tide creates both convergent and divergent flow in the same junction. Generally branch channel is not connected with main channel in a 90⁰ angled junction. For validity analysis 90⁰ confluence and diversion are considered for avoiding complexity of modeling. This study applied on natural confluence, is necessary for the prevention of erosion, siltation near the branch estuary and to improve uninterrupted navigability.

4.2 Governing Equation

4.2.1 Basic Flow Equation

The hydrodynamic component of the confluence model is based on the two-dimensional; depth averaged St. Venant Equations expressed in conservative form. These three equations represent the conservation of water mass and of the two components of the momentum vector. The dependent variables actually solved for are the depth and discharge intensities in the two respective coordinate directions.

Conservation of mass:

$$\frac{\partial H}{\partial t} + \frac{\partial q_x}{\partial x} + \frac{\partial q_y}{\partial y} = 0 \quad (4.1)$$

Conservation of x-direction momentum:

$$\frac{\partial q_x}{\partial t} + \frac{\partial}{\partial x}(Uq_x) + \frac{\partial}{\partial y}(Vq_x) + \frac{g}{2} \frac{\partial}{\partial x} H^2 = gH(S_{0x} - S_{fx}) + \frac{1}{\rho} \left(\frac{\partial}{\partial x} (H\tau_{xx}) \right) + \frac{1}{\rho} \left(\frac{\partial}{\partial y} (H\tau_{xy}) \right) \quad (4.2)$$

Conservation of y-direction momentum:

$$\frac{\partial q_y}{\partial t} + \frac{\partial}{\partial x}(Uq_y) + \frac{\partial}{\partial y}(Vq_y) + \frac{g}{2} \frac{\partial}{\partial y} H^2 = gH(S_{0y} - S_{fy}) + \frac{1}{\rho} \left(\frac{\partial}{\partial x} (H\tau_{yx}) \right) + \frac{1}{\rho} \left(\frac{\partial}{\partial y} (H\tau_{yy}) \right) \quad (4.3)$$

where H is the depth of flow, U and V are the depth averaged velocities in the x and y coordinate directions respectively. q_x and q_y are the respective discharge intensities which are related to the velocity components through

$$q_x = HU \quad (4.4)$$

And

$$q_y = HV \quad (4.5)$$

g is the acceleration due to gravity and ρ is the density of water. S_{0x} and S_{0y} are the bed slopes in the x and y directions; S_{fx} and S_{fy} are the corresponding friction slopes.

τ_{xx} , τ_{xy} , τ_{yx} , and τ_{yy} are the components of the horizontal turbulent stress tensor

4.2.2 Bed Resistance Model

The friction slope terms depend on the bed shear stresses which are assumed to be related to the magnitude and direction of the depth averaged velocity. In the x direction for example,

$$S_{fx} = \frac{\tau_{bx}}{\rho g H} = \frac{\sqrt{U^2 + V^2}}{g H C_s^2} U \quad (4.6)$$

where τ_{bx} is the bed shear stress in the x direction and C_s is a nondimensional Chezy coefficient. This coefficient is related to the effective roughness height k_s , of the boundary, and the depth of flow through

$$C_s = 5.75 \log \left(12 \frac{H}{k_s} \right) \quad (4.7)$$

For a given flow depth H , Manning's n and k_s are related by

$$k_s = \frac{12H}{e^m} \quad (4.8)$$

where m is

$$m = \frac{H^{1/6}}{2.5n\sqrt{g}} \quad (4.9)$$

The effective roughness height was chosen as the resistance parameter because it tends to remain constant over a wider range of depth than does Manning's n .

For very small depth to roughness ratios $\left(\frac{H}{k_s} < \frac{e^2}{12}\right)$, Equation 4.7 is replaced by

$$C_s = 2.5 + \frac{30}{e^2} \left(\frac{H}{k_s}\right) \quad (4.10)$$

which gives a smooth, continuous, non-negative relation for any depth of flow. There is no physical basis for this formula.

The effective roughness height (m) is the resistance parameter to be specified at every node in the mesh in the input files. For resistance due primarily to bed material roughness, a starting estimate of k_s can be taken as 1-3 times the largest grain diameter. The final values should be obtained by calibrating the model results to measured water surface elevations and velocities.

4.2.3 Transverse Shear Model

Depth-averaged transverse turbulent shear stresses are modeled with a Boussinesq type eddy viscosity formulation. For example:

$$\tau_{xy} = \nu_t \left(\frac{\partial U}{\partial y} + \frac{\partial V}{\partial x} \right) \quad (4.11)$$

where ν_t is the eddy viscosity coefficient. The eddy viscosity coefficient is assumed to be composed of three components: a constant, a bed shear generated term, and a transverse shear generated term.

$$\nu_t = \varepsilon_1 + \varepsilon_2 \frac{H\sqrt{U^2+V^2}}{C_s} + \varepsilon_3 H^2 \sqrt{2 \frac{\partial U}{\partial x} + \left(\frac{\partial U}{\partial y} + \frac{\partial V}{\partial x} \right)^2} + 2 \frac{\partial V}{\partial y} \quad (4.12)$$

where ε_1 , ε_2 and ε_3 are user definable coefficients.

The default value for ε_1 is 0. This coefficient can be used to stabilize the solution for very shallow flows when the second term in Equation 4.12 may not adequately describe ν_t for the flow. Reasonable values for ε_1 can be calculated by evaluating the second term in Equation 4.12 using average flow conditions (average flow depth and average velocities) for the modeled site.

The default value for ε_2 is 0.5. By analogy with transverse dispersion coefficients in rivers, values of 0.2 to 1.0 are reasonable. Since most river turbulence is generated by bed shear, this term is usually the most important.

In deeper lakes flows, or flows with high transverse velocity outlets gradients, transverse shear may be the dominant turbulence generation mechanism. Strong recirculation regions are important examples. In these cases, the third term ε_3 , becomes important. It is essentially a 2D (horizontal) mixing length model. The mixing length is assumed to be proportional to the depth of flow. A typical value for ε_3 is 0.1, but this may be adjusted by calibration.

4.2.4 Wet/Dry Area Treatment

In performing a two-dimensional model evaluation, the depth of flow, as a dependent variable, is not known in advance. The horizontal extent of the water coverage is therefore unknown. Significant computational difficulties are encountered when the depth is very shallow or there is no water at all over a part of the modelled area. This 2D model handles these occurrences by changing the surface flow equations to groundwater flow equations in these areas. A continuous free surface with positive (above ground) and negative (below ground) depths is calculated. This procedure allows calculations to carry on without changing or updating the boundary conditions. In addition, modeled area selection and boundary condition specification are greatly simplified. Specifically, the water mass conservation equation is replaced by:

$$\frac{\partial H}{\partial t} = \frac{T}{S} \left(\frac{\partial^2}{\partial x^2} (H + z_b) + \frac{\partial^2}{\partial y^2} (H + z_b) \right) \quad (4.13)$$

where T is the transmissivity, S is the storativity of the artificial aquifer and z_b is the ground surface elevation.

The transmissivity and storativity of the groundwater flow can be set by the user. The transmissivity should be set to a low value such that the actual groundwater discharge is negligible; the default is 0.1. For a given area, the storativity is a measure of the volume of water the ground will release per unit decline in the water table. The default storativity is set to 1. For accurate transient analysis or to speed up the groundwater response rate, the storativity should be reduced.

4.2.5 Boundary Extraction Module

The boundary extraction component is based on the concept of streamlines and stream tubes. A streamline is defined as an imaginary line in the field of flow such that at any point on the line, the velocity vector is tangential to it. Therefore in theory, there can be no flow across a streamline. For steady flow, a streamline is fixed in space since there is no change in direction of the velocity vector at any point in the field of flow. For two-dimensional flow, the equation of a streamline is

$$q_x dy - q_y dx = 0 \quad (4.14)$$

It is defined as a scalar function such that

$$q_x = \frac{\partial \psi}{\partial y} \quad \text{and} \quad q_y = -\frac{\partial \psi}{\partial x} \quad (4.15)$$

This scalar function $\psi(x, y)$ is called stream function. Consider the total differential of ψ ,

$$d\psi = q_x dy - q_y dx \quad (4.16)$$

which illustrates that the equation of a streamline (Equation 4.14) is just a special case of Equation 4.16 where $d\psi = 0$. This illustrates that ψ is constant along any streamline.

In Figure 4.1(a), we have two streamlines, ψ_1 and ψ_2 , some distance apart in a two-dimensional flow field. Since there can be no flow across either of the streamlines, the streamlines confine the flow into what is called a stream tube. Now consider two streamlines that are infinitesimally close, ψ and $\psi + d\psi$, also shown in Figure 4.5(a). From Figure 4.1(b), we can compute the flow or discharge in this elemental stream tube (across ds) as

$$dQ = q_x dy - q_y dx \quad (4.17)$$

which illustrates that,

$$dQ = d\psi \quad (4.18)$$

Hence the change in ψ across this elemental stream tube is numerically equal to the discharge through it. Now if the above expression is integrated between ψ_1 and ψ_2 , we find that the difference in the stream function between any two streamlines is equal to the flow between the streamlines:

$$Q_{1 \rightarrow 2} = \int_1^2 d\psi = \psi_2 - \psi_1 \quad (4.19)$$

In Figure 4.1(a), the flow is from left to right, since $\psi_2 > \psi_1$. If $\psi_2 < \psi_1$, the flow would be from right to left.

Due to this relationship between stream function and discharge, if one arbitrarily sets $\psi_1 = 0$ at one side of a channel (assuming the side of a channel is a no flow boundary, then by definition it is a streamline), then the value of ψ_2 at the other side of the channel will be equal to the total discharge across the channel. In this case, the value of

the stream function at any point in the flow, ψ_p will be equal to the discharge in the stream tube defined by the streamlines ψ_1 and ψ_p .

As ψ_p approaches the value of ψ_2 , the discharge in the stream tube approaches the total discharge in the channel. For this reason, the value of the stream function across a channel is also called the cumulative discharge.

In order to solve the computational mesh of a sub-site that is to be treated separately from the larger site from which it came, the boundary conditions along the boundary defining this sub-site must be known. If the boundary extends across the channel then the boundary conditions are known to be no flow at the sides of the channel. However, if the entire boundary is within the flow, then the problem is no longer trivial. Because streamlines by definition are no flow boundaries, they are logical paths to trace when defining a computational boundary within the flow. For this reason, the boundary extraction module in this 2D model uses the concept of streamlines and stream tubes when defining a computational boundary for a new small scale mesh from within a larger site.

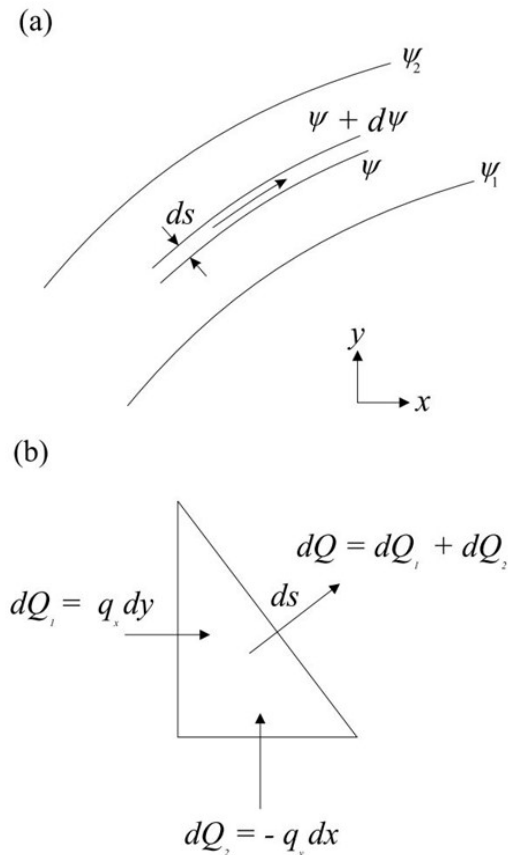


Figure 4. 1: The relationship between stream function and discharge: (a) a schematic of a stream tube and (b) the calculation of discharge across an elemental stream tube.

To map out streamlines, the value of stream function must be known at every node within the computational domain. If the stream function is calculated assuming that one of the no flow boundaries in the computational domain is a streamline where $\psi = 0$, then the stream function will also represent the cumulative discharge in the channel. Only the location of the streamlines is essential to this 2D model's boundary extraction process. However, when the values of stream function represent the cumulative discharge in a channel, then the concept of stream function takes on a physical meaning. In the 2D model, calculation of the cumulative discharge is performed in two steps. The first step involves calculating an approximate solution. In the second step, the approximate solution is refined using the Finite Element Method (FEM).

4.3 Numerical Method

Given a set of governing equations, there are two essential steps in developing a computational model.

- Discretization: The infinite number of equations for an infinite number of unknowns is reduced to a finite number of equations at a finite number of mesh or grid points in space and time. At this stage, calculus operations are reduced to algebraic operations.
- Solution: A scheme or process is devised where the algebraic equations developed in the first step can be solved for the unknown nodal values. The algebra is reduced to arithmetic which can be translated into computer code.

4.3.1 The Finite Element Method

The basis for the finite element method is a more general technique known as the weighted residual method. The idea is that the governing equations can be solved approximately by use of a "trial function" which is specified but has a number of adjustable degrees of freedom. In a way, the process is analogous to curve fitting, say a straight line, to observed data. The straight line is a specified function which has two degrees of freedom. Values for those two parameters are sought which gives the least error.

The continuity and momentum equations of depth averaged flow can be written in abbreviated form as

$$C(H,U,V)=0 \tag{4.20}$$

$$M_x(H,U,V)=0 \tag{4.21}$$

$$M_y(H,U,V)=0 \tag{4.22}$$

If we introduce trial functions for the variables H , U , and V ; denoted by \hat{H} , \hat{U} and \hat{V} substitute them into the equations, they will not exactly satisfy the equations. A "residual" will result.

$$C(\hat{H}, \hat{U}, \hat{V}) = R_C \quad (4.23)$$

$$M_x(\hat{H}, \hat{U}, \hat{V}) = R_x \quad (4.24)$$

$$M_y(\hat{H}, \hat{U}, \hat{V}) = R_y \quad (4.25)$$

The objective is now to make the residuals as small as possible. The weighted residual approach is to multiply the residual by a weighting function, integrate over the whole area and set the result to zero. For every degree of freedom in the trial function, a separate weighting function is used in order to generate the same number of equations as unknowns. The continuity equation, for example, becomes

$$\int N_i C(\hat{H}, \hat{U}, \hat{V}) dA = 0 \quad (4.26)$$

where N_i is the i th weight or test function. Integration over the area serves to reduce the spatial distribution to just a quantity.

The trick with the weighted residual method is to choose good trial and test functions in a general enough way that will work for different situations. The idea of interpolation becomes very useful here. If the trial function for H is set up such that there are a fixed number of points with the depths at those points being parameters to be solved for, then a function which interpolates between the points can be used as a trial function. Interpolation functions can be written in the form of "influence" or "basis" functions for each point, so that the trial function is a sum of terms

$$\hat{H} = \sum_{j=1}^n H_j N_j \quad (4.27)$$

The Galerkin weighted residual method uses the same set of functions for "basis" and for "test" functions, considerably simplifying the choices that have to be made.

The finite element method takes the method of weighted residuals a couple of steps further. First, the domain is divided into discrete areas, called finite elements, which are defined by connections between nodal points. The triangulation below, in Figure 4.2, is an example.

The nodes are at the vertices of the triangles. Simple interpolation or basis functions are easy to construct, allowing linear variations between nodes, for example. These basis functions are considered to be "local" in that they only extend from a particular node to near neighboring nodes. Outside of that area, they are zero. The basis function for node

j can be visualized as a "tent" function with the pole (of unit height) at node j and pegs at all of the nodes which are attached to node j by a triangle edge.

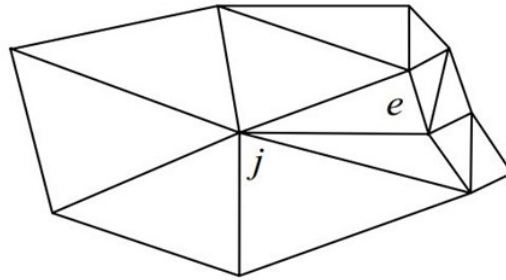


Figure 4. 2: A sample triangulation.

The integration operation in the method of weighted residual is carried out as a sum of element integrals in the finite element method. Because of the local nature of the basis functions, only those functions with nodes in the particular element need to be integrated. For a linear triangle, with three nodes, a total of nine integrals are required (combination of three basis functions with three test functions), even if there are thousands of other nodes.

The biggest advantage of the finite element method is geometrical flexibility. Elements can change size and shape readily, allowing complex boundaries to be traced, as well as allowing refinement of the mesh in particularly important or rapidly varying areas.

The Finite Element Method used in River2D's hydrodynamic model is based on the Streamline Upwind Petrov-Galerkin weighted residual formulation. In this technique, upstream biased test functions are used to ensure solution stability under the full range of flow conditions, including subcritical, supercritical, and transcritical flow. As a result, there is no need for mixed (unequal order) interpolations or artificially large transverse diffusivities.

A fully conservative discretization is implemented which insures that no fluid mass is lost or gained over the modeled domain. This also allows implementation of boundary conditions as natural flow or forced conditions. A fixed elevation is imposed as an equivalent hydrostatic force, for example, and known inflow discharges are used directly.

The model discretizations supported include equal order linear, quadratic, and cubic interpolation of all variables over triangular and quadrilateral elements. The mesh generator supports only linear triangles, however. These elements are the simplest possible in two dimensions and result in the minimum execution time for a given number of nodes.

4.3.2 Weighted Residual Methods

Weighted residual methods (WRM) assume that a solution can be approximated analytically or piecewise analytically. In general a solution to a PDE can be expressed as a superposition of a base set of functions

$$T(x, y) = \sum_{j=1}^N a_j(t) \phi_j(x) \quad (4.28)$$

where the coefficients a_j are determined by a chosen method. The method attempts to minimize the error, for instance, finite differences try to minimize the error specifically at the chosen grid points. WRM's represent a particular group of methods where an integral error is minimized in a certain way and thereby defining the specific method. Depending on the maximization WRM generate

- finite volume method,
- finite element methods,
- spectral methods, and also
- finite difference methods.

4.3.3 General Formulation of WRM

The starting point for WRM's is an expansion in a set of base or trial functions. Often these are analytical in which case the numerical solution will be analytical

$$T(x, y, z, t) = T_0(x, y, z, t) + \sum_{j=1}^N a_j(t) \phi_j(x, y, z) \quad (4.29)$$

with the trial functions $\phi_j(x, y, z)$. $T_0(x, y, z, t)$ is chosen to satisfy initial or boundary conditions and the coefficients $a_j(t)$ have to be determined. Possible trial functions are

$$\phi_j(x) = x^{j-1} \text{ or } \phi_j(x) = \sin(j\pi x) \quad (4.30)$$

The expansion is chosen to satisfy a differential equation $L(\bar{T}) = 0$ (where \bar{T} is the exact solution), e.g.,

$$L(\bar{T}) = \frac{\partial \bar{T}}{\partial t} - \alpha \frac{\partial^2 \bar{T}}{\partial x^2} = 0 \quad (4.31)$$

However, the numerical solution is an approximate solution, i.e., $T \neq \bar{T}$ such that the operator L applied to T produces a residual

$$L(T) = R \quad (4.32)$$

The goal of WRM's is to choose the coefficients a_j such that the residual R becomes small (in fact 0) over a chosen domain. In integral form this can be achieved with the condition

$$\iiint W_m(x, y, z) R dx dy dz = 0 \quad (4.33)$$

where W_m is a set of weight functions ($m=1, \dots, M$) which are used to evaluate (Equation 4.33). The exact solution always satisfies (Equation 4.33) if the weight functions are analytic. This is in particular true also for any given subdomain of the domain for which a solution is sought.

4.3.4 Upwind Type Finite Elements – A Petrov Galerkin Formulation

Consider the following 1D, steady Advection Diffusion equation

$$U \frac{dT}{dx} - v \frac{d^2T}{dx^2} = f \quad \text{in } [0, L] \quad (4.34)$$

$$T(0) = 0 \quad (4.35)$$

$$T(L) = 0 \quad (4.36)$$

where $T(x)$ is the scalar unknown, f is the known force function, U and v are the known constant velocity and diffusivity, respectively. (Galerkin Finite Element Method) GFEM formulation yields the following elemental stiffness matrix, written as the summation of elemental convection matrix C^e and elemental diffusion matrix D^e .

$$K_{ij}^e = C_{ij}^e + D_{ij}^e = \int_{\Omega^e} U S_i \frac{dS_j}{dx} dx + \int_{\Omega^e} v \frac{dS_i}{dx} \frac{dS_j}{dx} dx \quad (4.37)$$

Using linear elements and considering constant U and v , C^e and D^e matrices can be calculated as

$$[C^e] = U \int_{\Omega^e} \begin{bmatrix} S_1 \frac{dS_1}{dx} & S_1 \frac{dS_2}{dx} \\ S_2 \frac{dS_1}{dx} & S_2 \frac{dS_2}{dx} \end{bmatrix} dx = \frac{U}{2} \begin{bmatrix} -1 & 1 \\ -1 & 1 \end{bmatrix} \quad (4.38)$$

$$[D^e] = v \int_{\Omega^e} \begin{bmatrix} \frac{dS_1}{dx} \frac{dS_1}{dx} & \frac{dS_1}{dx} \frac{dS_2}{dx} \\ \frac{dS_2}{dx} \frac{dS_1}{dx} & \frac{dS_2}{dx} \frac{dS_2}{dx} \end{bmatrix} dx = \frac{v}{h^e} \begin{bmatrix} 1 & -1 \\ -1 & 1 \end{bmatrix} \quad (4.39)$$

As seen the contribution of the diffusion term to $[K^e]$ is symmetric, whereas the contribution of the advection term is not.

Considering the force function to be constant, elemental force vector becomes

$$F^e = f \int_{\Omega^e} \begin{Bmatrix} S_1 \\ S_2 \end{Bmatrix} dx = \frac{fh^e}{2} \begin{Bmatrix} 1 \\ 1 \end{Bmatrix} \quad (4.40)$$

Consider a mesh of 5 equi-length linear elements as shown below in Figure 4.3

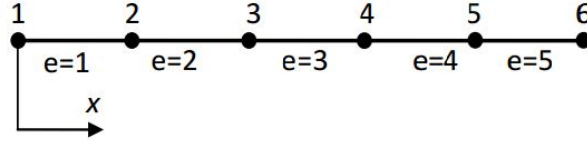


Figure 4.3: Mesh of 5 equi-length linear elements

The assembled system of equations will be

$$\begin{bmatrix} \frac{U}{2} \\ \frac{U}{2} \\ \frac{U}{2} \\ \frac{U}{2} \\ \frac{U}{2} \end{bmatrix} \begin{bmatrix} -1 & 1 & & & \\ -1 & 0 & 1 & & \\ & -1 & 0 & 1 & \\ & & -1 & 0 & 1 \\ & & & -1 & 0 & 1 \\ & & & & -1 & -1 \end{bmatrix} + \frac{v}{h^e} \begin{bmatrix} -1 & 1 & & & \\ -1 & 2 & 1 & & \\ & -1 & 2 & 1 & \\ & & -1 & 2 & 1 \\ & & & -1 & 2 & 1 \\ & & & & -1 & -1 \end{bmatrix} \begin{Bmatrix} T_1 \\ T_2 \\ T_3 \\ T_4 \\ T_5 \\ T_6 \end{Bmatrix} = \frac{fh^e}{2} \begin{Bmatrix} 1 \\ 2 \\ 2 \\ 2 \\ 2 \\ 1 \end{Bmatrix} \quad (4.41)$$

Therefore the algebraic equation for an interior node n is

$$\frac{U}{2}(T_{n+1} - T_{n-1}) - \frac{v}{h^e}(T_{n+1} - 2T_n + T_{n-1}) = fh^e \quad (4.42)$$

Dividing the equation by h^e we get

$$U \left(\frac{T_{n+1} - T_{n-1}}{2h^e} \right) - v \left(\frac{T_{n+1} - 2T_n + T_{n-1}}{(h^e)^2} \right) = f \quad (4.43)$$

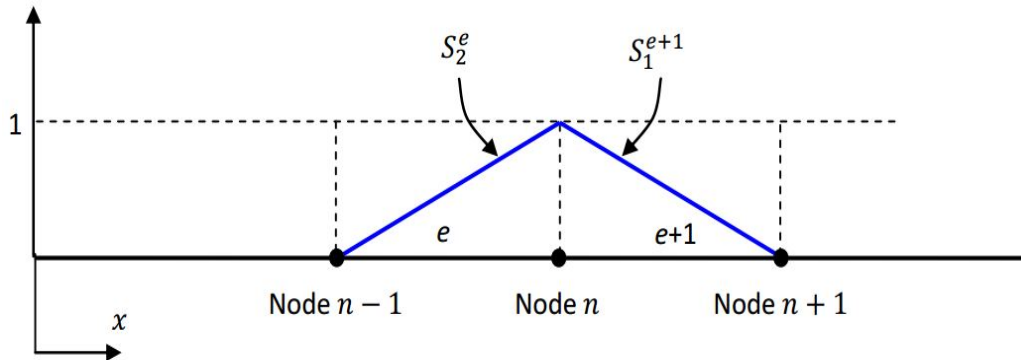


Figure 4.4: One dimensional mesh of equi-length linear elements

The upwind effect used in finite difference can be achieved in finite elements by using Petrov Galerkin formulations (Petrov GFEM) instead of GFEM, i.e. we use weight functions that are different than the shape functions used for unknown approximation.

Consider the following one dimensional mesh of equi-length linear elements in Figure 4.4.

Here only the shown two shape functions contribute to the equation written for node n . If $U > 0$, node $n-1$ is said to be on the upstream side of node n , and node $n+1$ is on the downstream side of node n . In Petrov GFEM, instead of selecting the weight functions to be the same as the shown shape functions, we distort them to the upwind side as shown below in Figure 4.5.

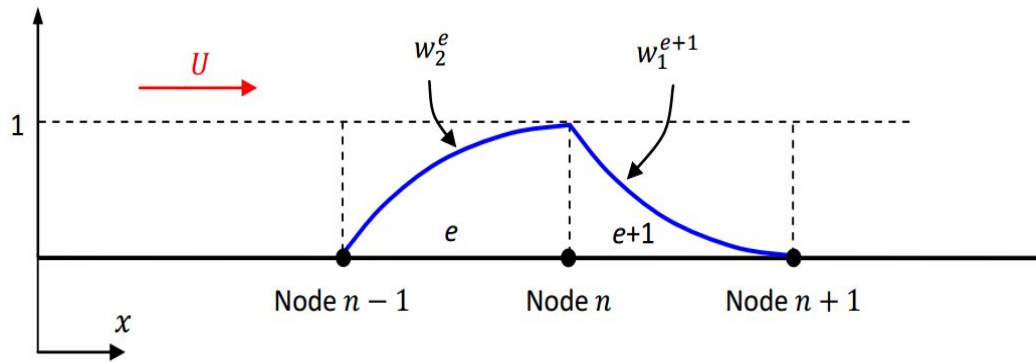


Figure 4. 5: Distortion of the upwind side

This kind of distorted weight functions can be obtained by adding bubble functions (they have zero values on the nodes and they are nonzero on elements' interiors, so when plotted they look like bubbles over the elements) to the original linear shape functions. One possibility is to use

$$w_2^e = \frac{1}{2}(1 + \xi) + \frac{3}{4}\beta(1 - \xi^2) \quad (4.44)$$

$$w_2^{e+1} = \frac{1}{2}(1 - \xi) - \frac{3}{4}\beta(1 - \xi^2) \quad (4.45)$$

where β is a parameter that controls the amount of upwinding we want to use. $\beta = 0$ corresponds to no upwinding, which corresponds to GFEM.

Elemental stiffness matrices using these modified weight functions are

$$C^e = U \int_{\Omega^e} \begin{bmatrix} w_1 \frac{dS_1}{dx} & w_1 \frac{dS_2}{dx} \\ w_2 \frac{dS_1}{dx} & w_2 \frac{dS_2}{dx} \end{bmatrix} dx = \frac{U}{2} \begin{bmatrix} -1 & 1 \\ -1 & 1 \end{bmatrix} + \frac{U}{2} \begin{bmatrix} \beta & -\beta \\ -\beta & \beta \end{bmatrix} \quad (4.46)$$

$$D^e = U \int_{\Omega^e} \begin{bmatrix} \frac{dw_1}{dx} \frac{dS_1}{dx} & \frac{dw_1}{dx} \frac{dS_2}{dx} \\ \frac{dw_2}{dx} \frac{dS_1}{dx} & \frac{dw_2}{dx} \frac{dS_2}{dx} \end{bmatrix} dx = \frac{v}{h^e} \begin{bmatrix} 1 & -1 \\ -1 & 1 \end{bmatrix} \quad (4.47)$$

Comparing these with Equation (4.38) and (4.39) obtained using GFEM, it is seen that modifying the weight functions using bubble functions changes the convection matrix, but not the diffusion matrix. However, extra terms of the convection matrix, shown in red, are similar in structure to the diffusion matrix and the overall stiffness matrix can also be thought of the following way

$$K^e = C^e + D^e = \frac{U}{2} \begin{bmatrix} -1 & 1 \\ -1 & 1 \end{bmatrix} + \frac{v + U\beta h^e / 2}{h^e} \begin{bmatrix} 1 & -1 \\ -1 & 1 \end{bmatrix} \quad (4.48)$$

In this form it is clearly seen that modifying weight functions using bubble functions to get an upwinding effect is numerically similar to using artificial diffusion. The amount of artificial diffusion is $\bar{v} = U\beta h^e / 2$.

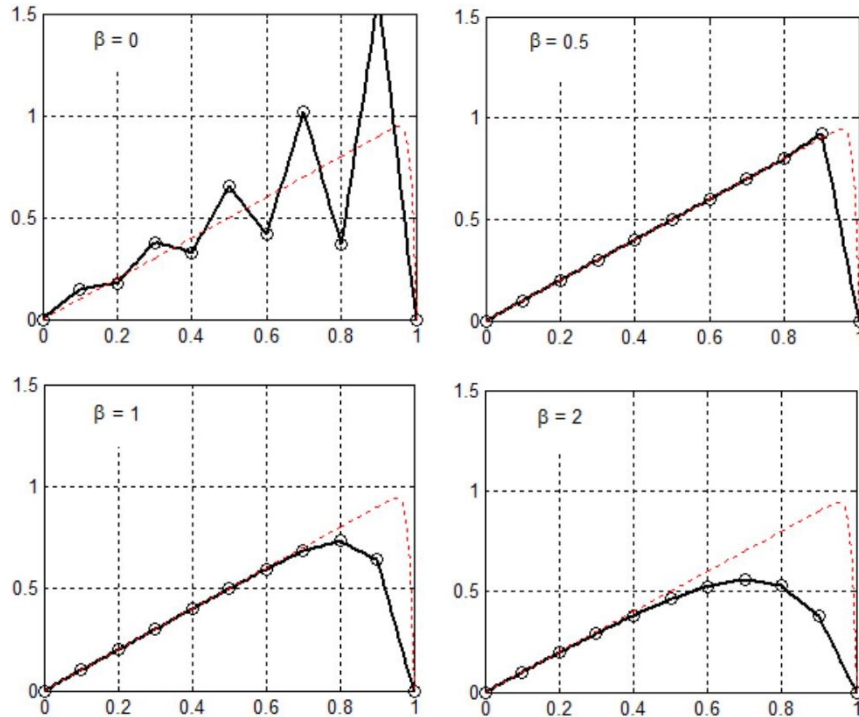


Figure 4.6: Performance of Petrov GFEM with bubble functions with four different upwinding parameters. All results are for $Pe = 5$

Test results obtained with this formulation for $Pe = 5$ with different β values are shown in Figure 4.6. As seen, by fine tuning the upwinding parameter β , it is possible to obtain stable results. The optimum value of $\beta = \coth(Pe) - 1/Pe$, which is not tried here, should provide a solution that is exact at the mesh nodes. As seen in Figure 4.6,

similar to the previous upwind solutions, these solutions are also excessively diffusive if the upwinding parameter β is used more than enough. Proper selection of β is problem and mesh dependent.

4.3.5 Discretization Error

Any discretization method, being approximate, engenders some error. Having an idea of the source and magnitude of that error is important in evaluating computational results and taking steps to improving them. For the purposes of this discussion, error will be defined as the difference between the numerical value at any point (not just at nodes) and the analytical solution at that point. Note that the difference between the analytical solution and the real world is another matter.

For the finite element method, there are two important sources of error related to the operations carried out. The first is interpolation error. Considering the curves below in Figure 4.7 and two different piecewise linear interpolations, it is obvious that the one with more pieces is better.

The second source of error is more subtle. The weighted residual method is really a weighted average process. The nodal value at any particular point reflects conditions surrounding that point. If there is a large variation in conditions, then the point value may be biased one way or another. A simple way to interpret this is to consider the computational result at a point to be average of what that value is in the surrounding elements.



Figure 4.7: Error related to piecewise interpolation.

There are two common examples of this problem in depth averaged flow calculations. The first is near a sloping bank. The node at the bottom of the bank reflects both channel (relatively uniform velocity) and bank (slower, decreasing velocity) conditions. The average tends to be lower than the velocity at the specific point. Another case is an isolated bar in a stream. If a node is placed on top of the bar and surrounding nodes are all in deep water, then the velocity on top of the bar

will be too fast, reflecting surrounding conditions. This will cause trouble as the depth at that point will be small, resulting in an excessively high, possibly supercritical, Froude Number.

The solution to both types of discretization errors is smaller elements. This means more elements and more nodes for the same physical area. The art of computer modeling is to provide enough refinement in important areas while maintaining reasonable solution times.

4.3.6 Solution Methods

The result of the finite element method, or any other discretization method, is a set of nonlinear algebraic equations for all the unknown depths and velocities. The process of solving these equations is what is demanding of computer resources.

Most computer models of depth averaged flow solve for transient conditions, even if steady state results are desired. This is a convenient way of providing a controlled and stable iteration scheme from an arbitrary first guess or initial condition. Two approaches are generally used, referred to explicit and implicit methods.

Explicit methods solve for the new variable values at any one node based on the values at surrounding nodes at the previous time. This approach has the tremendous advantage of calculating each value independently. No matrix solutions are necessary so storage is minimal and execution is fast. The disadvantage is that the time step is restricted to keep the solution stable. The Courant-Lewy Freidrichs (CFL) condition is a guide to the maximum time step allowed.

$$\Delta t < \min \left(\frac{\Delta x}{|V| + \sqrt{gH}} \right) \quad (4.49)$$

This condition is related to the time taken by a shallow water wave to travel from one node to the next. As mesh spacing is made smaller in any area, the time step for the whole solution process must be decreased.

The second approach is called implicit. Here values of all the variables at the new time are considered to depend on each other as well as the values at the previous time step. Since the unknowns are interrelated, considerable effort using nonlinear and linear algebra methods is required to solve the equations.

Typically, large matrices are formed. If there are N nodes in a mesh, then there are 3N unknown variables to solve for at each time step. The full matrix describing their interconnections would be 3N X 3N. If N is 10,000, then the matrix would require 7.2 Gigabytes of memory to store. Fortunately, the full matrix is not usually required. The vast majority of terms are zero. A more realistic estimate of storage is 3N X 3B where B is the bandwidth of the mesh. Roughly speaking, the bandwidth is the typical largest difference between node numbers for connected points. For the 10,000 node problem, the bandwidth will be in the order of about 100. The matrix required is then less than 100 Megabytes - large, but manageable.

Computation time for matrix solution is roughly proportional to N^2 . If B scales with the square root of N , then matrix size is proportional to $N^{3/2}$ and solution time is proportional to N^2 . The consequence is that adding a few more nodes to an already large problem is expensive in storage and computer time. Again, the problem of providing enough discretization to minimize errors and get a solution in a reasonable time is the central trade-off in computational modeling.

4.4 Applicability of Present Study for Modeling Flow in Confluence

For applicability analysis of flow modeling in confluence present study is analyzed and compared with experimental result and other model. Here experimental study of Weber et al. (2001) and numerical study of Thanh et al. (2010) are adopted for validity analysis of convergent flow in the channel confluence.

4.4.1 Laboratory Setup by Weber et al. (2001)

The experiments were performed in a 90° combining flow flume (Figure: 4.8), located at the Iowa Institute of Hydraulic Research by Weber et al. (2001). The floor of the entire flume facility is horizontal. Head tanks on both the main and branch channels supplied the discharge. To ensure properly developed flow entering into the junction branches, perforated plates and 100 mm thick honeycomb were placed at the main and branch channel inlets. A 37.3 kW, variable speed pump provided water from an underground sump to the flume through a 0.305 m supply pipe. Volumetric measurements were made with manometer readings from calibrated 0.203 m orifices in each of the 0.305 m supply pipes. The tail-water depth in the downstream channel was controlled by an adjustable tailgate.

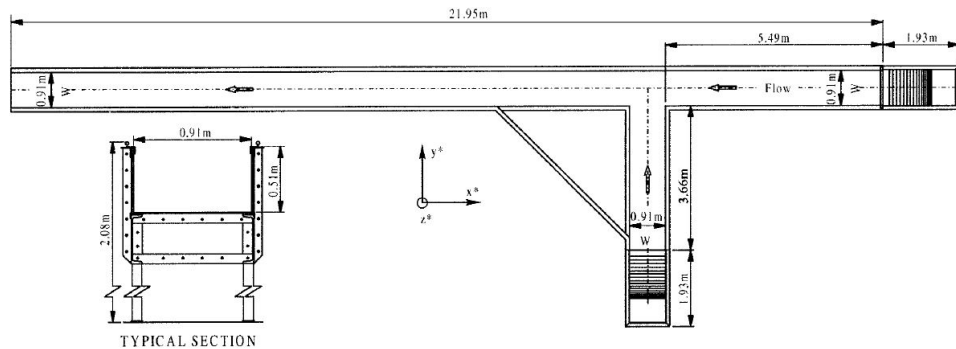


Figure 4. 8: Experimental Flume Layout by Weber et al. (2001)

The coordinate system defined for this testing had the positive x -axis oriented in the upstream direction of the main channel. The positive y -direction points to the main channel wall opposite of the channel junction. Thus the positive z -axis is upward in the vertical direction. The origin from which all points are measured was the bed at the upstream corner of the channel junction. All distances were normalized by the channel width, $W = 0.914$ m. The nondimensionalized coordinates are called x^* , y^* , and z^* for

x/W , y/W , and z/W , respectively. All test sections in this study were denoted by the distance in channel widths measured positive in the x -direction for upstream main channel measurements, negative in the x -direction for combined tailwater flow measurements, or negative in the y -direction for measurements in the branch channel. The velocity measurements have been nondimensionalized by the downstream average velocity, $V_t = 0.628$ m/s.

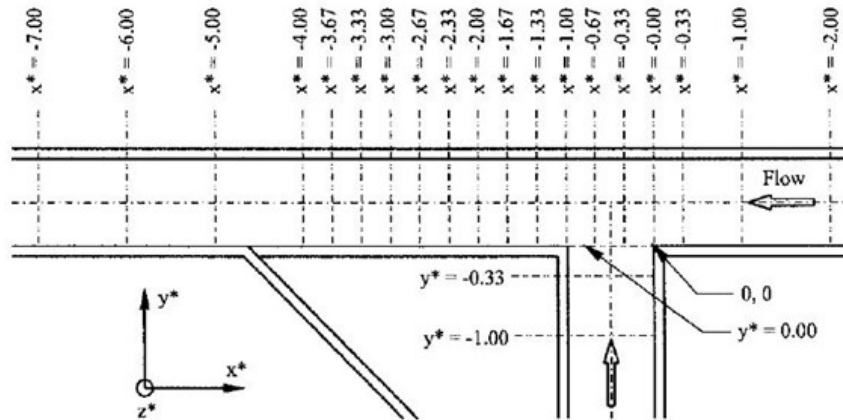
The upstream main channel, branch channel, and combined tailwater flow are denoted as Q_m , Q_b , and Q_t , respectively. The flow ratio q^* is defined as the ratio of the upstream main channel flow Q_m to the total flow Q_t . In this study, the total combined flow, $Q_t = 0.170$ m³/s, and the tailwater depth, 0.296 m, were held constant. This constant downstream flow rate and depth produced a constant tailwater Froude number, $F_t = 0.37$, and a constant tailwater average velocity, $V_t = 0.628$ m/s. The flow conditions tested are listed in Table: 4.1.

Table 4. 1: Experimental Flow Conditions

Q_m (m ³ /s)	Q_b (m ³ /s)	q^*
0.014	0.156	0.083
0.042	0.127	0.250
0.071	0.099	0.417
0.099	0.071	0.583
0.127	0.042	0.750
0.156	0.014	0.917

A Sontek three-component acoustic Doppler velocimeter (ADV) was used to measure velocities and turbulence intensities. The velocity measurements were taken at each sampling location for 60 s at a sampling rate of 10 Hz. The manufacturer's specifications state that the measuring accuracy of the ADV is 61% of the average velocity. The time series of velocity at each data point was analyzed to produce a normalized average velocity and corresponding turbulence intensity. Figure: 4.9 illustrates the locations of all velocity measurements. Each channel cross section, as indicated in Figure: 4.9 (top), consisted of seven evenly spaced vertical profiles with two additional vertical profiles, $y^* = 0.056$ and $y^* = 0.181$, taken near the branch-side wall on sections immediately downstream of the junction, as shown in Figure: 4.9 (bottom). Seventeen points were measured on each vertical, with the near bed points being more closely spaced. This testing grid produced approximately 2,850 velocity measurement locations for each flow condition studied.

(a)



(b)

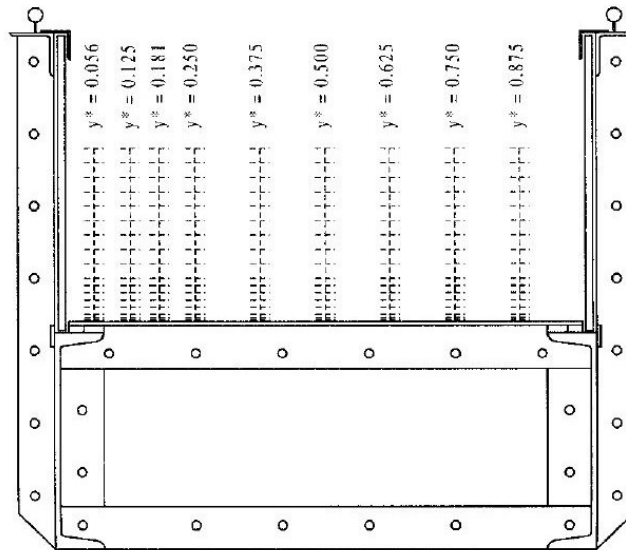


Figure 4. 9: (a) Location of: Cross Sections (b) Location of Flow Velocity Measurements (Weber et al., 2001)

To ascertain the repeatability of the measurements, a simple uncertainty analysis was performed. The ADV probe was positioned to measure the velocity components at a position in the flume with highly 3D flow ($x^* = 22.00$, $y^* = 0.50$, $z^* = 0.20$, and $q^* = 0.417$). Ten measurements of velocity were recorded with the setup and the flume stabilized. The pertinent information, based on normalized velocities, is presented in Table 4.2. Additionally, to ascertain the uncertainty of the measurements resulting from the setting of the pumps, inlet valves, positioning of the probe, and stability of the flow structures, 10 measurements were repeated with the flume being restarted and the probe being repositioned between each measurement. These results are shown in Table 4.3. As can be seen the experimental uncertainty is small compared to the mean values of velocity and turbulence intensity.

Depth measurements for this study were made using a point gauge with an accuracy of 1.0 mm. The water surface mappings were performed on a 76.2 mm square grid in the junction region. The water surface for a given flow condition was completely mapped in 1 day by the same individual without changing any flow settings during the time of the water surface data collection. These precautions ensured that the flow structure was continuous throughout the mapping and that uniform measurement techniques were employed

Table 4. 2: Repeatability of Measurements from Single Test Session

Value	Normalized Velocity			RMS		
	u^*	v^*	w^*	u^*	v^*	w^*
Minimum	-0.863	0.028	-0.007	0.032	0.034	0.018
Maximum	-0.842	0.036	-0.002	0.038	0.039	0.022
Mean	-0.847	0.031	-0.004	0.034	0.037	0.020
Standard deviation	0.006	0.003	0.002	0.002	0.002	0.001

Table 4. 3: Repeatability of Measurements from Multiple Test Sessions

Value	Normalized Velocity			RMS		
	u^*	v^*	w^*	u^*	v^*	w^*
Minimum	-0.876	-0.009	-0.037	0.036	0.035	0.020
Maximum	-0.848	0.038	-0.015	0.049	0.057	0.034
Mean	-0.861	0.021	-0.016	0.039	0.042	0.028
Standard deviation	0.009	0.017	0.019	0.004	0.006	0.004

4.4.2 Model Developed by Thanh et al. (2010)

Thanh et al. (2010) developed four models to simulate experimental result of Weber et al. (2001), with and without considering secondary flow. Among these four models one model considering secondary flow is not stable enough to simulate experimental result. So, final result shows a comparison among three simulated result by Thanh et al. (2010) and one experimental result by Weber et al. (2001). In developed three models by Thanh et al. (2010), one model does not consider secondary flow and other two models consider it. The fundamental equations are solved numerically using the finite volume method with a full staggered grid including conservativeness of physical quantities and computational stability. The QUICK scheme with second order accuracy in space is employed for convective inertia terms. The Adams Bashforth method with second order accuracy in time is used for time integration. In the present study, simulated result (without considering secondary flow) of experimental work by Weber et al. (2001) is compared with two models by Thanh et al. (2010), considering secondary flow and experimental result by Weber et al. (2001). The two models developed by Thanh et al. (2010) are as follows:

Model 1: a 2D model with effects of secondary currents and lag between the streamline curvature and development of secondary currents; and,

Model 2: a 2D model that consider effects of secondary currents, lag between the streamline curvature and development of secondary currents as well as change of mainstream velocity profile influenced by secondary currents.

4.4.3 Numerical Modeling of Weber et al. (2001) (Present Study)

The above mentioned experimental condition is simulated by solver River2D of iRIC. In this numerical solution, Bousinessq type eddy viscosity is used for the transverse shear modeling. Secondary flows are not considered during calculation, which is the main reason for losing energy of flow near the channel boundary. Total numbers of grids are 6765, arranged as figure 4.10. The calculation condition is represented in Table 4.4.

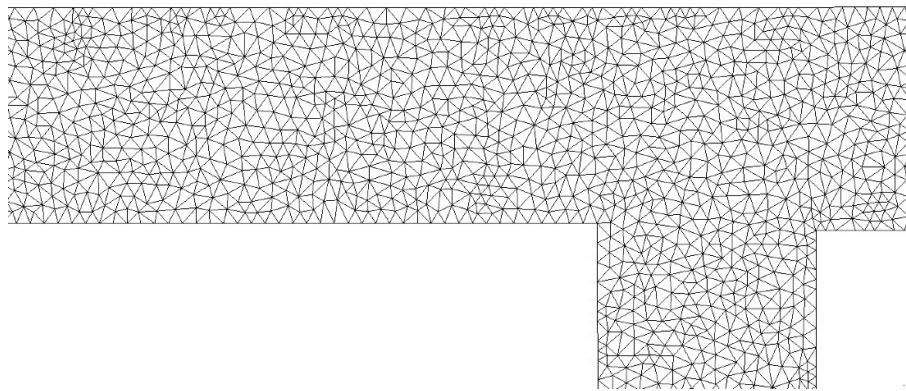


Figure 4.10: Grid shape for numerical simulation in present study

Table 4. 4: Calculation condition for modeling Weber et al (2001)

Start Time	0 second
Final Time	1000 second
Initial Time Increment	0.01 second
Maximum Time Increment	10 second
Goal Solution Change	0.1
Plot Increment	1
Solver Type	Direct (Active Zone)
Jacobian Type	Numerical
Upwind Coefficient	0.5
Maximum Depth to Groundwater Flow	0.01
Groundwater Transmissivity	0.1
Groundwater Storativity	1
Eddy Viscosity Coefficient – epsilon 1	0
Eddy Viscosity Coefficient – epsilon 3	0.1
Upstream Water Surface Elevation	1.187 meter
Downstream Water Surface Elevation	1.184 meter
Channel Roughness	0.011

In the present study, concept of geometric similarity is applied for better result. During simulation by River2D, very shallow depth of flow as compared with (Weber et al.,

2001) and Thanh et al. (2010) brings erroneous result. The condition of geometric similarity is expressed in Table 4.5.

Table 4. 5: Conditions of geometric similarity of present model with prototype by Weber et al (2001)

Length scale ratio	4
Area scale ratio	16
Volume scale ratio	64

4.4.4 Comparison of Present Study with Weber et al. (2001) and Thanh et al. (2010)

In this experiment (Weber et al., 2001), the channel consists of a main channel of 21.946m in length and a branch channel of 3.658 m in length located 5.486m downstream of the entrance of the main channel. Both these channels have the same width (W) of 0.914m. The total combined flow discharge (Q_t) is $0.170\text{m}^3/\text{s}$ and the downstream water depth is held constant at 0.296m. With these conditions, the averaged downstream velocity (U_0) is 0.628 m/s corresponding to a Froude number of 0.37. A total of two runs of the experiments were conducted for two various values of q^* defined as the ratio of the upstream main channel flow (Q_m) to the total flow (Q_t). In this study, two cases, $q^* = 0.25$, that is, Q_m (main channel discharge) = $0.043\text{ m}^3/\text{s}$ and Q_b (branch discharge) = $0.127\text{ m}^3/\text{s}$ and $q^* = 0.75$ ($Q_m = 0.127\text{ m}^3/\text{s}$ and $Q_b = 0.043\text{ m}^3/\text{s}$), are selected for computations. During comparison every dimension is normalized by dividing channel width (W) 0.914m and velocity is normalized by dividing averaged downstream velocity (U_0) 0.628 m/s.

Figure 4.11 and 4.13 represent the velocity contour at the confluence, for the case $q^* = 0.25$ and $q^* = 0.75$ of present study respectively. From these two figures it is observed that formation of separation zone mainly dominated by the volume of water passed through the branch estuary. Higher amount of volume passed through branch than main channel forms separation zone, higher in size. Figure 4.12 shows the streamwise velocity component profiles at some cross-sections along the post-confluence main channel for $q^* = 0.25$, while Figure 4.14 depicts those at the same places for $q^* = 0.75$. All velocity values are averaged over the depth. Positive values in Figure 4.12 and 4.14 indicate downstream motion, while negative ones show upstream motion. It is observed in Figure 4.12 that the results obtained with Thanh et al. (2010) performed Model 1 and Model 2 agree well with the experimental ones, except in the beginning reach of the separation zone (In this reach, all models by Thanh et al., 2010 over-predict velocity). However, the similar agreement is not obtained with present study, because in present study, length of the separation zone is under-predicted. The separation zone generated with present study seems to drop somewhere after the section of $x/W = -1.33$, while it, in reality, extends to a place around the section of $x/W = -1.67$. This can be realized, because velocity direction in the region near the inner bank of the main channel changes between the section of $x/W = -1.33$ and the section of $x/W = -1.67$ and the velocity profile in this region has a tendency to be flattened in the next sections as seen in Figure 4.12. The reason for this shortcoming of present study, as explained above, is

due to not considering effects of secondary current. Unlike the case of $q^* = 0.25$, Figure 4.14 shows that there is no significant difference in velocity profiles as well as in location where the separation zone drops between the results with present study and those two models by Thanh et al. (2010) for $q^* = 0.75$. The reason for this, as indicated above, is that as q^* is large, secondary current is weak, moreover in present study secondary current is not considered and has not significant effects on flow. All simulated results agree very well with the experimental ones.

From present study, it is quite clear that, energy of flow reduces along the boundary of the channel due to secondary current. Also secondary current effects the length of separation zone, not its position. Because modes developed by Thanh et al. (2010) and present study shows separation zone starts at the same position, only but it shows an elongated shape when secondary current is considered. So secondary current is a good means of having correct simulated result of experimental one. But results are over predicted by models considering secondary current at the starting point of separation zone, while present study shows more accurate result without considering secondary current. Secondary current is an important phenomenon that should be considered during flow model, responsible of energy loss along the boundary of the channel. It is very effective for modeling flow pattern near the channel boundary. Because it is clear that models developed by Thanh et al. (2010) considering secondary current and present study without considering secondary current shows almost same result at the middle channel, where secondary current is not effective enough and only active at the bottom of the channel. But over activeness of secondary current model at the starting point of separation zone should be minimized, so that result may be more accurate.

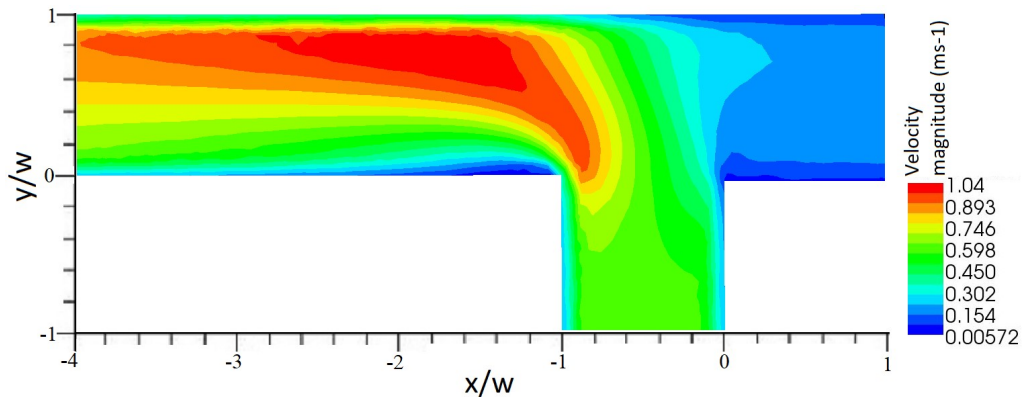


Figure 4.11: Color contour of velocity distribution for condition $q^* = 0.25$ (Present study)

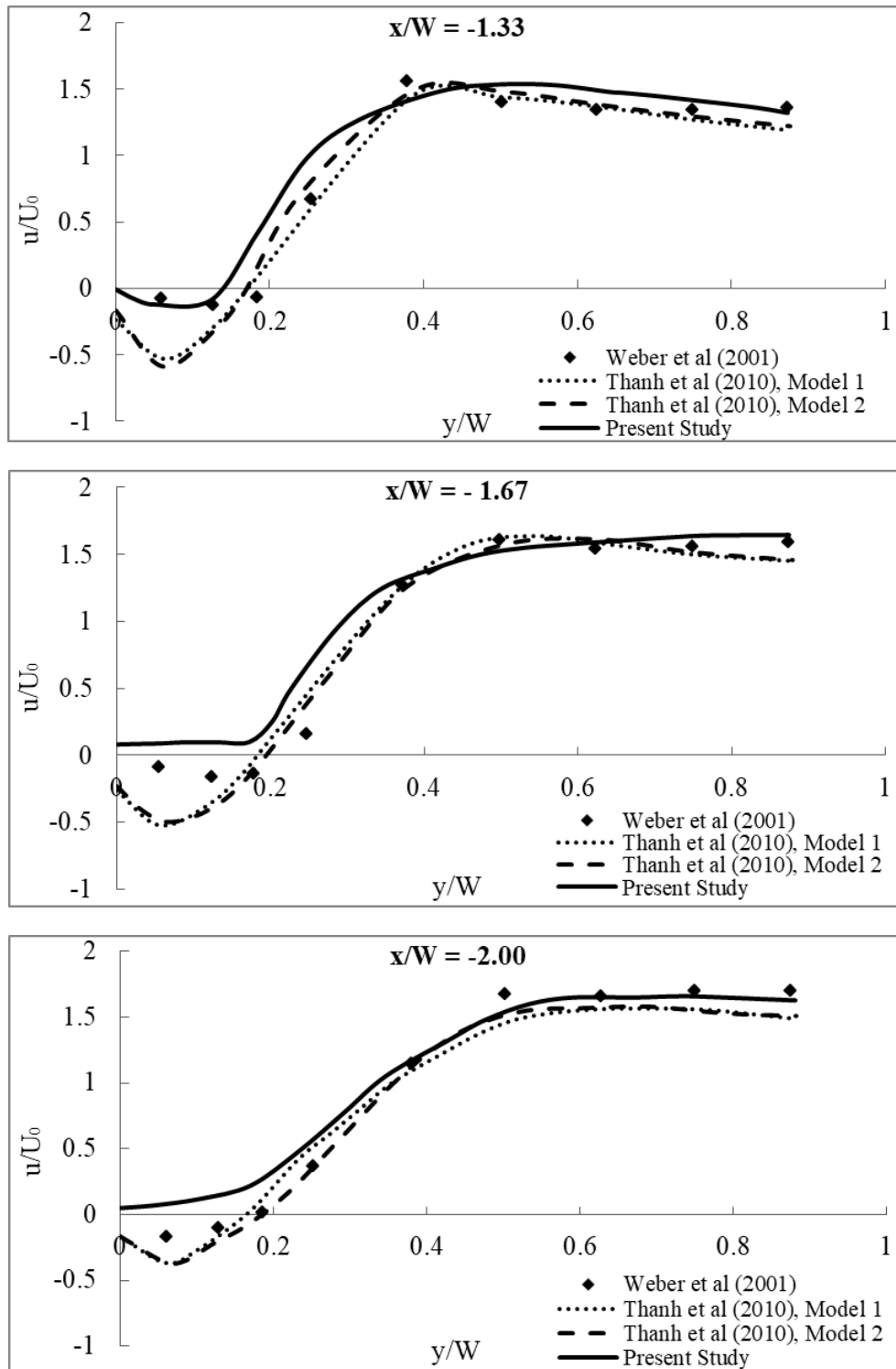


Figure 4.12: Comparison of longitudinal velocity component at some locations for $q^* = 0.25$ (Continued)

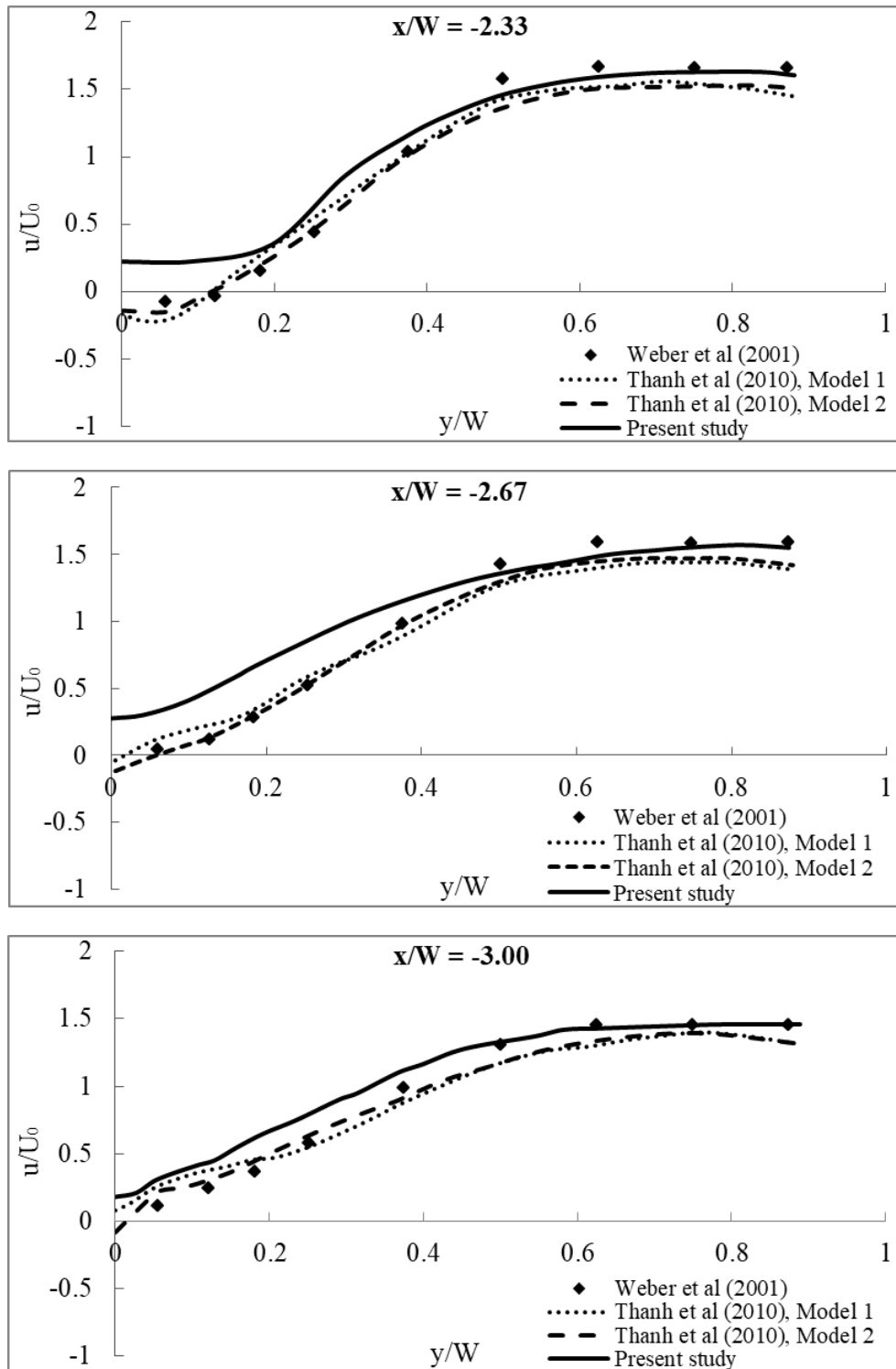


Figure 4. 12: Comparison of longitudinal velocity component at some locations for $q^* = 0.25$

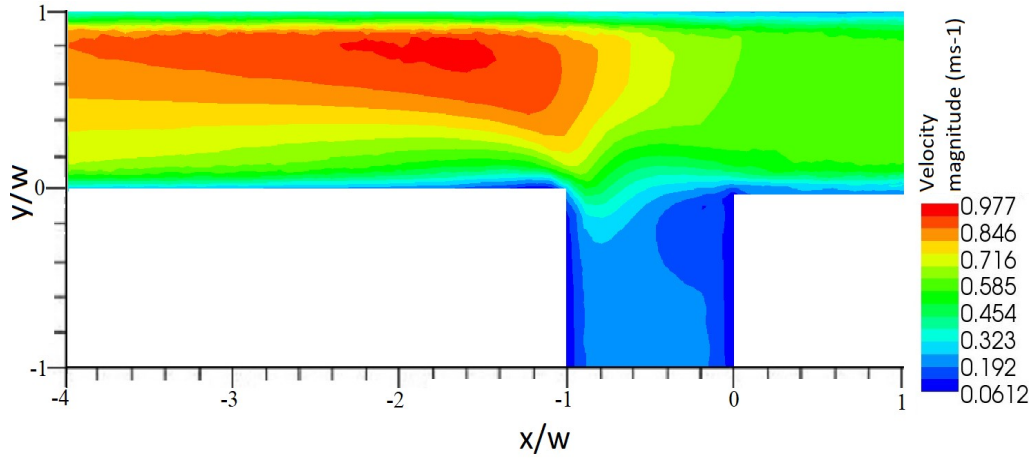


Figure 4.13: Color contour of velocity distribution for condition $q^* = 0.75$ (Present study)

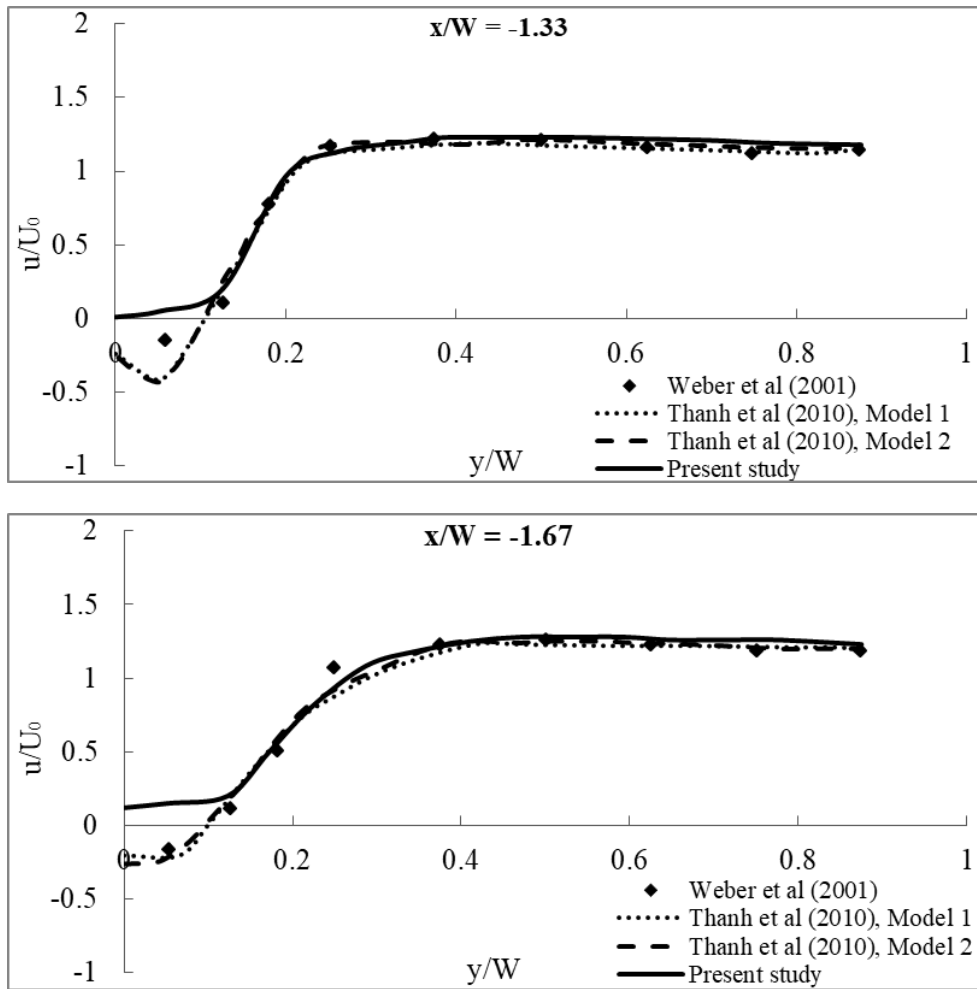


Figure 4.14: Comparison of longitudinal velocity component at some locations for $q^* = 0.75$ (Continued)

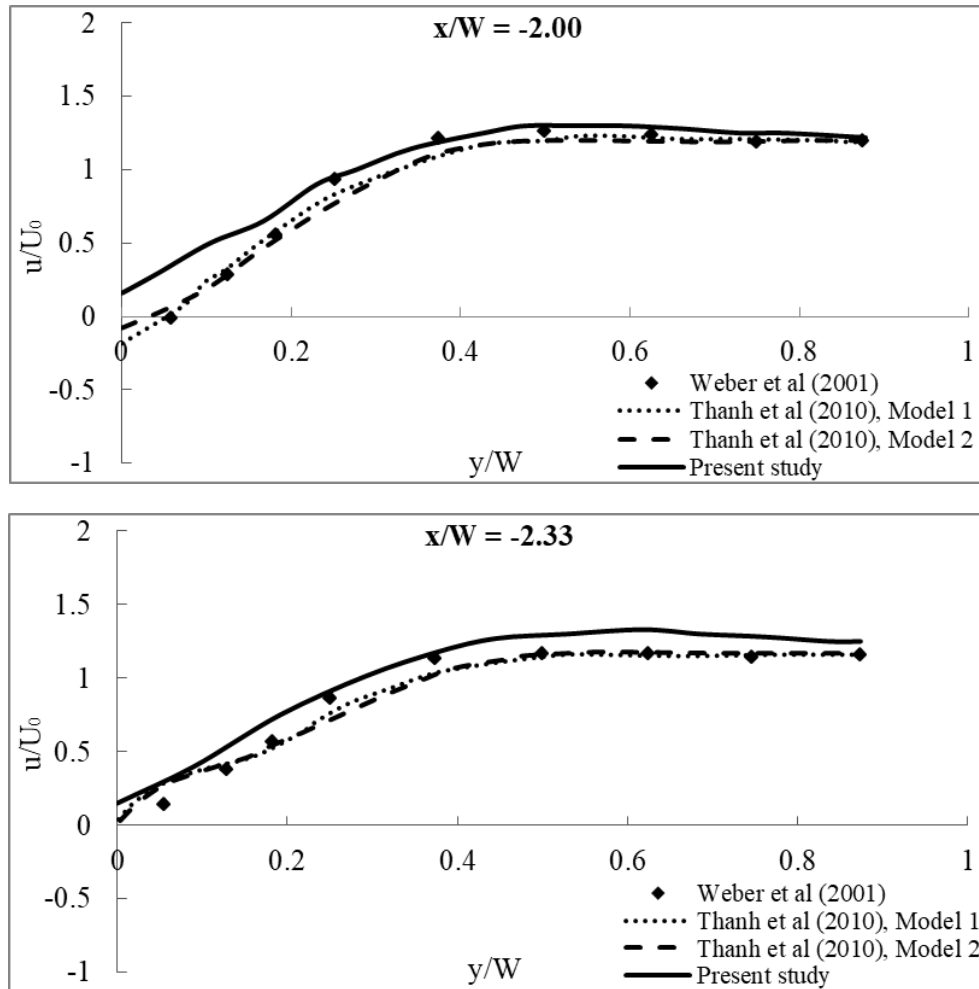


Figure 4.14: Comparison of longitudinal velocity component at some locations for $q^* = 0.75$

4.5 Applicability of Present Study for Modeling Flow in Diversion

For validity analysis of present study based on divergent flow, other experimental result and numerical model are compared with current numerical model. Experimental study of Barkdoll et al. (1998) and numerical developed by Ashari et al. (2015) are adopted for the comparison with present study and validity analysis for modeling divergent flow in the channel confluence.

4.5.1 Laboratory Setup by Barkdoll et al. (1998)

Experiments were performed in a recirculating flume, which had side walls made of fiberglass-coated plywood that ensured a hydraulically smooth surface (Figure 4.15). The main channel discharge was $0.011 \text{ m}^3/\text{sec}$; the main and branch channels were both 15.2 cm wide and 31 cm deep. Velocity measurements were conducted using a two-

the present study, but comparison of the data taken with the EVM and to data taken with LDV is assumed to be valid because both meters were used according to manufacturers' specifications and are well-proven for measuring mean velocities. Measurements were taken near the free surface, where vertical velocity gradients are small, thereby minimizing the potential discrepancies caused by differing sampling volumes. The upstream main-channel velocity measurements for both the EVM and LDV agree (except for the expected velocity dip), providing further confidence in the data.

The following measures were taken to ensure comparability between the two data sets: (1) A depth-to-width ratio of 2:1 was used to correspond with the 4:1 ratio used by Popp and Sallet (1983), since the free surface corresponds to the symmetry plane of duct flow. (2) Velocities were normalized using the maximum velocity taken at a section far upstream of the junction [0.26 m/sec at $x/b = -4.65$, $z/b = -0.27$, identical to the normalization criteria used by Popp and Sallet (1983)]. It should be noted, however, that for duct flow the maximum velocity occurred at the symmetry plane ($z/b = 0$). Therefore, the open-channel results would be higher than those shown here if normalized by the value at the free surface. (3) The discharge ratio (Q_3/Q_1) was maintained at 0.81. (4) The surface roughness was comparable (both studies used hydraulically smooth surfaces). (5) The main channel Reynolds number (38,800), based on maximum upstream velocity and channel width, was identical between studies. (6) Velocity profiles were measured at identical cross sections in the T-junction when normalized by the channel/duct width. (7) Velocity measurements were taken as close to the free surface as possible.

4.5.2 Model Developed by Ashari et al. (2015)

Ashari et al. (2015) developed two models to simulate experimental result of Barkdoll et al. (1998), considering $k-\epsilon$ -standard and $k-\epsilon$ -RNG turbulence model without considering secondary flow. Ashari et al. (2015) use Navier-Stokes equations are solved by three-dimensional Finite-Volume Method (FVM). FVM is based on direct discretization of the integral form of conservation laws in physical space. Flow analysis occurs at persistent mode and simple algorithm uses for velocity-pressure coupling. Several number of turbulence models exist in this numerical model. Method of discretization of momentum equation, loss and turbulence kinetic energy and Reynolds stress is two-order leading method. Also, standard method is use for discretization of pressure equation.

4.5.3 Numerical Modeling of Barkdoll et al. (1998) (Present Study)

The above mentioned experimental condition is simulated by solver River2D of iRIC. In this numerical solution, Bousinessq type eddy viscosity is used for the transverse shear modeling. Secondary flows are not considered during calculation, which is the main reason for losing energy of flow near the channel boundary. Total numbers of

grids are 2088 which is as arranged as Figure 4.16. The calculation condition is represented in table 4.6

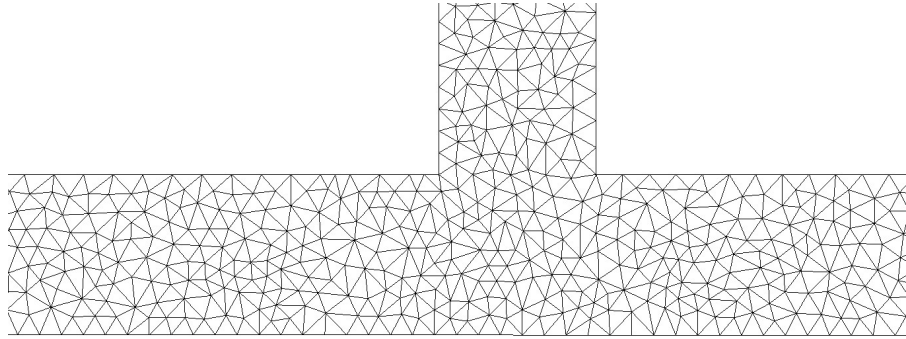


Figure 4. 16: Grid shape for numerical simulation in present study

Table 4.6: Calculation condition for numerical simulation

Start Time	0 second
Final Time	1000 second
Initial Time Increment	0.01 second
Maximum Time Increment	10 second
Goal Solution Change	0.1
Plot Increment	1
Solver Type	Direct (Active Zone)
Jacobian Type	Numerical
Upwind Coefficient	0.5
Maximum Depth to Groundwater Flow	0.01
Groundwater Transmissivity	0.1
Groundwater Storativity	1
Eddy Viscosity Coefficient – epsilon 1	0
Eddy Viscosity Coefficient – epsilon 3	0.1
Upstream Water Surface Elevation	1.25 meter
Downstream Water Surface Elevation	1.24 meter
Channel Roughness	0.011

In the present study, concept of geometric similarity is applied for better result. During simulation by River2D, very shallow depth of flow as compared with Barkdoll et al. (1998) and Ashari et al. (2015), brings erroneous result. The condition of geometric similarity is expressed in Table 4.7.

Table 4.7: Conditions of geometric similarity of present model with prototype by Barkdoll et al. (1998)

Length scale ratio	4
Area scale ratio	16
Volume scale ratio	64

4.5.4 Comparison of Present Study with Barkdoll et al. (1998) and Ashari et al. (2015)

U_0 is the maximum velocity at the cross-section $X^* = -4.65$ whose value is equal to 0.28 m/s, used to make velocity of different section dimensionless. And channel width $b = 0.152\text{m}$ is used to make every distance along x-axis and y-axis. This criteria is adopted from Barkdoll et al. (1998).

According to Ashari et al. (2015), the velocity profile retains its expanded state before reaching the intake and when approaching the entrance, because of the suction flow, the velocity profiles will be deviated towards the intake channel and the maximum velocity will be deviated toward the intake entrance (section $X^* = -0.5$).

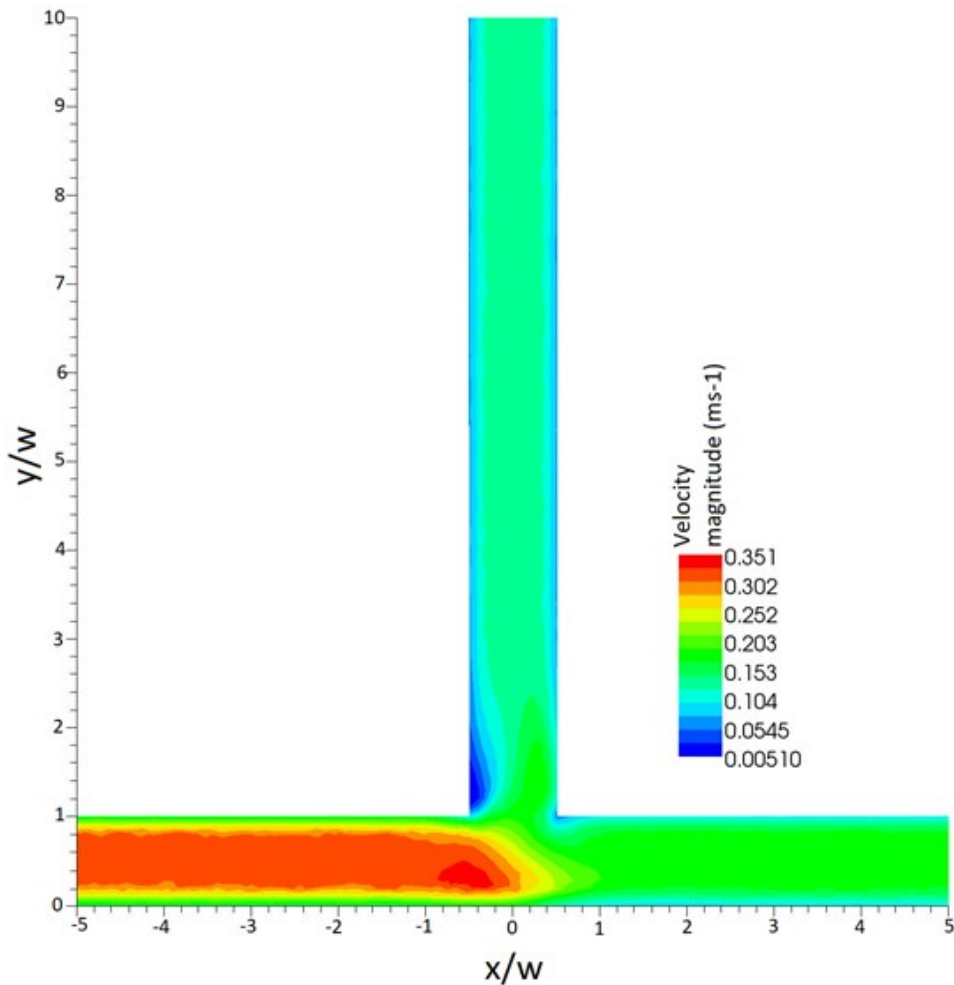


Figure 4.17: Color contour of velocity distribution

The results from Ashari et al. (2015) show that with flow entering to the intake, velocity resultant along the intake decreases in the downstream wall of the entrance (section $X^* = 0.5$). The maximum velocity is distant from the inner wall of the main channel. The flow remaining in the main channel develops within the section after

passing the intake entrance, but because of the effects of curved flow lines at the intake entrance, the maximum velocity will be deviated back towards the inner wall. The major cause of large variation of the expected velocity to the experimental value is ignoring the effect of different variables in the numerical modeling.

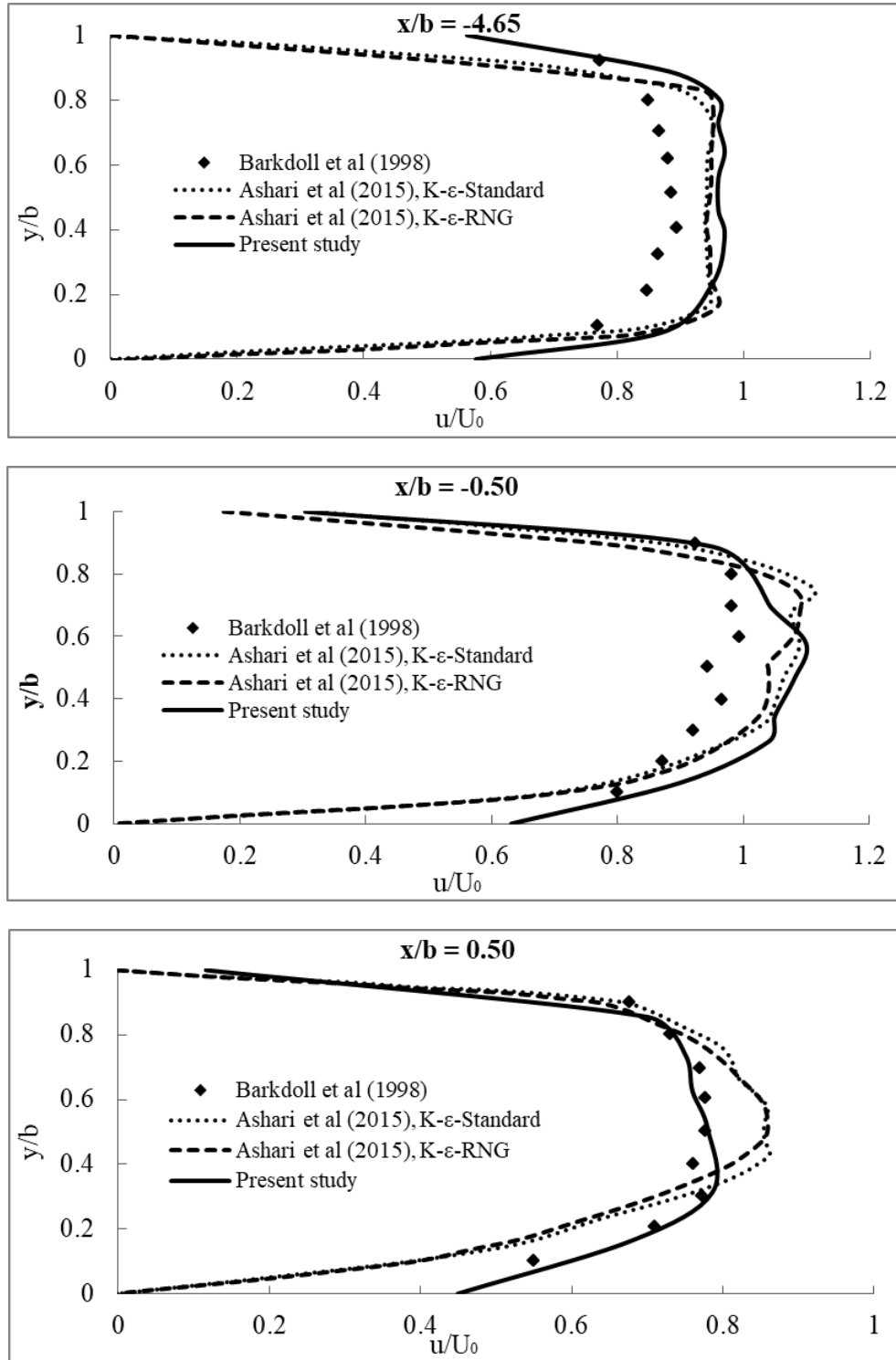


Figure 4.18: Evaluation of computational velocity profiles at different sections of the main channel (continued)

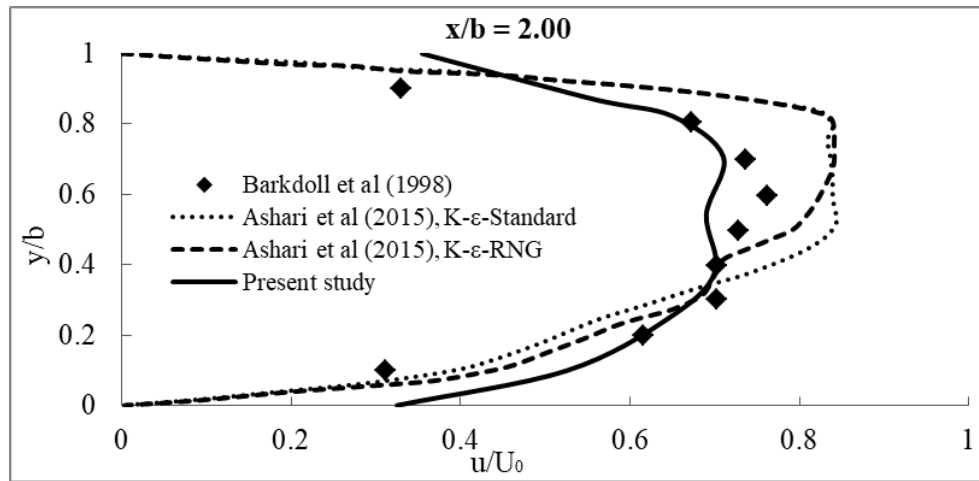


Figure 4. 18: Evaluation of computational velocity profiles at different sections of the main channel

Figure 4.17 shows the velocity contour created by present study during flow in a laboratory made diversion by Barkdoll et al. (1998). In this figure it is found that separation zone formed in the branch channel at side of upstream of the main channel. In Figure 4.18, present study shows quite similarity with Ashari et al. (2015) developed models, while provides good result at distance $X^* = 0.5$ and 2.0 . Present study shows that at every section of x -axis, calculated velocity, over-estimates results as compared with Ashari et al. (2015) and Barkdoll et al. (1998) at the channel boundary. One of the reasons may be Bousinesq type eddy viscosity is used for the transverse shear modeling, which very basic and works well for some free shear flows such as axisymmetric jets, 2D jets and mixing layers. Whereas Ashari et al. (2015) use $k-\epsilon$ turbulence model. The original impetus for the $k-\epsilon$ model was to improve the mixing length model, as well as find an alternative to algebraically prescribing turbulent length scales in moderate to high complexity flows. At distance $X^* = -4.65$ and -0.5 model developed by Ashari et al. (2015) and present study over estimates the experimental result at the middle of channel section. One of the dominating reason is secondary flow, which is neither considered in Ashari et al. (2015) developed model nor in present study. Although secondary current is less active at the middle of a channel, due to very small width and shallow water flow in the prototype by Barkdoll et al. (1998), effect of secondary current can reduce the energy of flow at the middle of a channel.

From following Figure 4.19, it is clear that in every case, present study shows similarity with Ashari et al. (2015) developed model. But at distance $Y^* = 2.5$ and 10.0 present study shows similarity with Barkdoll et al. (1998). At $Y^* = 2.5$ present study and Ashari et al. (2015) developed models slightly over estimate experimental study. The reason is not to consider secondary current as a variable. At $Y^* = 4.0$ present study and Ashari et al. (2015) developed models both under estimate the experimental result. This is due to not considering different real time and local variables. Different real time and local variables (like wind thrust, temperature) severely effects prototype during experimental work which is really difficult to model during numerical analysis.

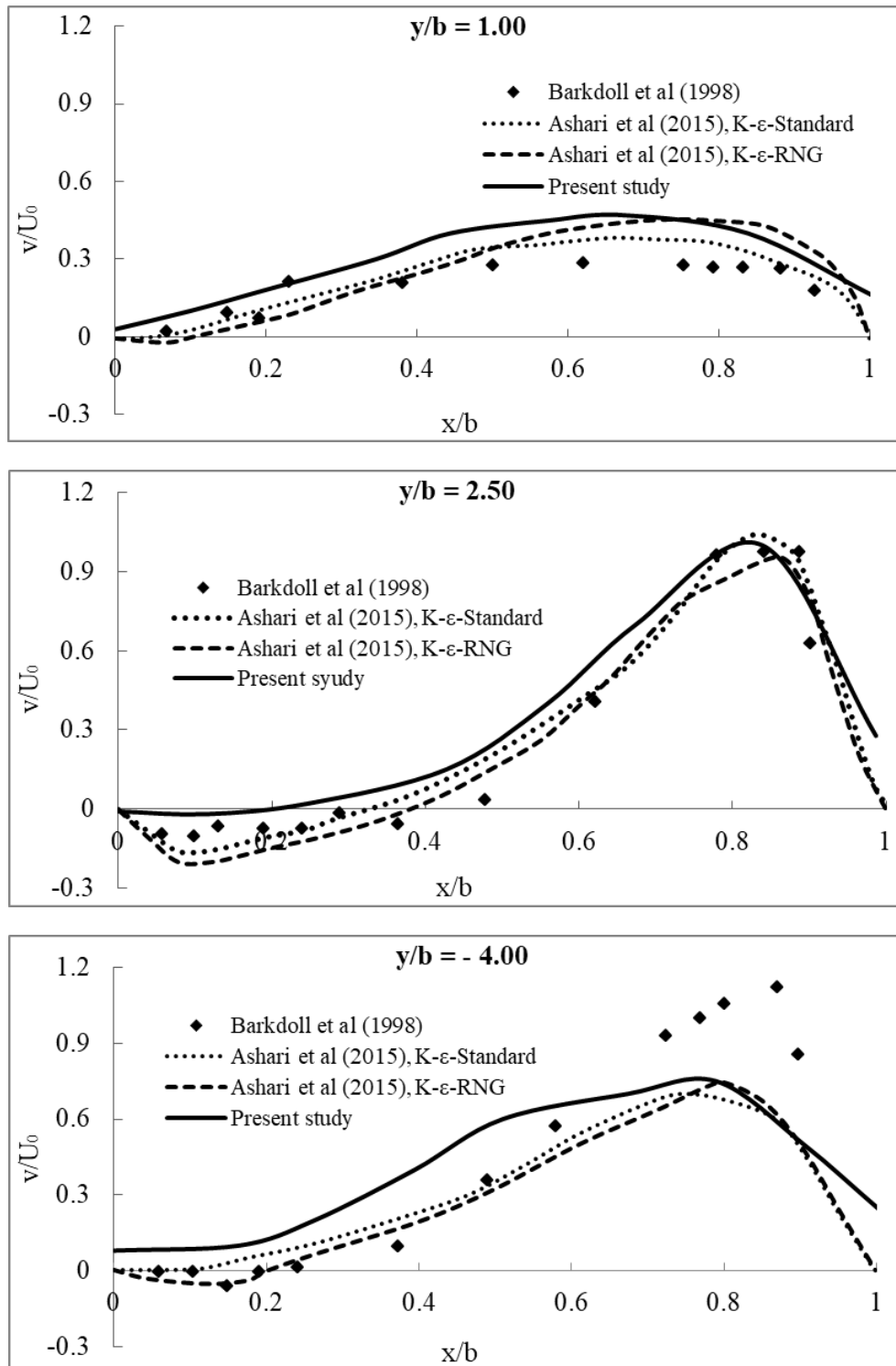


Figure 4.19: Evaluation of computational velocity profiles at different sections of the branch channel (continued)

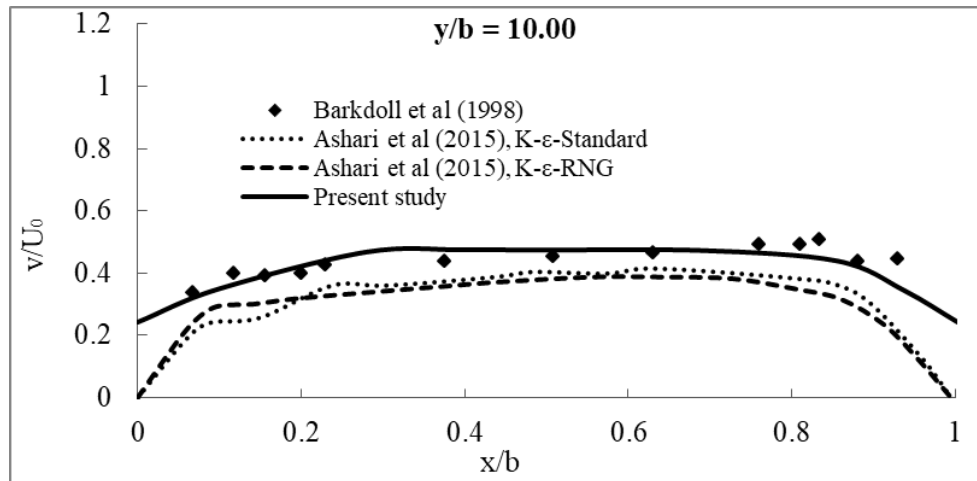


Figure 4.19: Evaluation of computational velocity profiles at different sections of the branch channel

4.6 Modeling of River Confluence

In this study, River2D solver is used for modeling Natural River confluence. Here combined flow of Bhairab, Atai, Rupsha River (Confluence 1) and Rupsha, Kazibasa (Confluence 2) are adopted for numerical modeling. Position of the two confluences are shown in Figure 4.20 and summarized in Table 4.8

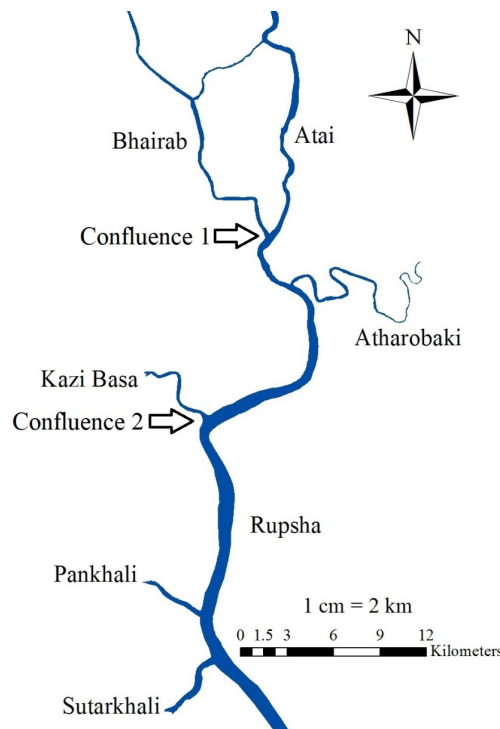


Figure 4. 20: Position of the two confluences in study area

Table 4.8: Position and accumulated rivers at the confluences

Confluence	Name of the Rivers meet at Confluence	Position
Confluence 1	Bhairab, Atai, Rupsha	22°50'52.05"N, 89°33'33.09"E
Confluence 2	Rupsha, Kazibasa	22°44'23.23"N, 89°31'26.84"E

4.6.1 Source of Data

Elevation of the surrounding area is extracted from DEM file. SRTM 1 Arc-Second Global DEM is downloaded from the website <https://earthexplorer.usgs.gov/>. From this DEM file area of interest is selected and the raster DEM is converted to point shape file by ArcGIS software and from the attribute table of the point shape file coordinate and elevation of each point is extracted.

4.6.2 Input of Elevation Data in River2D

An Elevation data file (*.tpo) is a file type for saving the x-, y- and z- coordinate values of a point. It can be used as a file type for importing elevation data for iRIC. The elevation data file is a tab-delimited text file. The top line shows the number of points in the data and the following lines are the actual data.

Each column has the following meaning:

- x-coordinate
- y-coordinate
- z-coordinate

Table 4.9: Example of an elevation data file

497	No. of data		
-57143.000098	-97348.699902	11.100000	
-57009.000098	-97371.100003	11.290000	
-56880.200110	-97402.499901	11.480000	
-56761.800086	-97451.599904	11.670000	
-56597.900122	-97579.099896	9.480000	
-56451.500098	-97739.099896	7.290000	
...	x-coordinate (m)	y-coordinate (m)	z-coordinate (elevation, etc.)

Figure 4.21 and 4.22 show the elevation contour of confluence 1 and confluence 2 generated in River2D, after importing *.tpo file created from DEM data.

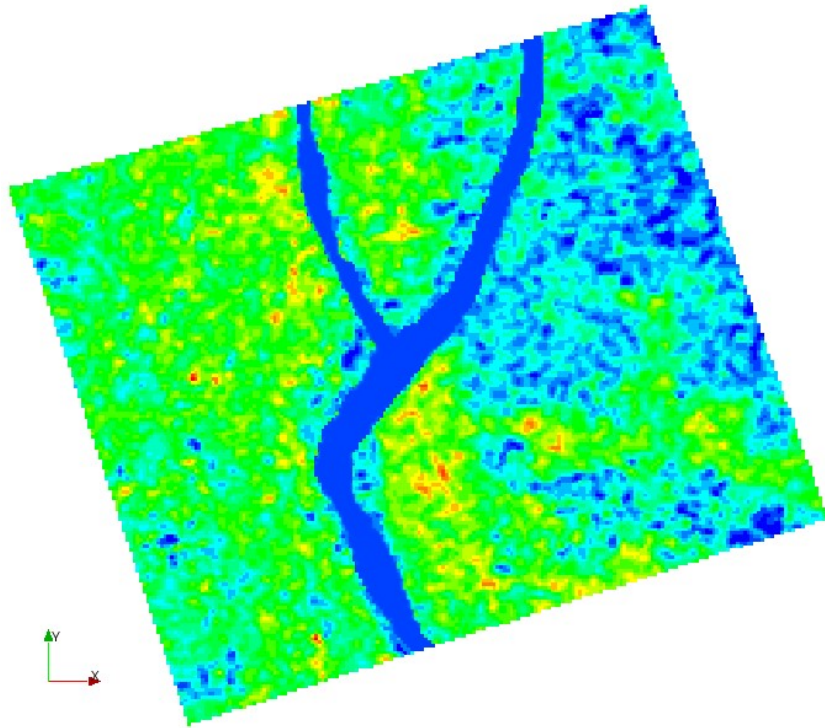


Figure 4. 21: Extracted elevation data of Confluence 1 from DEM after importing in River2D as *.tpo file.

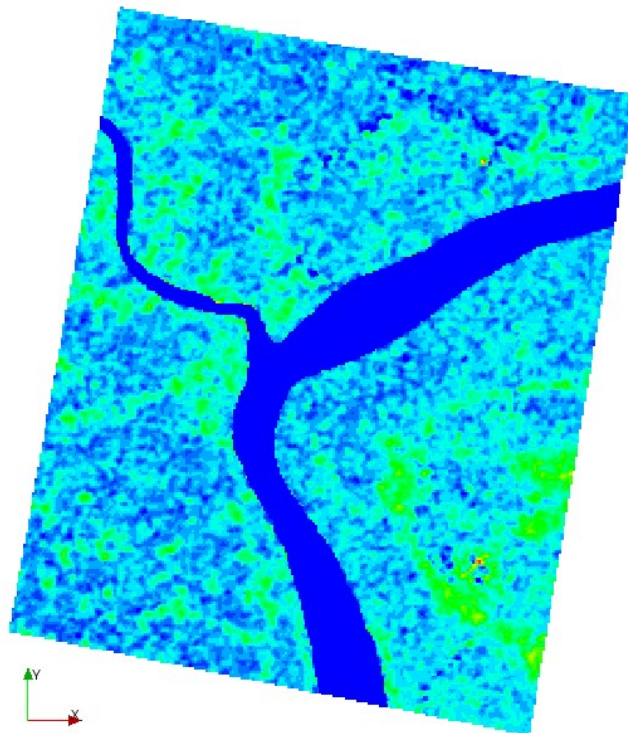


Figure 4. 22: Extracted elevation data of Confluence 2 from DEM after importing in River2D as *.tpo file.

4.7 Result

For numerical modeling certain hypothesis is considered for the simulation. Here total inflow and total outflow is considered equal as $6000 \text{ m}^3/\text{s}$, which is adopted from Mongla port data archive. During high-tide in both Confluence 1 and 2, discharge ($6000 \text{ m}^3/\text{s}$) from downstream at south, is considered to be divided in main channel and branch channel as $3600 \text{ m}^3/\text{s}$ and $2400 \text{ m}^3/\text{s}$ respectively. During ebb-tide, in both Confluence 1 and 2, flow from main channel ($3600 \text{ m}^3/\text{s}$) and branch channel ($2400 \text{ m}^3/\text{s}$) from upstream at north, are considered to flow ($6000 \text{ m}^3/\text{s}$) through downstream at south. Total simulation is run for 3600 second at a constant discharge.

It is observed that during high-tide velocity magnitude ranges from $1.81 - 2.96 \text{ m}^3/\text{s}$ more or less in main channel of Confluence 1 in Figure 4.23. Velocity magnitude drops at the main channel where the branch channel is connected with but it increases again in the main channel. In the main channel meander type nature is observed and every time velocity magnitude is higher in outer edge of the curve. Drops of velocity magnitude in the confluence zone and again its increment at the upstream can be possible due to the sharing of downstream flow at branch and gradual contraction of the cross-section of the main channel respectively. In the estuary of the branch channel, velocity magnitude drops significantly, especially separation zone is developed both side of the branch estuary.

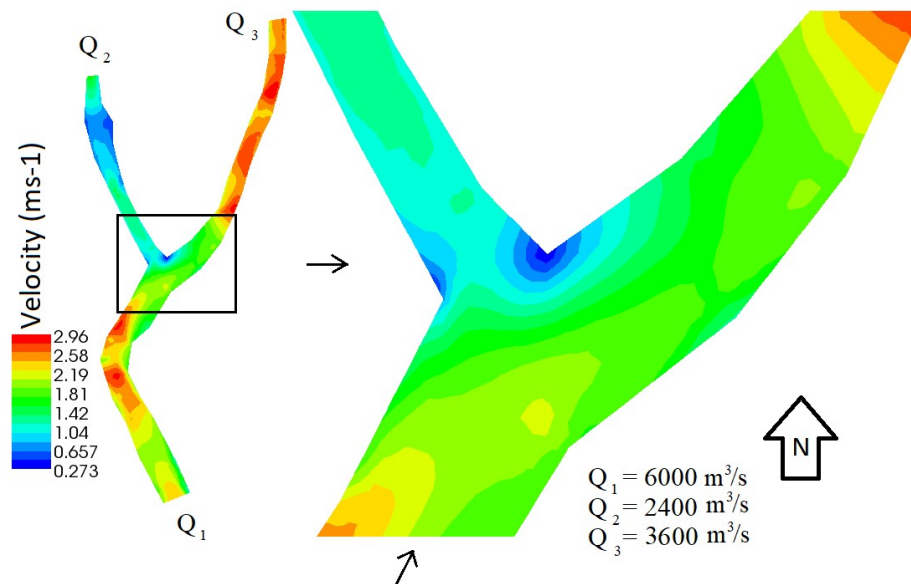


Figure 4.23: Velocity magnitude contour due to channel flow during high-tide at Confluence 1

Figure 4.24 shows the artificially created ebb-tide environment is represented in Confluence 1. In this case both in main and branch channel velocity magnitude increased, especially at the outer edge of the curve, similar like above mentioned high-tide condition, which is very similar with the practical condition. Increment of the

velocity in both main and branch channel are due of flow of stored water during high tide at the upstream. Also in this case separation and stagnation zones are developed at the estuary of the branch channel, where velocity is dropped suddenly and a mixing zone is developed.

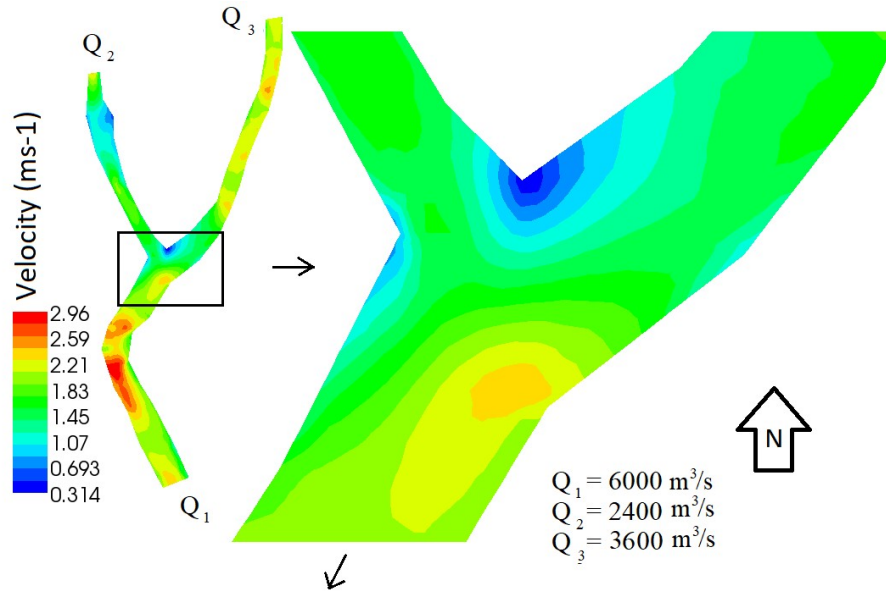


Figure 4.24: Velocity magnitude contour due to channel flow during ebb-tide at Confluence 1

Again high-tide condition is simulated in Confluence 2, where same result is observed as high-tide condition in Confluence 1. This result is shown in Figure 4.25. Here also velocity magnitude drops at the branch and only one separation zone is developed in the branch estuary. But in the same condition two separation zones are developed in Confluence 1. The reason is geographic condition, where in Confluence 1 branch junction with main channel forms a sharp turn, but in Confluence 2 it is very smooth on the south side of the estuary. Other reason is the branch is situated at the outer curve of the main channel where velocity magnitude is maximum. So fluid flow with higher energy diverted in such an intake whose junction point with main channel is very smooth, hence separation zone is eliminated. But on the north side of the branch estuary a separation zone is developed due to direct conflict of main channel flow with branch channel bank at north side and diversion of flow to main and branch channel. Here the branch channel forms a meander, where velocity magnitude is higher at the outer edge of the curve, which is associated to practical condition. Before reaching of the intake the velocity magnitude is higher in main channel but it drops suddenly after the estuary and it turns to minimum a value and again rises. The reason is, during crossing the branch estuary, several volume of water diverted to branch channel thus momentum of the flow is decreased. Again a sudden enlargement of channel width as well as the cross section, with the entrance of flow with low momentum triggers to reduce the velocity magnitude. But when the channel width or cross section decreases again, velocity magnitude increases.

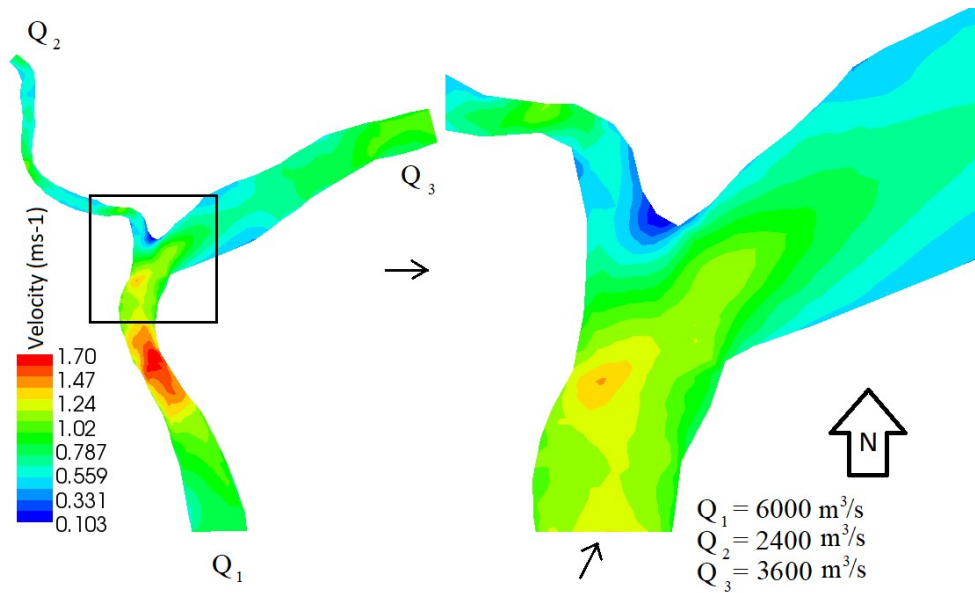


Figure 4.25: Velocity magnitude contour due to channel flow during high-tide at Confluence 2

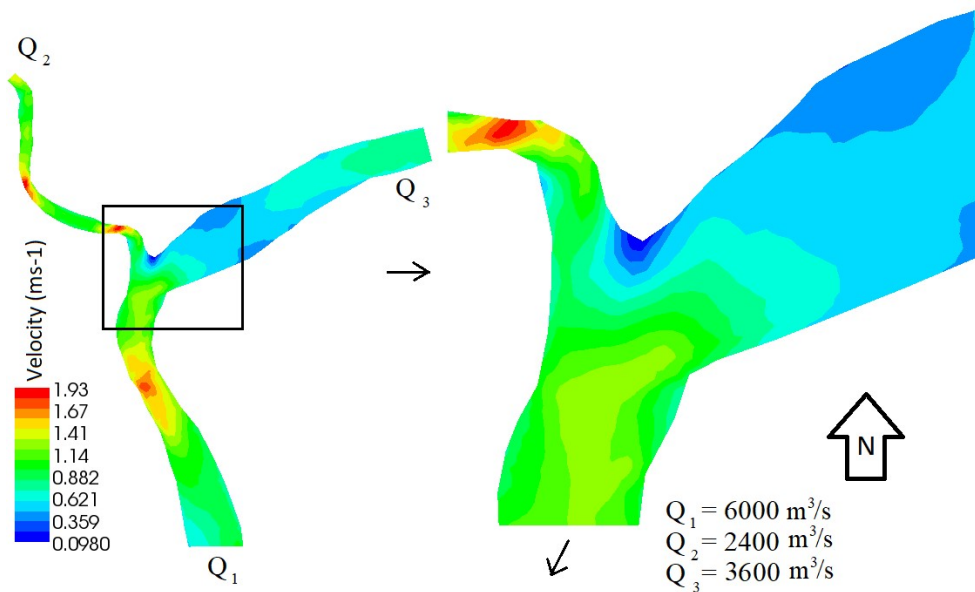


Figure 4.26: Velocity magnitude contour due to channel flow during ebb-tide at Confluence 2

Figure 4.26 shows the ebb-tide condition in Confluence 2, which is pretty much similar to ebb-tide condition of Confluence 1. Velocity magnitude is higher in branch channel than the high-tide condition, which is due to the flowing of stored water from upstream during high-tide. Also in this case flow velocity magnitude is higher at the outer edge of the branch meandering curve. And combined upstream flow from main and branch channel raises the velocity magnitude to a maximum level at outer edge of the main channel bend just after passing the branch channel estuary, similar to the ebb-tide

condition of Confluence 1. Also in this case a separation zone is developed at the same position of high-tide condition. Because at the reach of main channel, a sharp bend is present at the branch estuary, whose apex is north faced and opposite inner side meet with main channel very smoothly. If the branch estuary is considered as a part of a meander channel, then north side of the estuary near the bend apex acts like an inner side of the meander channel where velocity magnitude generally drops. Due to centrifugal force, the fluid particles have a tendency to rush to the outer curve, which brings the separation zone.

In the above mentioned four cases of two different type of confluence, some common features can be observed in the velocity profile as separation zone which is commonly formed at the bank of the branch estuary. Again during high-tide velocity magnitude decreases significantly at the branch channel in both type of confluences. Also in some case velocity drops severely at the main channel where width and cross-section increases suddenly. In the separation zone velocity drops suddenly with a respect to surrounding area, hence siltation problem is very common in the separation zone, thus bar formed at the river estuaries. This unnecessary bar interrupts the normal flow of the channel. This phenomenon creates a serious navigation problem at the estuaries and decreases navigability of the channel. Again in both high and ebb-tide condition velocity magnitude increases at the outer edge of the curved channel where bank erosion occurs.

4.8 Hypothesis of Changing Confluence Geometry

Generally in nature right angled channel confluence is very rare. If the main channel is considered as continues line and branch always meet at some points middle of the main channel, where it forms an acute angle and obtuse angle (Figure 4.27). Depends on the direction of flow, a flow separation zone and a flow stagnation zone always form in these acute and obtuse angled zone (Figure 4.28).

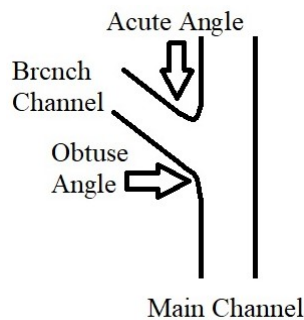


Figure 4.27: Concept of changing of branch estuary geometry

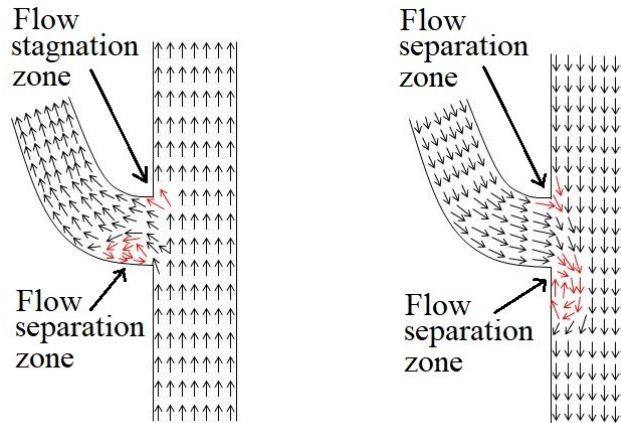


Figure 4. 28: Formation of flow separation and stagnation zone based on flow direction

In this study, a hypothesis can be considered to reduce the area and length of separation zone. In nature erosion is very common, so the acute and the obtuse angle of the estuary always change its shape. Here some bank protection work such as embankment and change of the geometry of branch estuary can reduce severity of the separation zone. For changing geometry of the estuary, cutting and filling operations are required near the obtuse and acute angled zone respectively (Figure 4.29). If the branch channel meets with main channel so smoothly, as the acute angle becomes more acute and junction of obtuse angle becomes smoother, then the formation of separation zone may be hoped to be minimized. According to this concept after converting the acute and obtuse angled zone, the junction must be protected by some erosion resistive embankment, otherwise the junction becomes fragile.

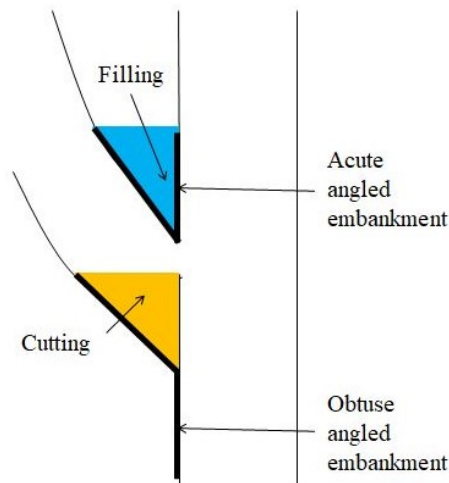


Figure 4. 29: Estuary geometry changing operation

The expected flow condition after conversion is presented in Figure 4.30. This converted shape of the acute angle can easily diverts flow from main channel to branch or accumulate flow from branch and main channel in downstream without mixing. On

the other hand smoothed junction of obtuse angle can easily make way for flowing water, without collision with sharp junction.

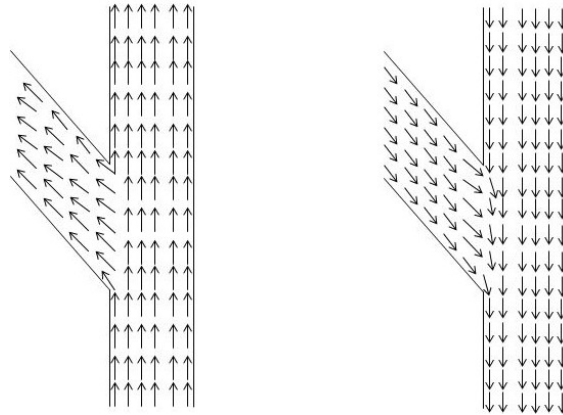


Figure 4.30: Expected flow scenario in converted estuary

This concept is applied in Confluence 1 and 2 by changing its geometry and applying the same boundary conditions.

4.9 Remodeled Result

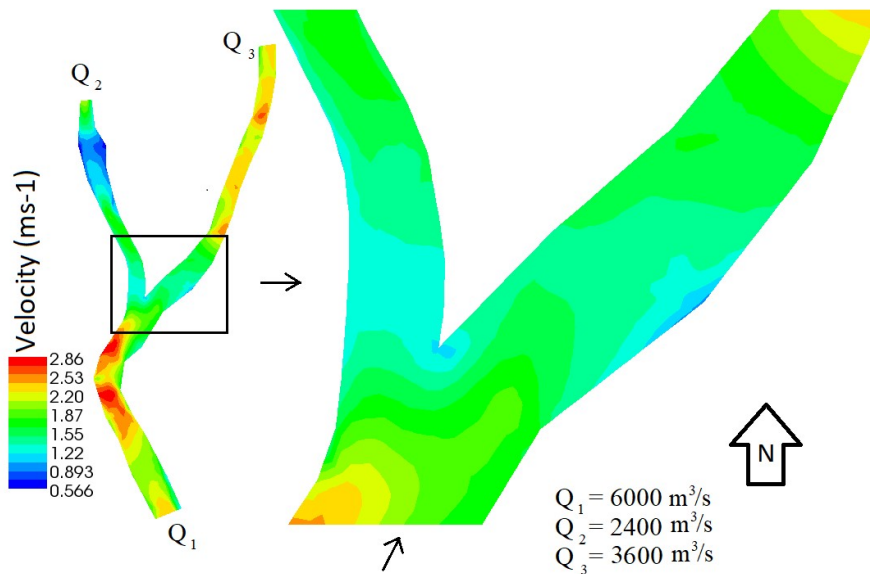


Figure 4.31: Velocity magnitude contour due to channel flow during high-tide at Confluence 1 after changing geometry

After changing the geometry of Confluence 1 according to the above mentioned concept, significant change in the velocity magnitude is observed. The high-tide and ebb-tide conditions are represented in Figure 4.31 and Figure 4.32. The concept is applied successfully in Confluence 1, where velocity increases significantly at the

separation zone area and separation zone is eliminated. This change of geometry can be helpful to prevent siltation and keep the navigability at the branch estuary accessible.

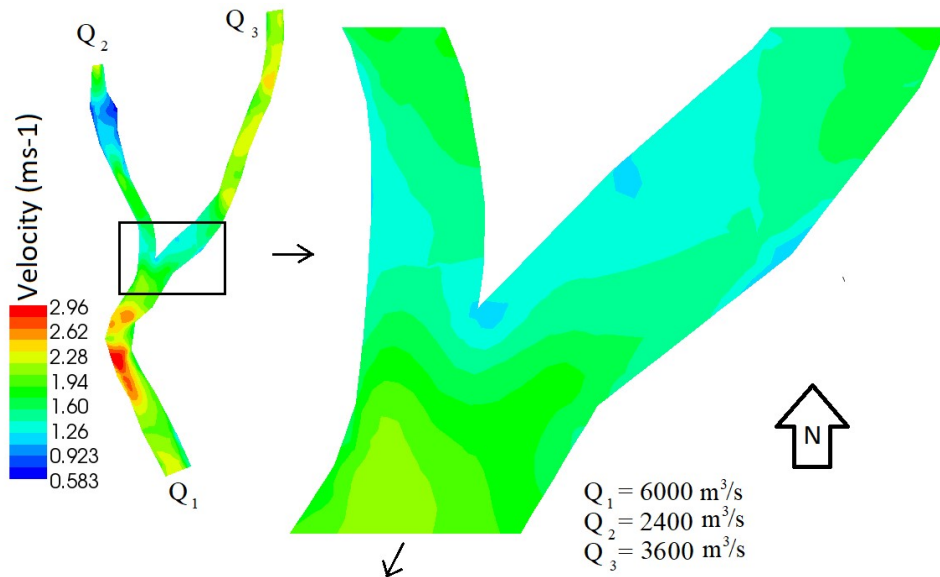


Figure 4.32: Velocity magnitude contour due to channel flow during ebb-tide at Confluence 1 after changing geometry

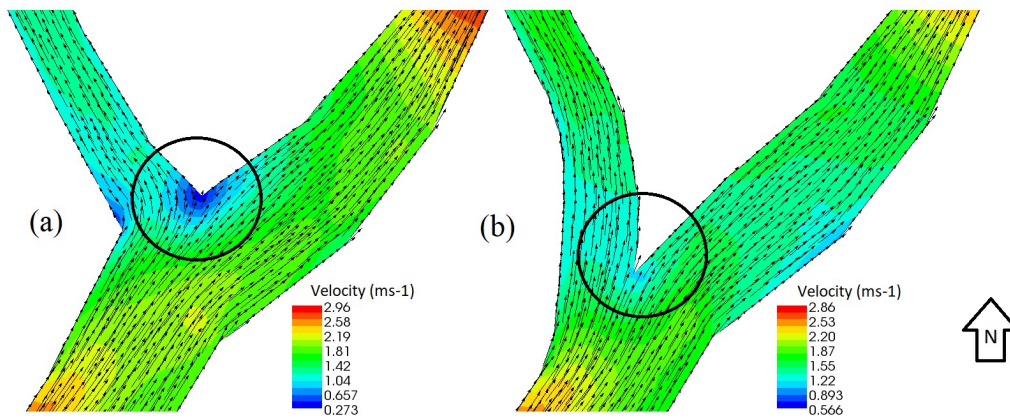


Figure 4.33: Comparison of Confluence 1 before (a) and after (b) changing geometry of branch estuary, during high-tide

In Figure 4.33, comparisons of flow before and after changing geometry of Confluence 1 is represented, to observe the change of flow pattern and velocity magnitude in during high-tide. Flow pattern in the changed geometry shows that flow is diverted very sharply in the branch channel rather than previous geometry. In previous geometry flow directly hit the bank area near the acute angle, then diverted but in changed geometry fluid particle cannot hit the acute angled area due its sharp pointy shape. Thus mixing zone is disappeared with the increment of velocity magnitude. In the junction of obtuse angle, fluid particles have enough space to change its direction of flow after smoothing the junction. Here separation zone is also eliminated and velocity magnitude increases.

In Figure 4.34 same comparisons are being made for Confluence 1 but in ebb-tide condition, where separation zone is eliminated and velocity magnitude is also increased. In the previous geometry flow particles collide with each other at the acute angled junction and change its direction suddenly at the obtuse angled junction thus loss its energy, which brings separation zone. But after changing the acute angle to a pointy shape fluid particles accumulate together gently from branch and main channel. On the other hand at obtuse angled junction after smoothing, particle moved to the main channel without any sudden change of direction, so velocity is increased and separation zone eliminated.

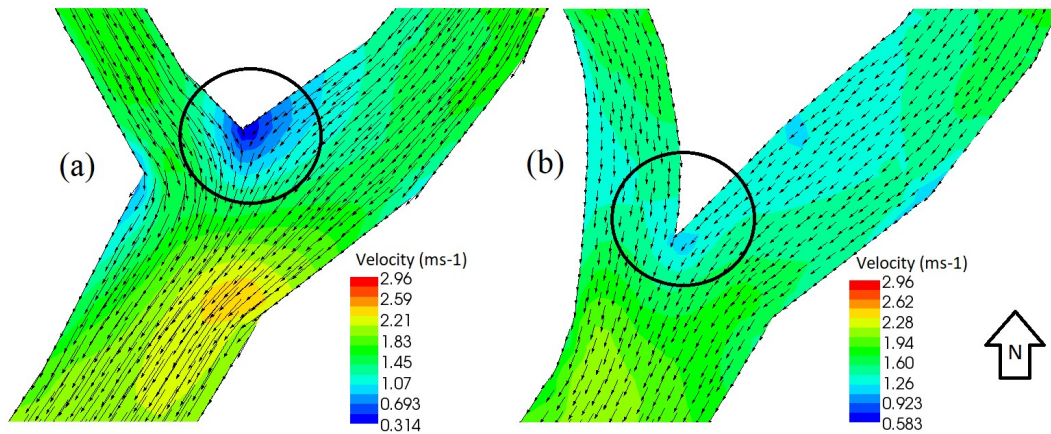


Figure 4. 34: Comparison of Confluence 1 before (a) and after (b) changing geometry of branch estuary, during ebb-tide

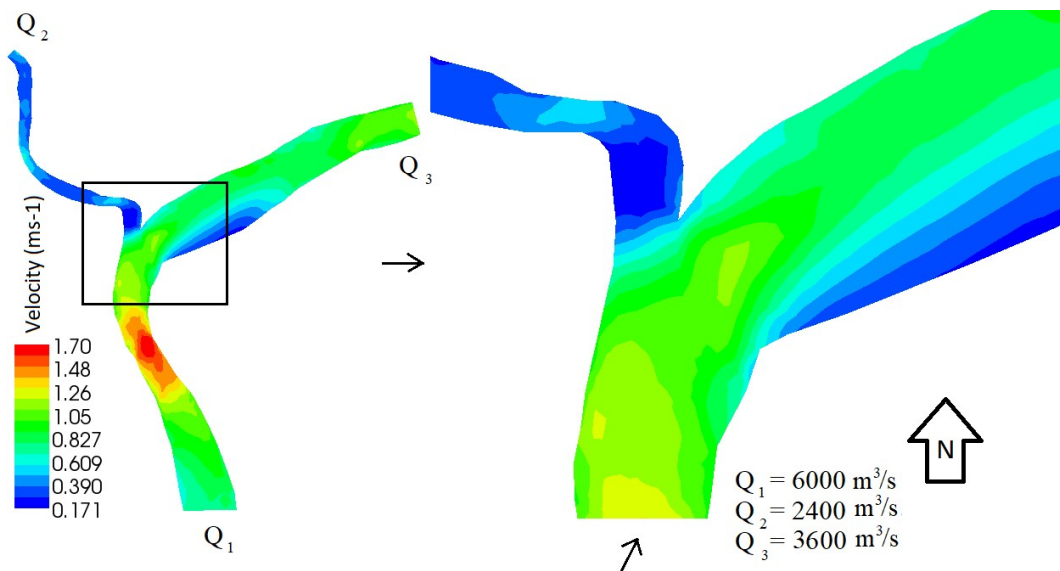


Figure 4.35: Velocity magnitude contour due to channel flow during high-tide at Confluence 2 after changing geometry

In figure 4.35 and 4.36 same concept of changing geometry is visualized for Confluence 2 for high-tide and ebb-tide condition. But in case of Confluence 2, this

concept is not effective enough. Basically velocity drops in the branch channel during high-tide and remains same during ebb-tide. And in main channel, velocity drops just opposite the junction between branch and main channel during high tide. During ebb-tide velocity of the main channel drops before reaching branch estuary as compared with this situation without changing geometry.

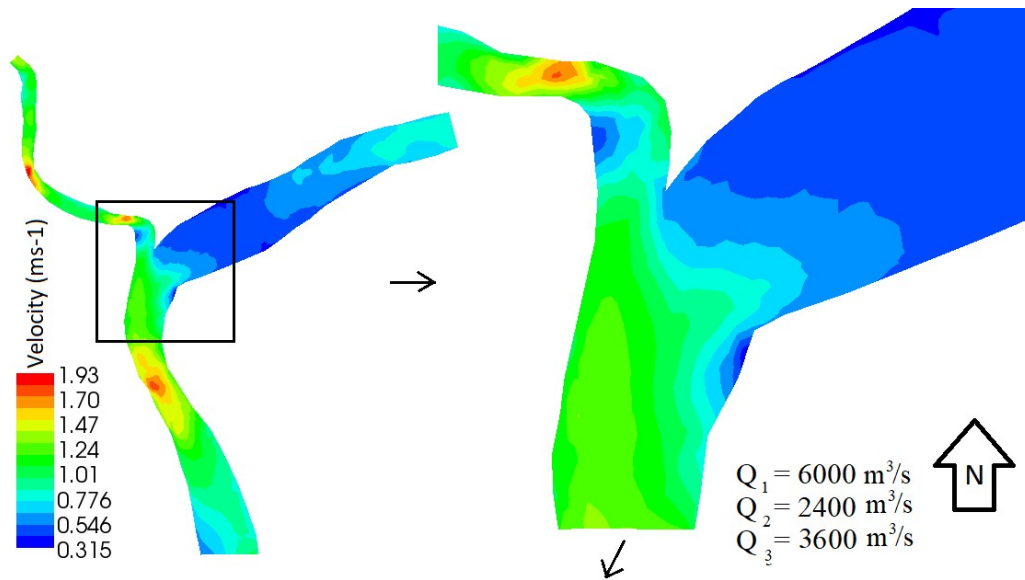


Figure 4.36: Velocity magnitude contour due to channel flow during ebb-tide at Confluence 2 after changing geometry

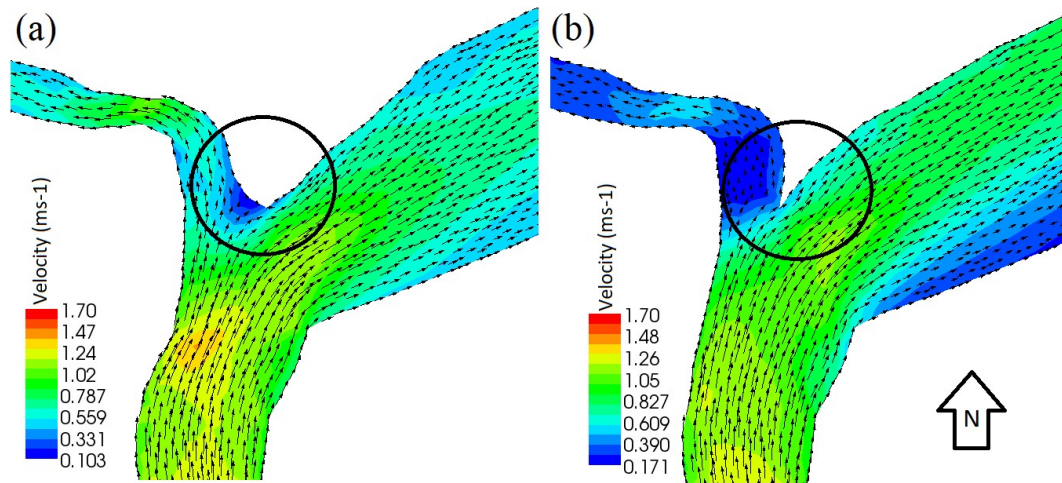


Figure 4.37: Comparison of Confluence 2 before (a) and after (b) changing geometry of branch estuary, during high-tide

Comparison between flow pattern before and after changing geometry of Confluence 2 during high-tide in Figure 4.37 and ebb-tide in Figure 4.38 show that fluid particle diverted and accumulated at the acute angled junction very smoothly after changing geometry. And in the obtuse angled junction particle also moved in the same way both

in high and ebb-tide conditions. But particle loss its energy almost every time after diversion or accumulation rather than unchanged geometry. One of the reason may be the branch changes its direction and forms a sharp bend. So in the second attempt, the sharp bend at the branch estuary is removed and the acute angle is sharpen more and the obtuse angle is smoothen more.

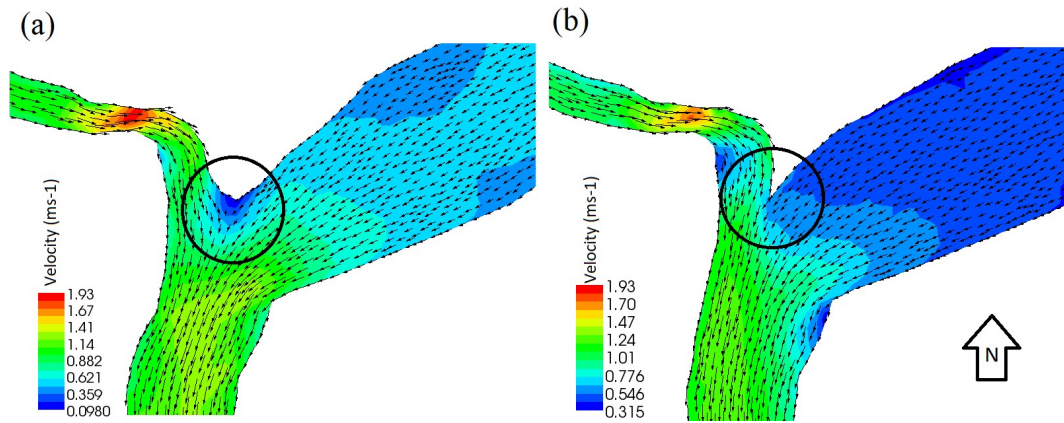


Figure 4.38: Comparison of Confluence 2 before and after changing geometry of branch estuary, during ebb-tide

Again in the second attempt, no significant result is observed, in Figure 4.39 and 4.40, during high and ebb-tide respectively. Separation zone is removed but velocity drops in branch and in the main channel just opposite side of branch estuary during high-tide. During ebb-tide, velocity drops again in main channel before reaching branch estuary.

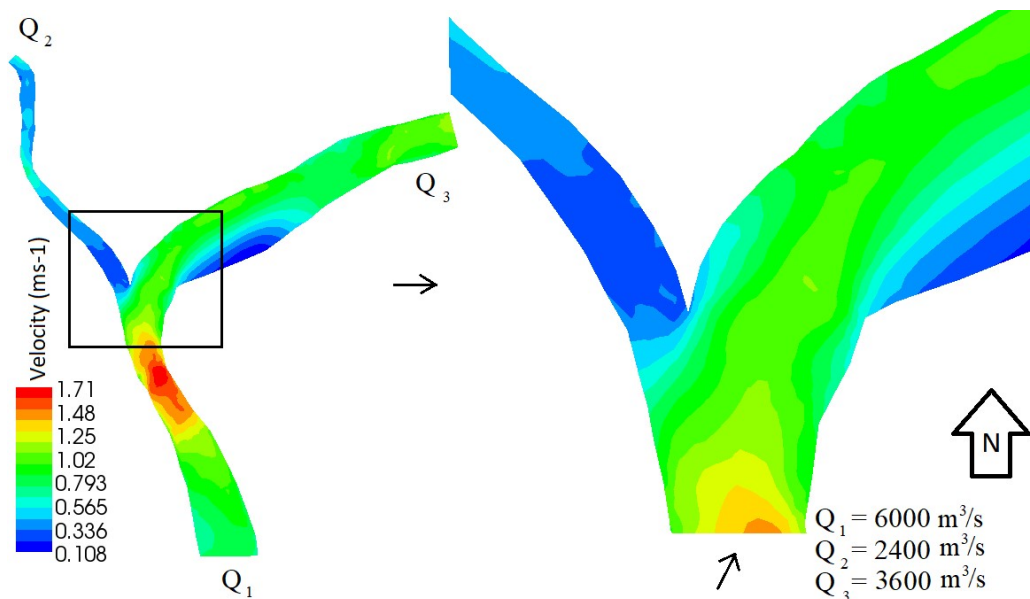


Figure 4.39: Velocity magnitude contour due to channel flow during high-tide at Confluence 2 after changing geometry (second time)

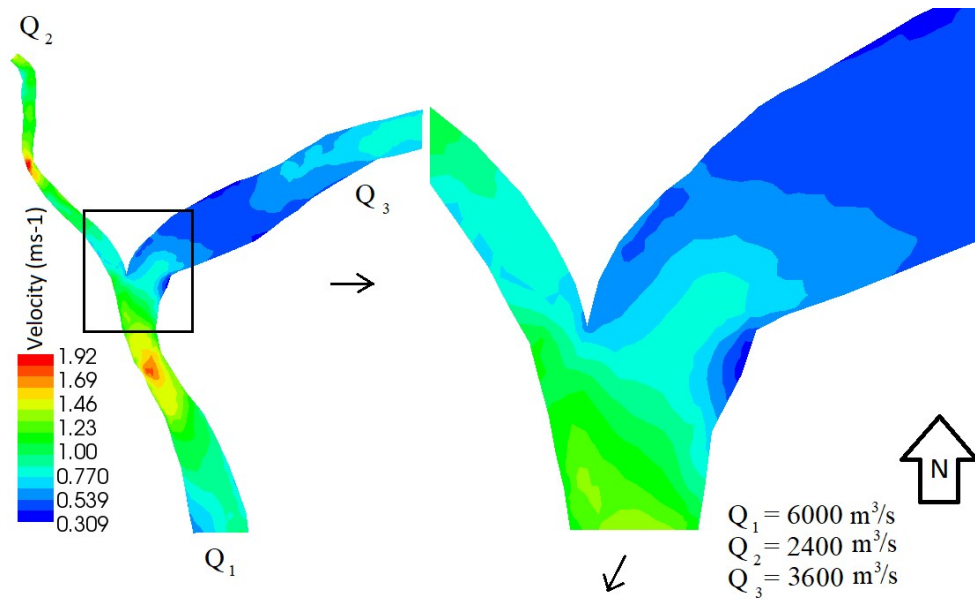


Figure 4.40: Velocity magnitude contour due to channel flow during ebb-tide at Confluence 2 after changing geometry (second time)

In figure 4.41 and 4.42, particle movement is as like as Figure 4.37 and 4.38, which brings no significant change after second attempt of changing geometry. Whatever it looks like the separation zone is eliminated near the branch estuary but velocity magnitude drops significantly at the branch. This means the concept of changing geometry works properly in Confluence 1 but almost fails in Confluence 2.

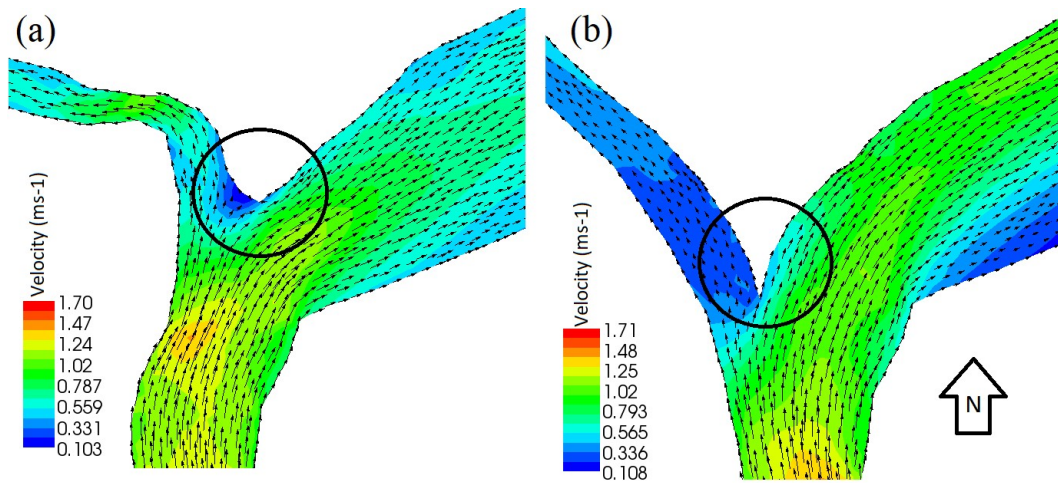


Figure 4.41: Comparison of Confluence 2 before and after changing geometry of branch estuary, during high-tide (second time)

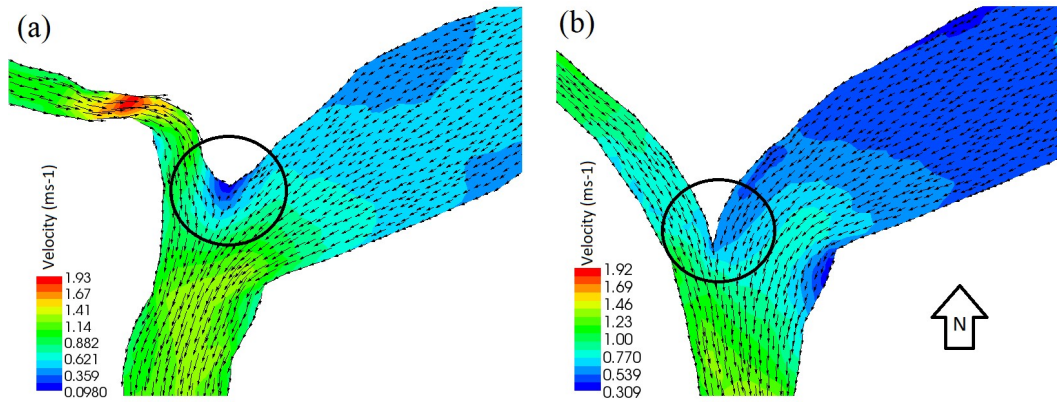


Figure 4.42: Comparison of Confluence 2 before and after changing geometry of branch estuary, during ebb-tide (second time)

The reason of this failure in changing geometry in confluence 2 is pretty simple. Firstly in Confluence 2 main channel more curved than Confluence 1. During flow diversion or accumulation main channel flow losses energy in a sharp bend. Secondly Confluence 2 is geometrically more complex than confluence 1. In confluence 2 branch channel is more meandered than Confluence 1 and a sharp bend exists in the branch estuary which is the main reason of energy loss in branch channel flow. Third and the main reason is the main channel width or cross-section increased suddenly at north side of the branch estuary. This is not common in natural case, because generally in upstream river cross-section or width is lower than downstream and flow velocity is higher. So more research is necessary to apply the above mentioned hypothetical concept in every type of confluence.

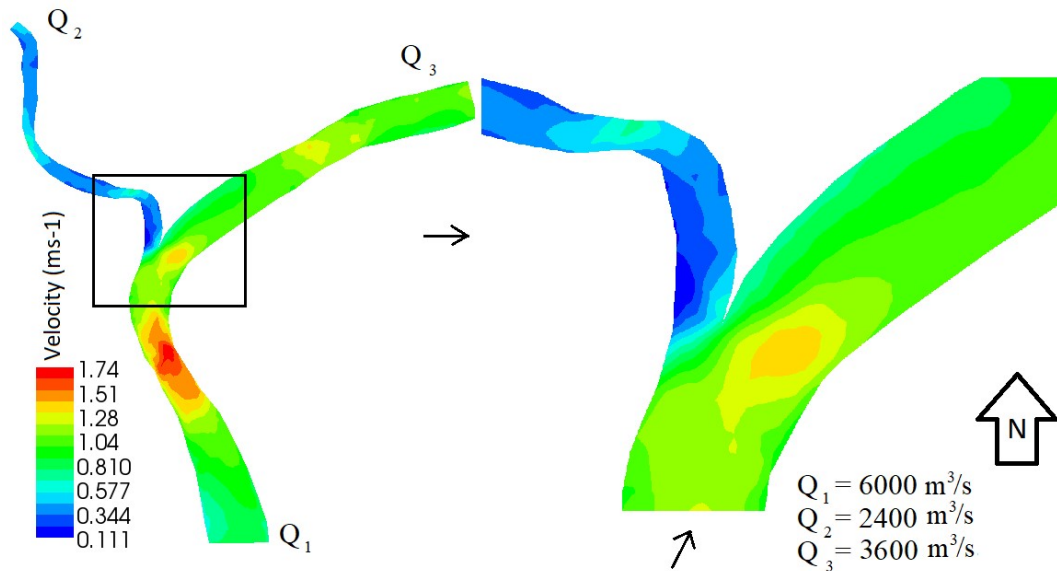


Figure 4.43: Velocity magnitude contour due to channel flow during high-tide at Confluence 2 after changing geometry (third time)

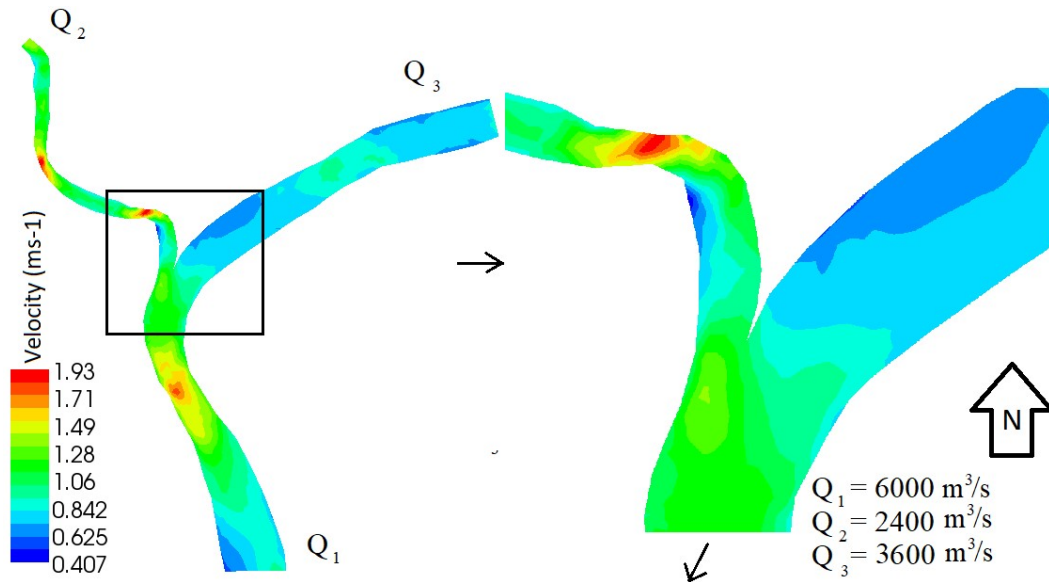


Figure 4.44: Velocity magnitude contour due to channel flow during ebb-tide at Confluence 2 after changing geometry (third time)

Third time, same concept is applied similar to attempt one, accept the acute angle converted to more acute one than attempt one and the main channel width decreases just after the branch estuary. This attempt shows pretty good results, are showed in Figure 4.43 and 4.44. Velocity in the main channel increases during high-tide but in branch channel it drops rather than high-tide condition without changing geometry. During ebb-tide velocity magnitude does not change significantly at upstream, before branch estuary and remains same as before mentioned unchanged geometric condition.

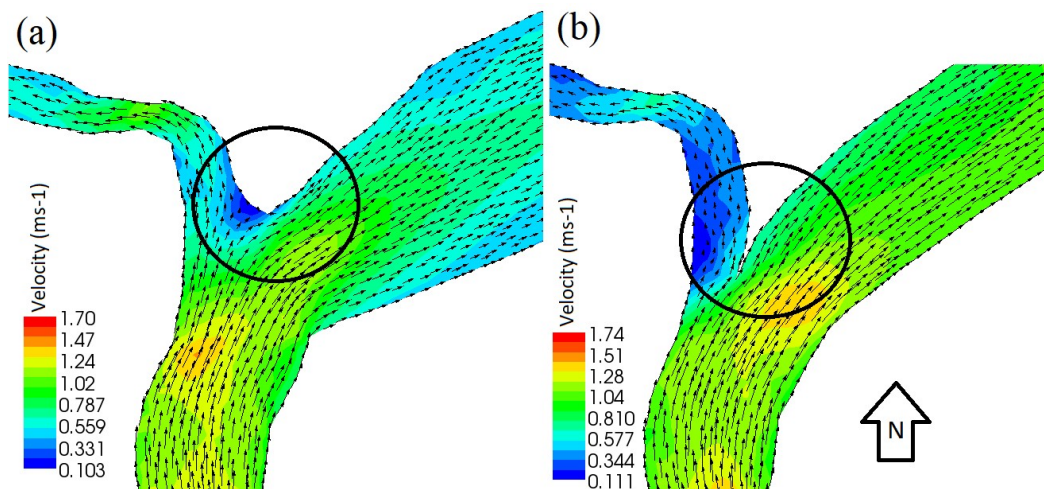


Figure 4.45: Comparison of Confluence 2 before and after changing geometry of branch estuary, during high-tide (third time)

Comparisons in Figure 4.45 and 4.46, show that fluid particle movement is similar to previous attempts of changing geometry. But in the third attempt, separation zone is

driven away from the acute angled junction without dropping velocity magnitude in the main and branch channel. In some position of both main and branch channel velocity drops. More research is necessary, for optimizing this proposed concept.

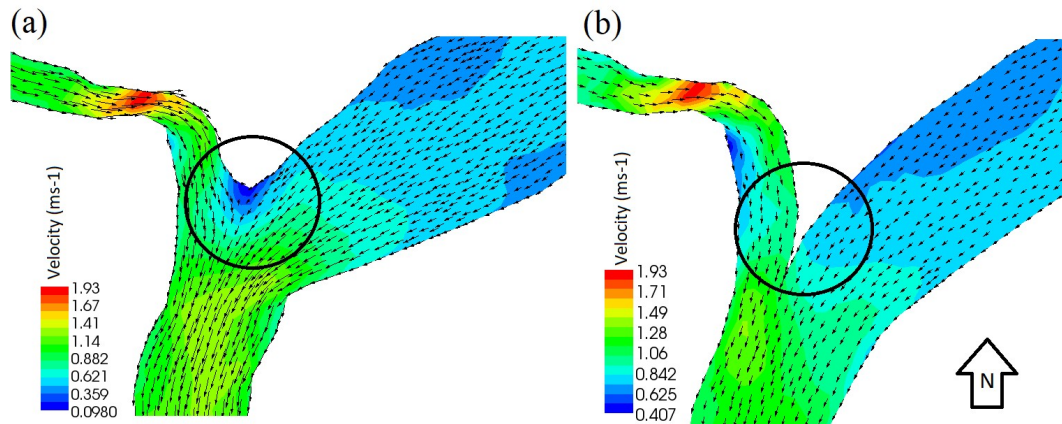


Figure 4.46: Comparison of Confluence 2 before and after changing geometry of branch estuary, during ebb-tide (third time)

4.10 Conclusion

From above analysis, following decision can be made precisely:

- From the simulation of the natural channel junction, position of separation zone and stagnation zone can be detected near the estuary of the branch channel. In this type of zone velocity drops significantly thus siltation occurs.
- During high-tide and ebb-tide, same channel junction acts as confluence and diversion, based on junction geometry. So, simulation of both high-tide and ebb-tide condition in the same junction shows the variation of separation zone and stagnation zone.
- If main channel cross section at upstream higher than the downstream, velocity magnitude decreases significantly in the main channel.
- Very sharp bend in the branch channel causes more velocity drop in that channel.
- If acute and obtuse angled junction in between branch and main channel turn to more acute and smooth respectively, velocity magnitude increases significantly at the separation and stagnation zone, as well as in the main and branch channel.

CHAPTER 5

Modeling of Bank and Confluence Shifting

5.1 Introduction

Erosion and deposition near the branch estuary at the confluence and at river bank is very common in nature. Erosion causes great harm to the habitat pattern as well as the land property, whereas deposition or siltation decreases navigability and reservoir capacity of the river. Both erosion and deposition affects ecosystem, especially deposition or siltation reduce the volume of the confluence zone and destroy the ecosystem underneath the water. Modeling of the river bank and the whole confluence is an important task for the prediction of the future condition of the land property near the river bank and confluence zone. It is also helpful for urban and regional planning. In this study an attempt is taken to predict the future pattern of the Confluence 1 and Confluence 2, during 2030, as mentioned at Figure 4.20 of the previous Chapter 4.

5.2 Methodology

Confluence 1 and Confluence 2 are divided in several sections, whereas Confluence 1 belongs to 12 sections and Confluence 2 belongs to 14 sections. The sections of these confluences are represented in Figure 5.1. Each section is named after English alphabet A-Z. Georeferenced images from 1988 to 2018 are collected to extract the latitude and longitude data from the image pixel along the cross sections. These images are Landsat Look Images with Geographic Reference produced from Landsat 5, 7 and 8 missions and downloaded from the website <https://earthexplorer.usgs.gov/>. Then using ArcGIS 10.4.1 software package, the latitude and longitude data of the left and right bank along the cross-section of each year is measured. In this way total 30 numbers of data set are collected from 1988 to 2017 for each 26 numbers of sections, also data set for 2018 is also prepared for accuracy analysis. Then linear regression statistical method is applied, using 30 numbers of data set from 1988 to 2017 to predict the latitude and longitude of the left bank and right bank of each 26 sections for year 2018.

This approach help to predict the data set for year 2018. After calculating the latitude and longitude of 2018, actual data set is compared with the calculated one to determine the percent error of the each calculated latitude and longitude data, for both left and

right bank. Then this statistical method is applied to predict the bank and confluence positions for the year 2030. In this study relative position is compared in between year 1988 and 2018, of the each confluence. Then predicted position of left and right bank of each section during 2030 is represented comparing with 2018.

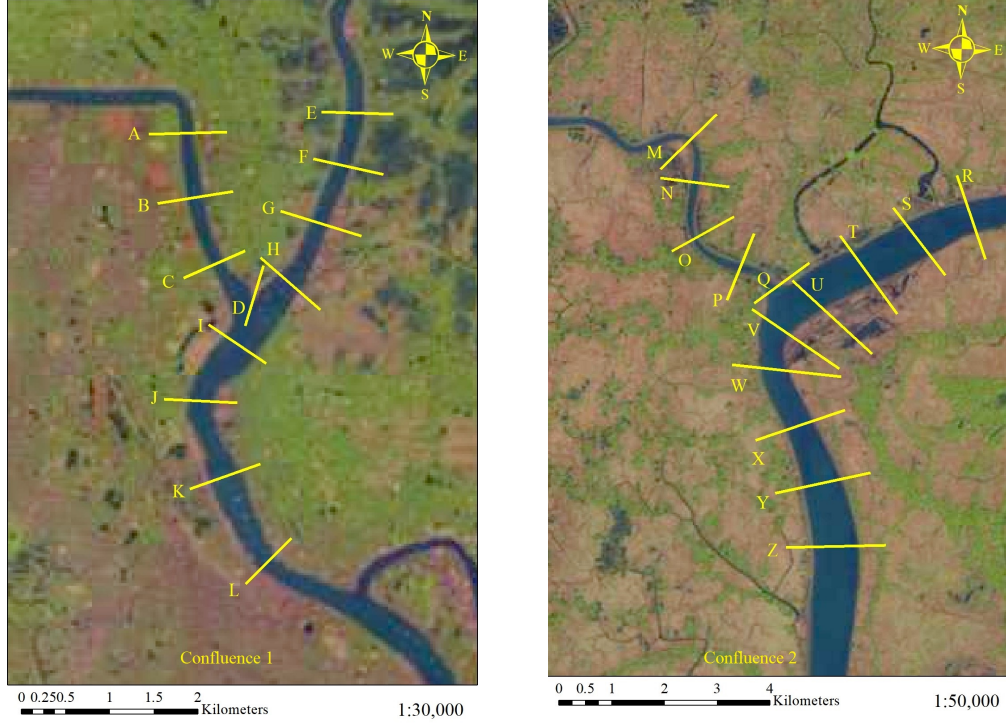


Figure 5. 1: Position of the cross-sections in Confluence 1 and Confluence 2 (RGB image 2018)

5.3 Governing Equation

In this study linear regression statistical method is used for predicting future latitude and longitude data and then percent error of the predicted data is calculated.

5.3.1 Linear Regression (Curtsey Wikipedia)

Given a data set $\{y_i, x_{i1}, \dots, x_{ip}\}_{i=1}^n$ of n statistical units, a linear regression model assumes that the relationship between the dependent variable y_i and the p -vector of regressors x_i is linear. This relationship is modeled through a disturbance term or error variable ε_i an unobserved random variable that adds noise to the linear relationship between the dependent variable and regressors. Thus the model takes the form

$$y_i = \beta_0 1 + \beta_1 x_{i1} + \dots + \beta_p x_{ip} + \varepsilon_i = x_i^T \beta + \varepsilon_i, \quad i = 1, \dots, n, \quad (5.1)$$

where T denotes the transpose, so that $x_i^T \beta$ is the inner product between vectors x_i and β .

Often these n equations are stacked together and written in vector form as

$$y = X\beta + \varepsilon \quad (5.2)$$

where

$$y = \begin{pmatrix} y_1 \\ y_2 \\ \vdots \\ y_n \end{pmatrix}, X = \begin{pmatrix} X_1^T \\ X_2^T \\ \vdots \\ X_N^T \end{pmatrix} = \begin{pmatrix} 1 & x_{11} & \cdots & x_{1p} \\ 1 & x_{21} & \cdots & x_{2p} \\ \vdots & \vdots & \vdots & \vdots \\ 1 & x_{n1} & \cdots & x_{np} \end{pmatrix}, \beta = \begin{pmatrix} \beta_1 \\ \beta_2 \\ \beta_3 \\ \vdots \\ \beta_p \end{pmatrix}, \varepsilon = \begin{pmatrix} \varepsilon_1 \\ \varepsilon_2 \\ \vdots \\ \varepsilon_n \end{pmatrix} \quad (5.3)$$

Some remarks on terminology and general use:

- y_i is called the regressand, endogenous variable, response variable, measured variable, criterion variable, or dependent variable (see dependent and independent variables). The decision as to which variable in a data set is modeled as the dependent variable and which are modeled as the independent variables may be based on a presumption that the value of one of the variables is caused by, or directly influenced by the other variables. Alternatively, there may be an operational reason to model one of the variables in terms of the others, in which case there need be no presumption of causality.
- $x_{i1}, x_{i2}, \dots, x_{ip}$ are called regressors, exogenous variables, explanatory variables, covariates, input variables, predictor variables, or independent variables (see dependent and independent variables, but not to be confused with independent random variables). The matrix X is sometimes called the design matrix.
 - Usually a constant is included as one of the regressors. For example, we can take $x_{i1} = 1$ for $i = 1, \dots, n$. The corresponding element of β is called the intercept. Many statistical inference procedures for linear models require an intercept to be present, so it is often included even if theoretical considerations suggest that its value should be zero.
 - Sometimes one of the regressors can be a non-linear function of another regressor or of the data, as in polynomial regression and segmented regression. The model remains linear as long as it is linear in the parameter vector β .
 - The regressors x_{ij} may be viewed either as random variables, which we simply observe, or they can be considered as predetermined fixed values

which we can choose. Both interpretations may be appropriate in different cases, and they generally lead to the same estimation procedures; however different approaches to asymptotic analysis are used in these two situations.

- β is a $(p + 1)$ -dimensional parameter vector, where β_0 is the constant (offset) term. Its elements are also called effects, and the estimates of it are called "estimated effects" or regression coefficients. Statistical estimation and inference in linear regression focuses on β . The elements of this parameter vector are interpreted as the partial derivatives of the dependent variable with respect to the various independent variables.
- ε_i is called the error term, disturbance term, or noise. This variable captures all other factors which influence the dependent variable y_i other than the regressors x_i . The relationship between the error term and the regressors, for example whether they are correlated, is a crucial step in formulating a linear regression model, as it will determine the method to use for estimation.

5.3.2 Percent error

During the calculation of results, which are aiming for known values, the percent error formula is useful tool for determining the precision of the calculations. The formula is given by:

$$\%error = \left(\frac{Value_{measured} - Value_{actual}}{Value_{actual}} \right) \times 100 \quad (5.4)$$

5.4 Result

Confluence 1 and 2, as well as the both left and right bank of the adjacent rivers are less susceptible to shift, which is clearly shown in Figure 5.2 and 5.3, where pattern of the two confluences during 1988 and 2018 are almost same.

During 1988, main and branch river is narrow in shape near the estuary of the Confluence 1 (Figure 5.2). Whereas in 2018 main and branch rivers are widened near the estuary. Especially the delta is eroded in a certain amount, which widens the estuary and the bank of the main river just opposite to the branch estuary also eroded. If the eroded mass of the particle is not migrated from estuary zone, then the volume must be deposited bottom of the confluence and makes it shallower. On the other hand main channel and branch remain same in position, all through the year from 1988 to 2018.

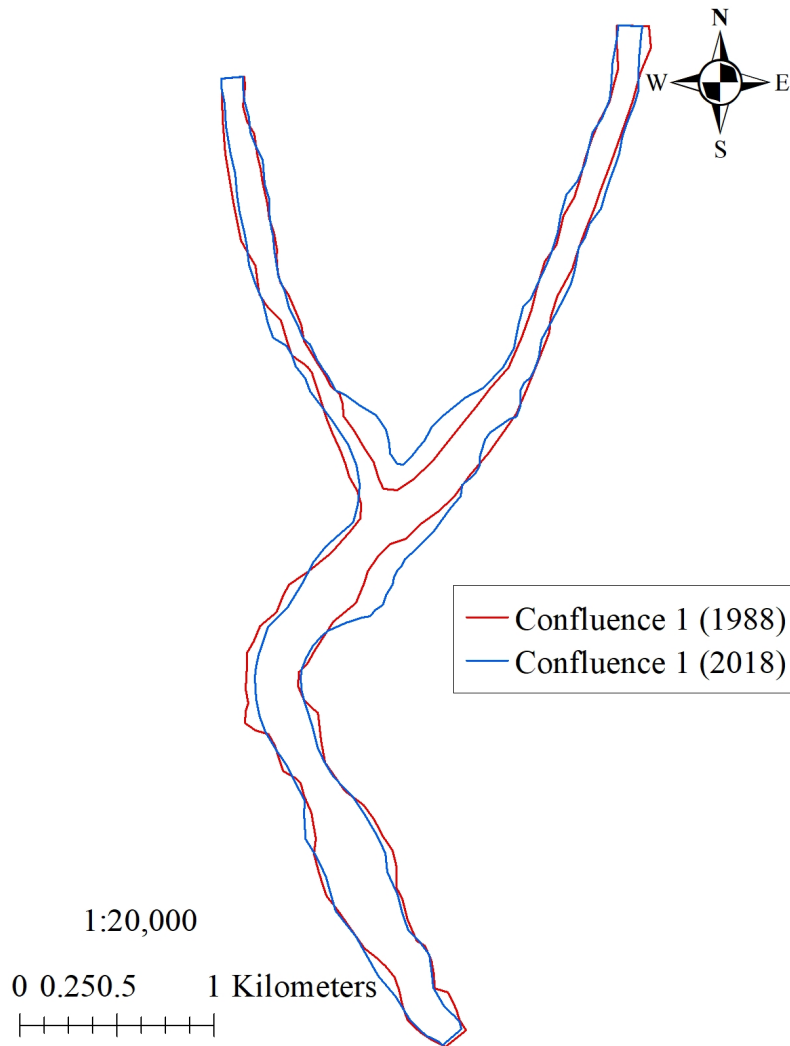


Figure 5. 2: Relative comparison of Confluence 1 in between 1988 and 2018

On the other hand Confluence 2 is changed enormously as compared with Confluence 1, especially near the branch estuary (Figure 5.3). Far end of the branch of the selected section is displaced from its original position during 1988. But the northern and southern corner of the main channel remains more or less same. The main channel is widened in most of its length. But the apex of the main channel curved is prolonged to the direction of branch estuary. Here in 2018, the branch mouth is reduced in section than 1988 and the reason is obviously erosion, which is very common at the outer curve of the meander. The delta between branch and the main channel is completely disappeared at 2018. On the other hand, right bank at the inner curve of the meander, just opposite to the branch estuary is moved towards West, which is caused due to the deposition of the eroded particle just from opposite bank.

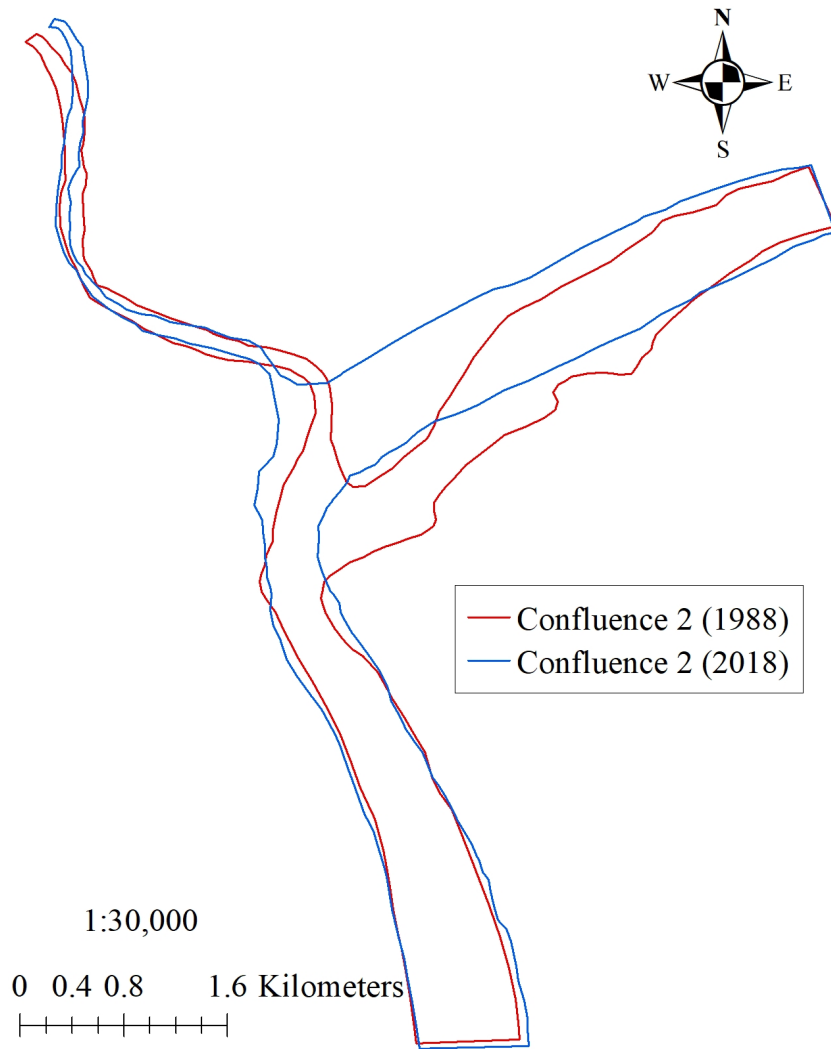


Figure 5. 3: Relative comparison of Confluence 2 in between 1988 and 2018

In this study, an attempt is taken to predict this bank and whole confluence pattern shifting process, as well as the erosion deposition process of the banks. For this prediction linear regression statistical method is used, to calculate the latitude and longitude of left and right bank of each section for year 2018. In Figure 5.4 and 5.5, this calculated coordinates are inserted on actual confluence pattern of 2018. The green points are the calculated coordinates of left and right bank of the sections and the blue lines are the actual confluence pattern. Figure 5.4 shows that, the calculated coordinates of the left and right bank fit perfectly with Confluence 1 pattern. Confluence 1 is less susceptible to change pattern. Only left and right bank of Section I and Point D at the apex of the delta is shifted significantly, which is shown in Figure 5.2. This method applied for the prediction of the coordinates during 2018, performs well to calculate near exact values of the of the coordinates of left and right bank of Section I and Point D, as well as other coordinates.

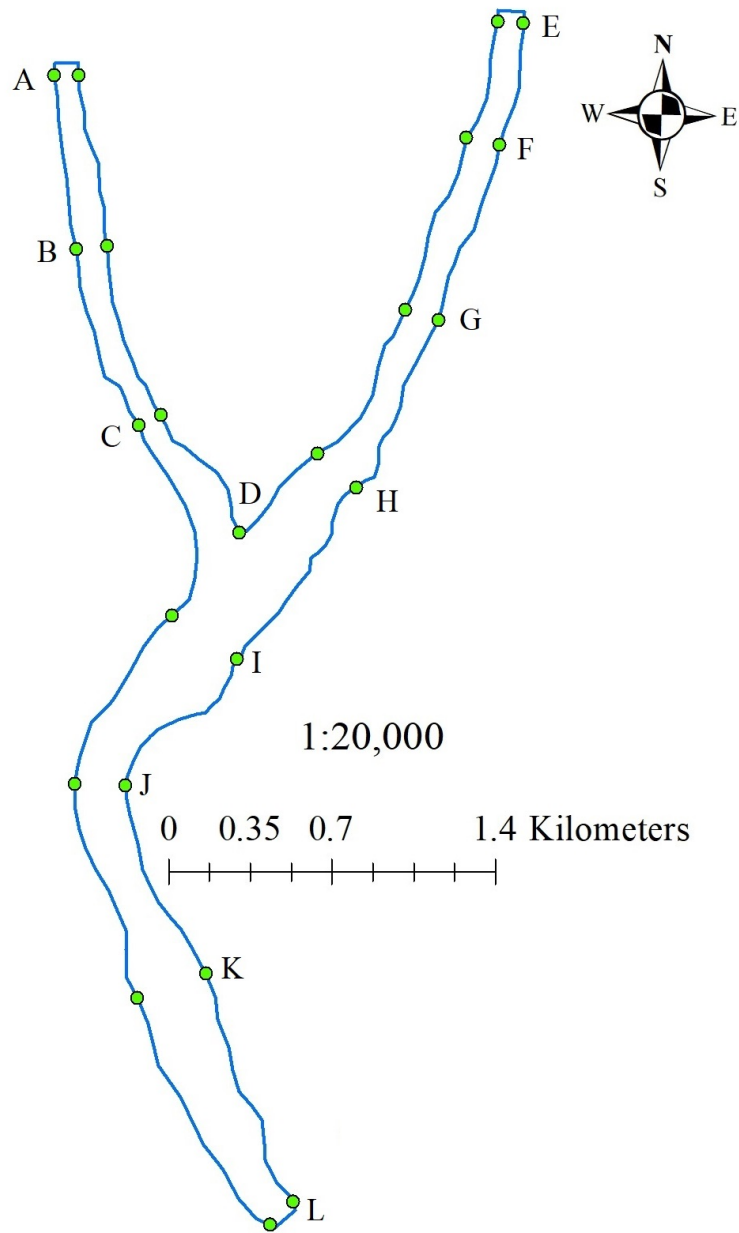


Figure 5. 4: Calculated coordinates of the left and right bank of each section on actual pattern of Confluence 1 during 2018

But Confluence 2 is more susceptible to change pattern than Confluence 1, which is shown in Figure 5.3. Following Figure 5.5 shows the position of calculated coordinates on actual Confluence 2 pattern in 2018. In this figure points shown as the calculated left and right bank coordinates of Section Q, are joined together with a line. This is simply to reduce the confusion of relative positions of the other coordinate denoting points.

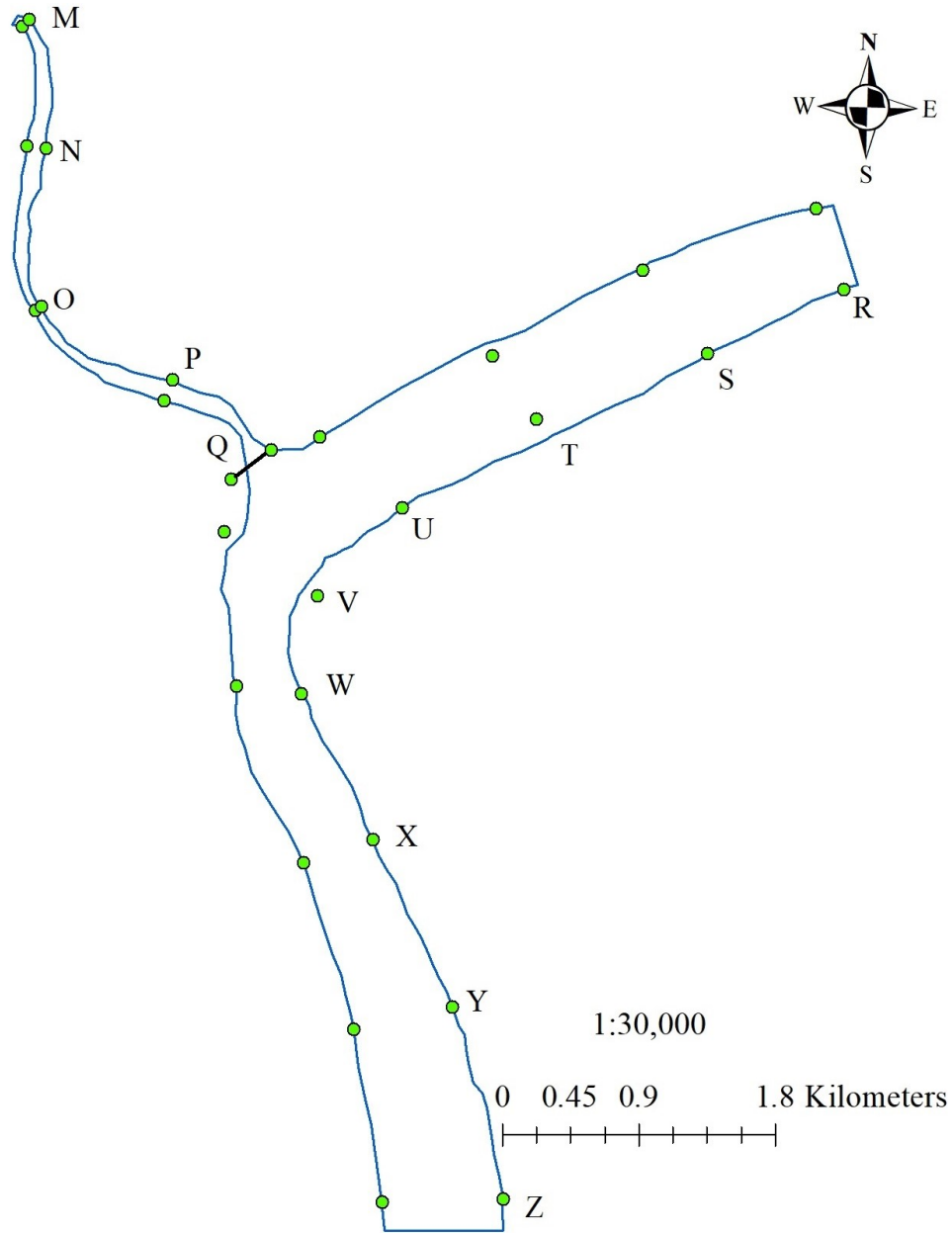


Figure 5. 5: Calculated coordinates of the left and right bank of each section on actual pattern of Confluence 2 during 2018

Figure 5.5 shows that calculated coordinates of the both banks of section T, V and left bank of Q, are failed to predict the actual position during 2018. As it is compared with other sections, then decisions can be made as it is not an error at all. Here left and right bank of Section M is shifted significantly, which is already shown in Figure 5.3. By this current method this shifted position is predicted perfectly. The reason of this miscalculation is human activities, which affects this natural shifting process. This calculation method considers the two confluences are under natural condition. Confluence 1 is situated at the center Khulna city, whose adjacent river's banks are

occupied by human activities for many years. So banks of the adjacent rivers are quite stable for different human usages like urbanization and industrialization. On the other hand Confluence 2 is situated in a rural area, which is urbanized now a day. The wrong prediction of Section T, V and Q is due to the recent urbanization process, took place surround the estuary, which makes the banks more stable to change their pattern (Figure 5.6). But calculation method over predicts the results, considering natural erosion and deposition rate of the adjacent river banks. In Table 5.1 the level of percent error of the calculated result to the actual data is represented.

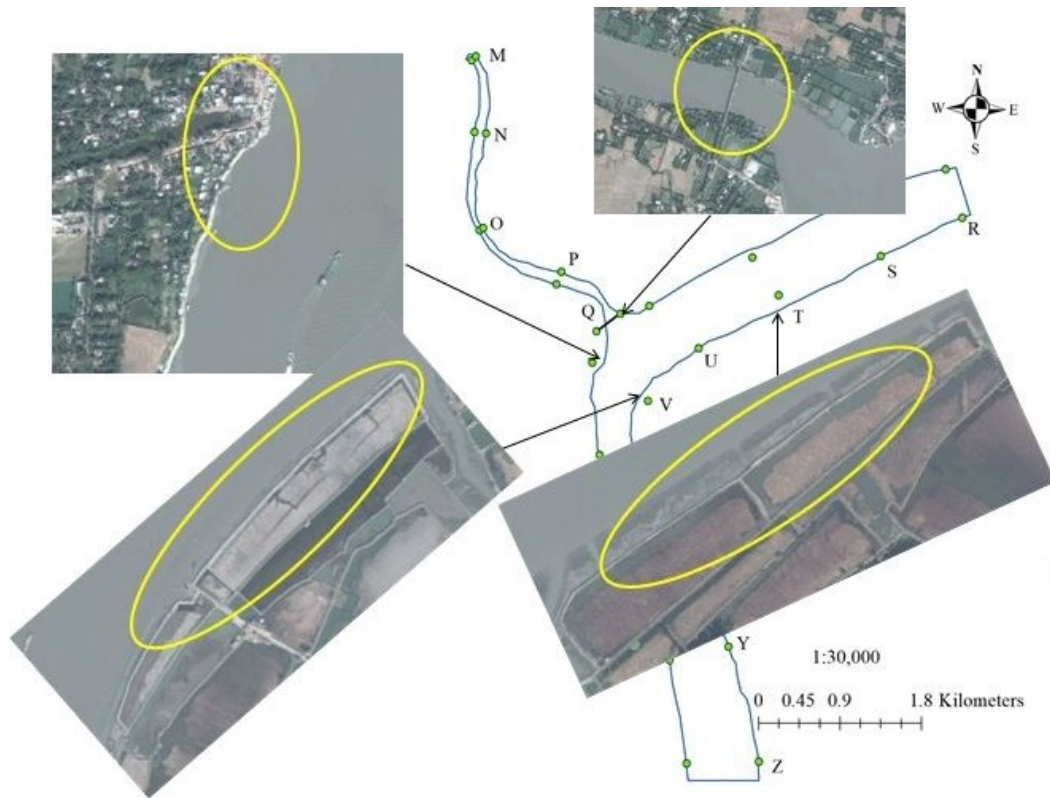


Figure 5. 6: Human activities around Confluence 2

Table 5.1: Actual, measured values and percent errors of coordinates of the sections (continued)

Cross section		Latitude (Left bank)	Longitude (Left bank)	Latitude (Right bank)	Longitude (Right bank)
A	Actual	22.86611	89.55078	22.86617	89.551807
	Measured	22.86608	89.55078	22.86611	89.55178452
	% error	0.000132	7.42E-06	0.000262	2.50982E-05
B	Actual	22.859445	89.551862	22.859659	89.553099
	Measured	22.859398	89.5518691	22.85954554	89.55314955
	% error	0.0002036	7.963E-06	0.000496312	5.64489E-05
C	Actual	22.852708	89.554587	22.853103	89.555477
	Measured	22.852647	89.5546317	22.85305984	89.55554471
	% error	0.0002691	4.9933E-05	0.000188852	7.56072E-05

Table 5.1: Actual, measured vales and percent errors of coordinates of the sections (continued)

Cross section		Latitude (Left bank)	Longitude (Left bank)	Latitude (Right bank)	Longitude (Right bank)
D	Actual	22.848686	89.558915		
	Measured	22.848562	89.558948		
	% error	0.0005412	3.6901E-05		
E	Actual	22.868621	89.569204	22.868619	89.570281
	Measured	22.868574	89.5692008	22.8685339	89.57026371
	% error	0.0002065	3.5804E-06	0.000372141	1.93029E-05
F	Actual	22.863325	89.567867	22.863082	89.569267
	Measured	22.864041	89.5680217	22.8637982	89.56941432
	% error	0.0031314	0.00017271	0.003132561	0.000164481
G	Actual	22.857358	89.565643	22.856994	89.567027
	Measured	22.857326	89.5656339	22.85697034	89.56704608
	% error	0.0001412	1.0172E-05	0.000103522	2.13056E-05
H	Actual	22.85174	89.562139	22.850479	89.563781
	Measured	22.851703	89.5621061	22.85043769	89.56377599
	% error	0.0001606	3.6692E-05	0.000180785	5.59031E-06
I	Actual	22.845363	89.556253	22.843733	89.558989
	Measured	22.845315	89.5562225	22.84368226	89.55895479
	% error	0.0002112	3.4014E-05	0.000222109	3.82025E-05
J	Actual	22.838737	89.552334	22.838708	89.554456
	Measured	22.838707	89.5523187	22.83869221	89.55444806
	% error	0.0001322	1.7058E-05	6.91204E-05	8.8638E-06
K	Actual	22.830587	89.555101	22.831575	89.557897
	Measured	22.830499	89.5551517	22.83150542	89.55799052
	% error	0.0003872	5.6656E-05	0.00030475	0.000104421
L	Actual	22.821852	89.560846	22.822802	89.56181
	Measured	22.821843	89.5608914	22.82274902	89.56181782
	% error	3.998E-05	5.0661E-05	0.000232133	8.73217E-06
M	Actual	22.767856	89.505476	22.76827	89.505933
	Measured	22.767798	89.5055306	22.76824625	89.50594802
	% error	0.0002539	6.0979E-05	0.000104319	1.67818E-05
N	Actual	22.760742	89.505964	22.760635	89.507228
	Measured	22.76072	89.5059745	22.76203219	89.50722579
	% error	9.705E-05	1.1758E-05	0.006138608	2.46561E-06
O	Actual	22.751003	89.506697	22.751231	89.507125
	Measured	22.750973	89.5067563	22.75121039	89.50715493
	% error	0.000132	6.6264E-05	9.05749E-05	3.34398E-05
P	Actual	22.745773	89.515135	22.74701	89.515639
	Measured	22.745794	89.5151444	22.74702236	89.5156771
	% error	9.048E-05	1.0516E-05	5.43307E-05	4.25662E-05
Q	Actual	22.741931	89.520527	22.743026	89.522059
	Measured	22.741217	89.5195797	22.74300308	89.52208063
	% error	0.0031376	0.00105821	0.000100766	2.41589E-05
R	Actual	22.758108	89.556806	22.753463	89.55862
	Measured	22.758099	89.5566795	22.75335588	89.55855532
	% error	3.994E-05	0.00014122	0.000470804	7.22162E-05

Table 5.1: Actual, measured vales and percent errors of coordinates of the sections

Cross section		Latitude (Left bank)	Longitude (Left bank)	Latitude (Right bank)	Longitude (Right bank)
S	Actual	22.754376	89.545676	22.749411	89.550033
	Measured	22.75421	89.5456376	22.74933759	89.54992933
	% error	0.0007311	4.2891E-05	0.000322676	0.000115767
T	Actual	22.749633	89.535659	22.744284	89.540076
	Measured	22.748898	89.5361211	22.74523348	89.53906588
	% error	0.0032299	0.00051612	0.004174569	0.001128125
U	Actual	22.743908	89.525321	22.73972	89.530471
	Measured	22.74385	89.5252014	22.73973583	89.53058448
	% error	0.0002538	0.00013355	6.96033E-05	0.000126753
V	Actual	22.737664	89.520102	22.735001	89.524532
	Measured	22.738081	89.5191922	22.73440325	89.52530953
	% error	0.0018333	0.00101635	0.002629214	0.000868512
W	Actual	22.729059	89.520165	22.728716	89.524338
	Measured	22.728966	89.5202475	22.72855974	89.5243904
	% error	0.0004109	9.22E-05	0.000687479	5.85316E-05
X	Actual	22.718606	89.524726	22.720089	89.52909
	Measured	22.718533	89.5247982	22.72003193	89.52918477
	% error	0.0003199	8.0664E-05	0.000251183	0.000105849
Y	Actual	22.708837	89.528264	22.710236	89.534517
	Measured	22.708742	89.5282737	22.71018646	89.53453413
	% error	0.000417	1.08E-05	0.000218161	1.91334E-05
Z	Actual	22.698584	89.530304	22.698902	89.538063
	Measured	22.69849	89.5303342	22.69884601	89.53808328
	% error	0.0004161	3.3724E-05	0.000246647	2.26527E-05

Based on this calculation method, a prediction is made to realize the future position of Confluence 1 and Confluence 2 in 2030. In this situation the confluences are considered in natural condition and change their pattern in a natural rate, similar to previous years. Figure 5.7 and 5.8 show the result.

From Figure 5.7, it is observed that, during 2030 Confluence 1 remains same in position. Point D at the apex of the delta slightly moves to the north. Left bank and right bank of every section is displaced slightly, especially section H and I. In case I left bank is eroded and right bank is deposited to a certain amount. Meanwhile right bank of I is eroded significantly.

In Figure 5.8, the futuristic condition of Confluence 2 is represented. Also, here coordinate points of left and right bank of Section Q are joined together to separate them from Section U and V related coordinate points.

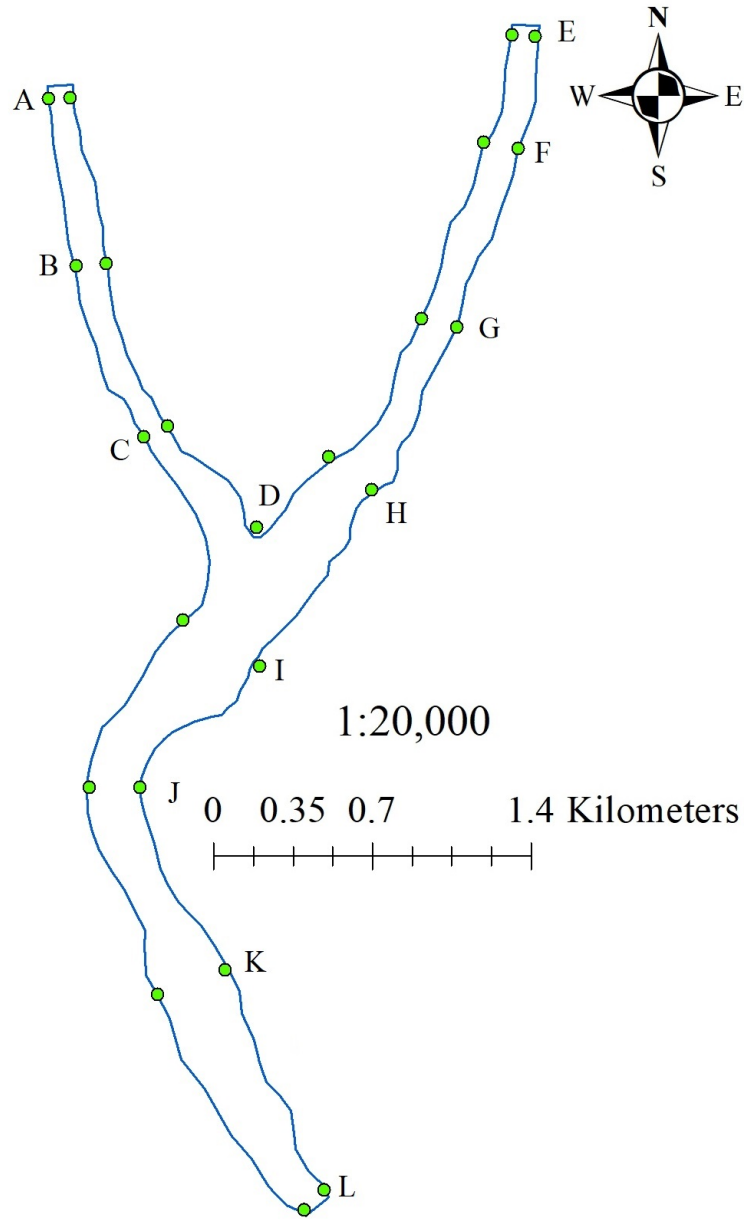


Figure 5. 7: Predicted coordinates during 2030 on actual pattern of Confluence 1 in 2018

In Figure 5.8 section M, Q, T, U and V show significant shifting characteristics. Shifting of T and V do not have any significance, as it is already observed in Figure 5.5. Again left bank shifting of Section Q is also predicted wrong. So it is important to observe the shifting process of Section M, U and right bank of Q. If the natural process is considered constant like 2018 till 2030, then shifting process of M and U, make the meander curve more acute than today. In case of Section Q, If the left bank will remain same in position, then shifting process of right bank will convert the branch estuary to a

narrow passage, even the branch may be died. The other sections are very less susceptible to change their pattern.

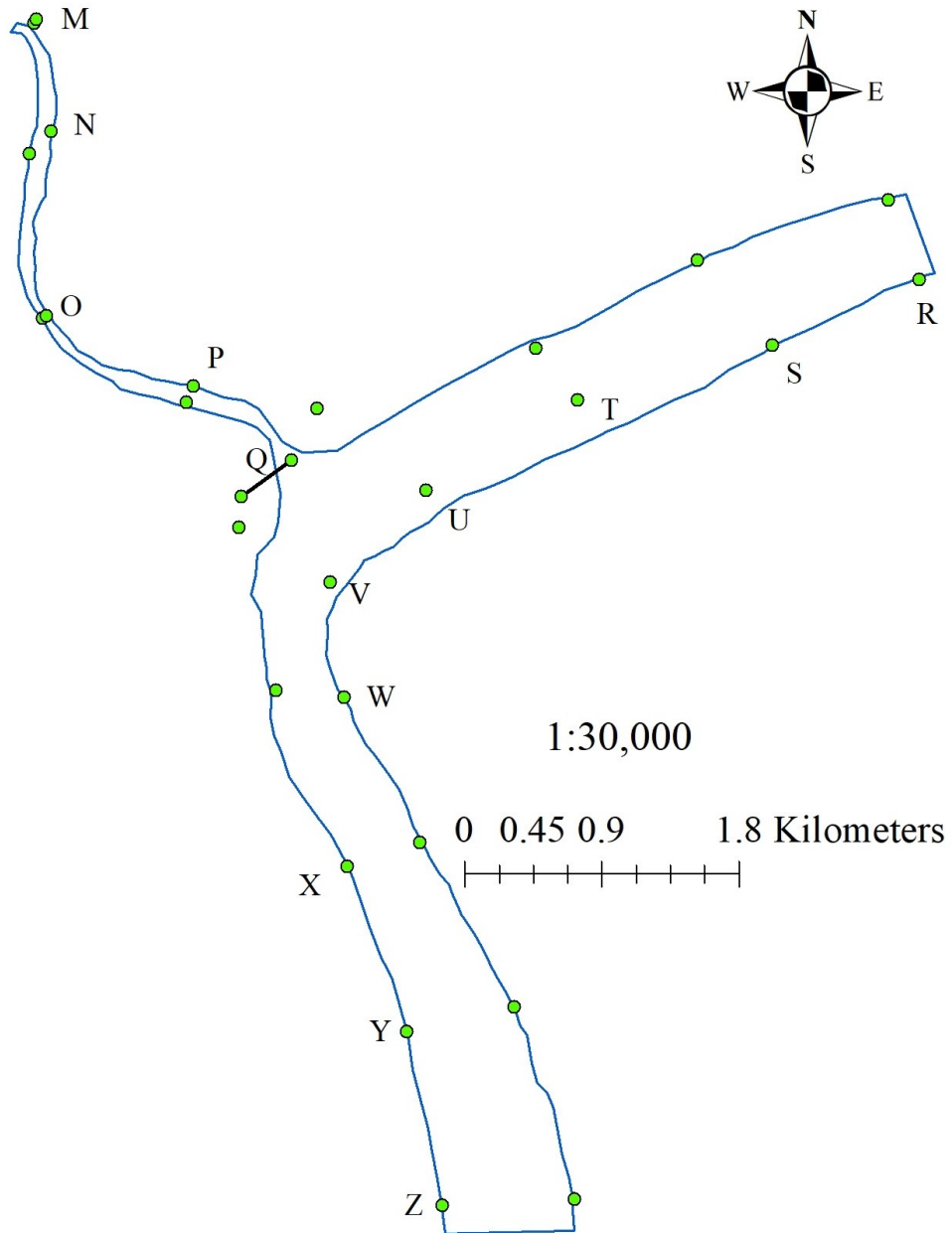


Figure 5. 8: Predicted coordinates during 2030 on actual pattern of Confluence 2 in 2018

5.5 Conclusion

From above analysis, following decision can be made precisely:

- Linear regression method can be applicable for the prediction of latitude and longitude, if the bank shifting process takes place linearly along a path. Thus a slope is developed from the simple Time vs. Latitude or Longitude graph and from the developed slope, coordinates of past and future can easily be calculated.
- In this process of prediction river bank is considered in natural state. If bank formation and shifting process is affected by human activities then the prediction method brings erroneous result.
- If the movement of the coordinates of bank is complex and non-linear in nature then this method is not applicable. In this situation more precise and complex solution method such as Machine Learning can bring more accurate result.
- In this method percent error is very small. That means calculated coordinate is very similar to the actual coordinate. But such a small difference can bring major error. Each degree of latitude is approximately 69 miles (111 kilometers) apart. The range varies (due to the earth's slightly ellipsoid shape) from 68.703 miles (110.567 km) at the equator to 69.407 (111.699 km) at the poles. Again a degree of longitude along the equator is exactly 60 geographical miles (96.54 kilometers), as there are 60 minutes in a degree. So small variation can be erroneous. Small time interval between the data collection can be more effective for prediction.

CHAPTER 6

Modeling of Land Surface Temperature (LST)

6.1 Introduction

Land Surface Temperature (LST) is one of the key parameters in the physics of land surface processes from local through global scales. It has a great influence on life cycle of plants and living organisms which play an important role to keep environment livable. Everyone should be careful about the changes of LST and regular observation is necessary. LST largely depends on vegetation, especially healthy vegetation, build-up or barren area and water body.

6.2 Study Area

The study area is the drainage basin (Catchment Area) of Atai-Bhairab-Rupsha river confluence which is an important place both for agriculture and trade in the south-western part of Bangladesh. The study area covers mainly Khulna district and some portion of Dhaka division. Mainly the center of the Khulna city is situated at the confluence area.

6.3 Resources and Techniques

For image analysis, different tools from ArcMap which is the central application of ArcGIS software have been used. The version of this software used in this study is ArcGIS 10.4.1. Total 27 years' time span is considered for study. Satellite images of different years such as 1991, 1996, 2002, 2006, 2011 and 2017 are downloaded from the website <https://glovis.usgs.gov/>. Landsat-5 TM images for years 1991, 1996, 2006, 2011; Landsat-7 ETM+ images for year 2002; Landsat-8 OLI and TIRS images for year 2017 at the middle of the February at UTM zone 46 are downloaded.

From May 31, 2003, Landsat-7 ETM+ images have a scan line fault, because on that day, Scan Line Corrector (SLC) in the ETM+ instrument failed, so the image data type is erroneous. Whereas there are some techniques to improve the quality of the images. In this study Landsat-7 images after 2002 are not used. SRTM 1 Arc-Second Global DEM is downloaded from the website <https://earthexplorer.usgs.gov/> to select the

drainage basin, as study area. Catchment area is selected from the DEM data; using basin delineation technique of ArcMap.

Area of the different land covers are determined from the number of pixels of the raster images represent different land cover. Each pixel of the images covers 30 square meters (except thermal images). So, number of pixels representing particular land cover is multiplied by 30 square meters and in this way total land cover area calculated. This is a type of unsupervised classification technique.

6.4 Governing Equation for LST and Other Indices

6.4.1 Normalized Difference Water Index

The Normalized Difference Water Index (NDWI) is a new method that has been developed to delineate open water features and enhance their presence in remotely-sensed digital imagery. The NDWI makes use of reflected near-infrared radiation and visible green light to enhance the presence of such features while eliminating the presence of soil and terrestrial vegetation features. It is suggested that the NDWI may also provide researchers with turbidity estimations of water bodies using remotely-sensed digital data. The NDWI maximizes reflectance of water by using green band wavelengths and minimizes low reflectance of NIR by absorbing maximum of wavelength . As a result, water features are enhanced owing to having positive values and vegetation and soil are suppressed due to having zero or negative values. Like NDVI its value also ranges from 1 to -1. Generally value higher than 0.5 denotes water body. The formula stands for NDWI is given below:

$$NDWI = \frac{VISG - NIR}{VISG + NIR} \quad (5.1)$$

where *VISG* is spectral reflectance measurements acquired in the visible green regions.

6.4.2 Normalized Difference Vegetation Index

Normalized Difference Vegetation Index (NDVI) quantifies vegetation by measuring the difference between near-infrared (which vegetation strongly reflects) and red light (which vegetation absorbs). NDVI always ranges from -1 to +1. But there isn't a distinct boundary for each type of land cover. For example, it has negative values, it's highly likely that it's water. On the other hand, if NDVI value close to +1, there's a high possibility that it's dense green leaves. But when NDVI is close to zero, there aren't green leaves and it could even be an urbanized area. Low positive values (approximately 0.2 to 0.4) represent shrub and grassland, high NDVI values (approximately 0.6 to 0.9) correspond to dense vegetation such as that found in temperate and tropical forests or crops at their peak growth stage.

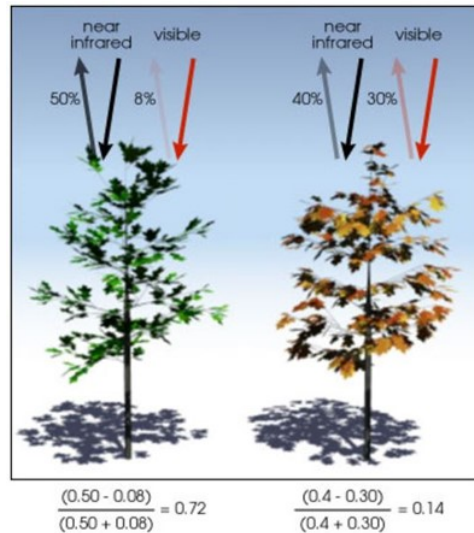


Figure 6. 1: Logic of variation of NDVI value due to vegetation health (courtesy NASA)

It also represents plant health as shown in Figure 6.1. In this figure a metaphoric example is represented, where healthy vegetation reflects 50 % near-infrared and absorbs 92% red light, while reflects only 8%. On the other hand if the plant is in unhealthy state like the condition during drought, absorbs more near-infrared (60%) and reflects 40%. Meanwhile it reflects much more red light (30%) than the absorption of near-infrared. According to Equation 5.2, the value of NDVI comes as 0.72 and 0.14 for healthy and unhealthy plant respectively. Again water body reflects more red lights. This is the main ethic behind NDVI analysis, to represent vegetation cover and its health.

The result of this formula generates a value between -1 and +1. If it has low reflectance (or low values) in the red channel and high reflectance in the NIR channel, this will yield a high NDVI value and vice versa. NDVI can be calculated by the following equation:

$$NDVI = \frac{NIR - VISR}{NIR + VISR} \quad (5.2)$$

where *NIR* is spectral reflectance measurements acquired in the near infra-red regions and *VISR* is spectral reflectance measurements acquired in the visible red regions.

6.4.3 Normalized Difference Built-up Index

The NDBI index was developed to analyze increments of reflectance on near infra-red regions and shortwave infra-red regions 1, for imaging urbanized and barren land areas. The researchers also observed that vegetation had a slightly higher or lower DN value on the same bands and that the minimum and maximum DNs in infra-red regions are much lower than those in shortwave infra-red regions 1 for the same land cover. From

this discovery, an index is developed to derive urbanized areas from TM/Landsat 5 or ETM+/Landsat 7 images or OLI/Landsat 8, as described by following equation:

$$NDBI = \frac{SWIR - NIR}{SWIR + NIR} \quad (5.3)$$

where *SWIR* is spectral reflectance measurements acquired in the shortwave infra-red regions.

6.4.4 Land Surface Temperature Calculation

During 1G-product rendering image pixels are converted to units of absolute radiance using 32 bit floating-point calculations. Pixel values are then scaled to byte values prior to media output. The following equation is used to convert DN's in a 1 G product back to radiance unit for TM and ETM+:

$$L_{\lambda} = \left(\frac{LMAX_{\lambda} - LMIN_{\lambda}}{QCALMAX - QCALMIN} \right) * (QCAL - QCALMIN) + LMIN_{\lambda} \quad (5.4)$$

Here L_{λ} is spectral radiance in watts/ (m²*ster*μm), *QCAL* is the quantized calibrated pixel value in DN, $LMIN_{\lambda}$ is the spectral radiance that is scaled to *QCALMIN* in watts/ (meter squared*ster*μm), $LMAX_{\lambda}$ is the spectral radiance that is scaled to *QCALMAX* in watts/ (meter squared*ster*μm), *QCALMIN* is the minimum quantized calibrated pixel value (corresponding to $LMIN_{\lambda}$) in DN, *QCALMAX* is the maximum quantized calibrated pixel value (corresponding to $LMAX_{\lambda}$) in DN

The following equation is used to convert DN's in a 1 G product back to radiance unit for TIRS:

$$L_{\lambda} = M_L * Q_{cal} + A_L \quad (5.5)$$

Here, M_L is radiance multiplicative scalling factor for the band (RADIANCE_MULT_BAND_n from the metadata), Q_{cal} is L1 pixel value in DN, A_L is radiance additive scaling factor for the band (RADIANCE_ADD_BAND_n from the metadata)

ETM+ Band 6 (thermal) and TIRS Band 10 and 11 imagery can also be converted from spectral radiance to a more physically useful variable. This is the effective at satellite temperatures of the viewed Earth-atmosphere system under an assumption of unity emissivity and using pre-launch calibration constants. The conversion formula is:

$$T = \frac{K2}{\ln\left(\frac{K1}{L_{\lambda}} + 1\right)} \quad (5.6)$$

T is brightness temperature (K), K_2 is calibration constant 2, K_1 is calibration constant 1

Proportion of vegetation P_v is determined by following equation:

$$P_v = \left(\frac{NDVI - NDVI_{MIN}}{NDVI_{MAX} - NDVI_{MIN}} \right)^2 \quad (5.7)$$

Land surface emissivity e is determined by following equation:

$$e = 0.004P_v + 0.986 \quad (5.8)$$

Land surface temperature LST ($^{\circ}C$) is determined by following equation:

$$LST = \frac{T}{1 + \frac{wT}{p} \times \ln(e)} - 273.15 \quad (5.9)$$

where w is wavelength of emitted radiance (μm), $p = hc/s = 1.438 \times 10^{-2}$ mK, h is Planck's constant (6.626×10^{-34} Js), s is Boltzmann constant (1.38×10^{-23} J/K), c is Velocity of light (2.998×10^8 m/s)

6.5 Result and Discussion

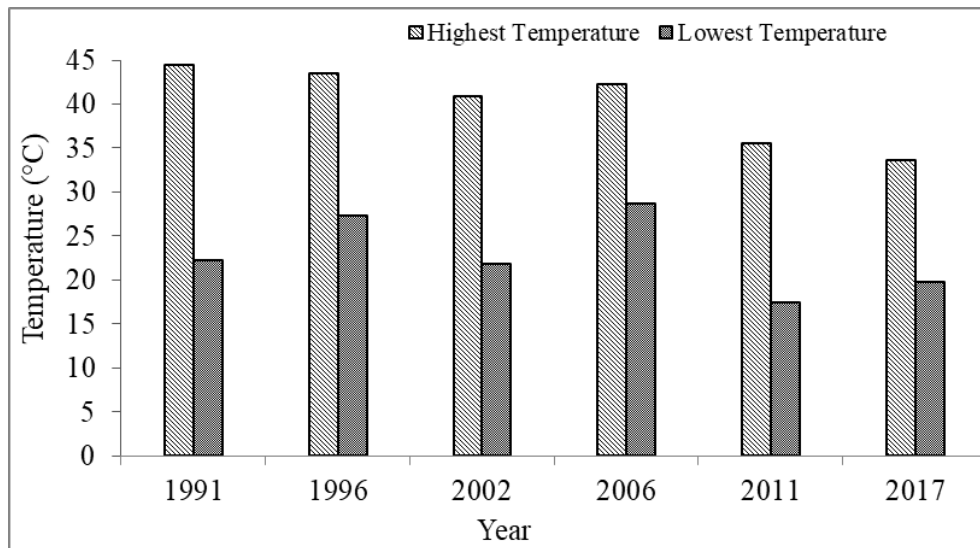


Figure 6. 2: Highest and lowest temperature of the study area in year 1991, 1996, 2002, 2006, 2011 and 2017

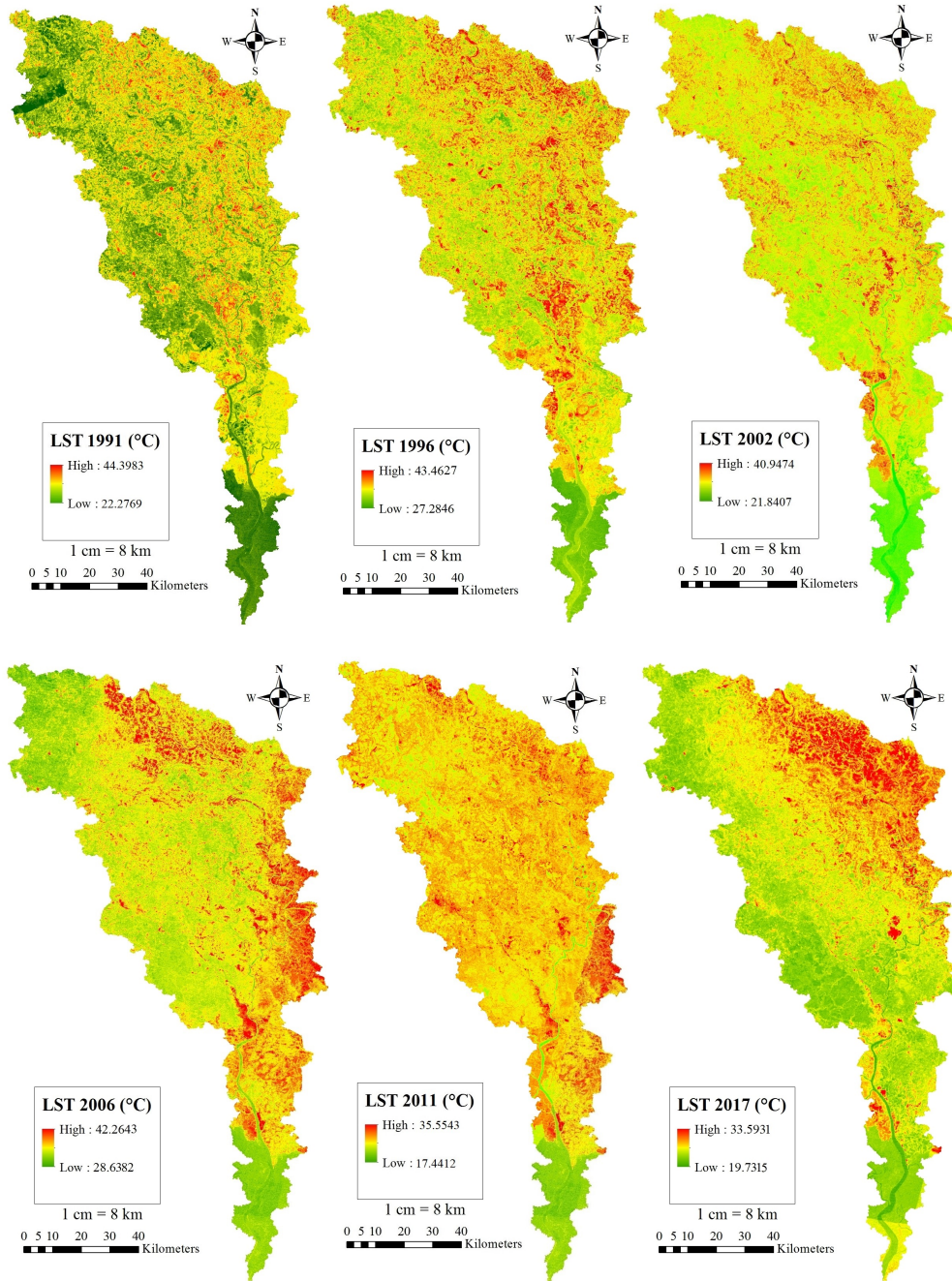


Figure 6. 3: Spatial distribution of temperature variation at study area in year year 1991, 1996, 2002, 2006, 2011 and 2017

From Figure 6.2, graphical representation of temperature variation is represented, where value of the specific temperature and its position is clearly observed. And in Figure 6.3, spatial distribution of highest and lowest temperature in the year 1991, 1996, 2002, 2006, 2011 and 2017 is observed. Figure 6.2 and Figure 6.3 represent that during year 1991, 1996, 2002 and 2006 highest LST is almost same. In these years lowest LST varies from 22.2769 °C to 28.6382 °C. In 2011 and 2017, highest and lowest LST drops dramatically, as can be compared with other four years. This is very

difficult to understand, the reasons of this temperature drop, as global temperature increases day by day. But in this study Land Surface Temperature (LST) is studied, rather than atmospheric temperature. LST is an important factor, which is influenced by different local parameters and influences local bio-diversity.

In the later study the reasons of dropping temperature will be clear, in the years 2011 and 2017, after studying NDVI, NDWI variations barren area coverage and their relation with LST. In Figure 6.4 according to the NDVI study, area covered by vegetation and other features is represented. Whereas in Figure 6.5 according to NDWI study, area covered by water-body and other features and in Figure 6.6 according to NDBI study, area covered by build-up and barren areas and other features is represented.

Figure 6.4 shows that, vegetation cover during 1991 and 1996 is reduced in size in 2002 and again it increases gradually to a maximum range at 2017, almost equal to other type of covering. But from Figure 6.5, it is clear that the lost area of vegetation covering in 2002 is partially replaced by some type of water logging. Because Figure 6.5 shows that, during 2002 area of water body is greater than 1996. And in 2017, area covered by water body and other features shows near same result as 1996. So during 2002 increase of water covering area is not a stable natural or man-made water body but some type of temporary water logging.

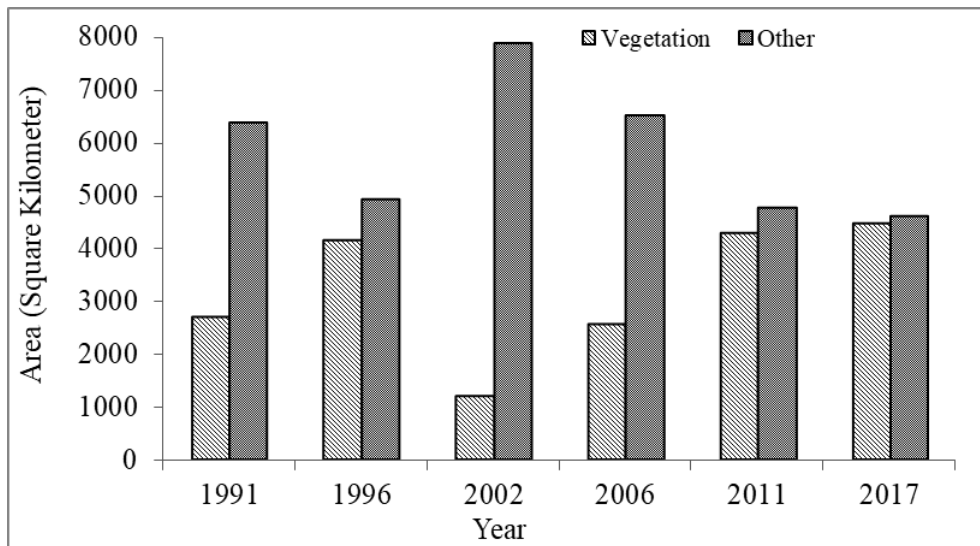


Figure 6. 4: Surface covered by vegetation and other type of features according to NDVI

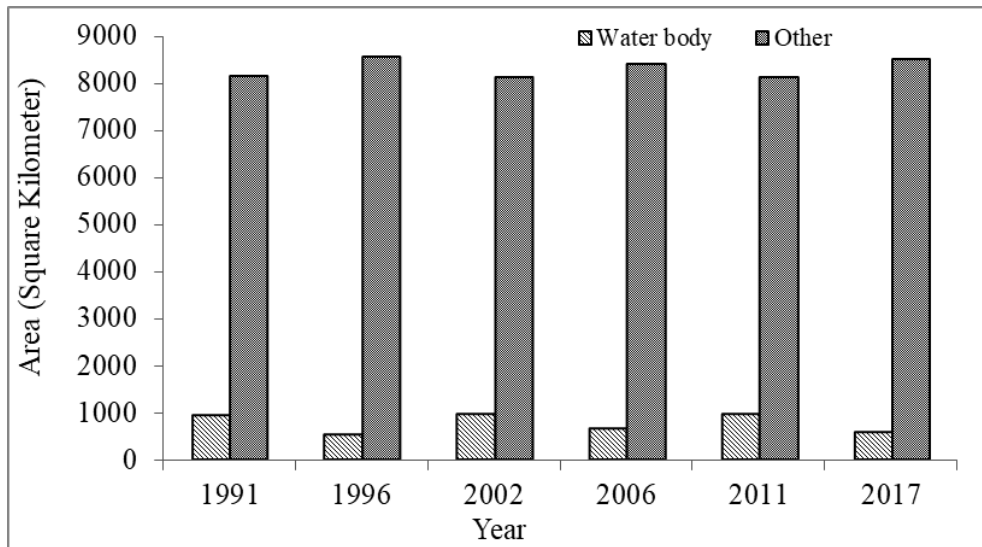


Figure 6. 5: Surface covered by water-body and other type of features according to NDWI

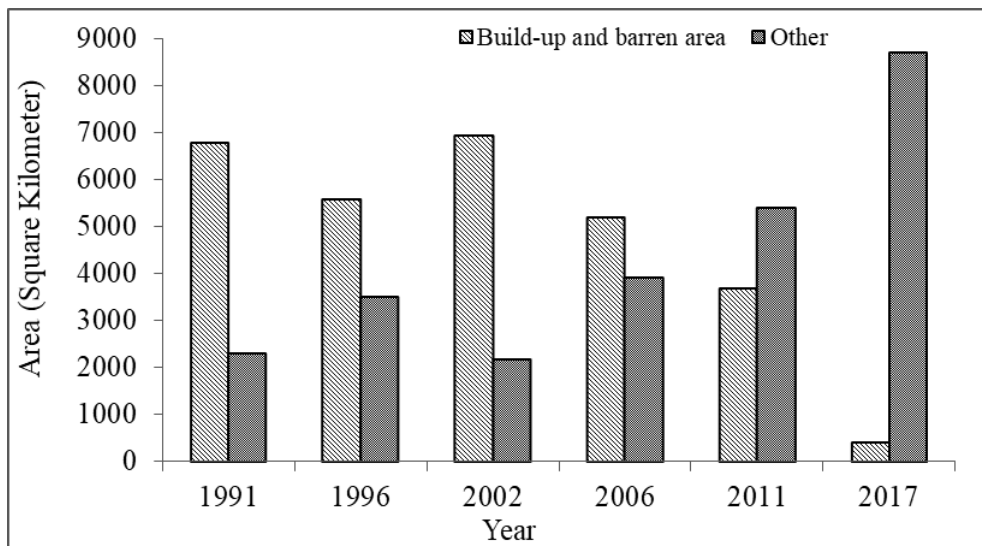


Figure 6. 6: Surface covered by build-up and barren area and other type of features according to NDBI

From Figure 6.6 the scenario of area covered by urban region and barren land is visualized. NDBI is such an index which highlights both urban and barren land area at a same time. Figure 6.6 shows that from 1991 to 1996 especially barren area (because urban area always increasing) slightly replaced by different features like water body or vegetation. In 2002 barren area again regain the same area as 1991. Then the barren area gradually losses the quantity during 2006 and 2011 time period. But in 2017, barren area is dramatically reduced and covered by other type of features like water body or vegetation. In the current situation, basically developed urban area is not reduced, which means the barren area is replaced.

From Figure 6.5 it is certainly observed that water body is not increased remarkably from 1991 to 2017. But in Figure 6.4, it is observed that vegetation cover is increased at a significant amount. Whatever during 2002, vegetation cover is reduced significantly. The possible reason may be excess drought condition, when small plants are less likely to survive. So from the above discussion it is clear that reduced barren area is replaced by mainly vegetation cover. Obviously some of the barren area is replaced by urban area. In NDBI analysis barren area cannot be separated from urban area. So amount of area of barren land is replaced by urban region, cannot be defined here. But from Figure 6.6, obviously rest of the amount of build-up urban area and barren land covers during 2017 is mainly urban region.

Figure 6.7 clearly shows the chronological replacement of barren area by the vegetation. Here also rapid increment of urban area is observed but vegetation covered area dominates the urban area increment. From this RGB true color image it is found that, during 1991 near the bank of the rivers and canals, dense vegetation is being found. Also greenness of this vegetation represents healthy state, which brings high NDVI value is represented in Figure 6.8. Except bank area other portion of the land area represents barren area visibly. This barren area is gradually replaced by land cover of more greenness in 2017, which represents vegetation. Presently barren area is occupied all through the year due to advanced and efficient irrigation system. So barren area may be said to be replaced by crop field mainly.

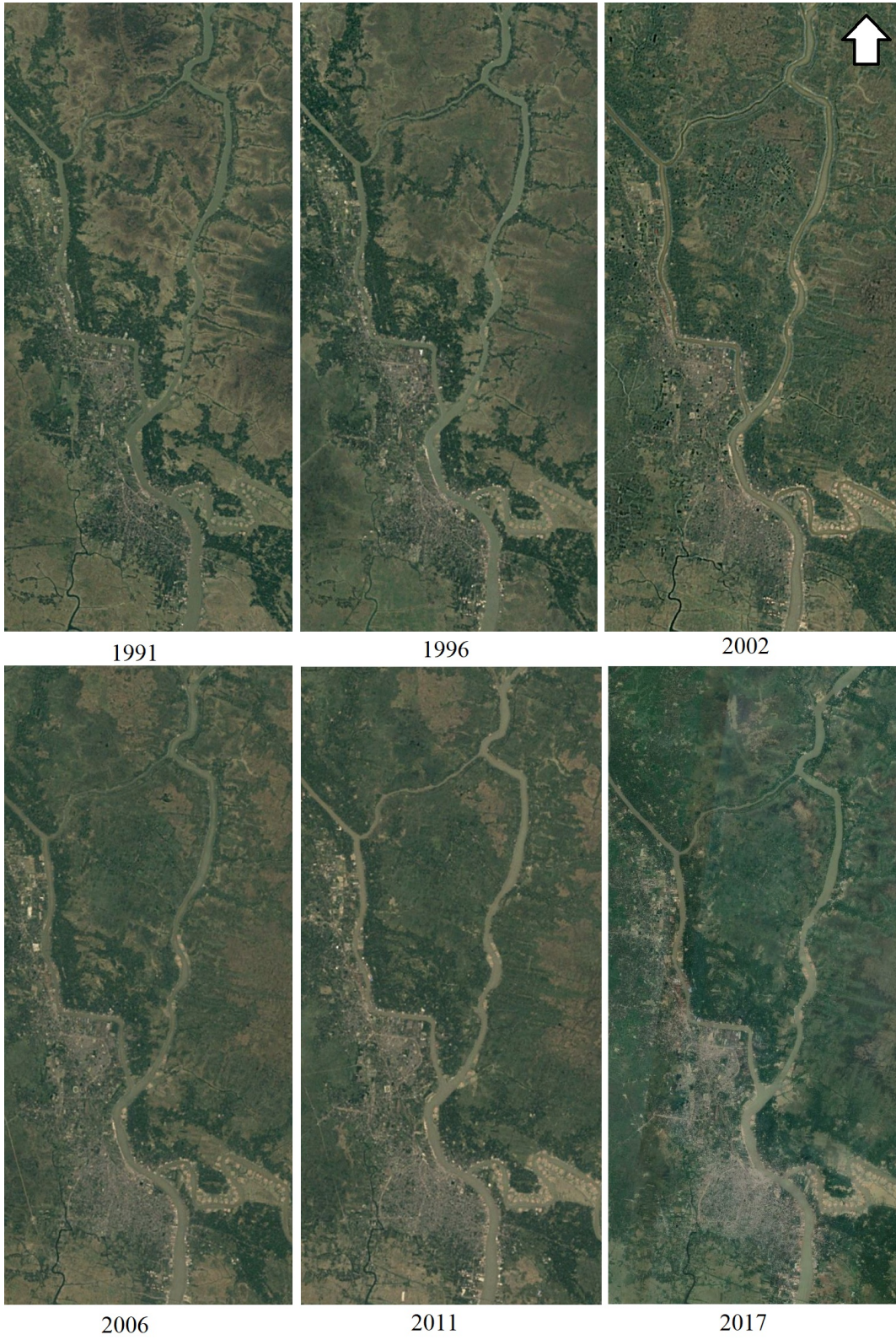


Figure 6. 7: Chronological conversion of barren area to vegetation covered area

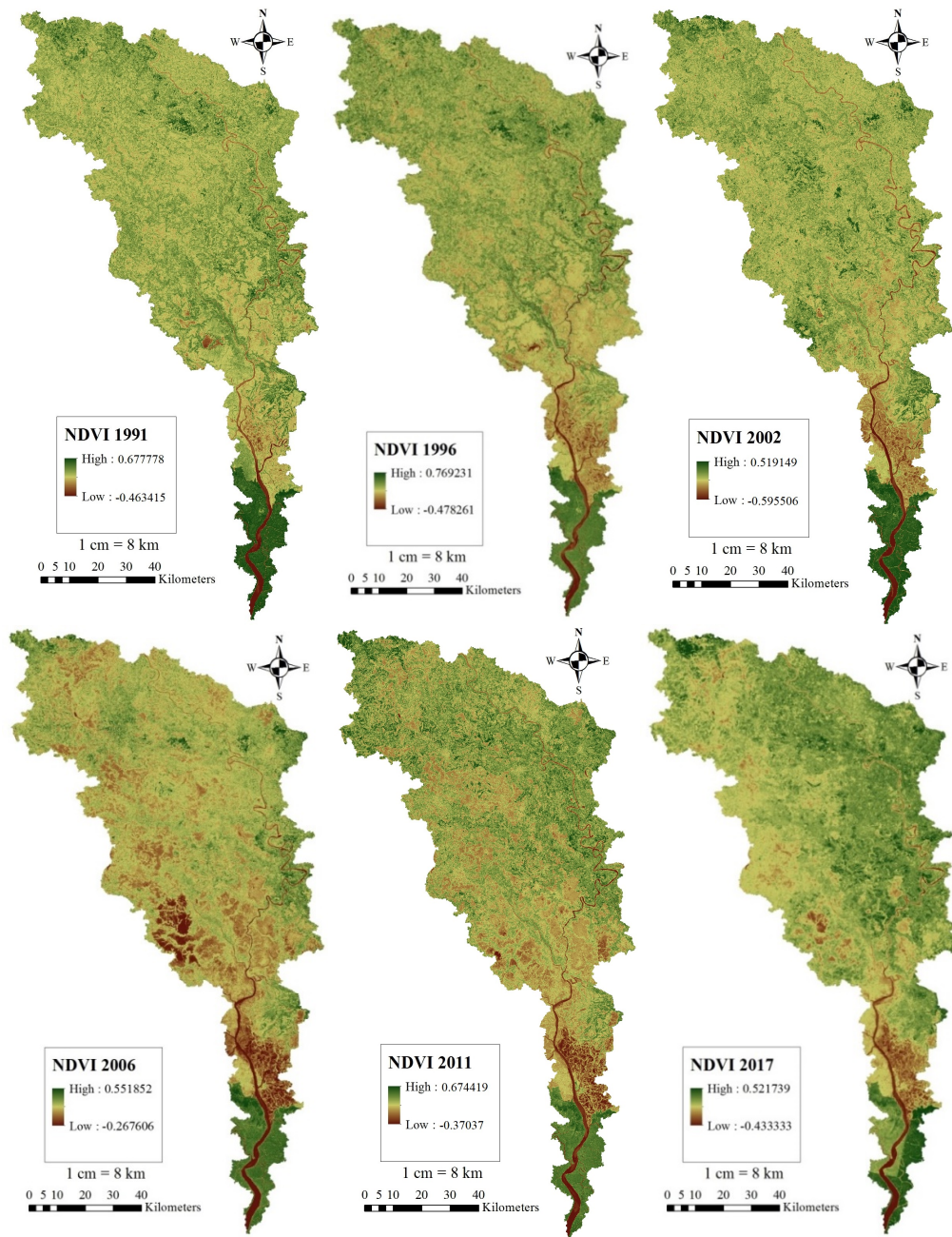


Figure 6. 8: Highest, lowest value of NDVI and spatial coverage of vegetation during 1996, 2006 and 2017

Figure 6.8 shows the NDVI value ranges in the study area in year 1991, 1996, 2002, 2006, 2011 and 2017, also the spatial distribution of vegetation cover. Here vegetation cover (green color) of 2017 shows maximum coverage than other years. But 1996 shows the highest NDVI value (0.769231), second lowest (0.677778) is in 1991 and 2017 has the lowest (0.521739) value, almost similar to 2002 (0.519149). NDVI value greater than 0.6 represents healthy vegetation, large tropical forest or tree and lower positive value means small bush like or unhealthy vegetation. Figure 6.7 shows that open barren area of year 1991 and 1996 along the river and canal bank is reduced by

crop field in 2017. This is why vegetation cover in 2017 is higher than 1991 and 1996 but NDVI value is lowest than other years (except 2002). One of the causes of reduced NDVI value in 2017 may be gradual increment of salinity in the southern part of Bangladesh and the study period is a dry season, which triggers the unhealthy condition of vegetation.

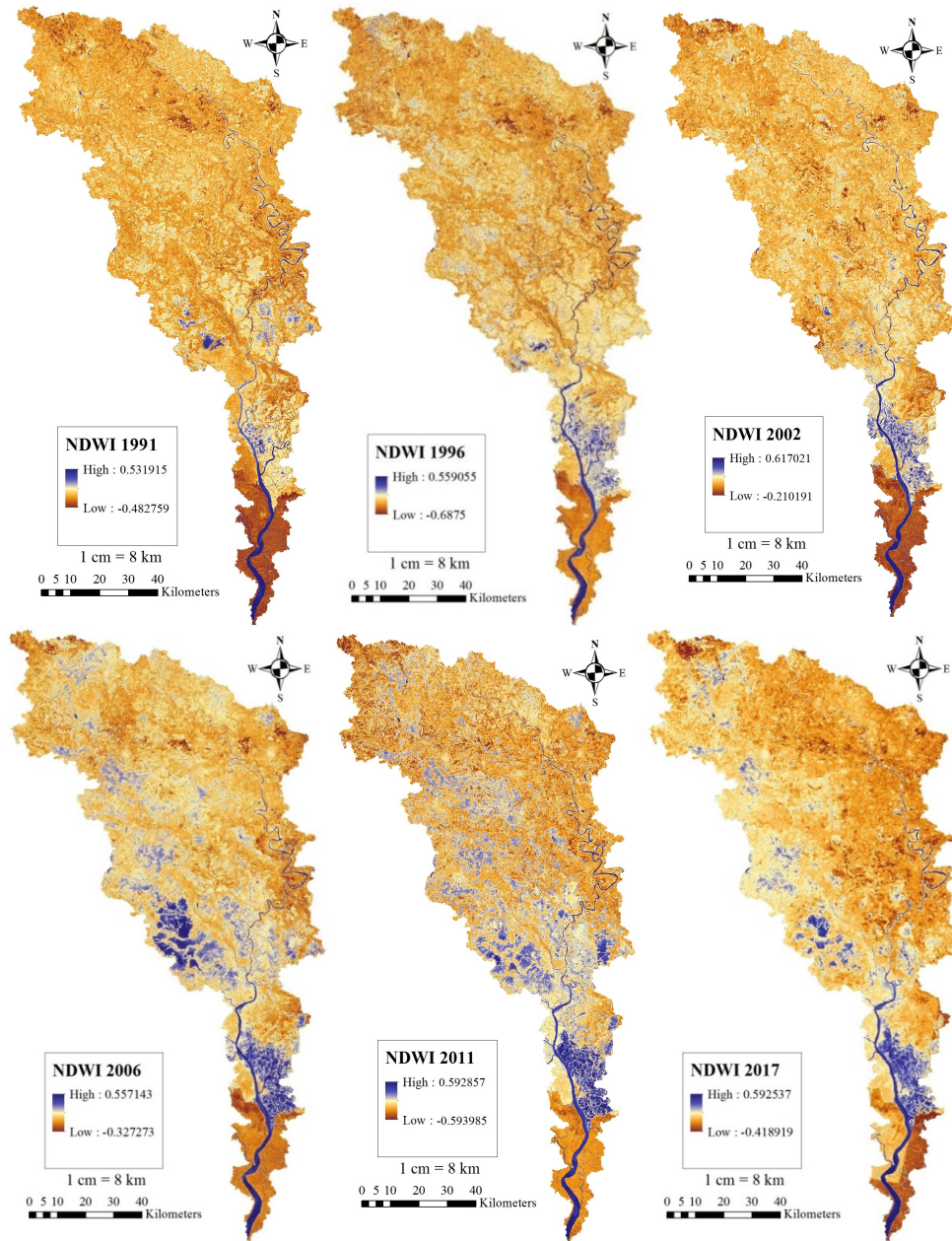


Figure 6. 9: Highest, lowest value of NDWI and spatial coverage of water body during 1996, 2006 and 2017

Figure 6.9 shows the spatial distribution of water body and value range of NDWI in year 1991, 1996, 2002, 2006, 2011 and 2017. NDWI value larger than 0.5 denotes the water body. Here every highest value of all these years is greater than 0.5.

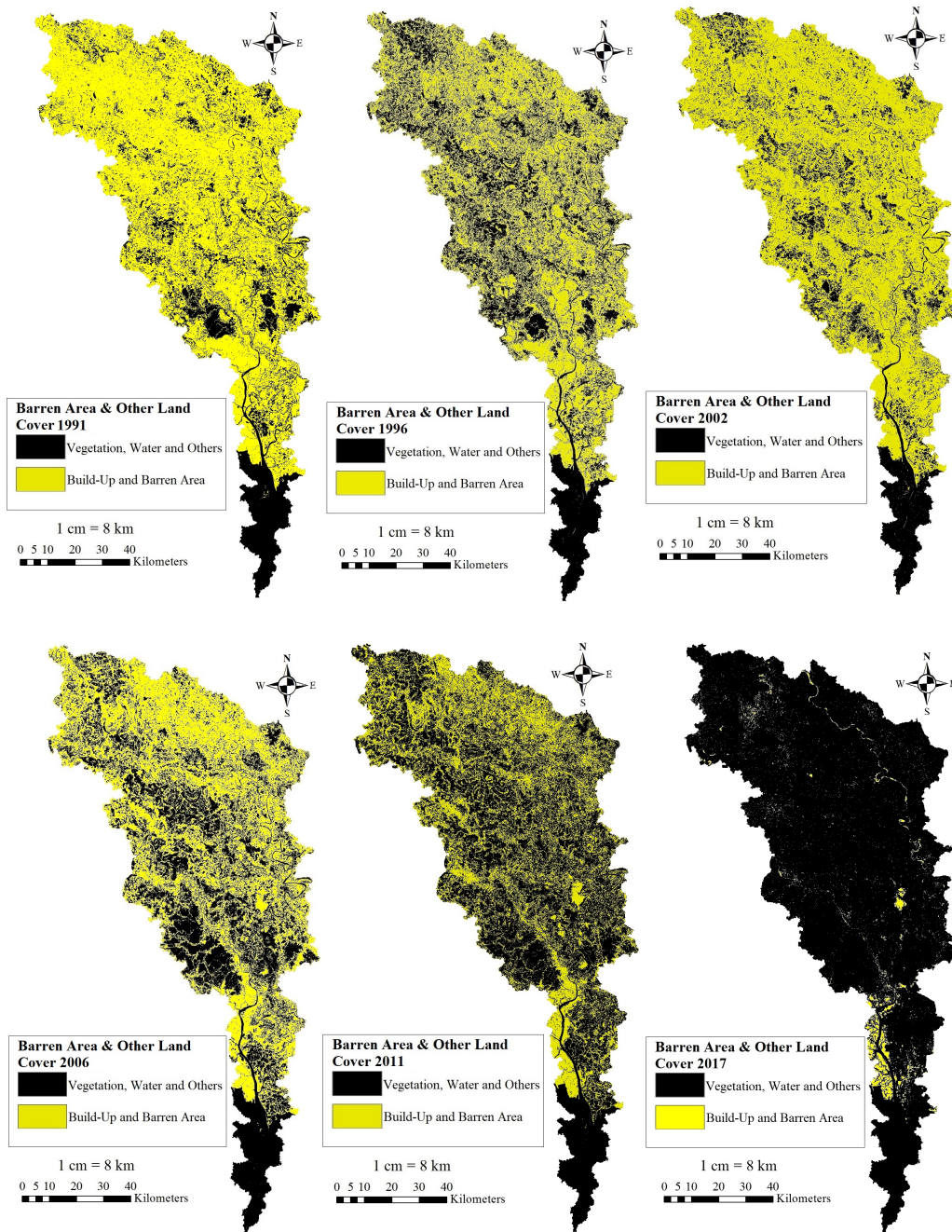


Figure 6. 10: Spatial distribution of build-up and barren areas and other type (vegetation, water) of coverage during year 1996, 2006 and 2017

Figure 6.10 shows the build-up and barren areas, as well as the other vegetation and water body type coverage. Result observed from Figure 6.6 is clearly visualized in Figure 6.10, here year 1991 and 2002 show almost same result but year 2017 shows

something different. If Figure 6.10 is compared with Figure 6.8 and 6.9, then it is clear that the black colored area in Figure 6.10 actually vegetation and water body covered area. So in the previous study years most of the area is covered with barren and build-up urban region, which is colored yellow in figure. But in 2017 most of the barren area is replaced by vegetation. Only south-western corner shows the build-up and barren area mainly. It is pretty sure, that zone is mainly build-up urban region because Khulna city and Mongla port are situated in this region along the Rupsha and Pasur river bank. The vegetation covers the barren area in 2017 is mainly crop field, which is clearly understood from the highest value of NDVI at Figure 6.8, in 2017. Some portion of the dense mangrove forest (Sundriban) is also situated in the southern side of the study area, which should bring higher NDVI value in 2017. But due to drought condition of the middle of February and probably the salinity, causes water stresses in the mangrove forest, which triggers low NDVI value in 2017.

From all the discussions above, the reasons of LST drop in 2017 can clearly be understood. From Figure 6.2 and 6.3, it is observed that highest LST in year 1991, 1996, 2002, and 2006 is near to each other and lowest LST ranges from 21.8407 °C to 28.6382 °C. But in 2017 both highest and lowest LST drop, as compared with 1991, 1996, 2002 and 2006. From above NDVI, NDWI and NDBI study, it is observed that NDWI has no significant effect on LST change. Because in Figure 6.9, highest values of NDWI in the study years are almost same to each other and every time these are greater than 0.5, means water body. Figure 6.5 shows the area of water body in 2006 is almost double in amount than 1996 and 2017 and this area during 2017, slightly increases than 1996. But LST of 2006 is almost same to 1996 and significantly higher than 2017. So neither LST of 2017, nor 1996 is related with LST of 2006, in the point of view of NDWI. The dominating factor controlling LST is NDVI, which is observed in previous discussion. From Figure 6.4 it is observed that vegetation cover is maximum in year 2017, whatever most of the vegetation includes grassland and crop field. Figure 6.6 shows the reduced condition of barren and urban area, which is actually replaced by crop or grassland that is already mentioned before. Again Figure 5.7 and 5.10 shows the present condition of the barren land area.

At present urban area is increasing gradually. In this study area, urban region is very small in size. Most of the area belongs to barren area, crop field, bushes, marsh land, water body and mangrove forests. Barren area without any covering, like vegetation, acts like desert. In a desert area temperature variation is observed in a massive amount. In a desert, temperature rises at a maximum level during day light and at night it drops in a minimum level and maximum variation of day and night time temperature is being observed. Also this study shows that, when maximum area is covered by barren land during 1991, 1996, 2002 and 2006, then LST is also maximum. Figure 6.6 and 6.10 show the same result and spatial distribution of barren and urban area during year first four study years and in this two year value of LSTs also same. And in year 2017 most of the barren land is covered by small vegetation and also LST drops, it means vegetation plays an important role for dropping LST in the study area. Recent years,

cultivation in a land property increases significantly. At the very past time generally rice produced once in a land property which was increased two times a year. Now a days extended use of fertilizer and irrigation increases the production of a land area. Which means, in Bangladesh some of the land area produces crops three times a year, even in dry season with the help of irrigation. This is the only reason of converting barren land area to a crop land in 2017, which is mainly responsible for dropping LST in the study area.

6.6 Conclusion

From above analysis, following decision can be made precisely:

- Land Surface Temperature (LST) may be slightly affected by the water body but this effect is not major over time. Because area of large water body changes very slowly.
- LST increases due to bareness of soil as well as the urbanization process.
- LST can be kept in a reasonable state by increasing vegetation area.
- Even if the vegetation is small bush type or large vegetation under draught condition, it will be more affective to reduce LST than an uncovered bare soil.

CHAPTER 7

Summary and Discussion

7.1 Introduction

The modeling of morphological behavior of a river network is very complex to understand and also very time consuming. In this study an attempt is taken to develop a model that is more user friendly and less time consuming. Modeling the flow nature in a meandered river, especially in a confluence needs more attention during considering the type of variables affects the flow. For example beside bed resistance, transverse shear stress secondary current also plays an important role to distort the primary flow pattern. This secondary current creates a three dimensional effect in the river flow, especially in the confluence zone. This study does not consider this parameter during modeling confluence. It's a disadvantage, but it simplifies the model to understand. This study also represents a model of the changing land surface pattern of the catchment area. Modeling a morphological pattern of the river with the environmental condition of its catchment area is helpful for predicting the future of it and taking engineering decision.

7.2 Summary of the study

Morphological modeling considering environmental terms of the catchment area brings more perception on river networks with its catchment area.

7.2.1 Morphological Model

River channel meander is very common in nature and turns to an acute condition which hampers both efficiency and length of navigation. After a long meandering process, a river becomes so shallow and sinuous that it loses its reservoir capacity and navigation quality. For this reason, frequent floods occur in the catchment area during the rainy season and drought comes during rainy season. Lack of navigation efficiency also affects local economies. A meandering process actually occurs due to natural erosion and deposition process. So modeling of a natural channel meander can be helpful to understand the morphological behavior of the channel.

In the present study three parts of a natural meandered river are studied to understand its natural characteristics. Different important variables like secondary flow model, transverse shear model etc. also considered. Consideration of a fixed discharge is totally hypothetical in this case, because this river is under tidal influence. This hypothesis are only considered for ease of calculation. More sophisticated result can be come out by considering variable discharge and more accurate data of frequently changed channel roughness. Bank side different local structure, their foundation and hydraulic structures prevent local scouring, but these structures hamper the natural flow process, which brings inaccuracy during modeling. Considering these types of variables also bring more accurate result. During the field survey, real time variables like wind effect should be considered for accurate data.

Total length of the river also simulated under high-tide and ebb-tide condition. When total length of the river is simulated in part, some values of the different variables such as velocity magnitude, Froude number seems over predicted. This over predicted value is not practical for natural river. But simulation of the total length brings more convenient result than part. But considering total length brings more complexity and time consumption. For this reason more powerful computer is required. Flow condition initialization before starting simulation may reduce unnecessary complexity.

The morphological behavior of a confluence is very difficult to understand in practical cases. It is very easy to develop a numerical model of a laboratory made experimental work from prototype. Because in a laboratory, number of variables that affects the result, actually very low in number. Moreover it very easy to execute the experimental work in a controlled environment. But in a natural condition variables are huge in number as compared with laboratory. If it is assumed in the point of view of channel roughness, then it is considered only one value of the Mannings roughness coefficient, which is appropriate for laboratory experiment. But if it is a natural condition, then channel roughness can be changed very frequently along its length of the channel. This tiny change can bring huge effect on result of modeling. Also there are other variables may arise like wind effect, variable bottom elevation, gravitational anomaly, variable width etc. In the above study an attempt is made to understand the complex flow characteristics in the natural confluence. An important variable like secondary flow is not considered here. Moreover these confluences are also under tidal influence, so fixed discharge also brings difference in result.

Modeling the shifting nature of river confluences is an important task to predict the future of the river bank habitats as well as the river's condition itself. This prediction requires a large amount of data, whose accuracy is largely depends on the human perception, because it is collected by human measure. Also this prediction may be distorted by current human activities, which alters natural shifting process. Considering more variables, which affects this alteration may produce more accurate data for prediction.

Results come from the modeling are not absolutely incorrect, but considering more sophisticated variables can bring more complete results. In real life, for modeling a natural prototype, practical field survey is really convenient for better modeling. It brings more accurate result, if a physical model is developed in a laboratory according to geometric similarity and result obtained from developing physical models recreated again numerically. Different real time variables like wind effect may affect the field survey data, which must be calibrated in the laboratory environment.

7.2.2 Spatial & Environmental Model

Land surface pattern of a catchment area changes very frequently. Especially urban and industrial domains are generated very frequently near the bank of the river. Besides river also feeds crop fields by supplying water for irrigation. Also mangrove type forest is grown near the bank of the river. So ecosystem of a catchment area is very complex and vulnerable in nature. Simple change of the land surface pattern can bring destruction of the ecosystem. So regular monitoring of alteration of local environmental parameters can be helpful for advance predictions of local and global environmental impact. Local environmental parameters mainly include level of urbanization, area and health of vegetation, amount of water body and especially land surface temperature. Land surface temperature can affect local ecosystem and generate a chain reaction for future anomaly. If the variable like land surface temperature can be linked with other variables like area of vegetation and urbanization, then monitoring of environmental anomaly can be effective.

In this present study, an attempt is taken to correlate land surface temperature, vegetation, water body and urban area with each other. Here satellite image is processed by software mainly using its reflectance value of different spectrum. Error is very common for ground haze and cloud. Different tools of the software are used to make the result more accurate. In this study both Landsat 5 and 7 images are used because both of two types of images are 8 bit type, which is most likely to each other. There is defect called scan line fault present in the Landsat 7 image, which is minimized to an at least limit by averaging the pixel value around the no-data region.

7.3 Conclusion

Bhairab, Atai and Rupsha River catchment area is commercially very important for the Khulna region. Modeling spatial characteristics such as meander and channel junction of these three rivers is very important task. The simulation of such a model which represents time dependent variation of the river's spatial characteristics, really helpful to understand the physical appearance of the river. From the model, value of velocity magnitude helps to predict the probable place of siltation in a meander or near the estuary of a junction. Also modeling such a spatial characteristics for certain duration helps to predict the navigability of the river.

Numerically developed confluence model of these rivers is very cheap to find out the zones most likely to be silted, thus navigation hampered. Also this modeling helps to find out a possible solution to reduce siltation or places are needed to be dredged regularly. Moreover, this type of modeling helps navigation more functional.

Environmental change as well as habitat change study reflects the spatial condition of the local area mainly depend on the river system. Studying the land cover change with time compared with indicator like LST which reflects a local environmental scenario, helpful for predicting future environmental hazard. Furthermore, this study helps to take necessary preventive measure to keep environment favorable for living.

7.4 Recommendation for Future Study

- Fixed discharge is considered, during modeling the flow pattern in meander. In future consideration of exact variable discharge can be helpful for modeling true nature of the river.
- Sediment budget can be an important parameter for modeling in this study area.
- Study on siltation process near the branch estuary in the channel junction can be helpful to predict the navigability.
- Secondary current is not considered in this study during modeling flow pattern in confluence. This is an important parameter that creates three dimensional effect near the estuary. In future consideration of this parameter can bring more convenient result.
- Actual prediction of the river shifting process needs more variable to consider for better result. In future considering urban area and vegetation near the river bank during calculation can be taken into account.
- The error is very certain to realize levels of urbanization during modeling combined barren and urban area. Separation of urban area from barren area can bring a clear understanding on urbanization.

References

- Ahmadi, H., & Nusrath, A. (2010). Vegetation change detection of Neka River in Iran by using remote-sensing and GIS. *Journal of geography and geology*, 2(1), 58.
- Ashari, A. A., Merufinia, E., & Nohani, E. (2015). Numerical investigation of velocity profiles in the lateral intakes using finite-volume method and comparison with experimental results in water distribution networks. *Aquaculture, Aquarium, Conservation & Legislation International Journal of the Bioflux Society (AACL Bioflux)*, 8(4).
- Barkdoll, B. D., Hagen, B. L., & Odgaard, A. J. (1998). Experimental comparison of dividing open-channel with duct flow in T-junction. *Journal of Hydraulic Engineering*, 124(1), 92-95.
- Bhatta, B. (2009). Analysis of urban growth pattern using remote sensing and GIS: a case study of Kolkata, India. *International Journal of Remote Sensing*, 30(18), 4733-4746.
- Collins, B. D., Montgomery, D. R., & Haas, A. D. (2002). Historical changes in the distribution and functions of large wood in Puget Lowland rivers. *Canadian Journal of Fisheries and Aquatic Sciences*, 59(1), 66-76.
- Crosato, A. (2008). Analysis and modelling of river meandering.
- Chen, H. B., & Lian, G. S. (1992). The numerical computation of turbulent flow in tee-junctions. *J. Hydrodynamics, Amsterdam Ser. B (3)*, 19-25.
- Cleve, C., Kelly, M., Kearns, F. R., & Moritz, M. (2008). Classification of the wildland-urban interface: A comparison of pixel-and object-based classifications using high-resolution aerial photography. *Computers, Environment and Urban Systems*, 32(4), 317-326.
- Darby, S. E., Alabyan, A. M., & Van de Wiel, M. J. (2002). Numerical simulation of bank erosion and channel migration in meandering rivers. *Water Resources Research*, 38(9).
- Duan, J. G. (2005). Analytical approach to calculate rate of bank erosion. *Journal of hydraulic engineering*, 131(11), 980-990.
- Duan, J. G., & Julien, P. Y. (2010). Numerical simulation of meandering evolution. *Journal of Hydrology*, 391(1), 34-46.
- Engelund, F. (1974). Flow and bed topography in channel bends. *Journal of the Hydraulics Division*, 100(Proc. Paper 10963).

- Gao, B. C. (1995, June). Normalized difference water index for remote sensing of vegetation liquid water from space. In *Imaging Spectrometry* (Vol. 2480, pp. 225-237). International Society for Optics and Photonics.
- Goudarzizadeh, R., Hedayat, N., & Jahromi, S. M. (2010). Three-dimensional simulation of flow pattern at the lateral intake in straight path, using finite-volume method. *World Academy of Science, Engineering and Technology*, 47, 656-661.
- Griffiths, P., Hostert, P., Gruebner, O., & van der Linden, S. (2010). Mapping megacity growth with multi-sensor data. *Remote Sensing of Environment*, 114(2), 426-439.
- Guindon, B., Zhang, Y., & Dillabaugh, C. (2004). Landsat urban mapping based on a combined spectral-spatial methodology. *Remote sensing of environment*, 92(2), 218-232.
- Hager, W. H. (1987). Discussion of "Separation Zone at Open-Channel Junctions" by James L. Best and Ian Reid (November, 1984). *Journal of Hydraulic Engineering*, 113(4), 539-543.
- IPCC. (2007). Fourth assessment report. Cambridge, Retrieved from https://www.ipcc.ch/publications_and_data/publications_and_data_reports.shtml
- Ikeda S, Parker G and Sawai K 1981 Bend theory of river meanders: 1. Linear development; *J. Fluid Mech.* 112, 363...377.
- Issa, R. I., & Oliveira, P. J. (1994). Numerical prediction of phase separation in two-phase flow through T-junctions. *Computers & fluids*, 23(2), 347-372.
- Jacquín, A., Misakova, L., & Gay, M. (2008). A hybrid object-based classification approach for mapping urban sprawl in periurban environment. *Landscape and urban planning*, 84(2), 152-165.
- Johannesson, H., & Parker, G. (1989). Linear theory of river meanders. *River meandering*, 181-213.
- Kim, H., Kimura, I., & Shimizu, Y. (2011). Numerical simulation of channel meandering processes. *River, Coastal and Estuarine Morphodynamics: RCEM2011*.
- Karaburun, A. (2010). Estimation of C factor for soil erosion modeling using NDVI in Buyukcekmece watershed. *Ozean Journal of applied sciences*, 3(1), 77-85.
- Knighton David 1984 *Fluvial Forms and Processes*; John Wiley&Sons Inc., New York
- Lambin, E. F. (2001). Global land-use and land-cover change: what have we learned so far?. *Global Change News*, 46, 27-30.
- Landsat, N. A. S. A. (7). Science Data Users Handbook. 2011-03-11]. http://landsathandbook.gsfc.nasa.gov/inst_cal/prog_sectS_2.html.

- Landsat, N. A. S. A. (8). Science Data Users Handbook. 2016-03-29]. <https://landsat.usgs.gov/sites/default/files/documents/Landsat8DataUsersHandbook.pdf>
- Law, S. W., & Reynolds, A. J. (1966). Dividing flow in an open channel. *Journal of the Hydraulics Division*, 92(2), 207-231.
- Lisar, S. Y., Motafakkerazad, R., Hossain, M. M., & Rahman, I. M. (2012). Water stress in plants: causes, effects and responses. In *Water stress*. InTech.
- Mosselman, E. (1998). Morphological modelling of rivers with erodible banks. *Hydrological Processes*, 12(8), 1357-1370.
- Neary, V. S., & Odgaard, A. J. (1993). Three-dimensional flow structure at open-channel diversions. *Journal of Hydraulic Engineering*, 119(11), 1223-1230.
- Neary, V. S., Sotiropoulos, F., & Odgaard, A. J. (1999). Three-dimensional numerical model of lateral-intake inflows. *Journal of Hydraulic Engineering*, 125(2), 126-140.
- Nicholas, A. P., & Sambrook Smith, G. H. (1999). Numerical simulation of three-dimensional flow hydraulics in a braided channel. *Hydrological Processes*, 13(6), 913-929.
- Osman, A. M., & Thorne, C. R. (1988). Riverbank stability analysis. I: Theory. *Journal of Hydraulic Engineering*, 114(2), 134-150.
- Popp, M., & Sallet, D. W. (1983). Experimental investigation of one-and two-phase flow through a tee junction. In *International conference on the physical modelling of multi-phase flow* (pp. 67-88).
- Ramamurthy, A. S., Qu, J., & Vo, D. (2007). Numerical and experimental study of dividing open-channel flows. *Journal of Hydraulic Engineering*, 133(10), 1135-1144.
- Remote Sensing Phenology (2015), [https:// Environmental study/Remote Sensing Phenology.html](https://Environmental%20study/Remote%20Sensing%20Phenology.html)
- Shettar, A. S., & Keshava Murthy, K. (1996). A numerical study of division of flow in open channels. *Journal of Hydraulic Research*, 34(5), 651-675.
- Schuurman, F., Marra, W. A., & Kleinhans, M. G. (2013). Physics-based modeling of large braided sand-bed rivers: Bar pattern formation, dynamics, and sensitivity. *Journal of geophysical research: Earth Surface*, 118(4), 2509-2527.
- Shamloo, H., & Pirzadeh, B. (2008). Investigation of characteristics of separation zones in T-junctions. *WSEAS transactions on Mathematics*, 7(5), 303-312.
- Thanh, M. D., Kimura, I., Shimizu, Y., & Hosoda, T. (2010). Numerical simulation of flow at an open-channel confluence using depth-averaged 2D models with effects of secondary currents. *Journal of Applied Mechanics*, 15, 769-780.

- Uysal, M., & Polat, N. (2015). An investigation of the relationship between land surface temperatures and biophysical indices retrieved from Landsat TM in Afyonkarahisar (Turkey)/Ispitivanje odnosa između temperatura na površini zemlje i biofizičkih pokazatelja dobivenih zemljinim satelitom Landsat TM u Afyonkarahisaru (Turska). *Tehnicki Vjesnik-Technical Gazette*, 22(1), 177-182.
- Weber, L. J., Schumate, E. D., & Mawer, N. (2001). Experiments on flow at a 90 open-channel junction. *Journal of Hydraulic Engineering*, 127(5), 340-350.
- Weng, Q., & Yang, S. (2004). Managing the adverse thermal effects of urban development in a densely populated Chinese city. *Journal of Environmental Management*, 70(2), 145-156.
- Xia, J. Q., Wang, G. Q., & Wu, B. S. (2003). Numerical simulation for the longitudinal and lateral deformation of riverbed in the lower Yellow River, 1, establishment of a 2-D composite model. *Advances in Water Science*, 14(4), 389-395.
- Xu, H. (2008). A new index for delineating built-up land features in satellite imagery. *International Journal of Remote Sensing*, 29(14), 4269-4276.
- Zhang, H. W., & Huai-Liang, C. H. E. N. (2016). The Application of Modified Normalized Difference Water Index by Leaf Area Index in the Retrieval of Regional Drought Monitoring. *DEStech Transactions on Engineering and Technology Research*, (sste).
- Zha, Y., Gao, J., & Ni, S. (2003). Use of normalized difference built-up index in automatically mapping urban areas from TM imagery. *International Journal of Remote Sensing*, 24(3), 583-594.
- Zolezzi, G., & Seminara, G. (2001). Downstream and upstream influence in river meandering. Part 2. Planimetric development. *Journal of Fluid Mechanics*, 438, 183-211.